ARDOT TRC TRANSPORTATION RESEARCH COMMITTEE

TRC1803

Mapping Subsurface Conditions for Transportation Applications

Dr. Clinton M. Wood, Ph.D,. P.E.
Michelle Barry, Ph.D., P.E.
Salman Rahimi
Vanessa Lebow

University of Arkansas - Fayetteville
College of Engineering, Department of Civil Engineering

Final Report

September 2022

TRC1803

Mapping Subsurface Conditions for Transportation Applications

Dr. Clinton M. Wood, Ph.D,. P.E.
Michelle Barry, Ph.D., P.E.
Salman Rahimi
Vanessa Lebow

University of Arkansas - Fayetteville
College of Engineering, Department of Civil Engineering

Final Report

September 2022

Arkansas Department of Transportation

Notice of Nondiscrimination

The Arkansas Department of Transportation (ARDOT) complies with all civil rights provisions of federal statutes and related authorities that prohibit discrimination in programs and activities receiving federal financial assistance. Therefore, the Department does not discriminate on the basis of race, sex, color, age, national origin, religion (not applicable as a protected group under the Federal Motor Carrier Safety Administration Title VI Program), disability, Limited English Proficiency (LEP), or low-income status in the admission, access to and treatment in the Department's programs and activities, as well as the Department's hiring or employment practices. Complaints of alleged discrimination and inquiries regarding the Department's nondiscrimination policies may be directed to Civil Rights Officer Joanna P. McFadden (ADA/504/ Title VI Coordinator), P. 0. Box 2261, Little Rock, AR 72203, (501) 569-2298, (Voice/TTY 711), or the following email address: joanna.mcfadden@ardot.gov.

Free language assistance for Limited English Proficient individuals is available upon request.

This notice is available from the ADA/504/Tittle VI Coordinator in large print, on audiotape and Braille

Disclaimer:

The contents of this report reflect the views of the authors, who are responsible for the facts and the accuracy of the data presented herein. The contents do not necessarily reflect the official views or policies of ARDOT and they assume no liability for the contents or use thereof. This report does not constitute a standard, specification, or regulation. Comments contained in this report related to specific testing equipment and materials should not be considered an endorsement of any commercial product or service; no such endorsement is intended or implied.

TECHNICAL REPORT DOCUMENTATION PAGE

1. Report No. TRC1803	2. Government Accession No.	3. Recipient's Catalog No.
4. Title and Subtitle Mapping Subsurface Conditions for Transportation Applications		5. Report Date September 2022 6. Performing Organization Code:
7. Author(s) Clinton M. Wood Michelle Barry Salman Rahimi Vanessa Lebow		8. Performing Organization Report No.
9. Performing Organization Name and Address University of Arkansas – Fayetteville 4190 Bell Engineering Center Fayetteville, AR 72701		10. Work Unit No. 11. Contract or Grant No. Project TRC1803
12. Sponsoring Agency Name and Address Arkansas Department of Transportation (SPR) 10324 Interstate 30 Little Rock, AR 72209		13. Type of Report and Period Covered FINAL 01/2019 - 09/2022 14. Sponsoring Agency Code
15. Supplementary Notes		

16. Abstract

Geophysical methods including Multichannel Analysis of Surface Waves (MASW) using both Rayleigh and Love waves, P-wave refraction, Horizontal to Vertical Spectral Ratio (HVSR), Capacitively-Coupled Resistivity (CCR), Electrical Resistivity Tomography (ERT), Ground Penetration Radar (GPR), and Electromagnetic Ground Conductivity (EM31) were used for bedrock mapping and slope stability investigations for several ARDOT transportation projects. For slope stability with a shallow and complex bedrock topography, which is the case for most ARDOT projects, a combination of HVSR, MASW, and ERT or P-wave refraction was observed to be viable. For such sites, a 3D image of bedrock topography is a key factor required for the development of a detailed slope stability model. In this regard, the HVSR is proposed as an effective tool when used in conjunction with other geophysical methods to create a 3D map of bedrock topography in a simple, rapid, cost-effective, and accurate manner.

17. Key Words Geophysical methods, MASW, HVSR, ERT, transportation projects, slope stability	18. Distribution Statement No restrictions. This document is available to the public through the National Technical Information Service, Springfield, VA 22161. http://www.ntis.gov		
19. Security Classif. (of this report) Unclassified	20. Security Classif. (of this page) Unclassified	21. No. of Pages 190	22. Price

Form DOT F 1700.7 (8-72) Reproduction of completed page authorized.

SI* (MODERN METRIC) CONVERSION FACTORS

APPROXIMATE CONVERSIONS TO SI UNITS

Symbol	When You Know	Multiply By	To Find	Symbol
		LENGTH		
in	inches	25.4	millimeters	mm
ft	feet	0.305	meters	m
yd	yards	0.914	meters	m
mi	miles	1.61	kilometers	km
		AREA		
in^2	square inches	645.2	square millimeters	mm^2
ft^2	square feet	0.093	square meters	m^2
yd^2	square yard	0.836	square meters	m^2
ac	acres	0.405	hectares	ha
mi^2	square miles	2.59	square kilometers	km^2
		VOLUME		
fl oz	fluid ounces	29.57	milliliters	mL
gal	gallons	3.785	liters	L
ft^3	cubic feet	0.028	cubic meters	m^3
yd^3	cubic yards	0.765	cubic meters	m^3
		NOTE: volumes greater than 1000 L shall be shown in m^3		
		MASS		
oz	ounces	28.35	grams	g
lb	pounds	0.454	kilograms	kg
T	short tons (2000 lb)	0.907	megagrams (or "metric ton")	Mg (or "t")
		TEMPERATURE (exact degrees)		
°F	Fahrenheit	5 (F-32)/9 or (F-32)/1.8	Celsius	°C
		ILLUMINATION		
fc	foot-candles	10.76	lux	lx
fl	foot-Lamberts	3.426	$candela/m^2$	cd/m^2
		FORCE and PRESSURE or STRESS		
lbf	poundforce	4.45	newtons	N
lbf/in^2	poundforce per square inch	6.89	kilopascals	kPa

APPROXIMATE CONVERSIONS FROM SI UNITS

Symbol	When You Know	Multiply By	To Find	Symbol
		LENGTH		
mm	millimeters	0.039	inches	in
m	meters	3.28	feet	ft
m	meters	1.09	yards	yd
km	kilometers	0.621	miles	mi
		AREA		
mm^2	square millimeters	0.0016	square inches	in^2
m^2	square meters	10.764	square feet	ft^2
m^2	square meters	1.195	square yards	yd^2
ha	hectares	2.47	acres	ac
km^2	square kilometers	0.386	square miles	mi^2
		VOLUME		
mL	milliliters	0.034	fluid ounces	fl oz
L	liters	0.264	gallons	gal
m^3	cubic meters	35.314	cubic feet	ft^3
m^3	cubic meters	1.307	cubic yards	yd^3
		MASS		
g	grams	0.035	ounces	oz
kg	kilograms	2.202	pounds	lb
Mg (or "t")	megagrams (or "metric ton")	1.103	short tons (2000 lb)	T
		TEMPERATURE (exact degrees)		
°C	Celsius	1.8C+32	Fahrenheit	°F
		ILLUMINATION		
lx	lux	0.0929	foot-candles	fc
cd/m^2	$candela/m^2$	0.2919	foot-Lamberts	fl
		FORCE and PRESSURE or STRESS		
N	newtons	0.225	poundforce	lbf
kPa	kilopascals	0.145	poundforce per square inch	lbf/in^2

*SI is the symbol for the International System of Units. Appropriate rounding should be made to comply with Section 4 of ASTM E380.
(Revised March 2003)

TABLE OF CONTENTS

LIST OF FIGURES

LIST OF TABLES

APPENDICES

Abstract

Geophysical methods including Multichannel Analysis of Surface Waves (MASW) using both Rayleigh and Love waves, P-wave refraction, Horizontal to Vertical Spectral Ratio (HVSR), Capacitively-Coupled Resistivity (CCR), Electrical Resistivity Tomography (ERT), Ground Penetration Radar (GPR), and Electromagnetic Ground Conductivity (EM31) were used for bedrock mapping and slope stability investigations for several ARDOT transportation projects. In Phase I, all geophysical methods were applied for two ARDOT test sites to investigate the advantages and limitations of each method. Based on the performance of each method in Phase I, the potential non-invasive geophysical methods best suited for slope stability investigations and bedrock mapping were identified. These methods were then implemented in Phase II for several ongoing ARDOT transportation projects. For slope stability with a shallow and complex bedrock topography, which is the case for most ARDOT projects, a combination of HVSR, MASW, and ERT or P-wave refraction was observed to be viable. For such sites, a 3D image of bedrock topography is a key factor required for the development of a detailed slope stability model. In this regard, the HVSR is proposed as an effective tool when used in conjunction with other geophysical methods to create a 3D map of bedrock topography in a simple, rapid, cost-effective, and accurate manner. This method was effectively used for three current slope stability sites in Arkansas that have recently experienced slope movements. For bedrock mapping and rippability estimates, the combination of the MASW and HVSR is recommended, with P-wave refraction also being a viable method. MASW or P-wave refraction should be used for easily accessible areas for bedrock mapping and rippability determination. HVSR can be used for locations where array-based testing is difficult to use (i.e. rough terrains and steep slopes) to cover a larger spatial extent. Using these methods, a continuous image of subsurface layering can be generated for a proposed highway alignment where significant material excavations are required. This information would be beneficial for both ARDOT and contractors as it can aid in the determination of the most cost-effective solutions for the highway alignment with the minimum amount of hard rock excavation, and it can prevent construction delays due to the unexpected subsurface conditions.

Keywords: Geophysical methods, MASW, HVSR, ERT, transportation projects, slope stability.

Executive summary

E.1. Introduction

This report provides the results and findings of the Arkansas Department of Transportation (ARDOT) TRC1803 research project. This research project is aimed at identifying the potential non-invasive geophysical methods best suited for slope stability investigations and bedrock mapping for ARDOT transportation projects. A summary of the research project is provided in Chapter 1. Chapter 2 discusses the different geophysical methods used in this research project. Information regarding the data processing and data interpretation of the geophysical methods are provided in Chapter 3. The results and findings from Phase I and Phase II of the project are presented in Chapter 4 and Chapter 5, respectively. Chapter 6 details the potential benefits and cost, and time savings of using geophysical methods instead of traditional in-situ methods (e.g. drilling and sampling) for slope stability and bedrock mapping for transportation projects. A summary of the conclusions is provided in Chapter 7. Appendices and guidelines are also provided that include supplemental information regarding this research project.

E.2. Methods and materials

Several geophysical methods were employed in this study, including Multichannel Analysis of Surface Waves (MASW) using both Rayleigh and Love type surface waves, P-wave refraction, Horizontal to Vertical Spectral Ratio (HVSR or H/V), Capacitively-Coupled Resistivity (CCR), Electrical Resistivity Tomography (ERT), Ground Penetration Radar (GPR), and Electromagnetic Ground Conductivity Survey (EM31). A brief explanation about the backgrounds, concepts, equipment used, and field testing configurations for each geophysical method is provided in Chapter 2.

In Phase I of the project, two sites were tested using each of the geophysical methods discussed above. These sites include the Hardy site in north-central Arkansas that contains shallow and highly variable bedrock conditions along some portions of the highway alignment that required excavation and rock-cut slope design, and the Sand Gap site in north-west Arkansas with slope stability issues that have recently caused several cracks in the pavement. The locations of the test sites along with the geophysical testing locations, are presented in Figure E.1.

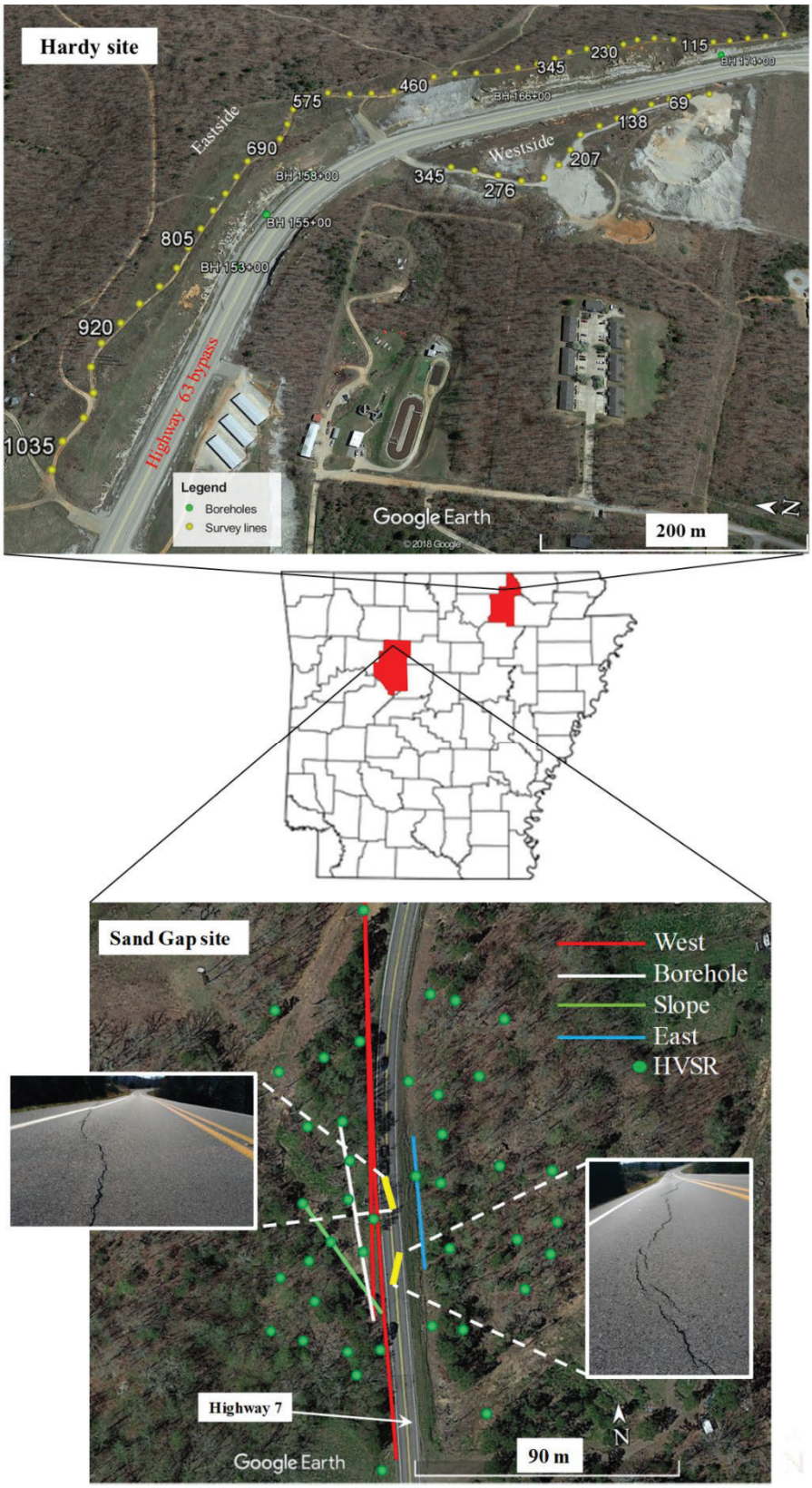

Figure E.1- Locations of the test sites for Phase I. Top) Hardy site and bottom) Sand Gap site along with the cracks observed in the pavement due to the slope movements.

Based on the performance of different geophysical methods in Phase I, the four best methods were selected for Phase II to further investigate and demonstrate their capabilities in bedrock mapping and slope stability investigation. These methods include MASW, HVSR, P-wave refraction, and ERT. These methods were applied at three ongoing ARDOT transportation projects, including bedrock mapping for two proposed highway alignments (Little Rock site in Figure E.2 and Hot Springs site in Figure E.3) and slope stability investigations for an active slope that has recently experienced several long cracks as a result of the slope movements (Ozark site in Figure E.4).

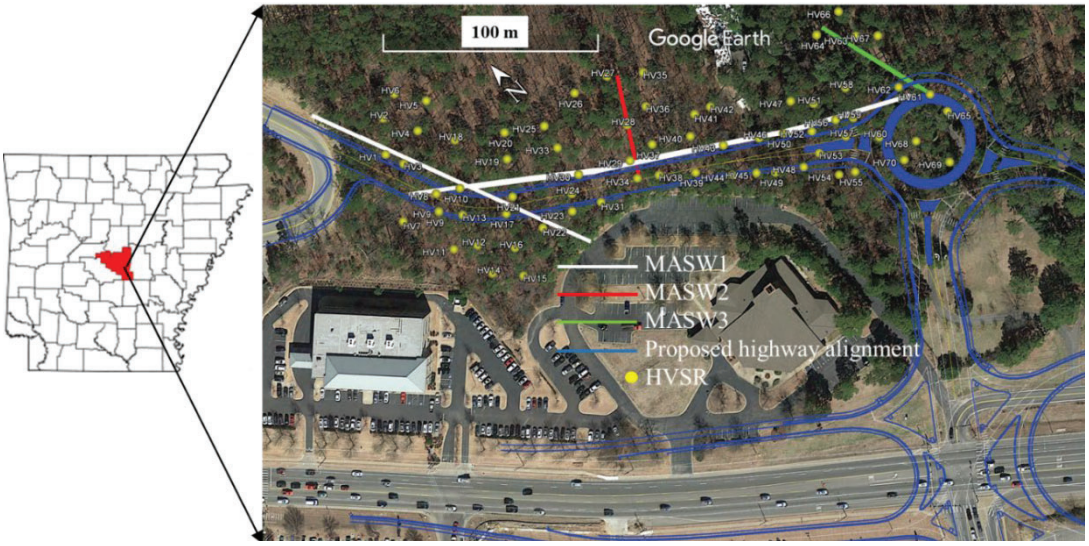

Figure E-2- Location of the Little Rock site for Phase II of the project.

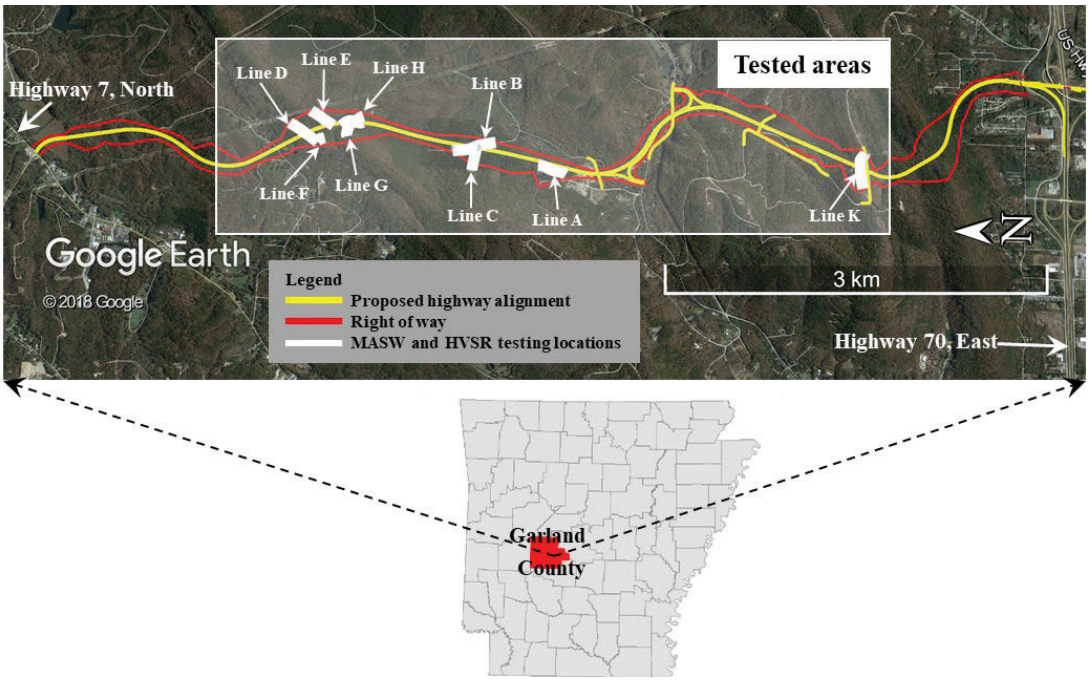

Figure E.3- Location of the Hot Springs site for Phase II of the project.

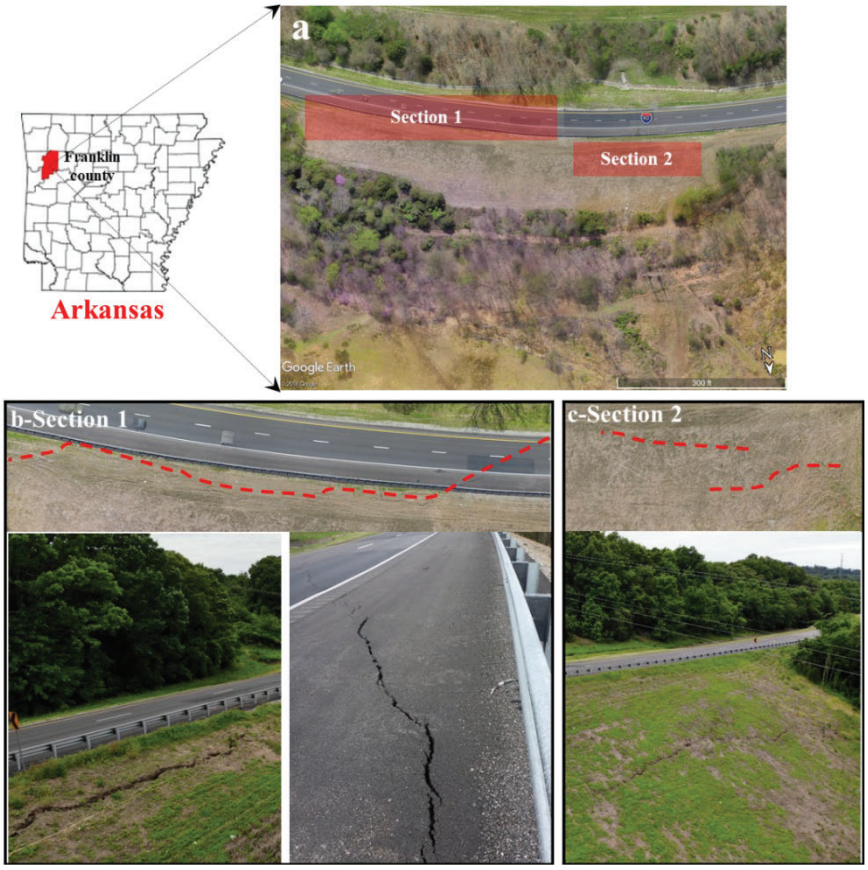

Figure E.4- Location of the Ozark site for Phase II of the project along with the cracks observed during the field measurements.

E.3 Data processing and data interpretation

Data processing procedures used for each geophysical method are discussed in Chapter 3 of the report. This includes different pieces of software and Matlab codes used to analyze the raw data from the field measurements. Data processing and interpretation can vary from very simple procedures (e.g. HVSR and EM31) to more complex procedures (e.g. P-wave refraction and MASW) depending on the testing method and site conditions. In addition, issues and challenges that might be faced in each method are discussed.

E.4 Results and discussions from Phase I

The processed data from the geophysical testing in Phase I are used to create 2D cross-sections for the Hardy and Sand Gap sites. The obtained cross-sections are compared with the pre-existing boring logs and available geotechnical site information. To quantify the discrepancies between the geophysical methods and the boring log records, an error index (EI) value (i.e., the cumulative error between the borings and the particular geophysical tests) is defined for the Hardy site. According to the error-index value calculated for the Eastside of Hardy (see Figure E.5), MASW using Love type surface waves and HVSR resulted in the lowest error-index values. However, for the Westside of Hardy, the two best geophysical methods were determined to be MASW using Rayleigh type surface waves and HVSR. Such inconsistencies between the results of the Eastside and Westside of the Hardy site are caused by differences between the subsurface layering of the two survey lines (i.e., very shallow bedrock <5 m for the Eastside versus deeper bedrock >5 m for the Westside). More discussions in this regard are provided in Chapter 4 of the report.

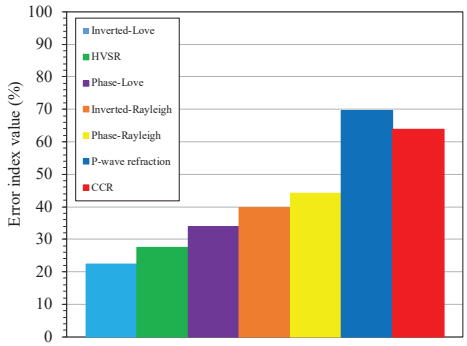

Figure E.5- Error index values related to each geophysical method for the Eastside of the Hardy site.

Shown in Figure E.6 and Figure E.7 are the results of the MASW testing using Love type surface waves and the HVSR measurements for the Eastside of the Hardy site, respectively. Soil/bedrock interfaces estimated from the MASW testing using Love type surface waves and the HVSR measurements are shown with a black dashed line in these figures. From Figure E.6 and Figure E.7, bedrock locations were estimated with high accuracy when compared to the available boring logs using both MASW testing using Love type surface waves and HVSR measurements.

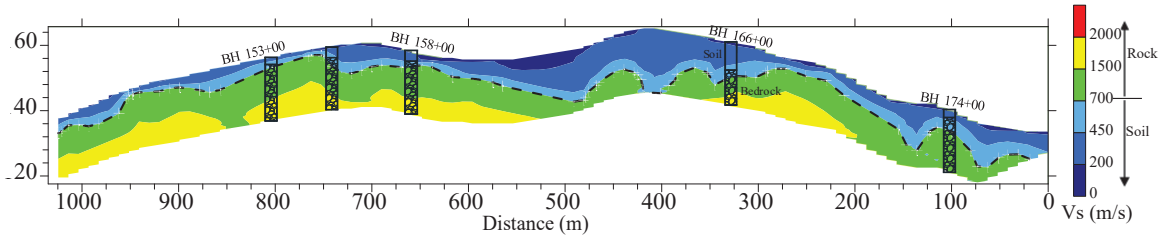

Figure E.6- Pseudo 2D Vs cross-section for the Eastside of the Hardy site generated from the MASW using Love type surface waves along with the boring logs.

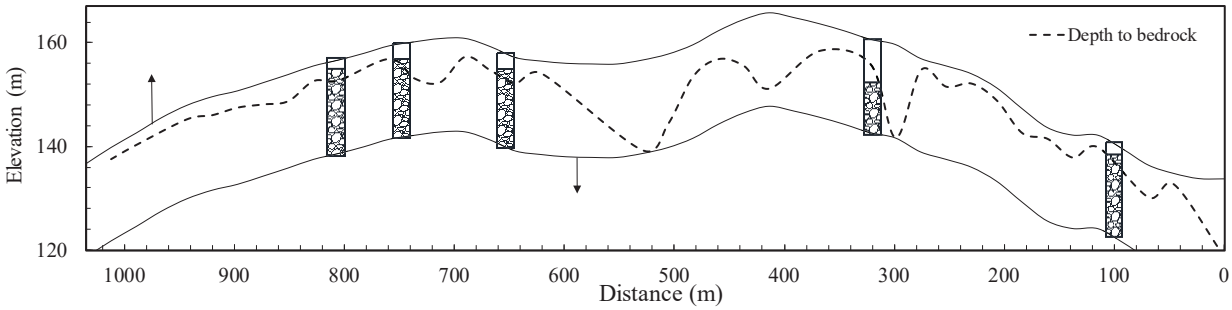

Figure E.7- 2D cross-section for the Eastside of the Hardy site generated from the HVSR measurements along with the boring logs.

For the Sand Gap site, three contour maps are created, including surface elevations from the GPS readings and Google Earth information (Figure E.8), depths to bedrock from the HVSR measurements (Figure E.9), and bedrock elevations determined from the surface elevations and HVSR measurements (Figure E.10). These contour maps are valuable for estimating the vertical and spatial variability of the bedrock layers below the ground surface across the tested areas for further slope stability analysis.

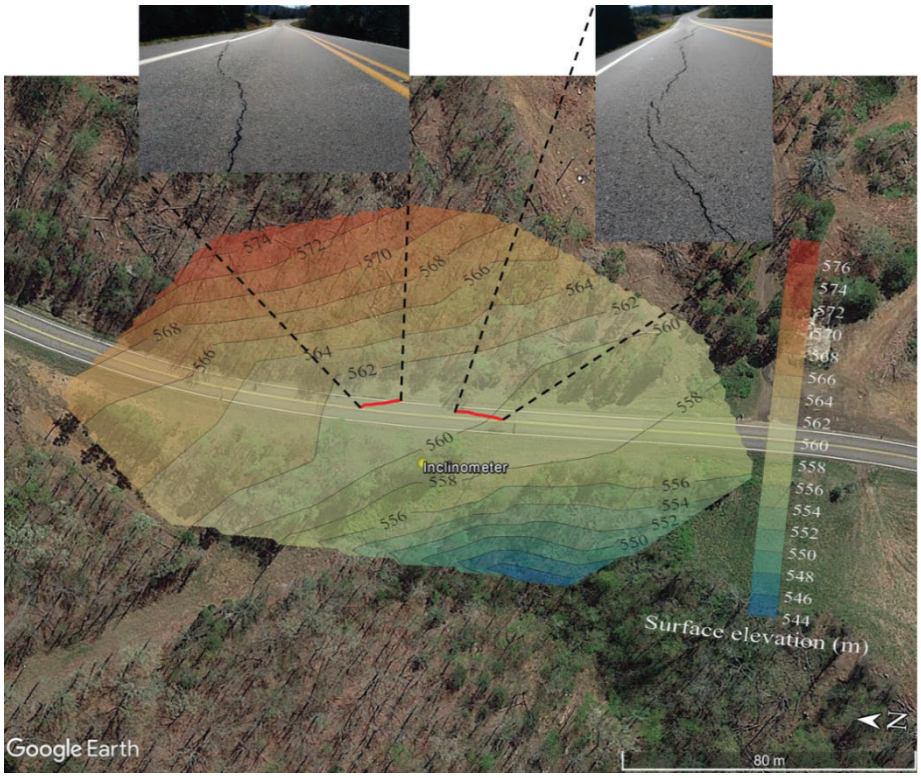

Figure E.8- Surface elevation contour map across the Sand Gap site along with the cracks observed in the pavement.

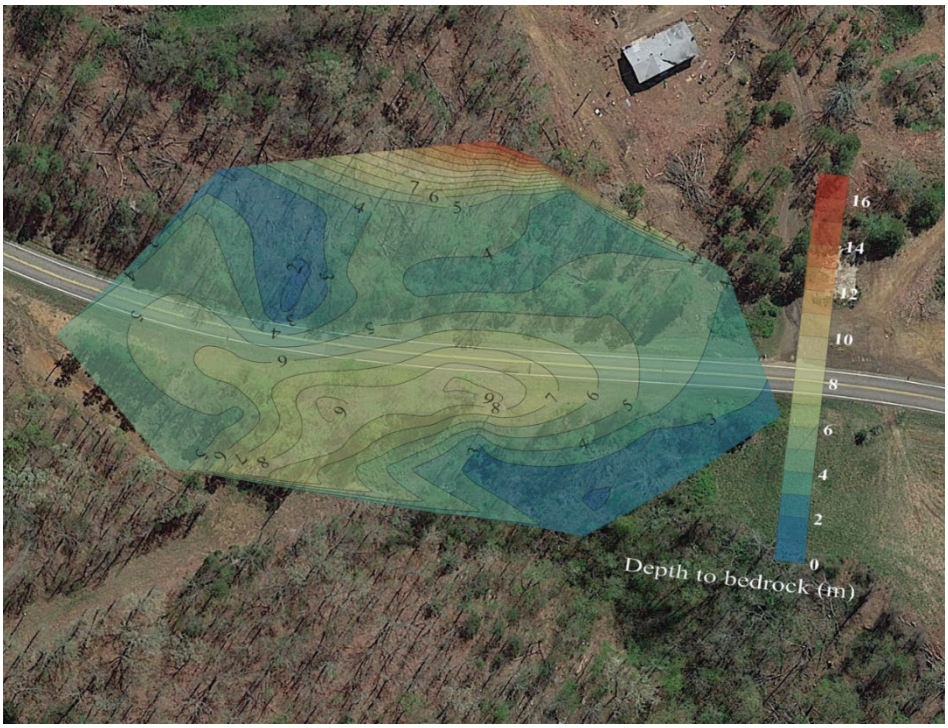

Figure E.9- Depths to the bedrock across the Sand Gap site using HVSR measurements.

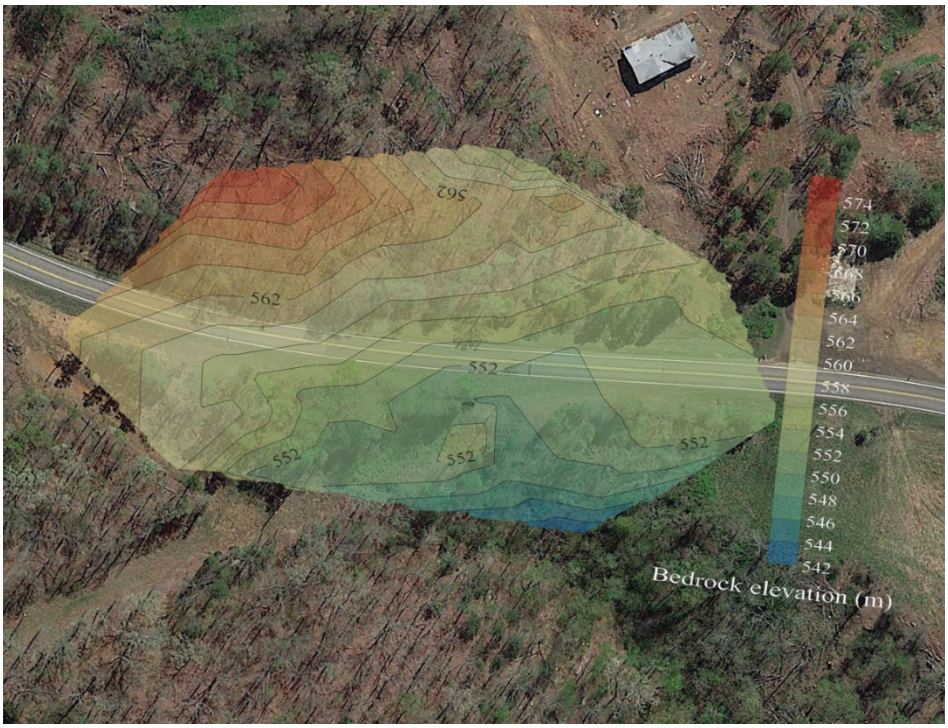

Figure E.10- Bedrock elevations across the Sand Gap site using HVSR measurements.

In terms of the slip surface detection, one of the interesting results of the MASW testing for the Sand Gap site is the pseudo 2D Vs cross-section for the slope survey line (Figure E.11), which was conducted longitudinal to the slope as shown in Figure E.1 with the green line. From Figure E.11, an increase in the bedrock elevation near the bottom of the slope survey line is observed. This hump in the bedrock elevation at the bottom of the slope can trap water at the bottom of the slide after a heavy rainfall event. The trapped water in this section can cause slope movements through different processes such as an increase in the total weight of the potential slip surface by saturating the soil layers inside the slip surface, reduction in soil grain-to-grain contacts which lead to a reduction in soil shear strength, and a reduction in the friction between the soil and bedrock at the soil/bedrock interface. More information in this regard is provided in Chapter 4 of the report.

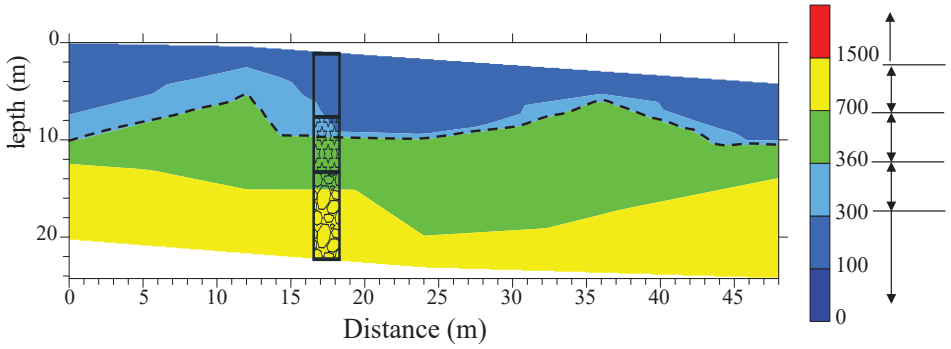

Figure E.11- Pseudo 2D Vs cross-section from the MASW using Love type surface waves for the MASW_Slope survey line.

Based on the obtained results, the soil/bedrock interface is considered the most critical slip surface, particularly at sections where a relatively steep soil/bedrock interface exists near the ground surface. This is confirmed by the inclinometer measurements in which a zone of displacement was observed from the ground surface to approximately 8 m depth. This depth matches well with the soil/bedrock interface detected from the MASW results at the inclinometer location, as illustrated in Figure E.12. Additionally, the most critical slip surfaces are determined to be likely on the Southwest of the Sand Gap site, which contains relatively steep soil/bedrock interfaces below the pavement. More discussions regarding the potential slip surfaces are provided in Chapter 4 of the report.

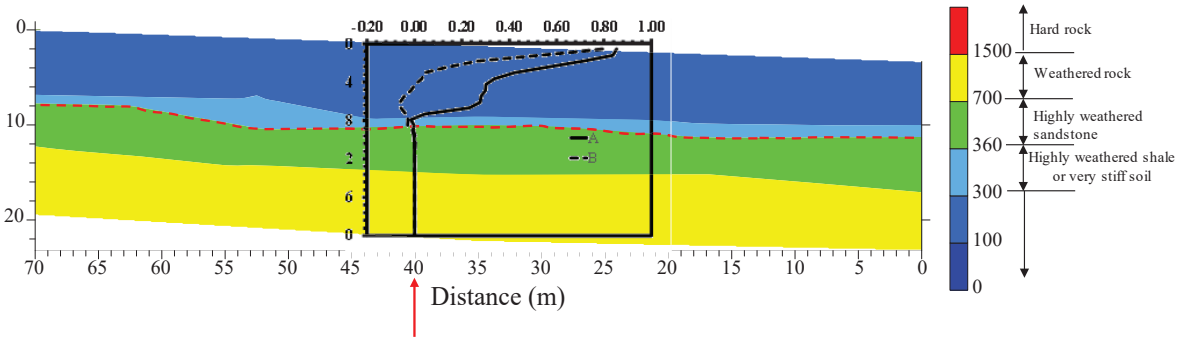

Figure E.12- Pseudo 2D Vs cross-section from the MASW using Love type surface waves for the Borehole survey line at the Sand Gap site along with the displacements recorded by an inclinometer.

E.5 Results and discussions from Phase II

The four best geophysical methods selected from Phase I were applied for three ongoing ARDOT transportation projects, including slope stability investigation for the Ozark site and bedrock mapping for the Hot Springs and Little Rock sites.

For the Ozark slope stability site, using the combination of the four selected geophysical methods from Phase I, a detailed image of the subsurface layering is generated that provides insight into the reason(s) behind the slope movements. This is done by identifying the key features of the bedrock topography (e.g. bedrock depression) using the MASW (Figure E.13c), HVSR (Figure E.14), and ERT (Figure E.13d) methods and by detecting the highly saturated zones and the water table location along the slope using the ERT and P-wave refraction methods (Figure E.13d).

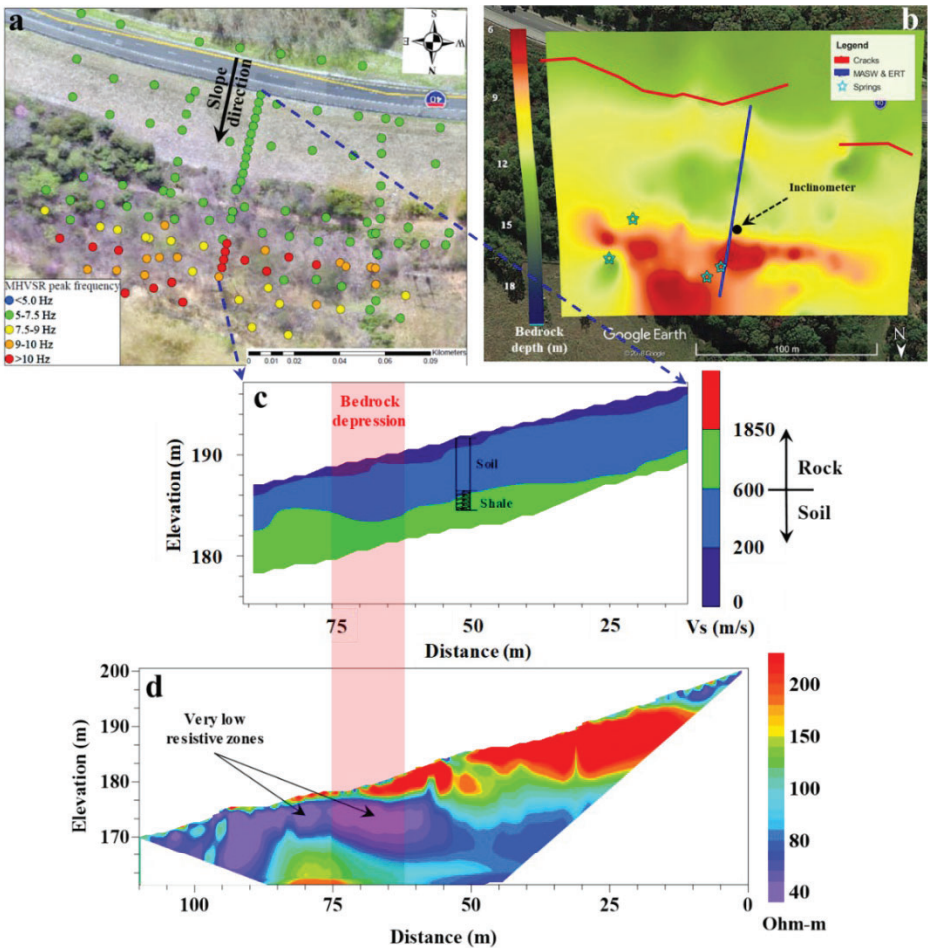

Figure E.13- Results for the Ozark slope stability site. a) locations of geophysical testing along with the variations of the HVSR peak frequencies shown with graduated colors, b) contour map of bedrock depth from HVSR, c) Pseudo 2D Vs profile from MASW revealing bedrock depression, d) ERT profile revealing bedrock depression and fully saturated area above it.

A full 3D map of bedrock elevation is created using the HVSR method, as shown in Figure E.14. This full 3D map is valuable for slope stability studies because it reveals several depressions in the bedrock layer at the very bottom of the slope, features that were not detected using the conventional in-situ methods (e.g. drilling and sampling). This highlights the capability of the HVSR method in detecting key features of the bedrock layer that contribute to the slope movements in a rapid and cost-effective manner.

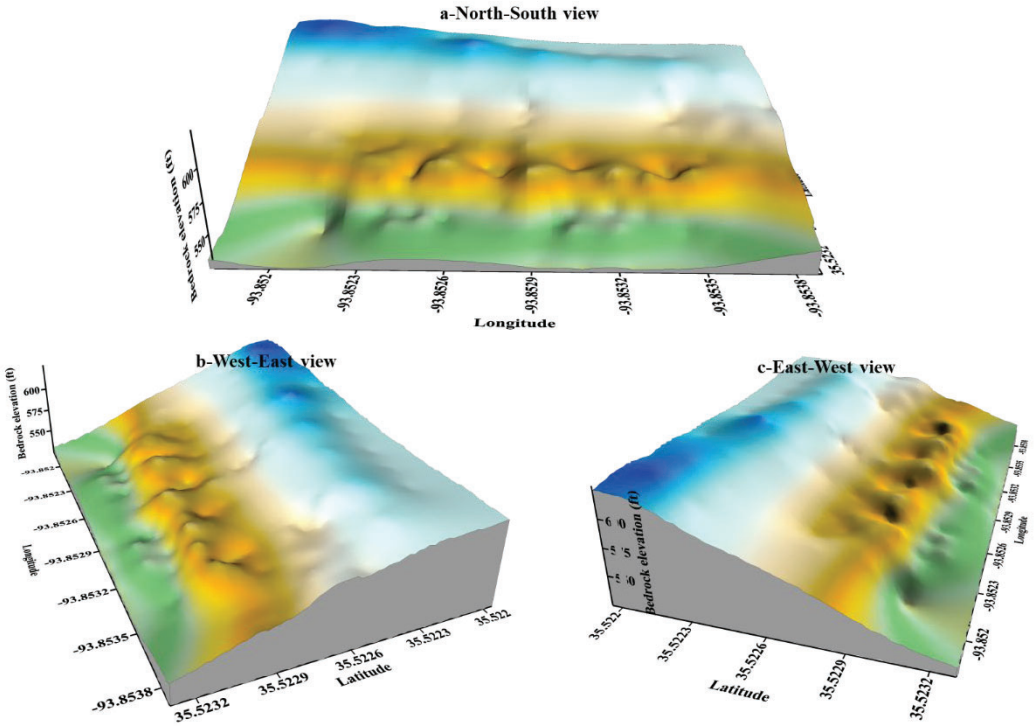

Figure E.14- Full 3D bedrock elevation generated for the Ozark site using the HVSR method.

Additionally, the MASW and HVSR methods are used for bedrock mapping for two proposed highway alignments with highly variable bedrock layers, where significant rock excavations are expected. Using the MASW method, the bedrock location, bedrock variation, and bedrock rippability are effectively identified along the proposed highway alignments. This information is provided in pseudo 2D Vs cross-sections, such as the one shown in Figure E.15a. Using the HVSR method, depth to different bedrock layers are generated along the proposed highway alignments for locations with steep slopes and areas densely covered with trees and bushes (see Figure E.15c), where geotechnical/geophysical (e.g. MASW) field measurements were difficult to use. The HVSR method is valuable for rapid bedrock detection for sites where only information regarding bedrock location is needed (not the stiffness of the bedrock materials) or for

supplementing other results over a larger spatial area. This method is capable of predicting both shallow and deep bedrock depths in a rapid, non-invasive, and cost-effective manner.

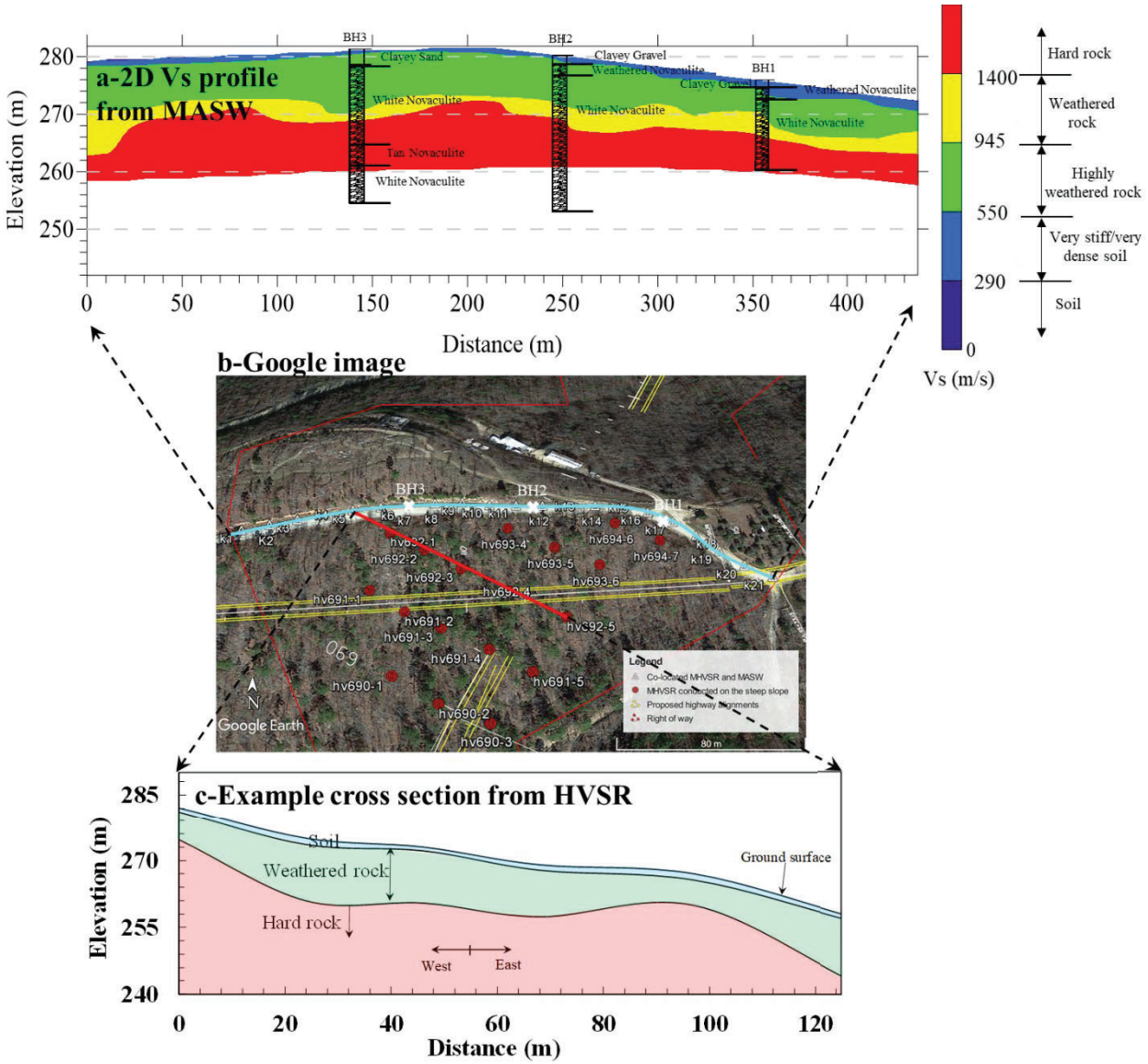

Figure E.15- Example results of the bedrock mapping using geophysical methods for the Hot Springs site. a) a pseudo 2D Vs profile from MASW, b) Google image of the tested locations, c) example cross-section from HVSR.

E.6 Potential time and cost savings

According to the results of this research, implementing non-invasive geophysical methods for bedrock mapping along proposed highway alignments or slope instability investigations can lead to significant cost and time savings for transportation projects in several ways:

- Preventing construction delays that can be caused due to unexpected subsurface conditions (i.e. hard rock layers or problematic soil layers located within the excavation areas).
- Locating the most suitable and cost-effective solution for the highway alignment that requires the minimum amount of hard (marginal or non-rippable) rock excavations.
- Aiding in preliminary deep foundation designs for bridge construction.
- Identifying the potential slip surface(s) and the reason(s) behind the slope movements to aid in slope remediation efforts and avoid a slope failure.

The Ozark slope stability site is provided as an example of an ARDOT case history, where a significant amount of money was saved by performing geophysical methods instead of drilling and sampling for investigating slope stability issues.

1 Introduction

Problem statement

Each year ARDOT spends millions of dollars to deal with problematic soil and rock conditions, which cause slope stability issues along roadways or require removal of rock layers. The remediation of slopes and the removal of bedrock can be both time consuming and expensive. While slope stability and shallow bedrock issues may be unavoidable or even expected on certain projects, encountering unexpected subsurface conditions during construction can lead to significant cost overruns, change orders, and construction delays. Currently, subsurface conditions are assessed on transportation projects using conventional in-situ methods such as drilling and sampling along the project alignment. While these methods provide an acceptable level of accuracy for projects where soil and rock layers are consistent in depth and thickness, significant errors can occur when conditions are variable both inline and crossline to the alignment. This is because the conventional in-situ methods (e.g. drilling and sampling) only provide discrete information about subsurface layering with material types between the boring logs determined based on engineering judgments. If a more accurate/complete 2D or 3D understanding of the subsurface conditions were available during the design phase, some problems could be avoided or at least scheduled and budgeted for in advance. For slope stability problems, a 2D/3D image of subsurface layering is needed in order to be able to identify the potential slip surfaces. The 2D/3D image of the subsurface conditions can also facilitate the development of a detailed slope stability model. Obtaining this understanding of the subsurface conditions using conventional in-situ methods is extremely time and cost-prohibitive; however, geophysical methods may offer a more practical solution for sites where the subsurface conditions are quite variable or for sites where conventional in-situ methods are difficult to be used such as steep or unstable slopes.

Both 2D and 3D subsurface maps can be developed rapidly and cost-effectively using geophysical methods such as MASW and HVSR. Each geophysical method has potential strengths and weaknesses for detecting various underground features. For example, CCR and ERT have shown to be effective at identifying the water table and changes in the subsurface, which have different electrical resistances (changes in soil type, clay vs sand). Surface wave methods and seismic refraction provide the advantage of measuring the rippability of rock or the strength of

clay deposits. HVSR provides the advantage of simple field testing procedures and analysis methods but sacrifices detailed information regarding the subsurface materials.

Project Objectives

The main goal of this research project is to examine the applicability of various geophysical methods to map problematic soil and rock conditions along highway alignments. Summarized below are the project objectives for the TRC1803.

1. *Identify two ARDOT test sites that could benefit from geophysical testing.* In Phase I of the project, two ARDOT test sites are selected based on the recommendation of the PI of the project and the ARDOT subcommittee. Two types of sites are targeted to achieve the goal of the project. This includes: (1) a site with shallow bedrock layers where excavations of rock and development of rock slopes are required, (2) a site with slope stability problems where remediation design could benefit from mapping the slip plane associated with the slide.
2. *Develop a proposed field investigation plan for each site and perform testing using various geophysical methods*. Once the two test sites are selected for Phase I, field investigation plans are developed for each of the test sites. Depending on the type of site, the goal of the testing is to either determine the location and stiffness of the bedrock layer or determine the location of the potential slip plane of the slide. Different geophysical methods are conducted at each of the test sites to develop 2D and/ or 3D maps of subsurface layering and conditions. The 2D or 3D map of subsurface layering would help locate the hard rock layer as well as the potential slip surface for the test sites.
3. *Analyze collected field data to determine the accuracy, advantages, benefits, cost, and limitations of each geophysical method for specific tasks.* All the data acquired from the field measurements at each of the test sites for Phase I are analyzed and processed to identify the capability of each geophysical method for detecting the bedrock location and stiffness as well as the potential slip surface for the slope stability site. A comparison is made between different geophysical methods in terms of the time required for the field measurements for a specific distance along the alignment, the time required to process the raw data, ambiguity in the data processing and data interpretation, capability of each geophysical method for locating the bedrock layers or the potential slip surface, maximum

depth of exploration, and the accuracy of each geophysical method for a specific task. The geophysical methods used in Phase I are ranked based on their performance for each of the specific tasks to determine the ones with the best performance.

4. *Apply the geophysical methods selected in Phase I for several ongoing ARDOT transportation projects.* In Phase II of the project, several ongoing ARDOT transportation projects, as recommended by the ARDOT sub-committee, are selected to validate the accuracy of the selected geophysical methods from Phase I. Similar to Phase I, two types of sites, including sites with shallow bedrock layers located within the proposed excavation areas and sites with slope stability issues are selected. The results from the geophysical methods are compared to other information from the boring logs, inclinometer readings, and other geophysical methods to identify their accuracy and advantages of each method for each task.
5. *Conduct slope stability analyses on sites using geophysical and other data from the tested slope stability site.* 2D or 3D numerical slope stability analyses are performed for each of the slope stability investigation sites using the subsurface layering information available from traditional drilling and sampling methods. Limit equilibrium procedures (SLIDE and UTEXAS software) are investigated to determine the most effective software and modeling techniques. Then, additional numerical slope stability analyses are generated by adding the information from the geophysical measurements for each of the slope stability investigation sites. For these models, the corresponding soil properties will be determined through correlations from the literature and those developed by the Co-PI based on laboratory testing. The two slope stability models generated using the subsurface layering from traditional drilling and sampling methods and the geophysical methods are compared to see how the addition of geophysical results into slope stability models is affecting the potential slip surface of each slope stability investigation site. The goal is to determine the most effective geophysical methods/parameters to locate a slip plane and compare the slope stability analysis using this more complete and continuous dataset with the traditional slope stability methods.

Sites selection and site backgrounds

1.1.1 Phase I

The first phase (Phase I) of the project was to select two available ARDOT project sites with pre-existing boring logs to conduct the geophysical surveys. One site with shallow and highly variable bedrock depths along some portions of the highway alignment that require excavation and potential rock cut slope design. Another site with previous slope stability issues (i.e., an active or moving section of the earth), especially one with an irregular failure surface (if known).

Two ARDOT project sites that meet the above requirements were selected for the field measurements. The Hardy site is located in north-central Arkansas and has quite variable bedrock depths, and the Sand Gap site is located in north-west Arkansas, which has been considered as an active slope with previous stability issues. The locations and geologic settings of the sites will be discussed in the following sections.

1.1.1.1 Hardy

The Hardy site is located in north-central Arkansas near a small city by the same name in Sharp County, as shown in Figure 1.1. The field tests were conducted along some portions of the Eastside and Westside of the Highway 63 bypass, which is an approximately 2.5 km long road around the city of Hardy. The exact location of the survey lines for each geophysical test is presented later in the report. The pre-existing borings were drilled and analyzed by ARDOT. Based on the geologic backgrounds and pre-existing boreholes, the subsurface conditions of the site are highly variable and depths to the bedrock are very shallow. These characteristics make the site ideal to investigate the efficiency of the available geophysical methods for rapid and cost-effective subsurface mapping, especially for bedrock detection for transportation applications.

Figure 1.1- Location of the test site at Hardy, AR.

According to the previous boring log information, the entire subsurface profile of the site consists of a hard fractured cherty dolomite, overlain by a stiff to very stiff cherty clay. The Rock Quality Designation (RQD) index reported by ARDOT for the cherty dolomite layer ranges between 0-99 %. This indicates that the degree of weathering for the cherty dolomite layer varies significantly in the tested areas. The thickness of the top cherty clay layer is also quite variable along the Highway alignment, ranging from less than 1 m to a maximum of 20 m. In Figure 1.2, a section of the rock cut slope along the Highway 63 bypass is shown. As shown in this figure, the elevation and depth to the bedrock are very shallow and quite variable along the Highway alignment.

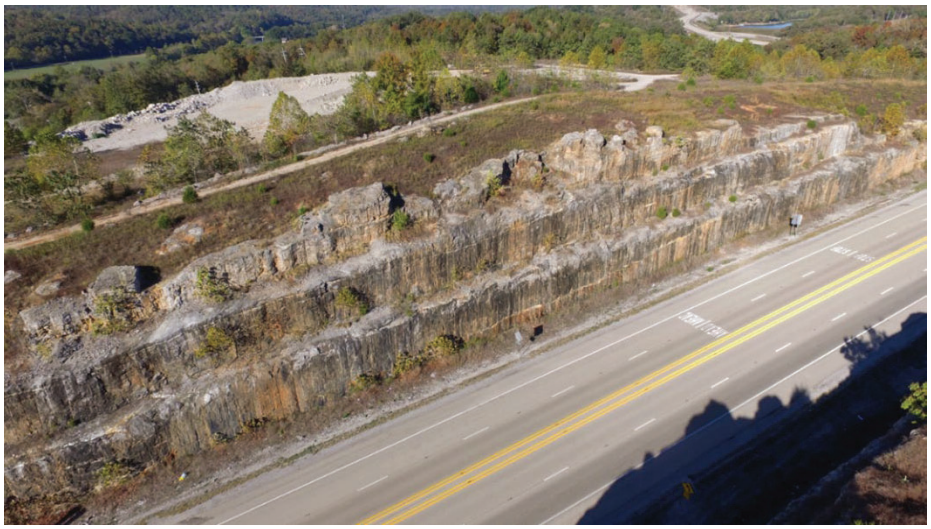

Figure 1.2- Example of the rock materials in tested areas at Hardy, AR.

1.1.1.2 Sand Gap

The Sand Gap site is located in the Ozark Mountain region in north-west Arkansas, along Arkansas Highway 7, as shown in Figure 1.3. The Ozark Mountains are a part of the Boston Mountains characterized by narrow V-shaped valleys and vertical bluffs of limestone and sandstone. The terrain is dominated by steep hillslopes underlain by varying rock types. Interbedded shale and sandstone layers make up the bedrock system within the study area (Koehn et al. 2019). According to the boring logs provided by ARDOT, the subsurface consists of a stiff clay layer with gravel from the ground surface to depths of 4-7 m, followed by bedrock. The bedrock layer mostly consists of sandstone, but a thin, highly weathered shale layer was also observed in one of the boreholes. It should be noted that all the boring logs are located on the Westside of Arkansas Highway 7, and very little information is available for the Eastside of the Highway.

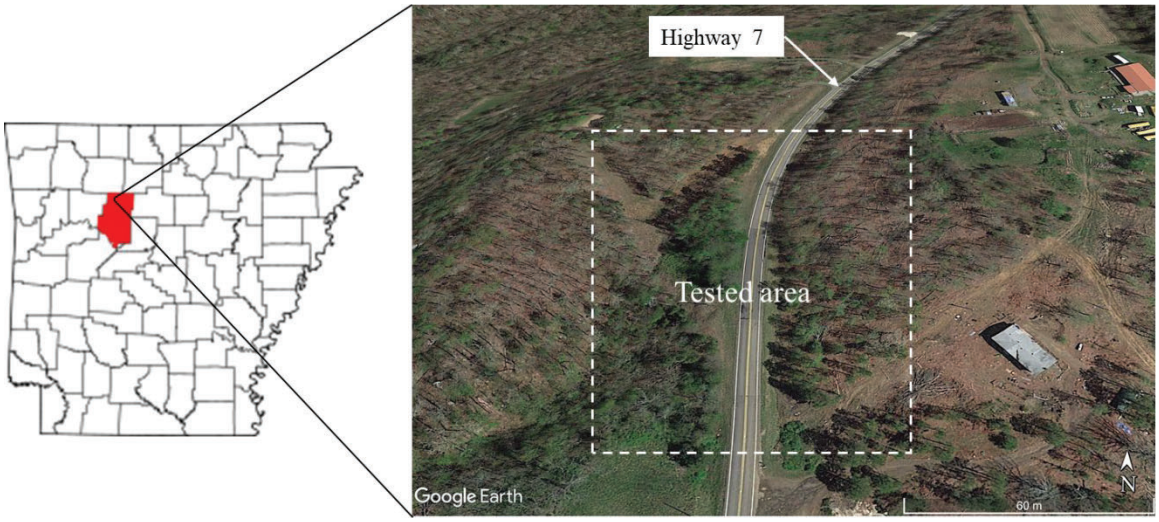

Figure 1.3- Location of the test site at Sand Gap, AR.

Geophysical field tests were performed along the Eastside and Westside of Arkansas Highway 7, but the most extensive field tests were conducted on the Westside of the Highway, which is considered as the potential slip surface. The exact locations of the survey lines for each geophysical test are presented later in the report. The site contains two slopes: one from North to South and one from East to West, but the East to West slope is the steepest slope moving toward the south-east. The slope movement has caused several longitudinal cracks in the pavement (see Figure 1.4), which has to be periodically inspected and repaired by ARDOT. As aforementioned,

in order to estimate the location of the potential slip surface, this section of Highway 7 has been extensively tested.

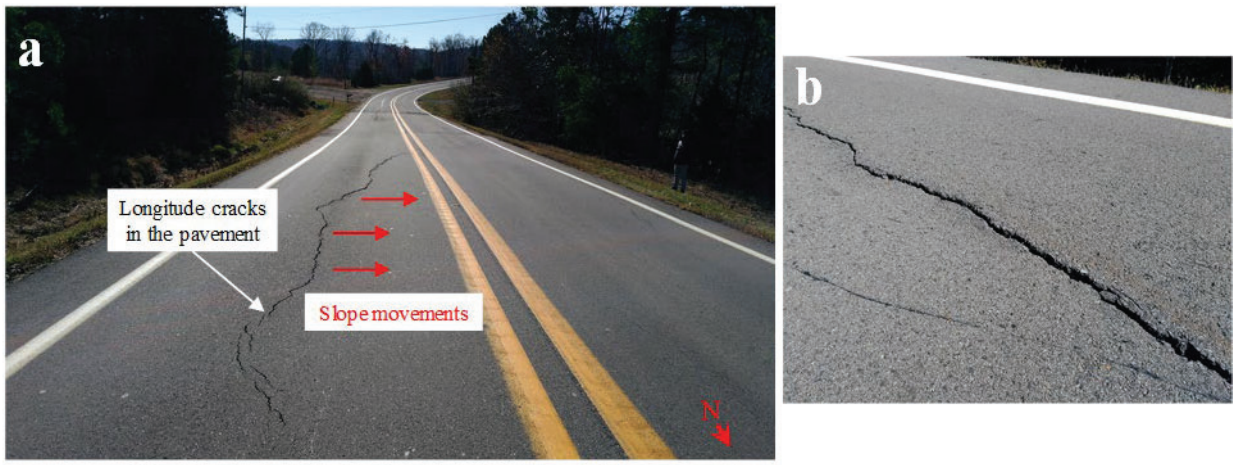

Figure 1.4- Longitudinal crack in the pavement. a) Slope movement b) longitudinal crack.

1.1.2 Phase II

The selected methods from Phase I were applied for three ongoing ARDOT transportation projects, including two bedrock mapping sites (Little Rock and Hot Springs) and one slope stability site (Ozark). The goal is to validate the accuracy of the selected geophysical methods from Phase I and further assess the advantages and limitations of the selected methods for bedrock mapping and slope stability investigations.

1.1.2.1 Ozark

The slope area tested for the Ozark site is located just north-west of Ozark, Arkansas, along I40 westbound, as shown in Figure 1.5. An orthomosaic image of the tested area along with the cracks observed during the field measurements are shown in this figure. The site slopes from South to North with an approximately 30-40% grade.

After the construction of the highway alignment, slope movements and settlement were observed along an approximately 150 m section of the highway. During a geotechnical field inspection in 1979, in which a large volume of materials had been excavated from the top part of the slope and moved down the Northside, a pipe was found to be broken underneath the highway. At that time, it was uncertain whether the long-term creep of the fill materials, settlement of the underlying natural slope or saturation of the slope caused the slope instability and the breakage of

the pipe. Due to the continuous movements of the slope, it had been redressed several times over 40 years, with a major slope repair job performed in 2018 that included the installation of 100 soil/rock anchors and horizontal drainage in three levels at the top section of the slope. While this slope repair has likely prevented a global slope failure, the cracks and the slope movements have continued to occur even after the repair (Rahimi et al. 2021). The slope movements have caused several long and thick longitudinal cracks, including a crack along the westbound lane with a length of approximately 150 m that starts from the pavement and moves eastward (see section 1 in Figure 1.5a and b) and additional cracking to the Westside of the slope area (see section 2 in Figure 1.5a and c).

MASW, P-wave refraction, HVSR, and ERT were conducted along different lines perpendicular and parallel to the slope. Geophysical testing includes 5 MASW/P-wave refraction lines, 8 ERT lines, and more 160 HVSR measurements acquired along the MASW and ERT lines and in a tight grid pattern at the very bottom of the slope. The goal of geophysical testing is to provide a high-resolution image of the subsurface conditions within the slope area to gain insight into the causes of the slope movements.

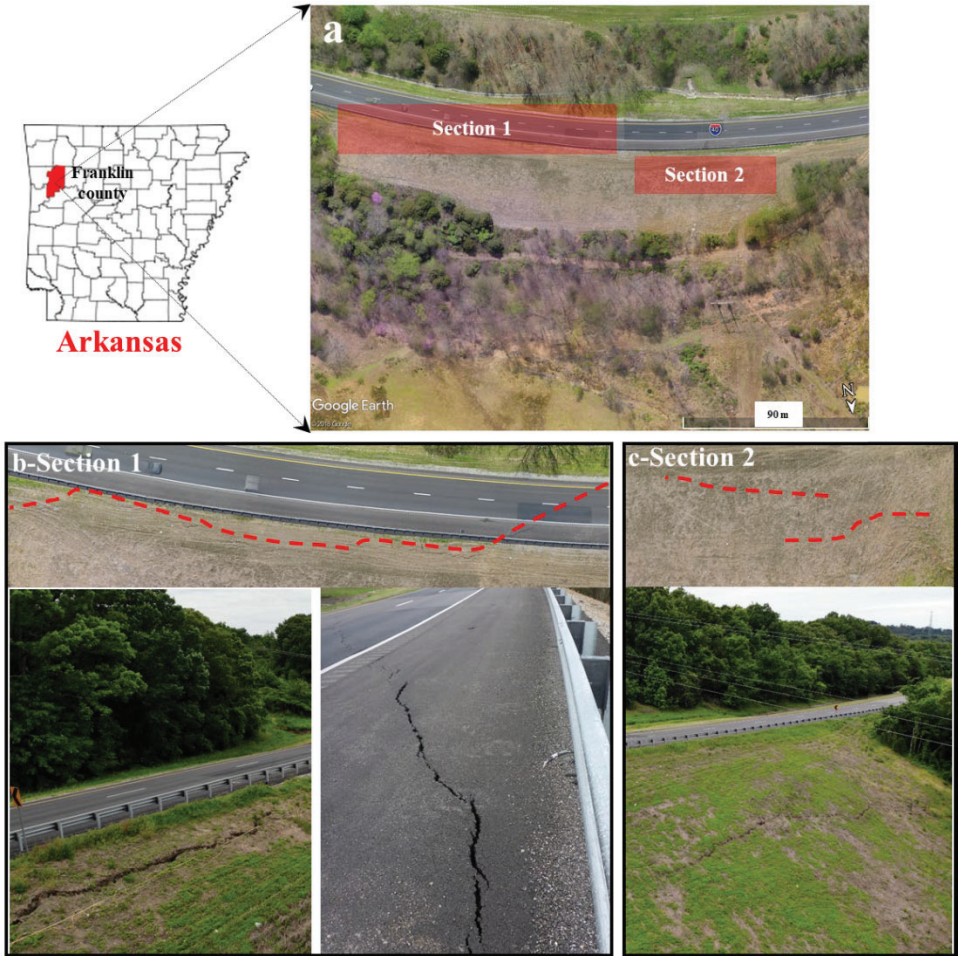

Figure 1.5- Location of the test site at Ozark, AR.

1.1.2.2 Hot Springs

The Hot Springs site (ARDOT Job #R60140) is located just North-East of Hot Springs, Arkansas, as shown in Figure 1.6. The proposed highway alignment of this project passes through mountainous regions with highly variable bedrock layers in terms of depth to bedrock and bedrock rippability. Moreover, the proposed highway alignment for the Hot Springs site involves different rock formations (Sandstone, Shale, Chert, and Novaculite) according to the Arkansas Geology map, as shown in Figure 1.6b. These factors make the Hot Springs site an ideal candidate to further investigate the capabilities of the selected geophysical methods from Phase I for bedrock mapping and bedrock rippability.

Extensive geophysical testing was performed for this site. These tests were conducted along trails and roads in areas where significant material excavations are expected based on the proposed cross-sections. MASW and HVSR testing were conducted along 9 survey lines.

Additionally, for some sections of the proposed highway alignment that involve steep slopes and rough terrains where MASW was difficult to use, extensive HVSR measurements were collected in a tight grid pattern to cover a larger spatial extent. The testing was conducted both perpendicular and parallel to the proposed highway alignment depending on the access in the area of interest. The goals of geophysical testing were to identify depth to different bedrock layers and bedrock rippability in the areas where significant rock excavations are expected.

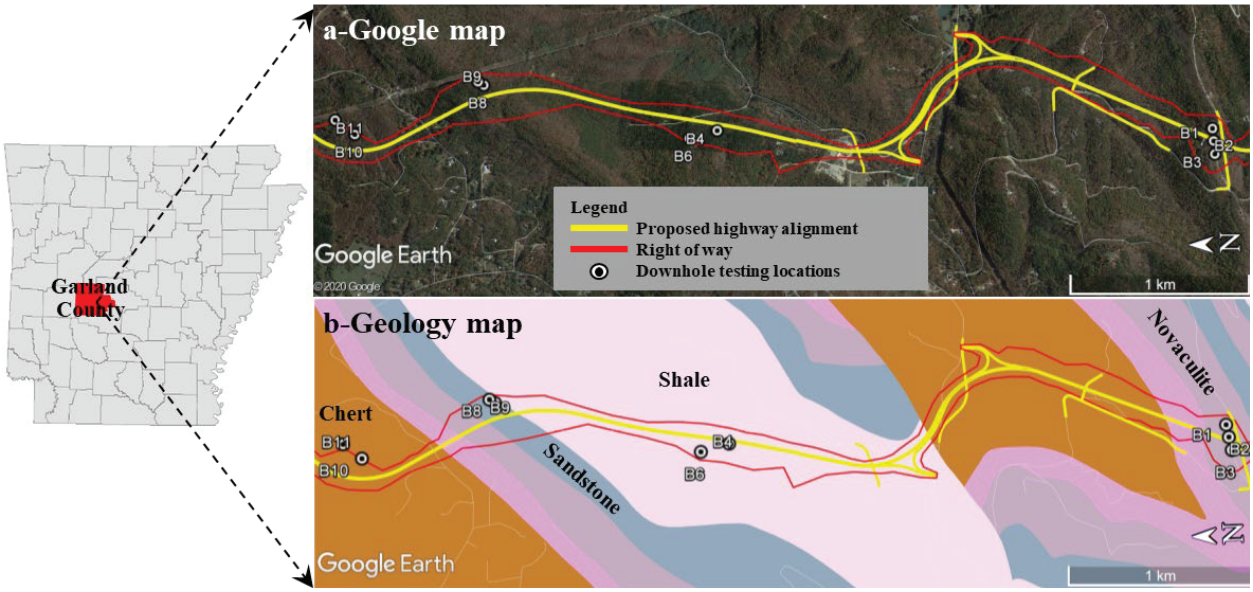

Figure 1.6- Location of the test site at Hot Springs, AR. a) proposed highway alignment for the Hot Springs site, b) Geology map of the study area.

1.1.2.3 Little Rock

The Little Rock site (ARDOT Job #061331, Southridge Extension) is located in Little Rock, Arkansas, close to Highway 10, as shown in Figure 1.7. According to the boring log information, the subsurface layers of this site include a thin soil layer followed by the bedrock unit. The bedrock unit could be quite variable along the proposed highway alignment. This makes the site a good candidate for bedrock mapping investigation using the geophysical methods selected in Phase I.

Geophysical testing, which includes MASW and HVSR were performed in the hatched area, as shown in Figure 1.7. The goals of geophysical testing are to identify the thickness of soil, depth to bedrock, and bedrock rippability along the proposed highway alignment.

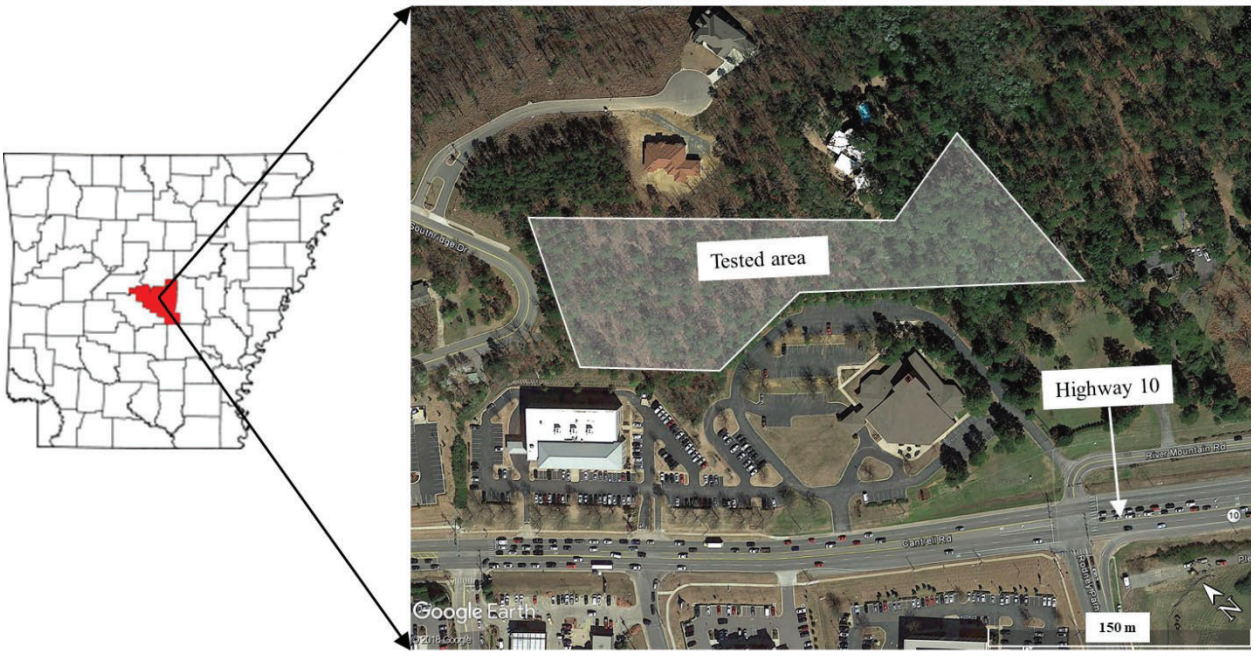

Figure 1.7- Location of the test site at Little Rock, AR.

2 Methods and materials

Introduction

Geophysical methods are routinely used to image the subsurface for geotechnical applications (e.g. Rix et al. 2002; Cardarelli et al. 2014; Rahimi et al. 2019; Wood et al. 2019). However, these methods are used less often for transportation projects (Sirles 2006; Coe et al. 2018). Commonly employed geophysical methods include seismic refraction, seismic reflection, surface wave methods, horizontal to vertical spectral ratio (HVSR), ground penetrating radar (GPR), electrical resistivity, magnetics, and gravity (Anderson et al. 2008). These geophysical methods measure the physical properties of the earth and are generally used to measure the spatial variation of the properties within a specific area. The main advantages of the geophysical techniques compared to the traditional geotechnical methods are:

- Testing larger areas at lower costs.
- A significantly higher rate for the field measurements
- Providing a continuous image of the subsurface.
- Applicable for rough terrains and steep slopes.

However, this is not to say that geophysical methods can replace traditional geotechnical methods. Geophysical methods are best utilized in conjunction with a traditional geotechnical method to fill in gaps between sample locations and provide more global information regarding the spatial variability of the subsurface materials.

Various non-invasive geophysical methods have been employed to determine the depth to bedrock and/or locate the potential slip surface (Sirles 2006; Friedel et al. 2006; Pastén et al. 2016; Berti et al. 2019). In this study, all the common geophysical methods were utilized for bedrock mapping and slope stability for transportation projects to identify the most suitable method(s) for these applications. The following geophysical methods are used in this study:

- Stress wave/seismic methods including Multichannel Analysis of Surface Waves (MASW) using both Rayleigh and Love type surface waves, and P-wave refraction
- Horizontal to Vertical Spectral Ratio (HVSR or H/V),
- Resistivity methods including Capacitively-Coupled Resistivity (CCR), and Electrical Resistivity Tomography (ERT)

- Ground Penetration Radar (GPR), and
- Electromagnetic Ground Conductivity Survey (EM31).

Each of these methods is explained below.

Stress wave or seismic methods

Stress wave or seismic geophysical methods utilize body or surface type stress waves to understand the subsurface layering and stiffness of the earth materials. Non-invasive seismic methods only require sensors and a source placed on the ground surface and not within the surface. This significantly reduces the cost of conducting the tests by not requiring boreholes. The results of stress wave methods are often the variation of either compression wave (P-wave, Vp) or shear wave (S-wave, Vs) velocity with depth and distance along a line (2D variation of Vp or Vs). Vp and Vs are fundamental properties of soils and rocks that are directly linked to the constrained modulus and shear modulus, respectively. For the shear modulus, the relationship is $G= \rho Vs^2$, where G is the shear modulus, and ρ is the mass density of the material. The equation is similar for constrained modulus.

Results from seismic methods can provide not only the location of the subsurface layers but also an understanding of the stiffness of the materials. This can be particularly important for bedrock profiling along a proposed highway alignment where rock excavations are required as well as for slope stability investigations that involve a very shallow bedrock layer, where the bedrock topography plays a key role in the stability analysis. For bedrock profiling, the methods provide a measure of the global stiffness of the bedrock materials. This knowledge of the stiffness has been used to understand the rippability of a particular rock layer, as in the Caterpillar Handbook on Ripping (2000), which describes the rippability of the rock units based on the P-wave velocity of the rock materials. This can be particularly useful to contractors prior to the bidding process to understand the required equipment needed for the job. Moreover, the velocity determined from seismic methods provides a more global representation of weathering conditions of rocks compared to a discrete core taken at one location (Rahimi et al. 2020; Rahimi et al. 2021). In addition, methods such as Rock Quality Designation (RQD) or Solid Core Recovery (SCR) can saturate near zero, reducing the understanding of the material stiffness (i.e., many highly weathered rock layers may have RQDs of zero but may have different seismic velocities). In addition to providing information regarding the rippability of rocks, seismic methods can also provide

information regarding rock cut slope design along the alignment (Ohio DOT 2016). The design of rock slopes using core samples in highly weathered rock can be difficult due to the very small sample size and potential damage to the rock samples during sampling. Similar to rippability studies, seismic velocity studies provide more of a global stiffness model of the weathered rock and a true in-situ stiffness unaffected by sample disturbance. This is one of the biggest advantages of the non-invasive geophysical methods in which the materials are tested in field conditions.

For slope stability applications, seismic methods can be used to interpret the location of the potential soft or stiff layers below the surface where slides can occur (Hack 2000). Several studies have utilized seismic methods for the identification of the potential slip surfaces (e.g. Friedel et al. 2006; Tingey et al. 2007; Jongmans et al. 2009). Seismic methods have an advantage over other geophysical methods due to their ability to recover mechanical properties (Vp or Vs) of the subsurface materials, which can be correlated to strength values such as undrained shear strength, N_{60} blow count, friction angle, or other geotechnical properties and parameters (e.g. Maheswari et al. 2010; Fabbrocino et al. 2015; Rahimi et al. 2020). These values can be used to map the location of these subsurface layers, providing additional information for slope stability analysis, which would only be available through an extensive drilling and sampling program.

Seismic methods are split into body wave and surface wave methods, with seismic refraction being the most popular body wave method and Multi-Channel Analysis of Surface Waves (MASW) being the most popular surface wave method. Each method is explained in more detail below. In this study, three different arrangements were used for seismic testing, including Rayleigh type surface waves, Love type surface wave, and P-wave refraction.

2.1.1 Multichannel Analysis of Surface Wave (MASW)

Multi-station seismic surface wave methods were first introduced in the 1980s (Gabriels et al. 1987; McMechan and Yedlin, 1981), but these methods became popular in many disciplines in the late 1990s and early 2000s with more powerful computers for sophisticated data processing. The multi-station seismic surface wave techniques have several advantages over the traditional two-sensor Spectral Analysis of Surface Waves (SASW) method. Using the multi-station array-based methods, the production rate in the field measurements is remarkably increased, and the data processing and data interpretation become less subjective and more robust (Foti et al. 2014). Additionally, the multi-station seismic surface wave techniques help to mitigate several limitations

associated with the traditional two-sensor SASW method. This includes poor resolution experimental dispersion image, failure to detect multiple modes of propagation which could be important for data interpretation, and inability to accurately identify near-field effects (Zywicki and Rix, 2005).

The multi-station seismic surface wave techniques came into popular use in geotechnical engineering for near-surface site characterization with the introduction of the MASW method by Park et al. in 1999. This method is appealing for near-surface site characterization (generally for depths shallower than 30 m) because it is nondestructive, rapid, and allows for the identification and rejection of unwanted data points, including higher mode data and near-field effects. MASW utilizes the dispersive nature of either Rayleigh or Love waves propagating through geomaterials aimed at estimating the variation of shear wave velocity (Vs) with depth. The experimental dispersion curve obtained from the field measurement is used in an iterative process called inversion to determine the variation of the shear wave velocity with depth. The standard procedure for MASW testing is presented in Figure 2.1.

It is important to realize that the MASW method suffers from nonuniqueness during the inversion process, meaning that there is no unique answer from the results but a number of possible answers. However, this limitation can be overcome by using local ground truth information, such as boring logs, for parametrization, or it can be reduced by the combined use of geophysical methods.

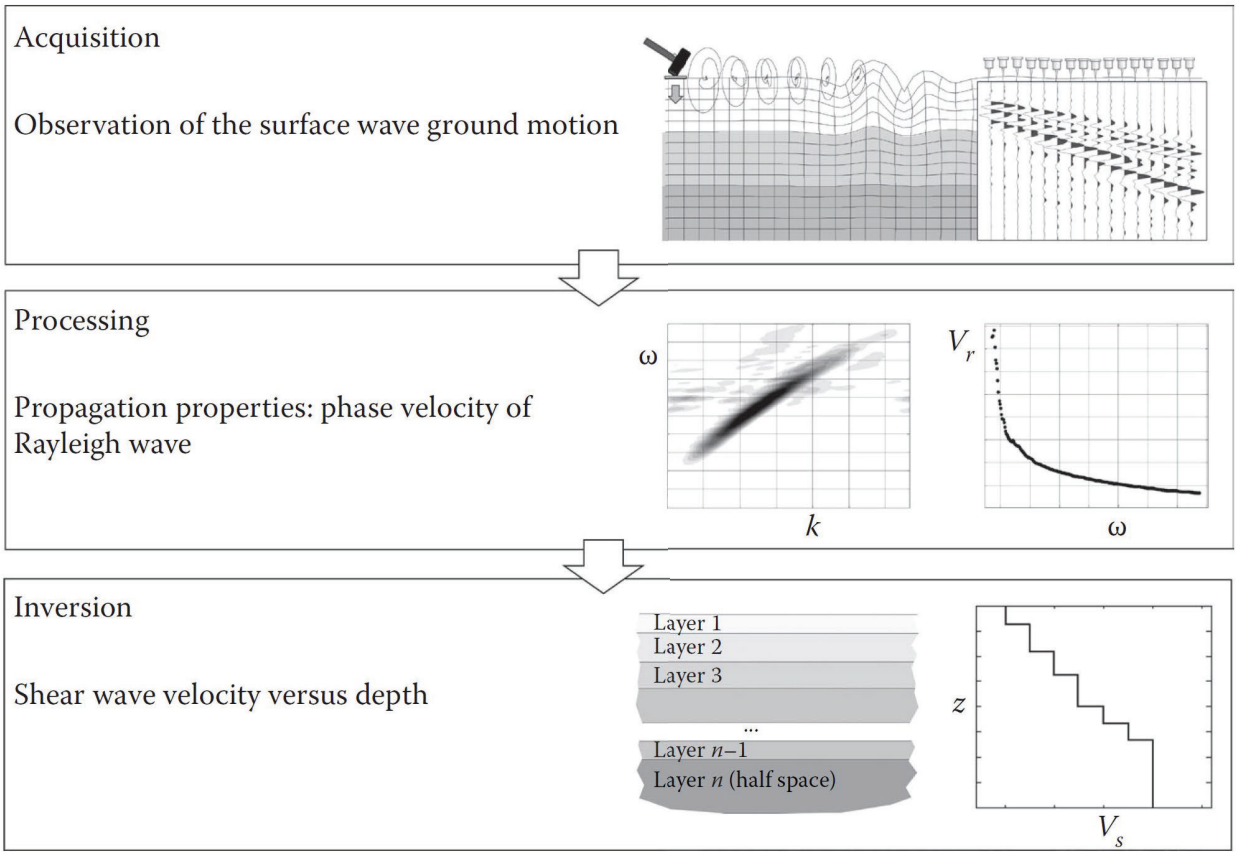

Figure 2.1- MASW data acquisition, data processing, and inversion (from Foti et al. 2014).

Currently, the MASW method is widely used in geotechnical engineering for various applications, including but not limited to near-surface site characterization (e.g. Rix et al. 2002; Socco and Strobbia, 2004), liquefaction assessment, and dynamic site characterization (e.g. Lai et al. 2002; Cubrinovski et al. 2010; Wood et al. 2017; Rahimi et al. 2020), infrastructure evaluation (e.g. Olafsdottir et al. 2017; Wood et al. 2017), and V_{S30} estimation (e.g. Comina et al. 2010; Martínez-Pagán et al. 2012). This method has also been used for both shallow bedrock mapping and slope stability investigations. For instance, Miller et al. (1999) used the MASW to determine the topographic variations and discontinuities of a shallow bedrock layer for hydrological purposes. This method was also used by Moon et al. (2017) to detect the spatial variation of the bedrock layer for two sites in Singapore. For slope stability investigations using the MASW method, the body of the slide can be separated from the unaffected zone based on the velocity contrast observed at the subsurface. Several studies have employed the MASW method for slope stability investigations (e.g. Tingey et al. 2007; Peng et al. 2017; Berti et al. 2019; Rahimi et al.

2021). For instance, Xu et al. (2017) used the MASW method to detect the critical slip surface for a landslide in China based on the variation of the shear wave velocity at the subsurface.

2.1.1.1 Rayleigh type surface wave testing

Surface wave testing using Rayleigh type surface waves is the most commonly used geophysical method in geotechnical engineering for near-surface site characterization because Rayleigh waves can be easily generated and detected at the ground surface. Surface wave testing using Rayleigh waves, which involves elliptical motions in the vertical plane, is conducted using a linear array of vertical geophones located at the ground surface to record the vertical component of the waves generated using vertical shots at the ground surface.

In this study, a linear array of 24 or 48, 4.5 Hz vertical geophones with a uniform spacing between each geophone was used for Rayleigh type surface wave testing. The spacing between each geophone and the number of vertical geophones were determined based on maximum target depth and site conditions. A refraction cable was used to connect all geophones to the Geode seismograph. The Geode seismograph is connected to a field laptop to record and view signals during field testing, as shown in Figure 2.2c. To increase the rate of field measurements for long survey lines, all geophones were attached via a landstreamer system (Figure 2.2a). The landstreamer allows all geophones in the array to be dragged as a single system to the new testing location instead of planting each geophone individually for each setup. The disadvantage of the landstreamer system is the reduced experimental data quality (i.e. low-resolution experimental dispersion curve) because the geophones are not coupled as well to the ground surface. Therefore, more noise is recorded for each experiment. Rayleigh waves were generated by vertical strikes on an aluminum plate overlain by a rubber damping pad placed on the ground surface via a 12 lb sledgehammer (Figure 2.2b). For each array setup, waves were generated at multiple source offsets to be able to account for the uncertainty regarding the experimental dispersion data points and increase the reliability of the experimental dispersion curve. A minimum of three blows were stacked at each source offset to increase the signal-to-noise ratio of the data. A typical MASW field testing configuration is shown in Figure 2.3.

The final output of the Rayleigh wave MASW testing is a 1D inverted shear wave velocity profile that shows the variation of the shear wave velocity of the subsurface materials with depth. This is explained in more detail in the next chapter.

Figure 2.2- Typical components of the MASW testing a) vertical geophone placed on a landstreamer plate, b) vertical shot being used to generate Rayleigh waves c) Geode seismograph and field laptop d) MASW setup array with 2 m spacing between geophones.

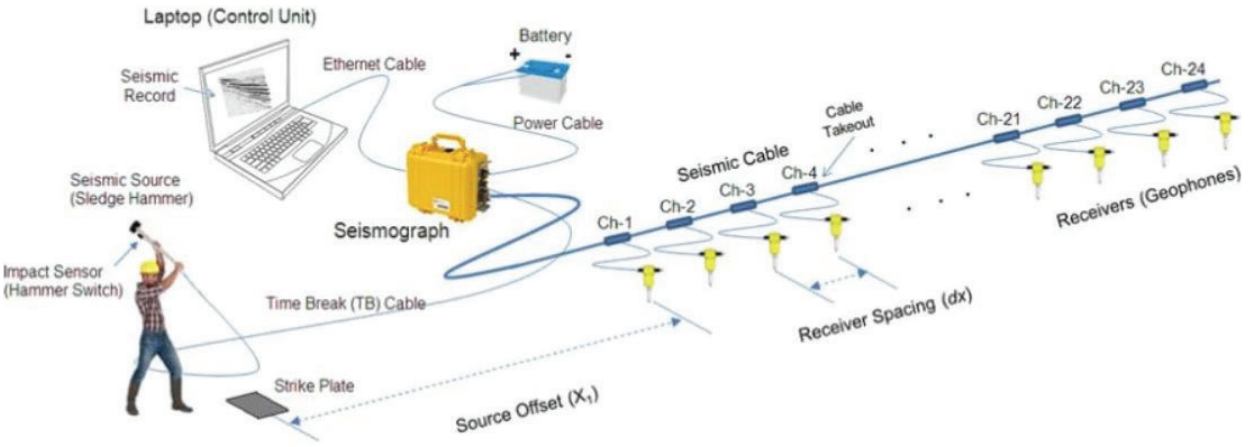

Figure 2.3-Typical MASW configuration (from www.masw.com).

2.1.1.2 Love type surface wave testing

Surface wave testing using Love waves is another method that can be utilized for near-surface site characterization. To date, surface wave methods have mostly focused on the use of Rayleigh waves, and Love waves are rarely utilized for near-surface site investigations due to the difficulties in generating Love waves, placing geophones, and limitations related to layer stratigraphy (Eslick et al. 2008; Foti et al. 2014). Love waves are horizontally polarized waves that can be generated via a pure horizontal source. Data acquisition and data interpretation for Love waves testing are similar to that of Rayleigh waves.

A linear array of 24 or 48, 4.5 Hz horizontal geophones with uniform spacing between each geophone was used for Love type surface wave testing. The geophones were leveled and oriented cross line to the setup array orientation. A 12 lb sledgehammer was used to generate Love waves by striking a wooden shear beam with aluminum ends horizontally cross line to the array (Figure 2.4b). For each array setup, waves were generated at multiple source offsets to be able to account for the uncertainty regarding the experimental dispersion data points and to increase the reliability of the experimental dispersion curve. A minimum of three blows was stacked at each source offset to increase the signal-to-noise ratio of the data.

Similar to the Rayleigh waves testing, the final output of the Love waves testing is a 1D shear wave velocity profile that represents the variation of subsurface layers' shear wave velocity with depth.

Figure 2.4- MASW testing using Love type surface waves. a) horizontal geophones leveled and oriented, b) wooden shear beam.

2.1.2 P-wave refraction

P-wave refraction utilizes the arrival time of seismic waves (body waves) that have refracted at layer interfaces. Waves are typically generated using a sledgehammer. Waves are detected by a linear array of geophones spaced uniformly along the ground surface and recorded via a seismograph. This method is applicable for the characterization of sites with a continuous increase in soil stiffness (i.e. normal dispersive sites without any velocity reversal layer within the target depth) and it has been used for the determination of groundwater levels, bedrock mapping, and slope stability investigations (Hack, 2000; Grelle and Guadagno, 2009; Krautblatter and Draebing, 2014).

Testing configurations and procedures for P-wave refraction are similar to the MASW testing, but typically a faster sampling rate is used for P-wave refraction testing. This is because the subsurface is characterized based on the arrival time of body waves at the ground surface, so it is important to determine the arrival times as accurately as possible. The source offset for the P-wave refraction survey should be placed close to the setup array for two main reasons: 1) body waves attenuate much faster than surface waves, and 2) the uncertainty and ambiguity of picking

arrival times increase with source offset. The same linear array of 24 or 48 vertical geophones was used for the P-wave refraction survey as the Rayleigh MASW survey. The same sledgehammer source was also used. However, a faster sampling rate of 0.125 ms was used for the P-wave refraction testing. Source locations close or within the array setup were used in the P-wave refraction analysis.

Horizontal to vertical spectra ratio (HVSR)

The HVSR technique, which was first introduced by Nogoshi and Igarashi in 1971 and then popularized by Nakamura in 1989, is a passive geophysical method that has been widely utilized for seismic microzonation and estimation of site fundamental frequency (e.g. Elker et al. 2015; Wood et al. 2019). This method is also extensively used for deep bedrock detection (e.g. Trevisani et al. 2017; Wood et al. 2019) as well as for the construction of the experimental dispersion curve at low (0.2-7 Hz) to intermediate (7-30 Hz) frequencies (Vantassel et al. 2018). The HVSR method has several advantages over the other array-based geophysical methods. These include applicability for any site conditions such as sites where array-based geophysical methods are difficult to use (e.g. rough terrain and steep slopes), and rapid, cost-effective, and straightforward data collection and data processing. Despite these advantages, this method has been rarely used for shallow bedrock mapping for transportation projects and slope stability investigations (Rahimi et al. 2021).

The HVSR technique is based on the analysis of horizontal and vertical components of background noise or microtremor. The method utilizes a single three-component sensor to record microtremors from the surface. The horizontal to vertical spectral ratio (H/V) is defined as the ratio between the Fourier amplitude spectra of the horizontal and vertical components of a single sensor. This ratio is calculated to identify the peak H/V which is linked to a fundamental property of a site.

The amplitude of the surface waves and the H/V peak(s) is a function of the source properties and subsurface velocity structure, but for a given source, the H/V peak is mainly controlled by the subsurface velocity structure of the site. Studies have proven that peak(s) of the HVSR typically occur at or close to the fundamental frequency (f_r) of the site, which indicates the presence of a sharp Vs impedance contrast (ratio) in the subsurface (Fäh et al. 2001). The Vs

Impedance Ratio (IR) is defined as the ratio of the product of mass density (ρ) and shear wave velocity (Vs) of two layers.

$$IR = \frac{\rho_2 \times V_{s2}}{\rho_1 \times V_{s1}} \quad (1)$$

The final output of the HVSR technique is a plot of HVSR amplitude versus frequency, as shown in Figure 2.5. If there is strong velocity contrast in the subsurface (e.g., an impedance ratio greater than approximately 2) (SESAME guideline, 2004), a peak will form in the frequency-spectral ratio domain, whose peak will approximate of the fundamental site period. Peak frequencies from multiple test locations can be combined together in a map to understand the spatial variation in bedrock depth along an alignment (Rahimi et al. 2020). It should be noted that in order to estimate depth to bedrock using the HVSR technique, additional information regarding the average shear wave velocity of soil deposits located above the bedrock or boring log information is required.

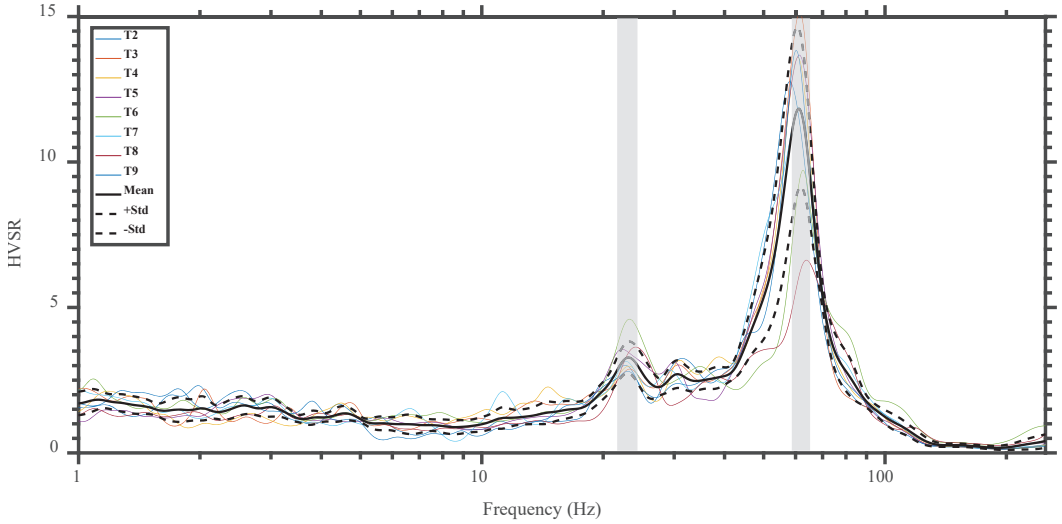

Figure 2.5- An example of the HVSR results from experimental data.

Extensive HVSR measurements were conducted at different sites in Phase I and Phase II of this research project using seismometers (Nanometrics Trillium compact), such as the one shown in Figure 2.6. Each sensor is recorded using a Nanometrics Centaur Digitizer. The Centaur digitizer is a high-resolution three-channel, 24-bit data acquisition system capable of recording at sample rates up to 5000 sps. The Centaur uses a GPS timing system to time stamp waveforms ensuring waveform records are synced between stations. A minimum of 14-20 minutes recording time was typically used for the HVSR testing. The minimum recording time should be determined

based on noise conditions and the expected bedrock depth. Typically, longer recording times are needed for sites where deep sediment exists.

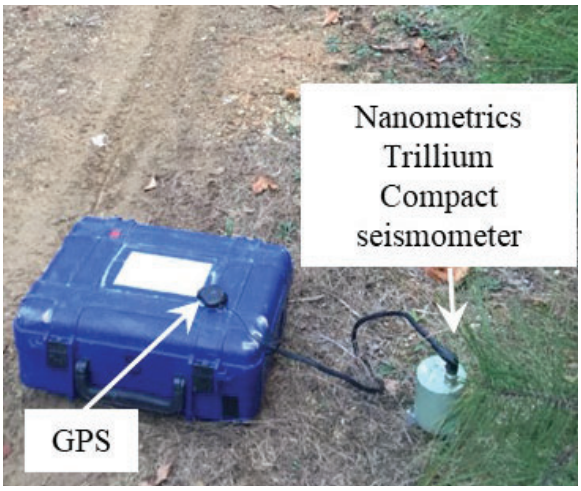

Figure 2.6- Seismometer placed at the ground surface for HVSR testing.

Electrical resistivity methods

While surface wave methods use stress waves propagation to map subsurface conditions, resistivity techniques characterize the subsurface materials based on their resistance to electrical current injected into the ground. The resistivity-based techniques are mainly useful for identifying the water table and changes in the subsurface, which have different electrical resistances (changes in soil type, clay vs. sand). Factors that affect the resistivity of earth materials are porosity, texture, degree of saturation, the chemical makeup of the pore water, temperature, and clay content (Kaufman and Hoekstra, 2001).

The resistivity methods are valuable for rain-induced landslides as they can detect the highly saturated zones within the slope areas (e.g. Naudet et al. 2008). Additionally, since the slide body is typically associated with low resistive materials, the potential slide body can sometimes be detected using the resistivity methods (e.g. Schmutz et al. 2000; Lapenna et al. 2003; Bichler et al. 2004). For example, Merritt et al. (2014) identified some flow regions along an active slope in North Yorkshire, UK by generating a detailed 3D image of the subsurface using the ERT method.

Electrical Resistivity testing is generally conducted using one of two methods: Electrical Resistivity Tomography (ERT) or Capacitively Coupled Resistivity (CCR). These methods are explained in more detail in the following.

2.1.3 Electrical Resistivity Tomography (ERT)

Electrical Resistivity Tomography (ERT) is the more traditional Direct-Current (DC) resistivity, which is conducted using multiple stainless-steel electrodes installed in the ground at a uniform spacing along a linear line for 2D surveys. Measurements are taken by energizing multiple electrodes with a direct current and taking electrical potential measurements at other electrodes in various sequences (inverse Wenner, Schlumberger, and dipole-dipole). The injection of current and measurement of voltage using multiple pairs of electrodes provides multiple readings of apparent resistivity at different representative depths. Through an inversion process, a model can be generated for true resistivity with depth. This method has been shown to provide accurate results and excellent depth of investigation (Karim et al. 2019). However, the installation of the probes and collection of data is time-consuming, often taking hours to conduct a survey over 100 meters. Therefore, the traditionally DC resistivity measurements are not practical for profiling large areas in an economic or timely manner.

Many efforts have been made to identify the range of resistivity values associated with different geomaterials, including soils and rocks. Summarized in Table 2-1, are the typical resistivity ranges of different soil types in Ohm-cm proposed by Palacky, (1988) and Kaufman and Hoekstra, (2001).

According to this table, there are some overlaps between the resistivity values of different soil types, which make it difficult to accurately differentiate between various soil types. This is one of the major issues of resistivity testing for soil and rock characterization. This issue is highlighted even more for the resistivity values acquired from the field measurements, as there are other factors influencing the resistivity of the geomaterials in the field, such as saturation degree and temperature. These parameters are difficult to be monitored and controlled during field testing.

While the definition of high and low resistive materials are site-specific rather than being consistent across different sites, for the purpose of this study, resistivity values lower than approximately 80 Ohm-m are considered to be low. This value can be related to clay, silt, and sand deposits as well as a highly fractured shale layer if they are located below the water table.

Table 2-1- Range of resistivity associated with different soil types (Palacky, 1988; Kaufman and Hoekstra, 2001).

Soil Type	Soil Classification	Resistivity (Ω.cm) (Kaufman and Hoekstra, 2001)	Resistivity (Ω.cm) (Palacky, 1987)
CLAYS	CH	1,000-5,000	300-10,000
	CL	2,400-6,000	-
	OL	2,650-7,500	-
SILTS	ML	2,650-7,250	-
	SC	4,650-17,800	-
	MH	7,150-24,000	-
SAND	SM	9,600-45,250	47,500-1000,000
GRAVEL	GW	56,300-91,800	47,500-1,000,000
	GC	12,900-40,500	-
	GP	91,500-233,250	-

ERT surveys were conducted with different electrode spacing. As an example, the ERT testing conducted for the Sand Gap site is shown in Figure 2.7. The Supersting R8 from Advanced Geoscience Inc. was used to collect all datasets. A Dipole-Dipole and strong-gradient arrays were used to collect all datasets within this study. A strong-gradient array is an optimized array, which uses electrode configurations to collect additional data on top of the standard Dipole-Dipole configuration. This provides a measured dataset with good vertical and horizontal resolution, allowing for the identification of vertical and horizontal discontinuities.

Figure 2.7- ERT survey conducted at the Sand Gap site on the Eastside of Highway 7.

2.1.4 Capacitively-Coupled Resistivity (CCR)

To improve the speed for resistivity data collection, the Capacitively-Coupled Resistivity (CCR) method was introduced. CCR uses a transmitter and several receivers coupled in a dipole-dipole configuration in which the transmitter and receivers are placed in line and separated with various dipole lengths. The main components of the CCR consist of transmitters, receivers, and dipole cables (Figure 2.8). CCR works by utilizing five receivers to detect current injected into the ground via a transmitter at varying rope lengths (Rahimi et al. 2018). A schematic view of the CCR testing along with the geometry (dipole length and rope length) is shown in Figure 2.9. The final product of the CCR survey is a pseudo section profile showing the variation of resistivity with positions and effective depths.

CCR was conducted using two setups of 5 m dipole length with 5 m rope length and 10 m dipole length with 10 m rope length. Varying the dipole and rope lengths allows the survey to assess materials at varying depths, i.e. short dipole lengths in combination with short rope lengths measure near-surface materials while longer dipole lengths and longer ropes lengths measure deeper materials. A typical field configuration of the CCR survey is shown in Figure 2.10. All setup configurations were dragged along the survey lines as a single unit, thus enabling rapid field measurements over long distances.

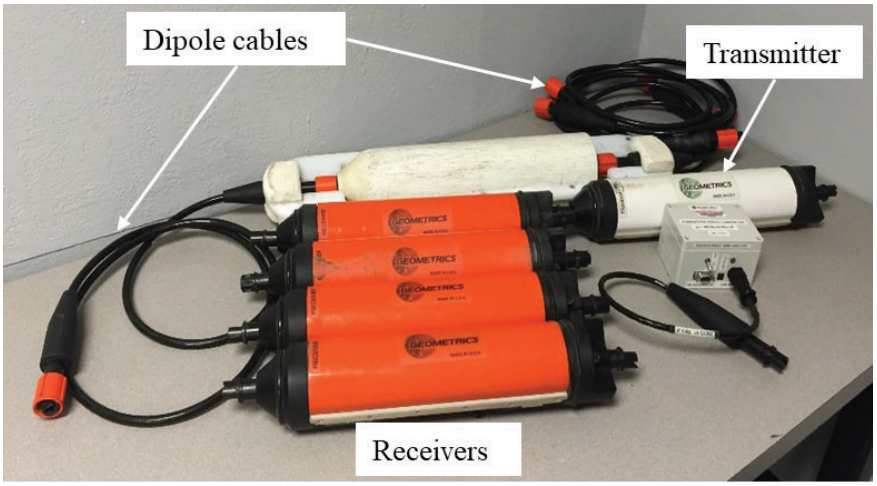

Figure 2.8- Main components of the CCR method.

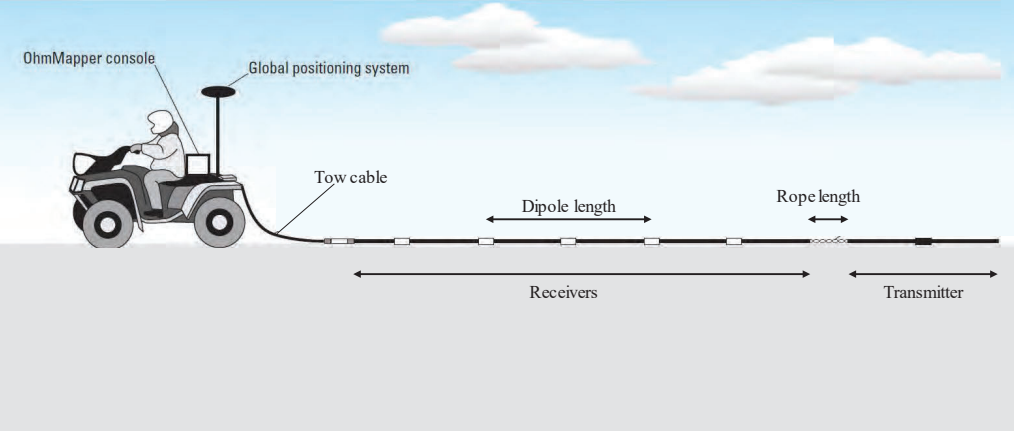

Figure 2.9- Schematic configuration of the CCR testing and geometry (modified from Burton et al. 2011).

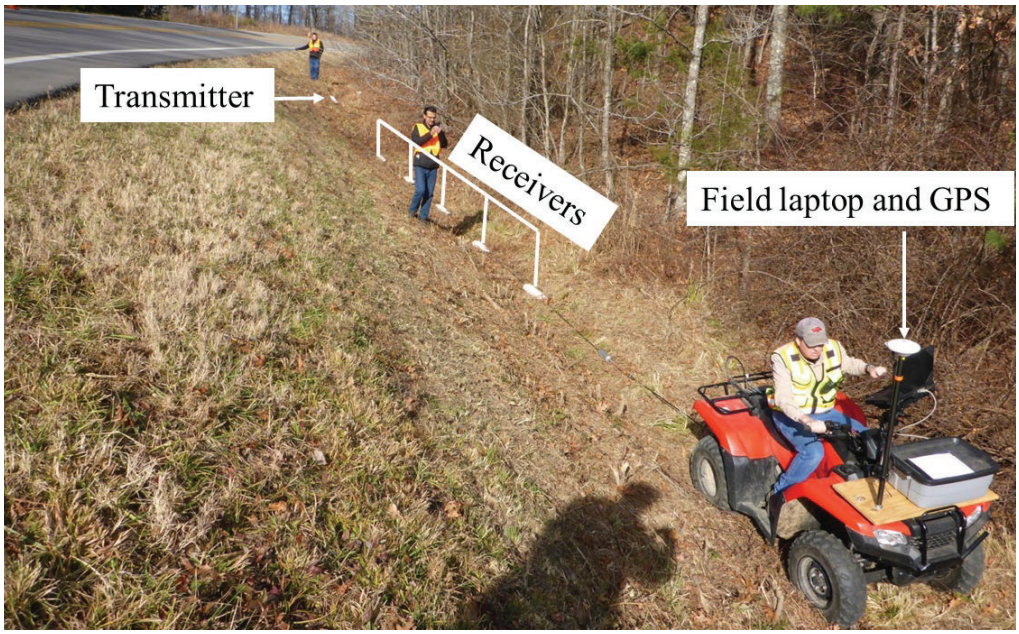

Figure 2.10- CCR testing at the Sand Gap site.

Ground Penetration Radar (GPR)

Ground penetration radar (GPR) detects reflections of electromagnetic waves from subsurface materials. The reflection is a function of soil type, rock properties, bulk density, and water content (ASTM D6432-11). Studies have shown that GPR is a valuable tool for detecting underground utilities such as pipes and cables, estimating the depth to the groundwater table, and locating subsurface cavities (Słowik, 2012; Chlaib et al. 2014; Steelman et al. 2015). The most common configuration of GPR includes a transmitting antenna and a receiving antenna in a fixed position moving along the survey line. Presented in Figure 2.11 is a schematic view of a typical

GPR system (ASTM D6432-11). The transmitting antenna, which is typically placed on the ground surface, radiates high-frequency electromagnetic waves into the ground. These waves are reflected at layer interfaces or utility locations where considerable electromagnetic contrast exists. The electromagnetic waves reflected back are detected by the receiving antenna. Antennas can range from >2 GHz down to <100 MHz. As the frequency decreases, the depth of investigation increases but the minimum target size also increases. For most geophysical surveys with the goal of locating subsurface layering, an operating frequency of 50-400 MHz is most common as it allows for a deeper depth of investigation.

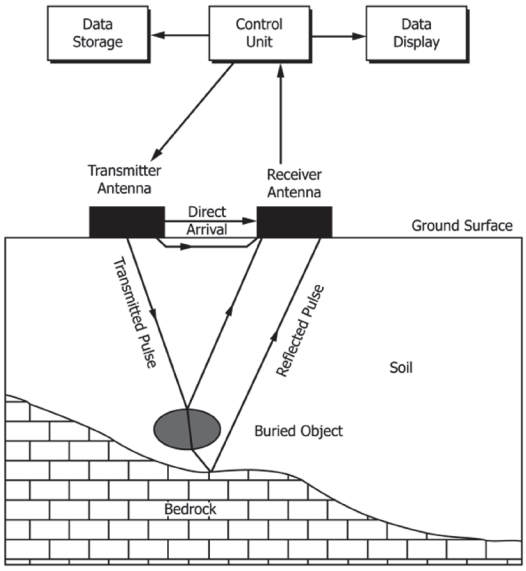

Figure 2.11- Common configuration of the GPR system (ASTM D6432-11).

The output of GPR testing is a pseudo section profile showing the variation of electromagnetic wave amplitude with position and time, as shown in Figure 2.12. The vertical axis is in units of nanosecond (ns), which is the time it takes for an electromagnetic wave to travel down to an interface/object and reflect back to the ground surface. The vertical axis can be converted to depth if the average velocity of electromagnetic waves in the subsurface materials is known.

GPR testing was conducted using the Noggin GPR system (Figure 2.13). The main components of the GPR system consist of transmitter, receiver, antennas, GPS unit, and field laptop. The transmitting and receiving antennas were fixed on their positions with 1 m between the antennas. Tests were performed using antennas with 50 MHz and 100 MHz frequencies. The signals were controlled and viewed via the field laptop.

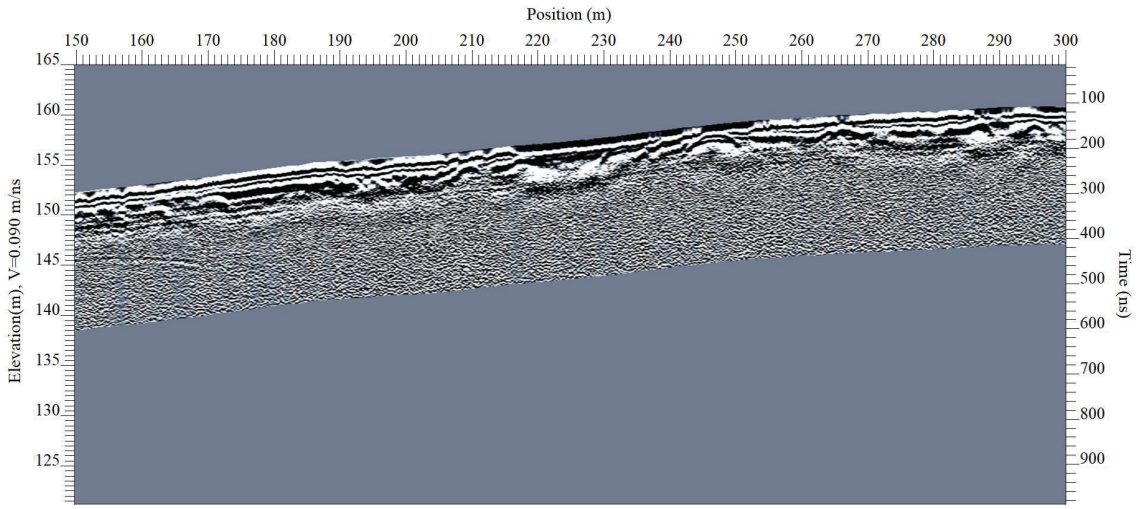

Figure 2.12- An example output data from GPR testing.

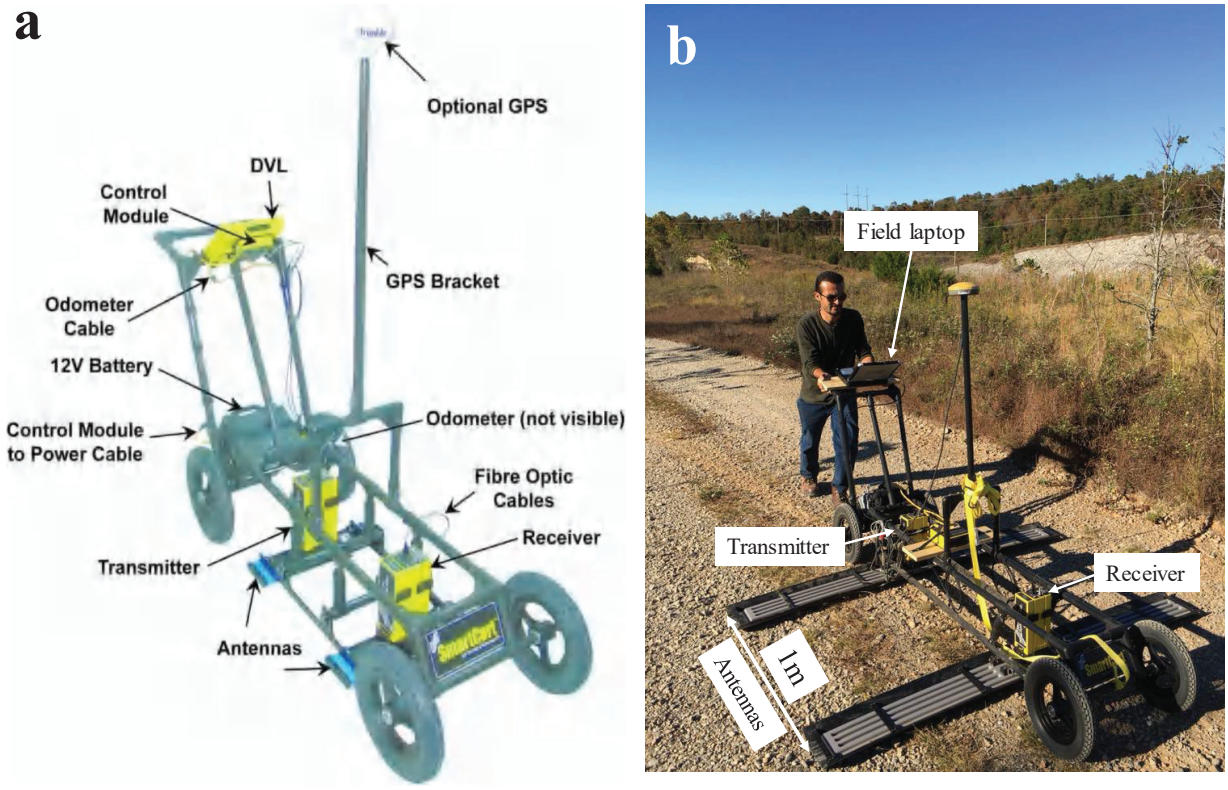

Figure 2.13- Noggin GPR system. a) system configuration, b) GPR testing using 100 MHz antennas' frequency.

Electro-Magnetic Survey

Electro-Magnetic survey (EM) initially was introduced for the determination of soil salinity, but the use of this technique has been expanded for mapping soil type, locating depth to

bedrock, and detecting underground utilities (Doolittle and Brevik, 2014). This method utilizes the electromagnetic inductive technique to acquire subsurface conditions based on the variations of the subsurface materials' conductivity/resistivity. An electromagnetic field is transmitted in the air via a coil of wire which is separated from a receiver by a fixed distance. The boom, as shown in Figure 2.14b, is carried horizontally along the survey path with a constant distance above the ground surface. A secondary electromagnetic field is generated in the subsurface via the transmitted energy due to the effects of soil type, underground utilities, or soil moisture. The resulting secondary electromagnetic field proportional to the ground current is utilized for estimating the apparent electrical conductivity of subsurface materials. The primary outputs of the EM survey are electrical conductivity and in-phase. This is explained in more detail later in the report.

Em31-MK2 device, shown in Figure 2.14, was used to conduct the field tests. This device has an intercoil spacing of 3.66 m, operating frequency of 9.8 KHz, conductivity ranges of 10/100/1000 millisiemens per meter (mS/m), and in-phase ranges of -20 to +20 part per thousand (ppt).

Figure 2.14- EM 31-Mk2 device. a) the main components of the EM31-MK2 device, b) field testing using EM31-MK2 device.

3 Data processing and data interpretation

Introduction

This chapter details data processing and data interpretations of the geophysical methods used in this study. Different MATLAB codes, software, and procedures were used to process the raw data acquired from the geophysical field measurements to identify bedrock locations and/or potential slip surfaces. These methods are discussed below. Moreover, the challenges and issues associated with data processing and data interpretation of the geophysical methods employed in this study are discussed.

MASW

3.1.1 Data processing

Data processing of MASW testing using Rayleigh type surface waves and Love type surface waves are almost identical with some differences in the inversion process, which are out of the scope of this study. Therefore, the steps presented below were followed for data processing of both Rayleigh and Love type surface waves.

The raw MASW data is a set of time-domain signals (amplitude versus time) recorded at each geophone location, as shown in Figure 3.1a. The first step in the MASW data processing is the construction of the experimental dispersion curve that represents the variation of the phase velocity with frequency (Figure 3.1c). To do so, the original time-space domain records (Figure 3.1a) need to be transformed into another domain such as frequency-wavenumber (f-k), frequency-slowness (f-p), or frequency-velocity (f-v) using transformation techniques. Four different transformation techniques are commonly used for this purpose. These include slant stack or frequency-slowness (τp) (McMechan and Yedlin, 1981), frequency-wavenumber (FK) (Nolet and Panza, 1976; Yilmaz, 1987; Foti et al. 2000), Frequency Domain Beam-Former (FDBF) (Hebeler and Rix, 2007; Zywicki, 1999), and phase shift (PS) (Park et al. 1999). Rahimi et al. (2021) has shown that the FDBF transformation technique provides the highest resolution experimental dispersion curve over a wide range of subsurface layering and noise field conditions compared to the other transformation techniques. Therefore, in this study, this method is used for the construction of the experimental dispersion curve.

The FDBF transformation technique was first introduced by Lacoss et al. (1969) and then later modified and popularized by Zywicki (1999) for the MASW data processing. The FDBF method utilizes a steering vector, which is an exponential phase shift vector, to calculate the power associated with each particular frequency-wavenumber (f-k) data pair. For a particular f-k data pair, the power (energy) is calculated by multiplying the spatiospectral correlation matrix (R) by the steering vector and then summing the total power over all the receivers. After applying the FDBF method to the raw shot-gather data, the maximum spectral peak in the frequency-wavenumber domain is picked automatically for each frequency to identify the dispersion data points (Figure 3.1c). More information regarding the detail of the FDBF transformation method is provided in Zywicki, 1999.

Dispersion data points generated from each source offset were combined to create the raw experimental dispersion curve, which may include data from the fundamental mode, higher modes, effective mode, and/or data affected by near field effects. All the points identified as affected by near-field effects or propagating at an effective or higher mode were removed from the raw experimental dispersion curve to isolate the fundamental mode of propagation (Figure 3.1d). Typically, the fundamental mode is considered as the mode of interest for the inversion process (Foti et al. 2014). For each test setup, the final dispersion data from all source offsets were divided into 100 frequency bins from 1-125 Hz using a log distribution. The mean and standard deviation of each data bin were calculated to determine the mean experimental dispersion curve with the associated standard deviation.

Once the mean experimental dispersion curve was identified, an iterative inversion process within the Geopsy software package (www.geopsy.org) was used to solve for the shear wave velocity profile at each setup location. The inversion process consisted of determining theoretical dispersion curves for an assumed shear wave velocity profile and then comparing the results with the experimental dispersion curve to find the one that matches best using the neighborhood algorithm. The assumptions made in the iterative process consist of 1) horizontal soil layering, 2) constant shear wave velocity for each soil layer, and 3) homogenous and isotropic soil layers. For each site, various parameterizations (number of layers and layer thickness) were picked to determine the best layering ratio (the rate of thickness increment per layer). To accomplish this goal, a comparison was made between the soil layering determined from the shear wave velocity profile and the available boring logs. As an example, shear wave velocity profiles associated with

four different layering ratios are shown along with the boring log information at the Sand Gap site in Figure 3.2. As shown in this figure, the layering ratio that corresponds best with the boring log information is 1.4. The best layering ratio and a-prior information about the geologic setting of the site were used for the final parameterization. The goodness of fit between the experimental and theoretical dispersion curves was first judged based on the value of the calculated misfit parameter (collective squared error between experimental and theoretical dispersion curves) and then checked by visual comparison of the experimental and theoretical dispersion curves. This is necessary because the misfit parameter can only be used to compare the relative quality of fit of the theoretical dispersion curves for the same experimental dispersion data, as the values of the misfit parameter depends on both the quality and quantity of experimental dispersion data (i.e., misfit values lower than a particular value do not necessarily indicate a high-quality fit) (Griffiths et al. 2016). Finally, the median of the 1000 lowest misfit Vs profiles was taken as the 1D Vs profile for each setup location. Presented in Figure 3.1e, is an example of the Vs results for an MASW test setup with the 1000 lowest misfit Vs profiles, lowest misfit profile, median Vs profile, and sigma ln(Vs) for the 1000 lowest misfit Vs profiles.

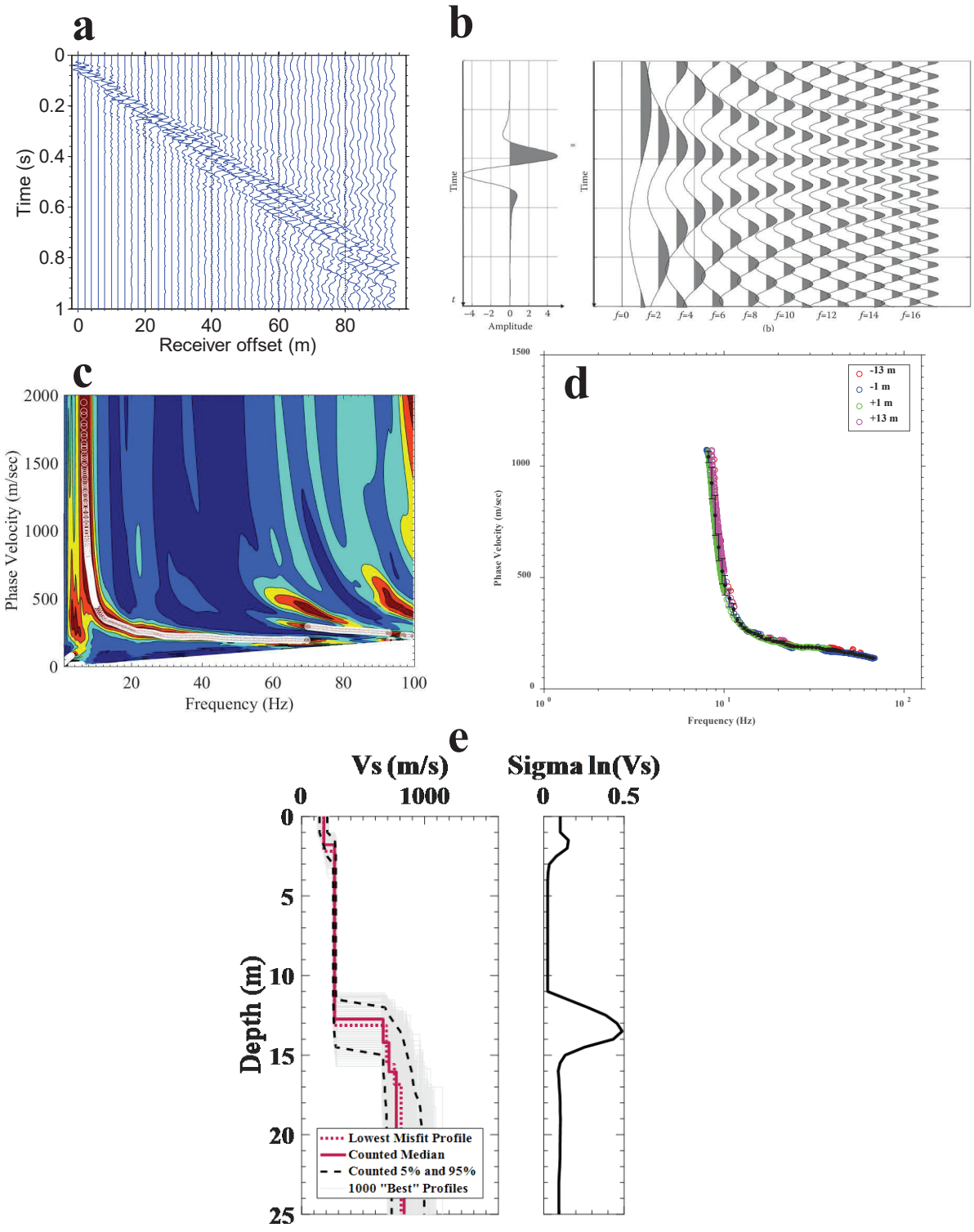

Figure 3.1- MASW data processing. a) raw geophone records in time-space domain, b) decomposition of a time domain signal into sum of frequency domain signals (Foti et al. 2014), c) raw experimental dispersion curve from one shot location, d) mean experimental dispersion curve, e) the 1000 lowest misfit Vs profiles, lowest misfit profile, median Vs profile, and sigma ln(Vs) for the 1000 lowest misfit Vs profiles.

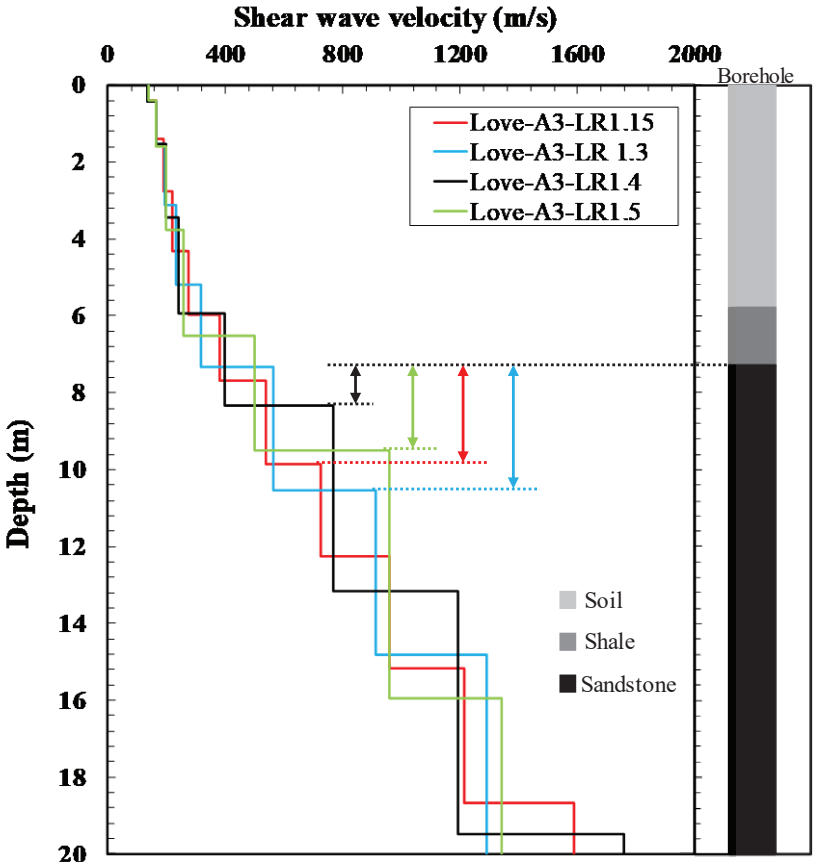

Figure 3.2- Identification of the best layering ratio for the Sand Gap site.

For sites where the co-located MASW and HVSR measurements were available, the joint inversion within the Geopsy software package was used to increase the reliability of the inverted shear wave velocity profile. To do so, the final experimental dispersion curve from the MASW and the peak frequency from the HVSR were inverted jointly within the Geopsy software package using weighting factors of w_{disp} =0.8 and $w_{H/V}$ =0.2, respectively (Teague et al. 2018). The combined misfit (m_c) parameter is calculated based on the misfit value related to the dispersion data (m_{disp}) and the misfit value related to the ellipticity peak ($m_{H/V}$) as below:

$$m_c=m_{disp}\times w_{disp}+m_{H/V}\times w_{H/V}=\sqrt{\sum_{i=1}^{n}\frac{(V_{di}-V_{ti})^2}{n_f\times\sigma_i^2}}\times 0.8+\sqrt{\frac{(f_{ellp,e}-f_{ellp,t})^2}{\sigma_{f_{ellp}}^2}}\times 0.2 \qquad 2$$

Where V_{di} and V_{ti} are, respectively, the experimental and inverted theoretical Rayleigh phase velocities at frequency f_i, σ_i is the standard deviation related to the experimental dispersion data at frequency f_i, n_f is the number of frequency samples used for misfit calculation, $f_{ellp,e}$ and $f_{ellp,t}$ are the experimental (HVSR) and theoretical ellipticity peaks, and σ_{ellp} is the standard

deviation associated with the experimental HVSR peak. Shown in Figure 3.3 is an example of joint inversion results from the MASW and HVSR measurements that represents one sharp impedance contrast in the subsurface, as shown in Figure 3.3a. From Figure 3.3, the low-frequency peak (f_1 = 6.9 Hz) from the HVSR measurement corresponds quite well with the peak from the theoretical ellipticity curve (see Figure 3.3c) and the sharp Vs impedance contrast in the Vs profile in Figure 3.3a.

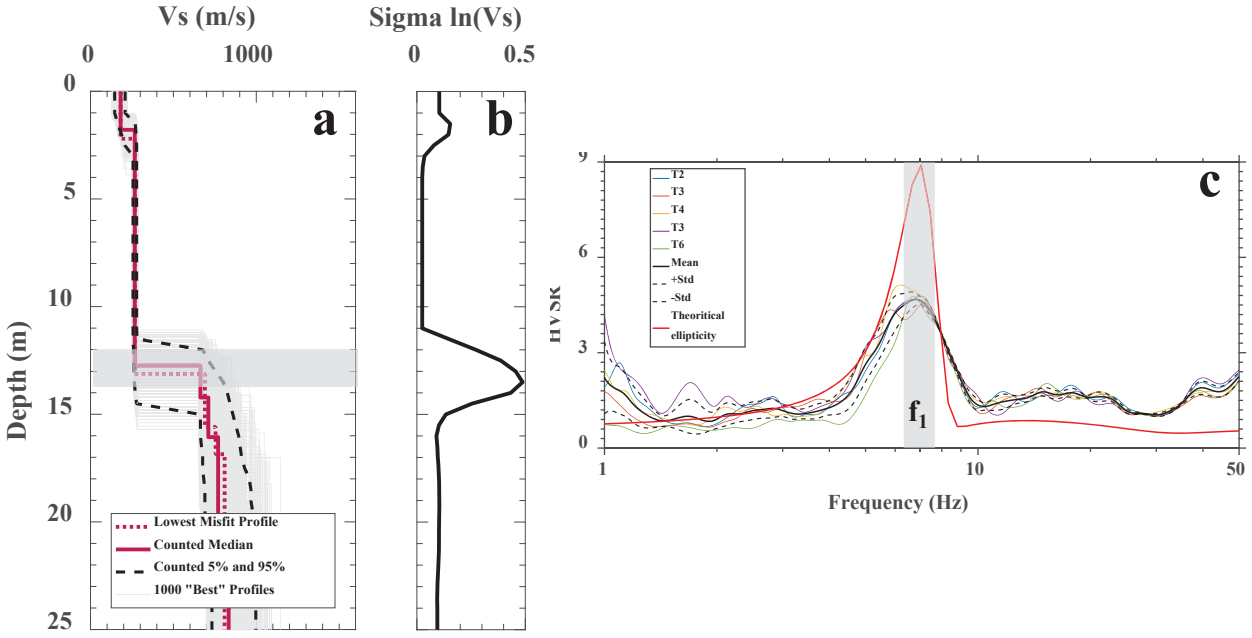

Figure 3.3- An example joint inversion results from the MASW and MHVSR measurements with one impedance contrast in the subsurface. a) Vs profile, b) sigma ln (Vs), c) experimental MHVSR along with the theoretical ellipticity curve.

3.1.2 Challenges and issues

The first and most important challenge in the MASW data processing is the accurate identification of the true fundamental mode of propagation. This affects the rest of the data processing steps since the final experimental dispersion curve is the main input of the inversion process. Generally, experimental dispersion data points can be classified into three main categories in terms of their quality, as follows:

- High-quality experimental dispersion data points: In this case, due to the high quality of the experimental dispersion data points, only one option is available as the dispersion curve associated with the fundamental mode of propagation, as shown in Figure 3.4a.

- Moderate quality experimental dispersion data points with several options for experimental dispersion curve: In some cases, it is possible to observe multiple modes of propagation (Figure 3.4b) at a single temporal frequency for sites with a heterogeneous soil profile. Identifying different modes of propagation is important in the MASW technique since the accuracy of the inversion results can be enhanced by including different modes in the inversion process (Xia et al. 2003). However, the presence of different modes of propagation in the experimental dispersion data points makes the mode identification complex, and sometimes it can lead to mode misidentification, which makes this process more challenging (Tremblay and Karray, 2019; Rahimi et al. 2021). For example, the experimental dispersion data points for one of the MASW testing locations in Hardy and the three potential options as the dispersion curve associated with different modes of propagations are shown in Figure 3.4b. Given that the fundamental mode of propagation corresponds to the maximum energy, the dispersion curve with the lowest phase velocity is typically considered as the most probable option for the fundamental mode. However, for cases like the one in Figure 3.4b, due to the absence of identifiable fundamental mode energy at certain frequencies, no measure of confidence/quantification of uncertainty is obtainable for Vs profiles corresponding to this frequency range (17-45 Hz).
- Poor quality experimental dispersion data points: In some cases, no dispersion curve can be extracted from the raw experimental dispersion data points due to their poor quality, as shown in Figure 3.4c.

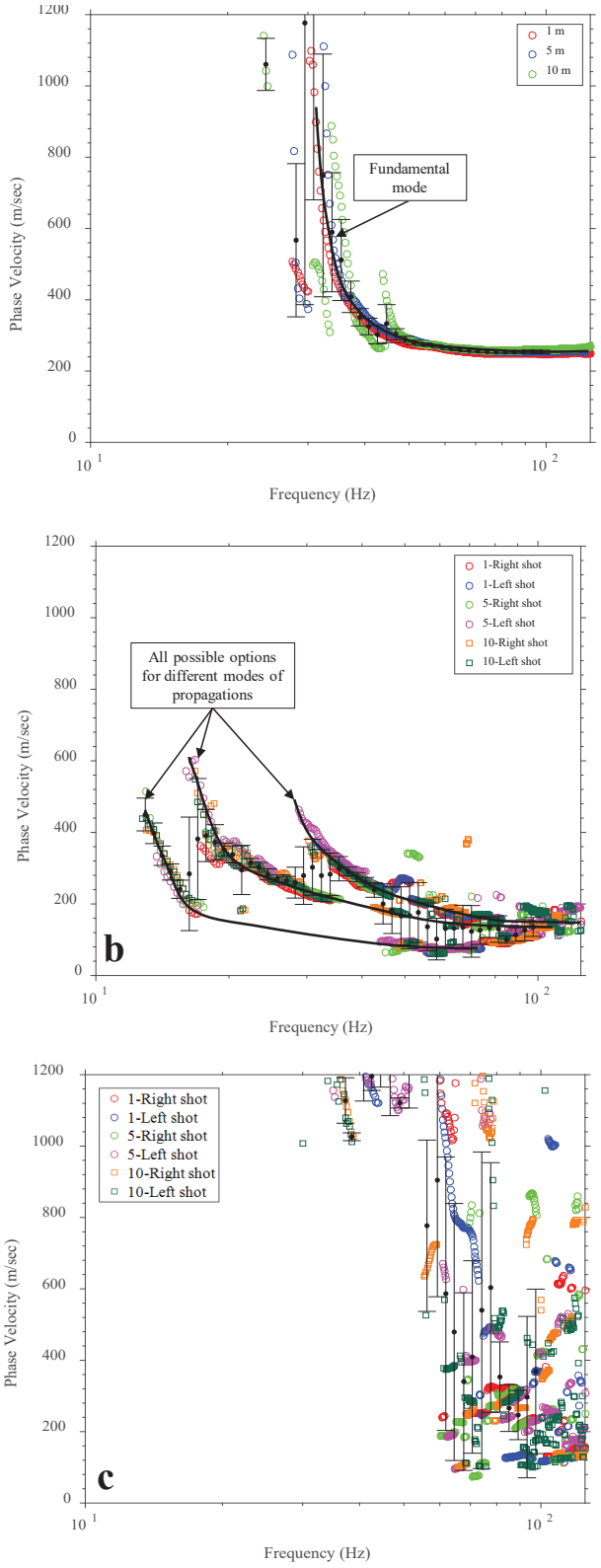

Figure 3.4- Experimental dispersion data points demonstrating. a) high quality experimental dispersion data points, b) medium quality experimental dispersion data points with several options mode identification, c) poor quality experimental dispersion data points.

Although the quality of the experimental dispersion data points can be controlled to some extent during the field measurements and the resolution of the experimental dispersion curve can be enhanced by using the FDBF transformation technique (Rahimi et al. 2021), there are some unfavorable conditions, such as contamination of the data by coherent (unwanted source generated noise) and incoherent noise (background noise) that cannot be eliminated during the field measurement and data processing.

Another common issue in the MASW method is the near-field effects. Near-filed effects are considered as the most commonly encountered issue in the MASW method, significantly reducing the maximum resolvable depth, quality, and resolution of the experimental dispersion curve. Near-field effects are mainly caused due to two assumptions: (1) pure plane wavefield for the surface waves, and (2) pure surface waves in the wavefield with no interaction from the body waves. The regions where these assumptions are invalid are called the near-field.

The near-field effect of modeling a cylindrical wavefield with a plane wave field is called the model incompatibility effect (Zywicki and Rix, 2005). The model incompatibility effect can lead to a roll-off in phase velocity of the fundamental mode of propagation, whereas the existence of the body waves can generate some oscillations in the fundamental dispersion curve. The near-field effects typically corrupt the low frequencies part of the experimental dispersion curve. The low frequencies part of the dispersion curve is important since it has the information regarding the deeper subsurface layering (e.g. stiff soils and bedrock units). Provided in Figure 3.5a and b are two examples of the near-field effects caused by the model incompatibility and the presence of the body waves in the wave field, respectively.

Another issue with the MASW method is the non-uniqueness of the solution, meaning that several theoretical dispersion curves can be identified that equally match the experimental dispersion curve. This issue can be addressed by supporting the MASW measurements with boring logs information or by the combined use of multiple geophysical techniques. Overall, users of the MASW method need to realize and account for the uncertainties associated with this technique to assess the reliability and accuracy of the inverted shear wave velocity profile.

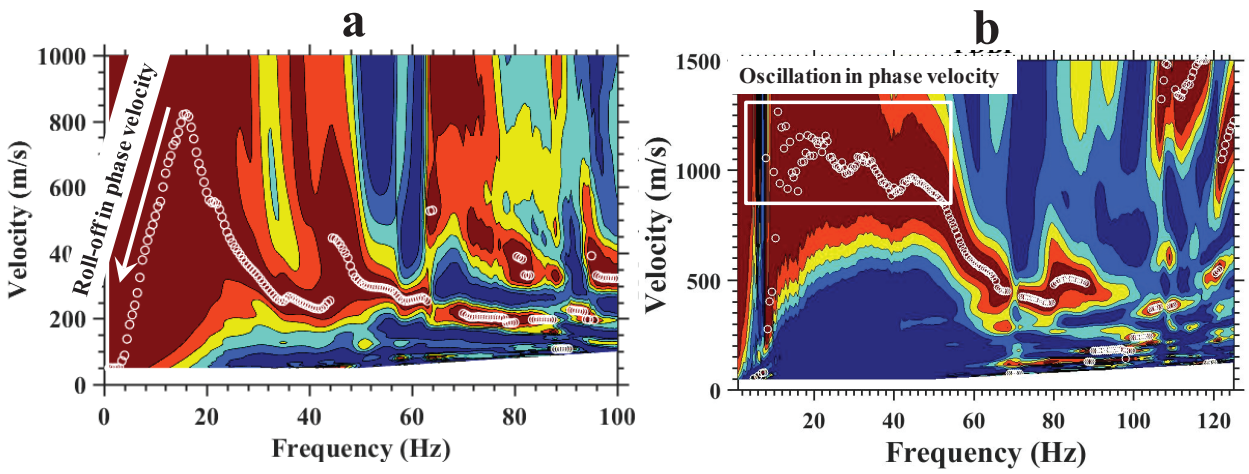

Figure 3.5- Example near-field effects. a) Near-field effect caused due to the model incompatibility, b) Near-field effect caused by the interference of the body waves.

P-wave refraction

3.1.3 Data processing

The data analysis method for the P-wave refraction was originally introduced by Redpath in 1973. In this study, the procedures proposed in ASTM D5777-00 were followed for the P-wave refraction data processing. The recorded signals from each hammer strike were averaged together to increase the signal-to-noise ratio of the data for each geophone location. The raw P-wave refraction data is a suite of amplitude versus time plots called a waterfall plot. As an example, the waterfall plot related to one of the P-wave refraction setups for the Sand Gap site, consisting of 48 vertical geophones with uniform spacing of 1.5 m is shown in Figure 3.6. The source position was located in the center of the array for this setup.

For refraction testing, the instant of the source pulse (e.g., the sledgehammer hitting the ground), “zero time” is recorded by the seismograph, and the time it takes the first wave to arrive at each geophone (see pink stars in Figure 3.6) is identified. The raw data is then displayed as the travel time to each receiver (first wave arrival) versus receiver distance from the source. The number of layers is determined based on the variations in the slope of the lines fit through the P-wave arrival times. Each considerable change in the slope of the lines fit through the data is an indicator of either sharp variation in the ground surface elevation or changes in the P-wave velocity of the subsurface materials. Therefore, it is important to account for sharp variations in the ground surface elevation for the P-wave refraction data processing to avoid misinterpretation of the data. The slopes of the arrival times to each geophone are used to determine the velocity of subsurface

layers, while an application of Snell's law of refraction of waves is used to determine the depth-to-layer interfaces.

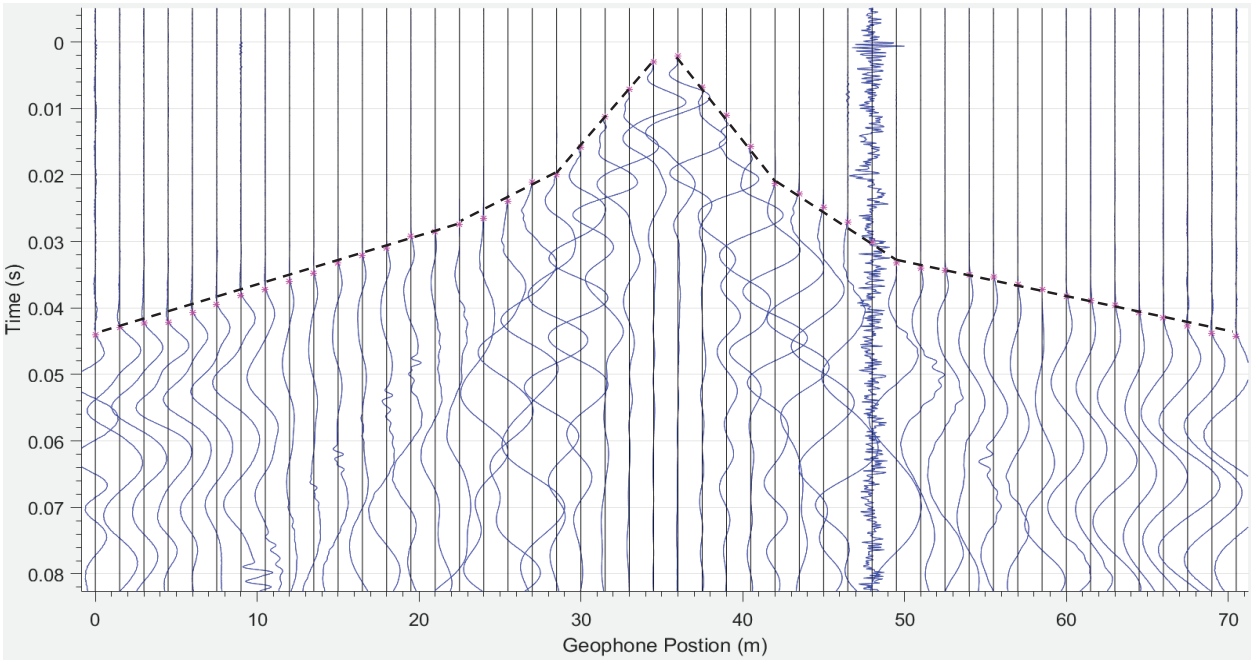

Figure 3.6- An example of a waterfall plot for one of the MASW testing setups for the Sand Gap, AR site.

The P-wave arrival time information was then exported to Plotrefa, one of the modules of SeisImager software for further processing (SiesImager/2D manual). This software is used to control or modify the P-wave arrival times, add topographic information to the data, and create a velocity cross-section for site characterization. An example of a travel time versus distance plot with velocity labels in m/s is shown in Figure 3.7. Each arrival time consisted of geophone position and elevation, shot or source position, and first arrival time. The number of layers assigned to each travel time is determined based on the changes in the slope of the travel time. Typically, between 2-4 layers were able to be detected from the P-wave arrivals. A minimum of 50 iterations of the non-linear raypath inversion were used to construct the subsurface layering based on the arrival times. The final inversion results were exported to Surfer for presentation.

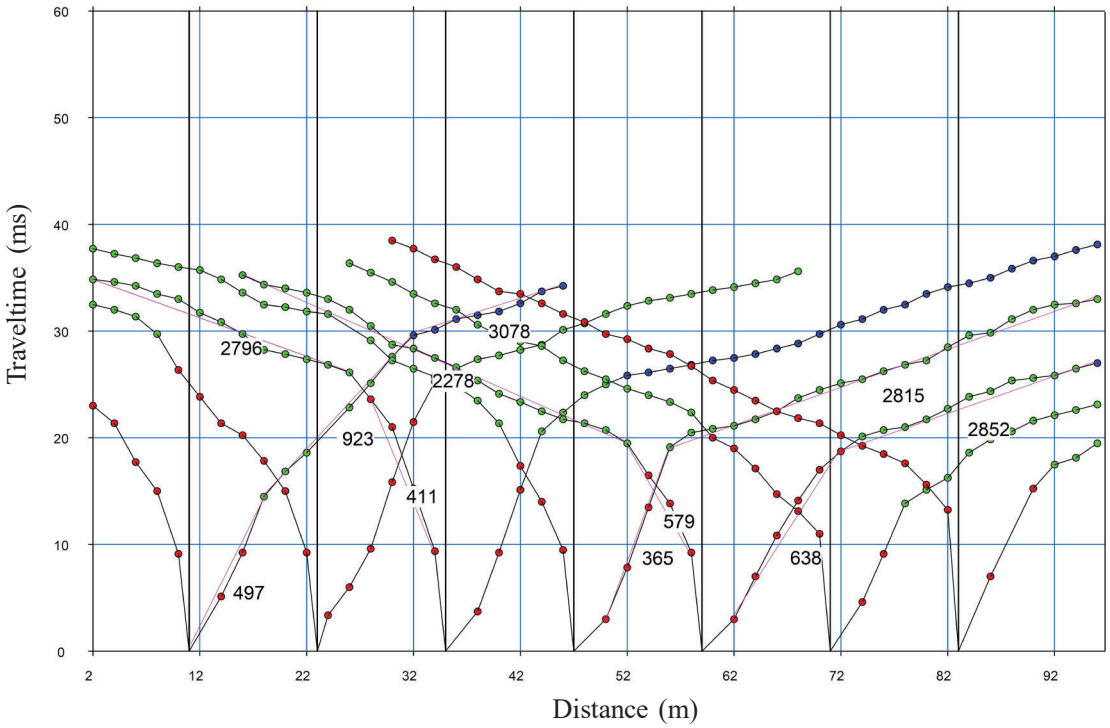

Figure 3.7- An example of distance versus travel time plot (velocity in m/s).

3.1.4 Challenges and issues

Data processing and data interpretation of the P-wave refraction survey is straightforward for sites with clear first arrival times. However, this is not always the case because there are several parameters that may affect the quality of the P-wave refraction results. These include interference of the air waves (generated from the hammer strike) or surface waves with body waves, quick attenuation of the body waves, presence of dipping layers in the subsurface, environmental noise interfering with the signals, and the existence of a velocity reversal layer in the subsurface.

Generally, the first arrival time at geophones located further from the source becomes increasingly ambiguous due to the rapid attenuation of the body waves. Presented in Figure 3.8 is a waterfall plot of the P-wave arrivals with the dashed line indicating first arrivals picked from 8-23 m and a rectangle indicating the area where P-wave arrivals become ambiguous. If the apparent arrival times within the rectangle were picked, the resulting line would indicate negative velocity for the soil, which is physically impossible and therefore erroneous. Being able to identify the first arrival times from geophones located far from the source is important because they have the information regarding deeper subsurface layers. Therefore, P-wave refraction data processing

requires diligence and skill to minimize errors. Figure 3.8 has examples of the P-wave refraction data with ambiguity in the picking process.

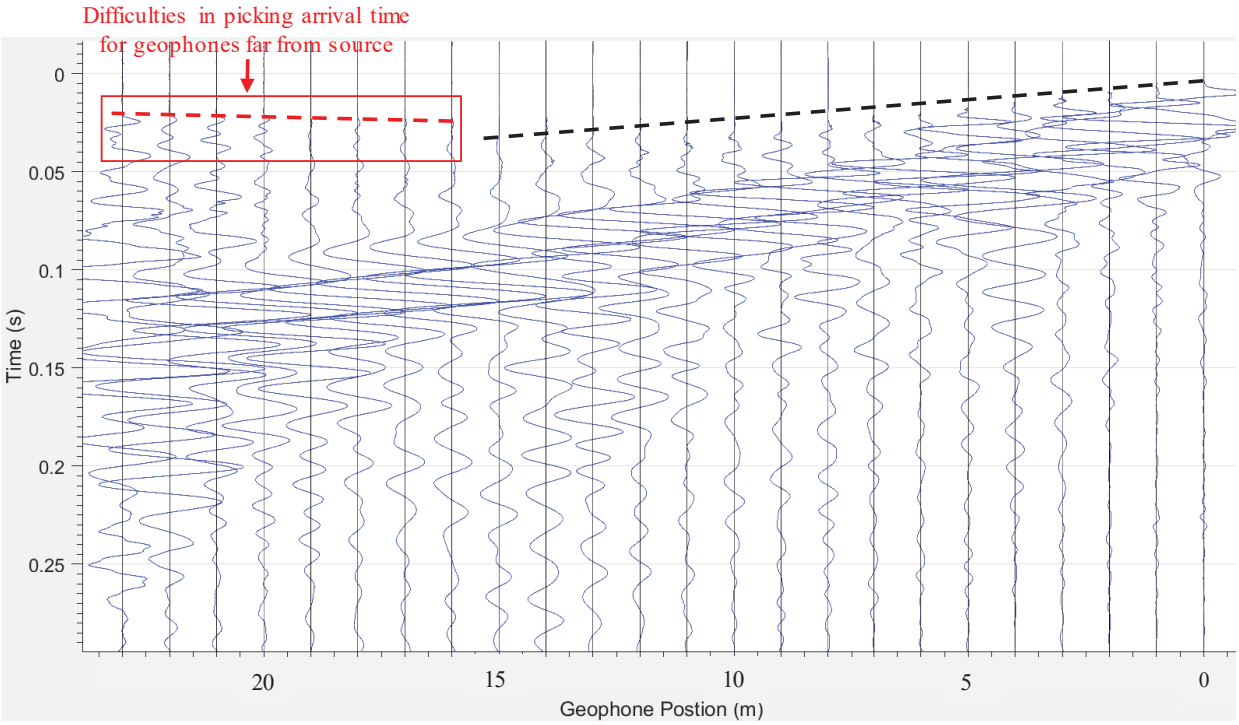

Figure 3.8- A waterfall plot of the P-wave arrivals with the dashed line indicating picked first arrival times and the rectangle indicating the area where P-wave arrivals become ambiguous.

Three other issues with the P-wave refraction methods are (1) maximum depth of exploration, (2) presence of shallow water table, and (3) presence of a velocity reversal layer (i.e. stiff over soft layer). Typically, a P-wave refraction survey is only useful for near-surface site characterization. The maximum depth of exploration can be increased using a longer setup array. However, uncertainty regarding the first wave arrivals (see Figure 3.8) and the P-wave refraction results increase with distance from the source and so, these limit the maximum depth of exploration. At locations with a shallow water table, the water controls the P-wave refraction survey since the P-wave velocity of water (~1500-1600 m/s) is significantly higher than the P-wave velocity of shallow soil deposits. Therefore, the P-wave refraction survey would not be valuable in terms of characterizing soils for sites with shallow water tables. Additionally, the P-wave refraction method would lead to erroneous results for sites where a velocity reversal layer present within the penetration depth of the P-waves. This is because the P-wave refraction method cannot resolve for the velocity reversal layer.

Overall, P-wave refraction data processing and interpretation can be ambiguous. However, P-wave refraction surveying may be valuable for assessing the depth of the water table or bedrock at sites with a shallow water table or bedrock depth.

HVSR

3.1.5 Data processing

The raw data for the HVSR technique contains two records for the horizontal components (North-South and East-West) and one record of the vertical component. The HVSR is defined as the ratio of the Fourier amplitude of horizontal to vertical components as a function of frequency. The HVSR data was processed using the following steps:

- Each record was divided into different time windows. The window length of 1-2 minutes was selected as it satisfies all the criteria proposed by SESAME guideline (2004).
- Fourier amplitude of each component was computed using the discrete Fast Fourier Transform (FFT) function.
- Smoothing: several methods are available for HVSR smoothing, but the Konno and Ohmachi approach (Konno and Ohmachi, 1998) is typically recommended as it accounts for the various number of low frequencies points (Brad, 2004). Therefore, the Konno and Ohmachi smoothing approach with a bandwidth coefficient of b=40 was used to smooth the Fourier amplitude of each component. The Konno and Ohmachi smoothing function is a logarithmic smoothing filter which is defined:

$$W(f, fc) = \left[\left(\sin \left(\log_{10} \left(\frac{f}{fc} \right)^b \right) \right) / \left(\log_{10} \left(\frac{f}{fc} \right)^b \right) \right]^4 \quad 3$$

  where f and fc are frequency and center frequency, respectively, and b is the smoothing bandwidth. The smoothing bandwidth is the main factor controlling this smoothing function.
- The two horizontal components were merged using the geometric mean equation. Horizontal to vertical (HVSR) spectral ratio was computed for each individual time window (Figure 3.9a).

- Anomalous time window rejection: The mean frequency peak of the HVSR (f_M) and its standard deviation (σ) were computed from all individual time windows. A new frequency-domain window rejection tool was developed and used in Matlab to reduce the uncertainty in the HVSR peak frequency (f_I) estimates. Time windows that fail to satisfy the amplitude criterion (Amplitude > 2 at f_I) and the peak sharpness criterion (The difference between the amplitude at f_I and the mean amplitude for frequencies range between $[(2*\sigma - f_M), (2*\sigma + f_M)]$ is greater than 15%) were first removed from the HVSR data. Then, the frequency-domain window rejection is conducted in an iterative process. The rejection process stops when the data satisfies the conditions defined by the user. An example of HVSR results before and after excluding anomalous time windows is shown in Figure 3.9 a and b, respectively.
- The rest of the time windows were used to determine the mean HVSR spectra ratio with associated standard deviation. The mean HVSR spectra ratio was used to estimate the sediment thickness. This is explained in more detail in the next section.

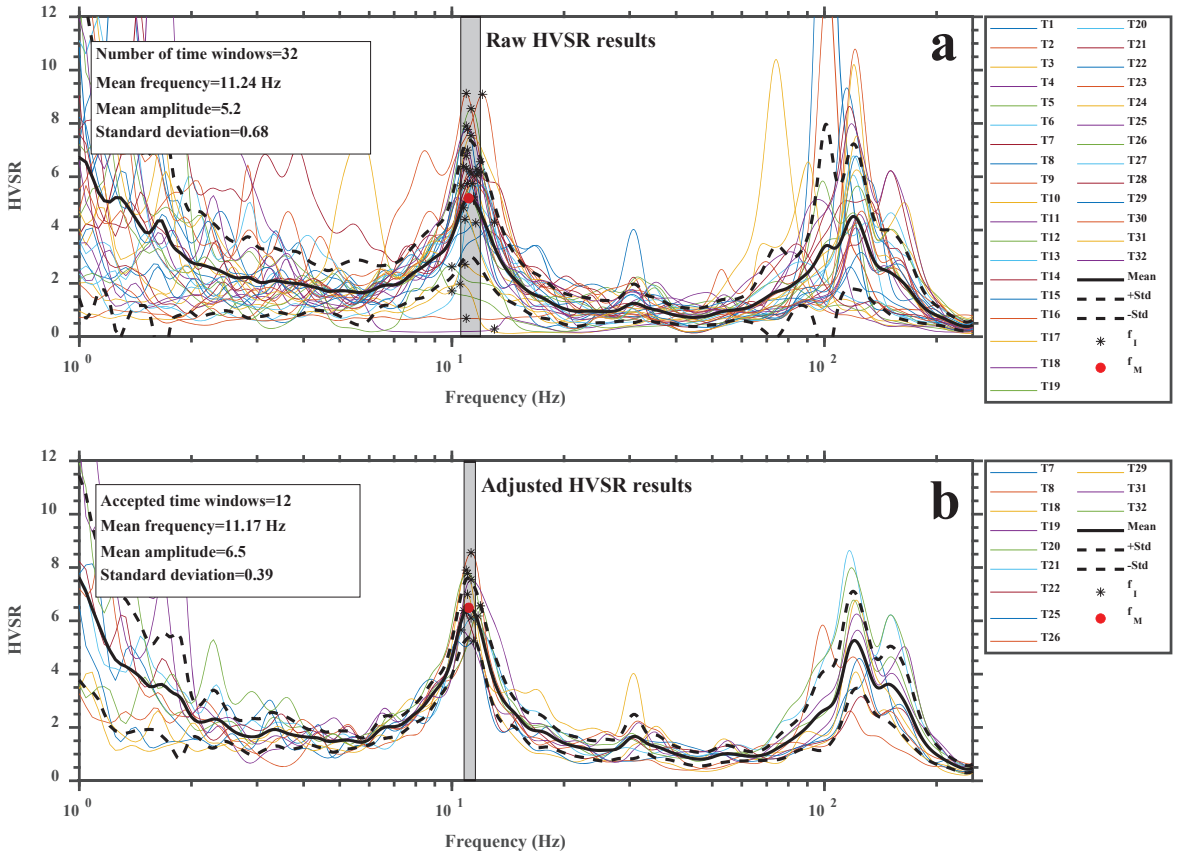

Figure 3.9- An example of HVSR data processing. a) HVSR curve before excluding the anomalous time windows, and b) final HVSR results after excluding the anomalous time windows.

3.1.6 Challenges and issues

HVSR is one of the simplest geophysical methods in terms of data processing and data interpretation for sites where a clear HVSR peak is available. However, this is not always the case for the HVSR measurements. In some cases, the HVSR measurement may contain multiple peaks, broad peaks, or may not have a clear peak (each case is explained in detail below), each case may complicate the interpretation of HVSR measurements as follows:

- HVSR curve with multiple peaks: In some cases, the HVSR curve may exhibit multiple peaks, all of which satisfy the requirement of a true HVSR peak, as shown in Figure 3.10a. This might be caused by several large impedance contrasts in subsurface materials (e.g. soil/rock interface). However, the existence of multiple peaks in the HVSR curve is not always related to the geologic setting of the area, given that one of the peaks may have an industrial origin (Brad, 2004; Rahimi et al. 2020). It is recommended to reprocess the data using various smoothing parameters to check if the HVSR peaks are stable (SESAME guideline, 2004).
- HVSR curve with a broad peak: In some cases, HVSR amplitude related to the maximum HVSR value occurs in a broad range of frequencies (Figure 3.10b). As shown in Figure 3.10b, the peak HVSR value occurs within a range of frequencies from 14-27 Hz resulting in a wide range of depth to bedrock. If a broad peak is encountered, it is recommended to decrease the smoothing bandwidth parameter as this may narrow or transform a broad peak into multiple narrower peaks (SESAME guideline, 2004).
- HVSR with no clear peak: In some cases, the HVSR ratio is close to 1 for all ranges of frequencies, indicating that no clear peak exists in the HVSR measurement, as shown in Figure 3.10c. Although this is possible for sites without any significant impedance contrast in the subsurface material, it is not always related to site conditions.

In all three cases, HVSR data interpretation can be associated with great uncertainty. These issues can be addressed to some extent by supporting the HVSR measurement with boring log or other geophysical information.

More information regarding the HVSR technique can be found in “guidelines for the implementation of the H/V spectral ratio technique on ambient vibrations: measurements, processing, and interpretation” which is provided in (SESAME guideline, 2004).

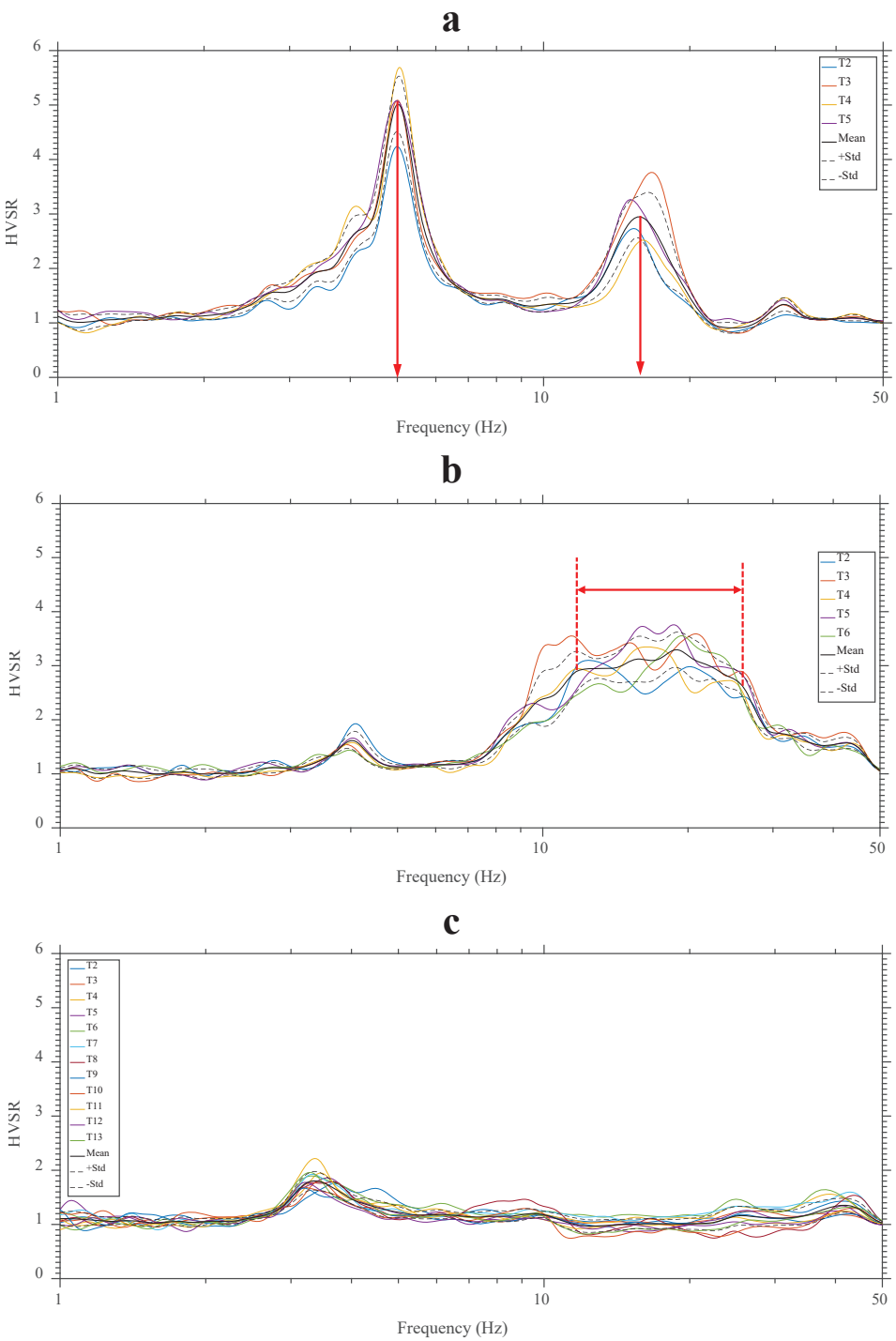

Figure 3.10- Experimental HVSR results with different behavior in terms of peak HVSR. a) HVSR curve with multiple peaks, b) HVSR curve with a broad peak, c) HVSR curve with no clear peak.

CCR

3.1.7 Data processing

In order to process the raw CCR data, different software are used including OhmImager, MagMap, Res2Dinv (Geotomosoft), and Surfer (Golden software).

The acquired raw CCR data was first processed in OhmImager software to check testing geometries (dipole length, rope length, and operator offset) for potential metadata errors, to combine raw CCR data with different testing geometries along the same survey line, and to convert the data to a readable format for the MagMap software.

MagMap is used to convert GPS readings to a standard UTM system, remove noisy CCR readings by removing spikes and dropouts from the raw data, and then export the data into a format that can be read using Res2Dinv.

The raw CCR values (apparent resistivity) are converted to true resistivity values using Res2Dinv through an iterative process called inversion. The inversion process is carried out until the measured and estimated data reaches a certain error value defined by the user. The final Res2Dinv results consist of several files containing true resistivity values, distance, elevation, and GPS readings in a format that can be opened in Surfer.

The Surfer software is mainly used to generate a pseudo section profile showing the variation of true resistivity values with positions (distance) and with effective depths. Different gridding methods are available in this software for data processing. The triangulation with linear interpolation method was used in this study for gridding. An example of the final output of CCR data processing is presented in Figure 3.11 for one of the survey lines, showing the variation of true resistivity values of subsurface materials with depth and distance.

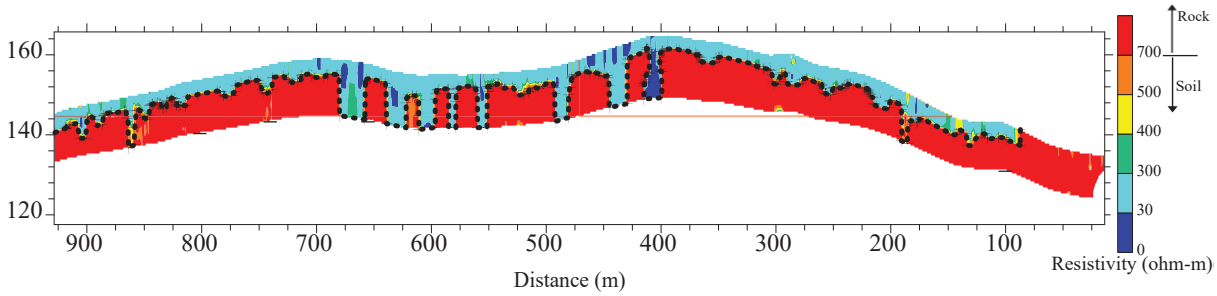

Figure 3.11- An example of the final output of the CCR data processing.

3.1.8 Challenges and issues

As explained before, CCR data processing is a relatively straightforward procedure, whereas the interpretation of the processed data could be very ambiguous. The most important step toward CCR data interpretation is the accurate determination of resistivity ranges associated with different geomaterials. It has been shown that the resistivity range associated with a soil type can vary significantly given that soil resistivity is dependent on several parameters including soil gradation and mineralogy, temperature, soil cavity, and particularly soil degree of saturation (Kaufman and Hoekstra, 2001). For example, it has been shown that while the resistivity of wet clay/silt can vary from 0-80 ohm-m, this range can change to 0-500 ohm-m for dry clay/silt, indicating the importance of the degree of saturation for resistivity surveys (Garman and Purcell, 2004; Hayashi et al. 2010). This points to the need for more studies to explore the effects of the parameters mentioned above on soil resistivity, especially the combined effects of these parameters, which have not yet been investigated.

Mapping subsurface layering based solely on CCR could lead to some misinterpretation because it is difficult to control/monitor the parameters influencing soil resistivity during CCR field tests, especially for a long survey line. This ambiguity in data interpretation can be overcome to some extent by utilizing a-priori information about the subsurface conditions. However, often times the ambiguity regarding the data processing of the CCR cannot be significantly reduced even with the addition of the a-priori information.

Another challenge is the maximum depth of exploration in the CCR survey. The depth of exploration can be adjusted in the CCR survey by varying rope length and dipole length. However, for depths greater than typically 10 m, the measured resistivity values are typically not accurate enough due to the data averaging process.

ERT

3.1.9 Data processing

The raw data of the ERT surveys were inverted using the EarthImager2D software. This software uses the Occam style inversion algorithm to find subsurface models within a pre-defined tolerance. Through an iterative process called inversion, the experimental apparent resistivity data measured in the field tests are compared with the theoretical response of the modeled subsurface to find the modeled subsurface matches best with the experimental data. The Gauss-Newton method is used to solve the inversion problem. The goodness of fit between the experimental data and theoretical model is evaluated based on the values of the calculated misfit (root mean squared) and L2-norm parameters (Karim et al. 2018; Koehn et al. 2019). RMS values less than 10% and L2-norm values less than 1 are used as indicators of a relatively good and acceptable fit (Snapp et al. 2017).

3.1.10 Challenges and issues

The challenges and issues associated with the ERT method is similar to that of the CCR as both methods measure the resistivity of the subsurface materials (see Section 3.5.2).

GPR

3.1.11 Data processing

Ekko-Project software developed by Sensors & Software Company, which includes basic and advanced processing tools, was used for the GPR data processing. Most researchers have recommended using only the basic processing steps for the GPR data processing because over processing could introduce bias into data resulting in data misinterpretation (Jol, 2008). Post-acquisition GPR data processing was carried out using basic processing steps, including dewow filter, time zero correction, background subtraction, topographic correction, and depth conversion. Each step is explained in the following.

- Dewow filter: In this step, the initial DC signal component, the potential DC bias, and unwanted low-frequency energy are removed from the raw GPR data by applying a high-pass filter. The typical dewow filtering effects are shown in Figure 3.12.

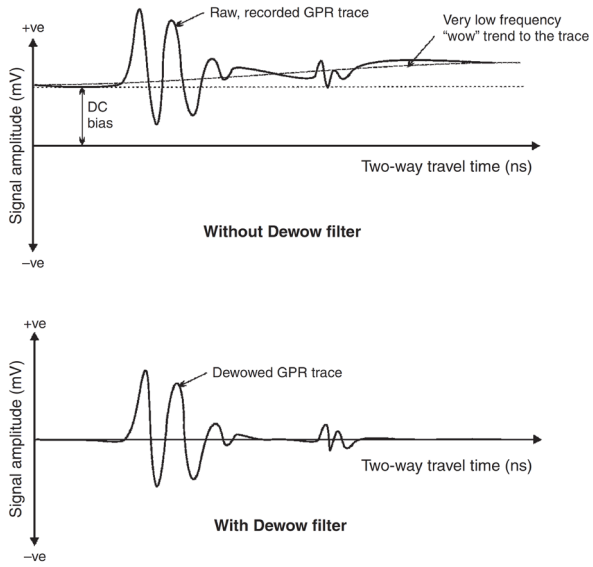

Figure 3.12- Dewow filter of a GPR signal (from Jol, 2008).

- Time zero correction is used to remove any travel time which is not related to the subsurface layers, such as travel time in the air.
- Background subtraction: Background noises that can create a continuous horizontal line signal and poor antenna-ground coupling can be removed using the background subtraction. Background subtraction is typically done by removing the average of all GPR traces from each trace.
- Topographic correction: Given that variations in surface elevation can change GPR data significantly, it is important to account for this during GPR data processing.
- Depth conversion: As mentioned previously, GPR works by measuring the double travel time from the surface to an interface/object and reflected back to the ground surface. This time can be converted to depth if any information regarding the average velocity of the electromagnetic waves in the subsurface materials is available.

Presented in Figure 3.13, are the raw and processed GPR data for one of the survey lines. The raw GPR data without any processing is shown in Figure 3.13a. This data is corrected for topographic effects, and the result is shown in Figure 3.13. The final GPR profile after all the processing steps is presented in Figure 3.13. The pre-existing boring log information was used to convert travel time to depth.

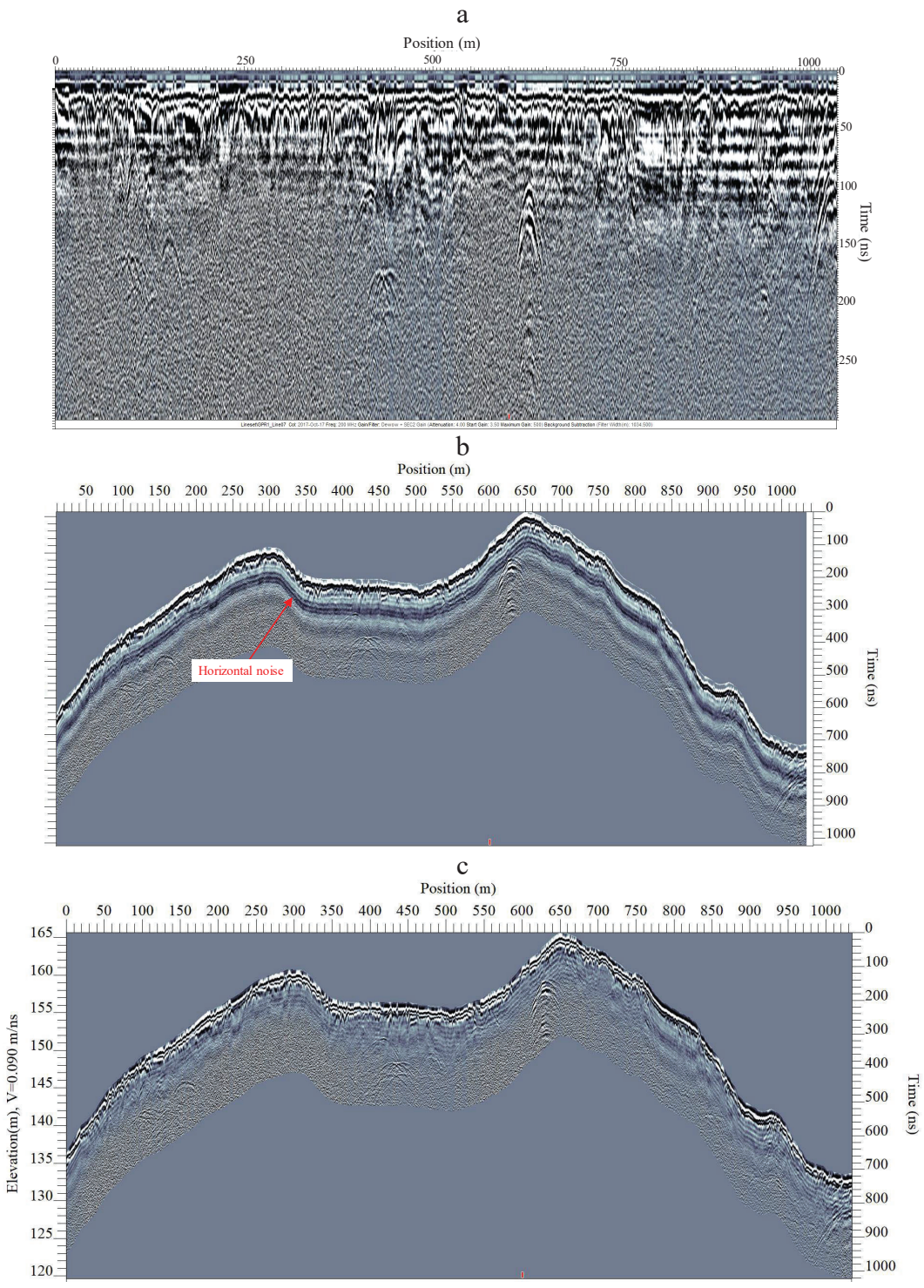

Figure 3.13- GPR data processing demonstrating a) raw data, b) correcting for topographic effects, c) final output of GPR data processing.

3.1.12 Challenges and issues

GPR is one of the most ambiguous geophysical methods in terms of data interpretation, especially for new users. For example, in the book "Ground penetrating radar theory and applications" written by Jul (2008), it is mentioned that "There have been many times I have processed/interpreted a section to death only to revisit it some months later as I have seen something new in the data or have developed a new processing approach", indicating the level of complexity and ambiguity of the GPR data processing. Users have to classify subsurface materials and detect buried utilities based on electromagnetic waves reflected back from large contrasts. For most geotechnical applications, especially for soil/bedrock interface detection, this process has the potential for much ambiguity and uncertainty. To better illustrate this subject, the results of a GPR survey for a portion of GPR testing in Hardy are shown in Figure 3.14. Figure 3.14a, which shows the processed GPR data for this section of the survey, is the final profile used for the data interpretation. As shown in this figure, multiple flat-lying and dipping reflectors are evident in this profile along with several wide hyperbolas. The locations of the wide hyperbolas are illustrated in Figure 3.14b with red color. As shown in this profile, it is difficult to identify the soil/bedrock interface without a-priori information regarding the subsurface conditions. Therefore, GPR results should be compared with other available information regarding the subsurface conditions to avoid data misinterpretation. However, this is not the case in all situations, and it depends on several parameters, including site conditions, GPR testing geometry, and frequency of antennas used for the field measurements.

Another issue related to the GPR technique, which is clear in Figure 3.14, is the resolution of the recorded signals and the maximum depth of penetration. These are two important factors influencing the applicability of any geophysical method dealing with wave propagation. The GPR technique is most effective for very shallow investigations since it suffers from quick loss of resolution with depth (Słowik, 2012). As shown in Figure 3.14, the resolution of the GPR signals are remarkably reduced for depths greater than 4 m, even for a 50 MHz antenna. This is caused by the top clay layer which exists at the Hardy site, as it rapidly attenuates the electromagnetic waves. This is explained in more detail in the next chapter.

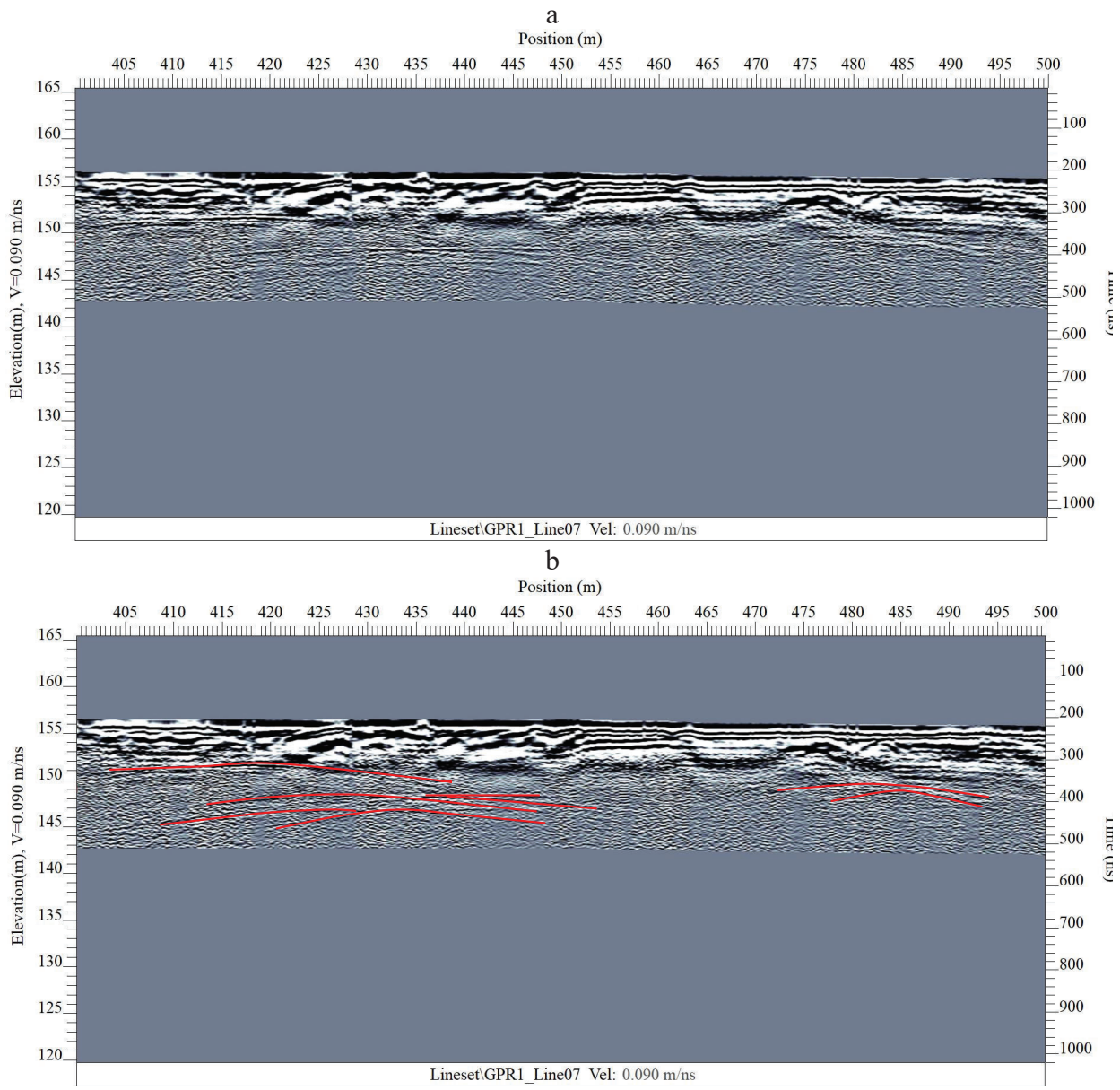

Figure 3.14- The results of GPR testing at the Hardy site demonstrating a) Processed data, b) identification of large hyperbolas in GPR testing.

Another challenge in the GPR data interpretation is an accurate determination of the average velocity of the electromagnetic waves in the subsurface materials in order to convert the travel time to depth. Typical values for velocity of electromagnetic waves for various geomaterials have been proposed in several investigations and codes (ASTM D6432-11; Chlaib et al. 2014), which may be used to estimate the penetration depth of the GPR testing. However, the selection of electromagnetic velocity for a particular soil type may be difficult since most codes and studies recommend a wide range of velocity for each soil type. For example, the values reported in ASTM

D6432-11, presented in Table 3-1, are often provided as a range of velocities (pulse velocity) for many geomaterials (e.g. clay, and sand). Therefore, a single value must be selected from the range, which may not be representative of the true velocity of the material.

Table 3-1- Recommended values for pulse velocity (ASTM D6432-11).

Material	Relative Permittivity, K	Pulse Velocities, m/Ns	Conductivity, mS/m
Air	1	0.3	0
Fresh water (f,t)	81	0.033	0.10 - 30
Sea water (f,t,s)	70	0.033	400
Sand (dry) (d)	4-6	0.15-0.12	0.0001 - 1
Sand (saturated) (d,w,f)	25	0.055	0.1 - 1
Silt (saturated) (d,w,f)	10	0.095	1 - 10
Clay (saturated) (d,w,f)	8-12	0.106-0.087	100 - 1000
Dry sandy coastal land (d)	10	0.095	2
Fresh water ice (f,t)	4	0.15	0.1 - 10
Permafrost (f,t,p)	4-8	0.15-0.106	0.01 - 10
Granite (dry)	5	0.134	0.00001
Limestone (dry)	7-9	0.113-0.1	0.000001
Dolomite	6-8	0.122-0.106	
Quartz	4	0.15	
Coal (d,w,f, ash content)	4-5	0.15-0.134	
Concrete (w,f, age)	5-10	0.134-0.095	
Asphalt	3-5	0.173-0.134	
Sea ice (s,f,t)	4-12	0.15-0.087	
PVC, epoxy, polyesters vinyls, rubber (f,t)	3	0.173	

It should be noted that even though GPR data interpretation is quite ambiguous for geotechnical applications, it has been shown that GPR could be valuable in some conditions for the detection of shallow buried utilities, Karst features, groundwater table, and sinkholes (Carrière et al. 2013; Chlaib et al. 2014; Busato et al. 2016).

EM31

3.1.13 Data processing

As aforementioned, the EM31 device directly measures and records electrical conductivity and in-phase values of subsurface materials. No data processing is required since the two components of the signals (electrical conductivity and in-phase) are directly measured. The electrical conductivity of a material is the ability to conduct a current, and it is expressed in units of milliSiemens per meter (mS/m). The in-phase parameter defines the relative quantity of the primary magnetic field which is expressed in units of parts per thousand (ppt). This parameter is closely linked to the magnetic susceptibility of the subsurface materials, so it is often used for the detection of buried metallic objects.

3.1.14 Challenges and issues

Like all the other geophysical methods, the first and most important step toward EM31 data interpretation is the identification of the ranges of electrical conductivity in mS/m unit associated with different geomaterials. Given that EM31 has been mostly used for agricultural applications such as the determination of soil salinity, there is not much background information regarding ranges of the electrical conductivity related to different geomaterials. Very shallow depth of penetration is another drawback of the EM31 survey. In the EM31 survey, depth of penetration is mainly controlled by the distance between the coil centers of the transmitter and receiver. The maximum depth of penetration is typically close to 5 m (GF Instruments, 2016). Moreover, the presence of underground metallic objects can shadow the subsurface conditions and layering.

4 Results and conclusions from Phase I

Introduction

The results of the geophysical measurements for Phase I that includes two sites located in Hardy and Sand Gap, AR are presented in this section, and then comparisons are made between the results of different geophysical measurements, boring logs, and other available information to determine the geophysical technique(s) that best suited for the purpose of bedrock mapping and slope stability investigations for transportation projects.

Hardy Site

As aforementioned, different geophysical methods were carried out along some portions on the Eastside and Westside of the Highway 63 bypass at Hardy, AR. Shown in Figure 4.1 are yellow points indicating the survey paths on the Eastside and Westside of the Highway 63 bypass along with green points indicating the boring log locations. All the field tests, including MASW using both Rayleigh and Love type surface waves, P-wave refraction, CCR, HVSR, GPR, and EM31 were conducted on the same survey paths, as shown in Figure 4.1. The numbers along the survey paths are distances from the start point of the survey line in meters. These numberings are used in all the cross-section profiles acquired using different geophysical methods to compare the results later in the report.

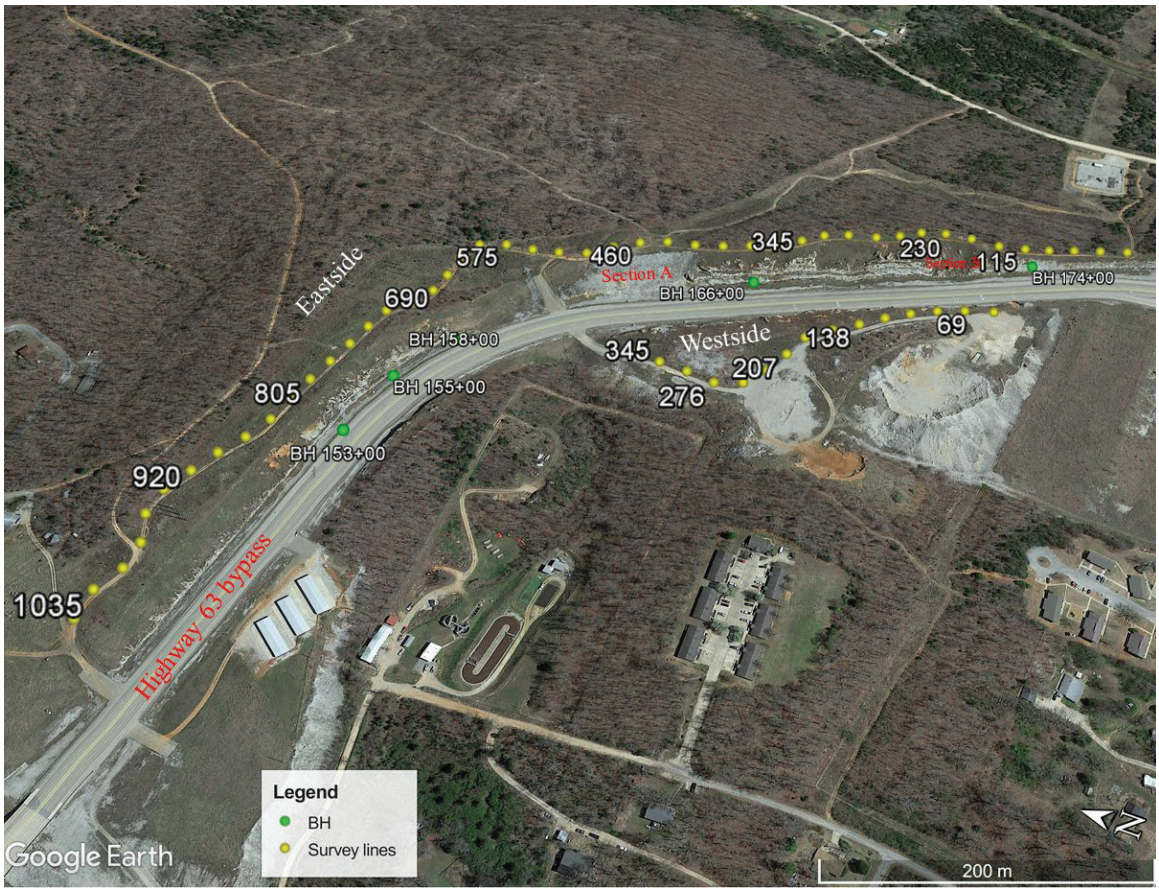

Figure 4.1- Survey line and boring log locations at the Highway 63 bypass in Hardy, AR.

As shown in Figure 4.2, some portions of the Eastside survey line (from 0-506 m) are adjacent to the vertical rock cuts along the Highway 63 bypass; therefore visual inspection of the cuts can provide useful information regarding the potential bedrock locations. According to the photos taken from the cuts and the Google Earth image of the area, there are two sections of interest, Section A (see Figure 4.3) and Section B (see Figure 4.4), which possibly consist of relatively deep sediment compared to the rest of the survey line. The locations of these sections along the survey line are illustrated in Figure 4.2. While the side slopes of the cuts are approximately vertical for the majority of the Eastside survey line, these sections (particularly Section A) have a more gentle side slope, as presented in Figure 4.3 and Figure 4.4. The thickness of the sediments for these sections is expected to be higher than the rest of the survey line. These sections along with the pre-existing boring log information are used as ground truths of the Eastside survey line for comparison purposes.

Figure 4.2- Sections of interest along the Eastside of Highway 63 bypass.

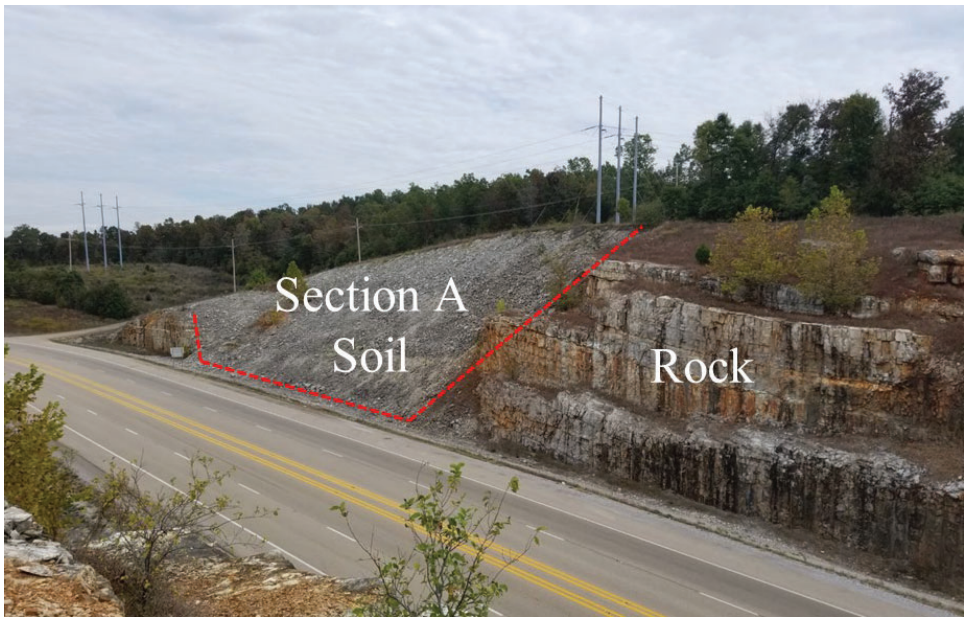

Figure 4.3- Section A with a relatively gentle slope on Eastside of Highway 63 bypass.

Figure 4.4- Evidence of relatively deeper sediment in Section B.

4.1.1 MASW testing using Rayleigh type surface waves

Two different post-processing procedures are employed to characterize subsurface materials using Rayleigh type surface waves measurements, as explained below.

4.1.1.1 Raw phase velocity method

The use of the raw phase velocity method (before running the inversion) for site characterization has been shown to be promising for the MASW data processing as it can provide an unbiased view of subsurface conditions in a faster way by eliminating the inversion process, which is the most complex and time-consuming step in the MASW data processing. The maximum depth of penetration (pseudo depth) for each of the MASW setup arrays is considered to be approximately half of the maximum resolvable wavelength (Foti et al. 2014). This formula only provides a rough estimation of the penetration depths and might lead to some misinterpretation regarding the exact locations of the subsurface layers. The main problem with this method is the accurate estimation of the ranges of the phase velocity that correspond to various geomaterials which is required for site characterization. In this study, the Rayleigh wave phase velocities (V_R) that correspond to the point of maximum curvature in the experimental dispersion curve are considered as the minimum phase velocity of the rock materials. This method is used to identify bedrock locations from the MASW surveys using both Rayleigh and Love types surface waves.

The spatial variation of Rayleigh wave phase velocities (V_R) (hereafter called Phase-Rayleigh) before running any inversion processes for the Eastside and Westside of the Highway 63 bypass are presented in Figure 4.5a and b, respectively. In addition, to compare the results of the geophysical field measurements with traditional geotechnical methods, the information from the five pre-existing boring logs (collected by ARDOT) are provided in the pseudo 2D V_R cross-section for the Eastside survey line. The potential soil/rock interface for each of the pseudo 2D V_R cross-sections is also shown with a black dashed line.

Examining the variation of the V_R along the Eastside and Westside survey lines in Figure 4.5, the Hardy site is comprised of three main layers, including a stiff/dense to very stiff/very dense soil layer at the top (light blue color), a weathered rock layer (green color), followed by a hard rock material (yellow color).

Based on the Eastside profile in Figure 4.5a, the topsoil layer is very shallow along the entire profile with a maximum thickness of approximately 5 meters. The thickness of the soil layer in Section A and Section B is slightly greater than the rest of the survey line, but not as much as expected. As shown in Figure 4.5a, the results of the Phase-Rayleigh survey for bedrock detection are consistent with most of the boring log information, except for BH166+00 that exhibits a deeper soil layer relative to the geophysical results. Given that it is difficult to visually differentiate between the results of geophysical tests and boring logs information at some locations, a summary of the estimated bedrock locations from geophysical tests along with the boring logs information is provided in Table 4-1. As shown in this table, the bedrock locations estimated using Phase-Rayleigh are in good agreement with those from the boring logs at BH155+00, BH158+00, and BH174+00. Depth to the bedrock is slightly overestimated (maximum value of 1.4 m) at these locations using the Phase-Rayleigh method. However, the results of MASW tests are different from the boring logs at BH153+00 and BH166+00. The maximum difference occurred at BH174+00, where bedrock is identified at a depth of 7.3 m based on the boring log and at a depth of 3.3 m based on the MASW, indicating underestimation of the bedrock location using Phase-Rayleigh at this location.

The results of the Phase-Rayleigh method for the Westside survey line in Figure 4.5b display a thin soil (approximately 2.5 m) layer at the surface from 0-160 m along the profile. The thickness of this layer increases from 160-275 m with a maximum thickness of about 13 m.

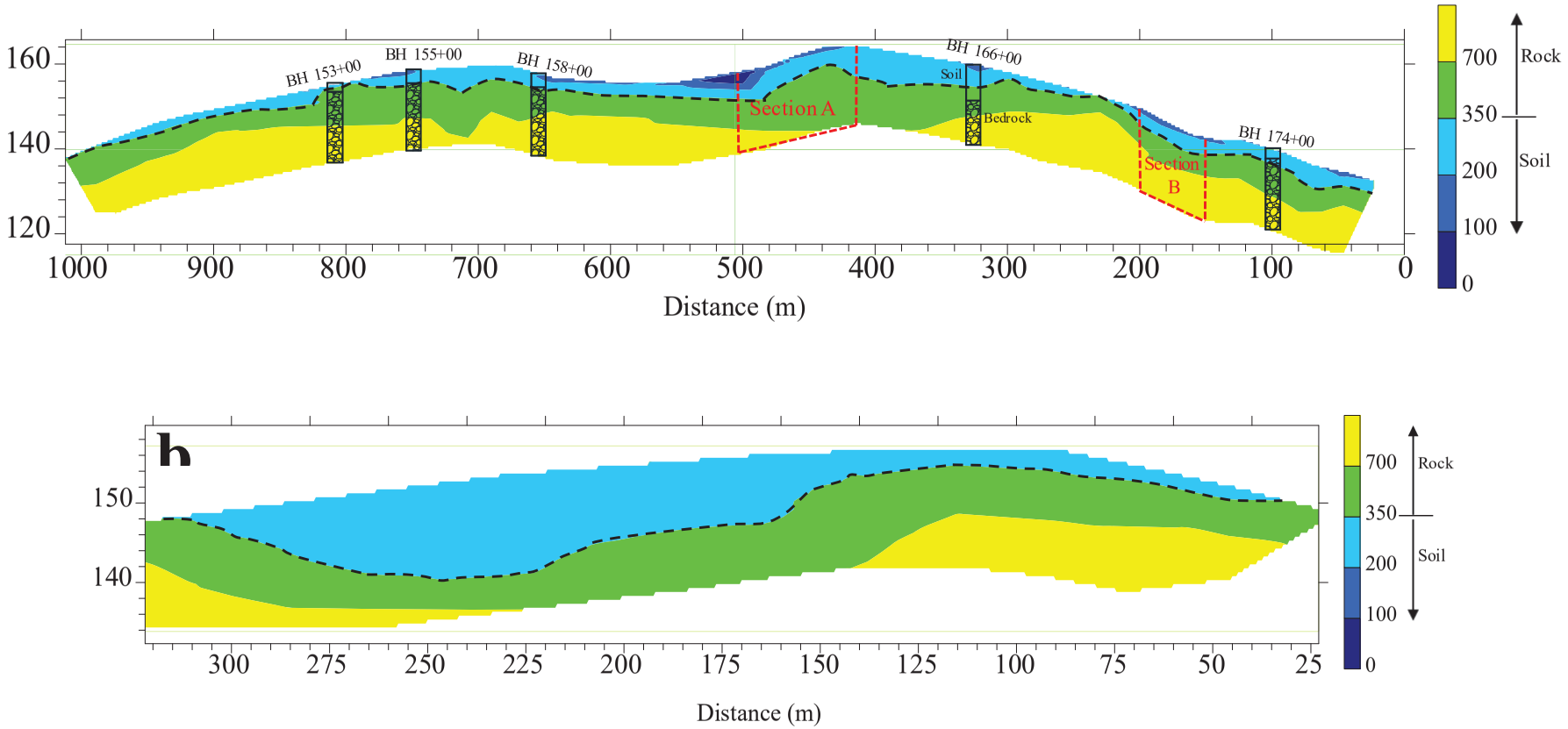

Figure 4.5- Pseudo 2D V_R cross-sections from the MASW using Rayleigh type surface waves at the Hardy site. a) the Eastside of the Highway 63 bypass, b) the Westside of the Highway 63 bypass.

Table 4-1- Comparison of the depth to bedrock at boring logs locations

	Depth to the bedrock (m)							
BH No.	Boring logs	Phase-Rayleigh	Shear-Rayleigh	Phase-Love	Shear-Love	Refraction	HVSR	CCR
153+00	1.9	2.1	4.4	2.3	1	3.2	1.5	3.4
155+00	3	3.5	2.7	3.3	4.4	3.5	8.5	6
158+00	3	3.1	3.2	4.4	3.4	3.5	3.9	3.5
166+00	7.3	8.2	6.4	5.2	3.3	5.8	2.1	3.1
174+00	2.2	4.4	5.2	3.9	3.2	3.2	2.3	4.1

4.1.1.2 Inverted shear wave velocity method

Although the phase velocity method is useful for rapid MASW data interpretation, it suffers from the effects of averaging with depth. This issue can be resolved by inverting the dispersion data to develop a shear wave velocity profile at each survey location. Therefore, in addition to the phase velocity method, the shear wave velocity (Vs) profiles generated from the inversion process are also utilized to create pseudo 2D Vs cross-sections along the survey lines.

Similar to the Phase-Rayleigh method, shear wave velocity ranges associated with different soil and rock types are required for mapping subsurface conditions. The main parameters affecting ranges of Vs for different geomaterials are soil and rock types, the relative density of soil, and rock quality and degree of weathering (Caterpillar Inc, 2000; Mayne et al. 2002; Lin et al. 2014; Rahimi et al. 2019). Typically, the depth at which a large jump occurs in the shear wave velocity profile is considered as the bedrock location (Figure 4.6b). To better illustrate this, three dispersion curves associated with different Vs profiles from the MASW measurements for the Eastside of the Hardy site that are quite different in terms of the shape of the dispersion curve are presented in Figure 4.6. From this figure, the MASW test at 425 m reveals a flat experimental dispersion curve resulting in a deep soil layer in the Vs profile in Figure 4.6b. However, the other two experimental dispersion curves exhibit sharp rises in the phase velocity for frequencies ranging between 20-45 Hz, which lead to shallow bedrock depths in the Vs profiles, as shown in Figure 4.6b.

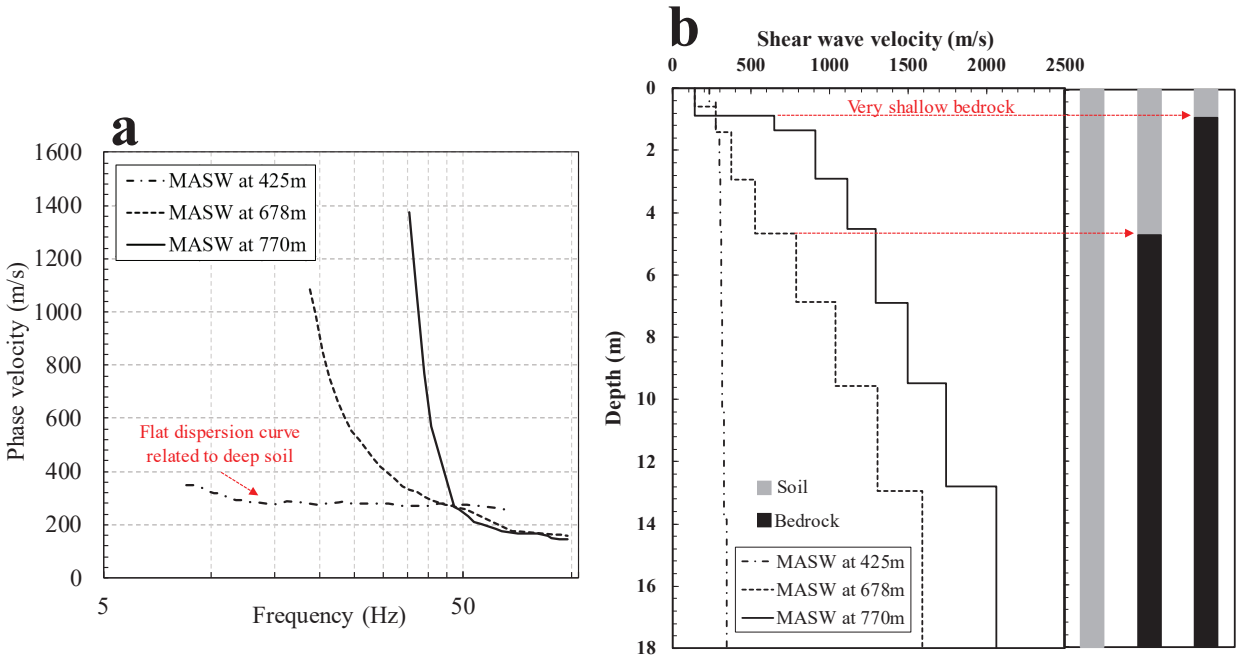

Figure 4.6- Example of bedrock detection using shear wave velocity profiles. a) dispersion curves for three different MASW setups in Eastside of the Hardy site, b) shear wave profiles associated with each dispersion curves.

Different Vs ranges have been proposed as the representative Vs values for rock materials in the literature (ASTM/SEI 7-10; Aung and Leong, 2012; Moon et al. 2017). In this report, different Vs values are considered as the boundary that separates the soil deposits from rock materials. These values are determined based on the recommendations from the literature (Caterpillar Inc, 2000; ASTM/SEI 7-10; Anbazhagan and Sitharam, 2008; Olona et al. 2010; Sun et al. 2012; Aung and Leong, 2012; Moon et al. 2017), the behaver and shape of the experimental dispersion curve and the inverted shear wave profile, and the a-priori information regarding the rock materials at each test site. For example, for the Hardy site, the Vs value of 700 m/s is considered the transition point from soil deposits to rock materials. This value corresponds well with considerable jumps in shear wave velocity profiles, as shown in Figure 4.6b. This value is also in good agreement with the recommended Vs value for the rock materials in ASTM/SEI 7-10.

The pseudo 2D Shear-Rayleigh ($V_{S\text{-}R}$) cross-section for the Eastside and Westside of the Highway 63 bypass along with the pre-existing boring logs are displayed in Figure 4.7a and b, respectively. The soil/bedrock interface is also illustrated with a black dashed line in this figure.

According to Figure 4.7, the Hardy site consists of a four-layer system: a stiff/dense soil layer at the surface with Vs ranging between 200-450 m/s, a very stiff/very dense soil layer with Vs from 450-700 m/s, followed by a weathered rock layer with Vs between 700-1500 m/s, underlain by a hard rock material.

Based on the spatial variations of the Shear-Rayleigh for the Eastside profile in Figure 4.7a, depth to the bedrock is very shallow along most portions of the survey line, confirming the soil and rock materials identified in two of the boring logs including BH155+00, and BH158+00. The differences between the Shear-Rayleigh results and the boring log information are less than 0.3 m at BH155+00 and BH158+00 (Table 4-1). In addition, the bedrock location estimated from Shear-Rayleigh at BH166+00 matches the boring log information (with approximately 1 m underestimation) as shown in Figure 4.7a and confirmed in Table 4-1. However, MASW tests using Shear-Rayleigh fail to accurately predict bedrock locations at BH153+00 and BH174+00. The bedrock was encountered at a depth of about 2.2 m at BH174+00 based on the boring log, while Shear-Rayleigh predicted the bedrock to be at a depth of 5.2 m indicating significant overestimation of the bedrock location using the Shear-Rayleigh method. The reason for such remarkable inconsistency between the boring log and Shear-Rayleigh results may be the poor quality of the dispersion data points for this station which led to great uncertainties in the process of predicting the bedrock location. As an example, the experimental dispersion data points acquired for one of the shots at this station are presented in Figure 4.8, showing the poor quality of the Rayleigh experimental dispersion data points (See Section 3.3.2). In total, the bedrock location identified using the Shear-Rayleigh method was overestimated at three locations (BH153+00, BH158+00, and BH174+00) and underestimated at two locations (BH155+00 and BH166+00) as presented in Table 4-1.

As shown in Figure 4.7a, similar to the Phase-Rayleigh results, the thickness of the sediments determined from the Shear-Rayleigh method in Section A and Section B are much lower than expected based on the available ground truths.

The pseudo 2D Vs cross-section for the Westside of the Highway 63 bypass in Figure 4.7b is similar to the phase velocity results in Figure 4.5b, but with a thicker sediment from 160-275 m.

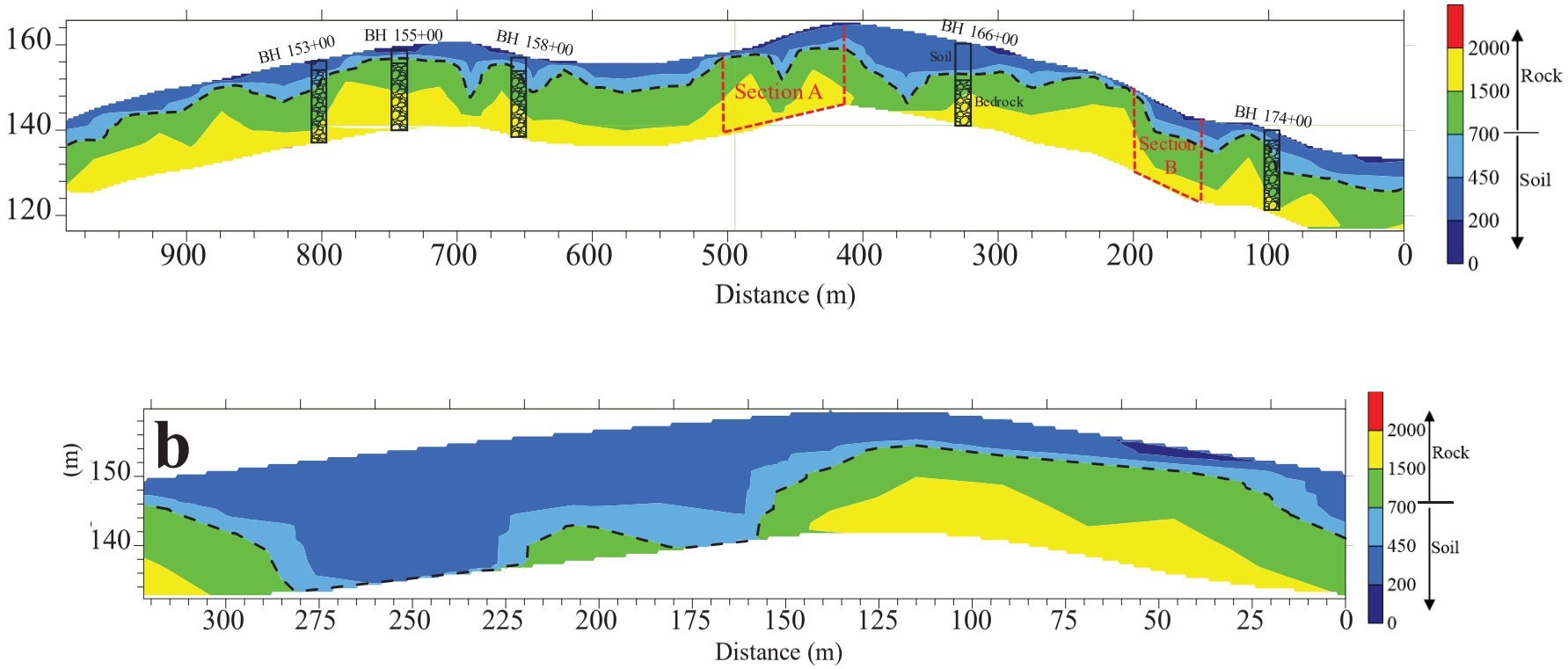

Figure 4.7- Pseudo 2D $V_{S\text{-}R}$ cross-sections from the MASW using Rayleigh type surface waves at the Hardy site. a) the Eastside of the Highway 63 bypass, b) the Westside of the Highway 63 bypass.

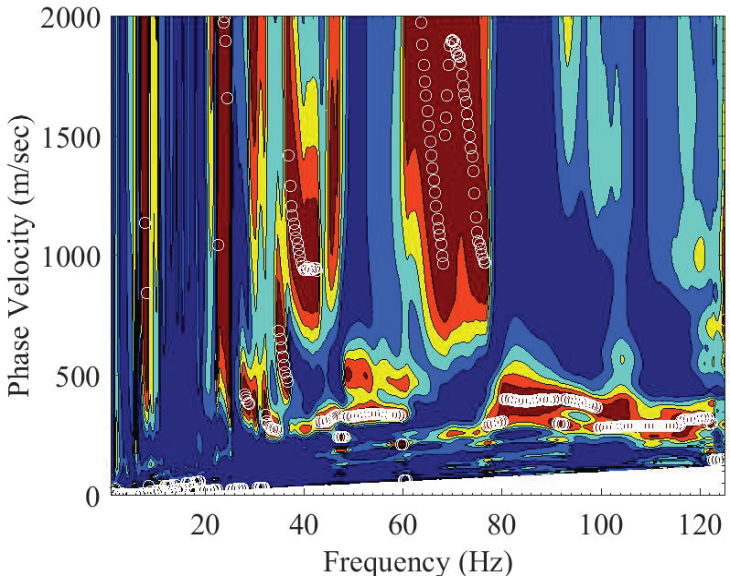

Figure 4.8- Example of the Rayleigh wave experimental dispersion data points with poor-quality experimental dispersion curve (Section 3.3.2).

4.1.2 MASW testing using Love type surface waves

A similar procedure, as described in the previous section, is followed to create pseudo 2D Phase-Love velocity (V_L) and Vs cross-sections for the Hardy site using Love type surface waves and the results are presented below.

4.1.2.1 Raw phase velocity method

Shown in Figure 4.9a and b are the spatial variation of the Phase-Love velocity for the Eastside and Westside of the Hardy site, respectively, along with the boring log data. The potential soil/bedrock interface for each of the profiles is also shown in this figure with a black dashed line.

Based on the 2D Phase-Love profile for the Eastside of the Highway 63 bypass, the subsurface consists of three main layers: a stiff/dense to very stiff/very dense soil layer from the ground surface to depths between 2-20 m, a weathered rock layer extends from the base of soil layer to depths varying from 12-20 m, followed by a hard rock layer.

As shown in Figure 4.9a, the bedrock locations are mostly shallow along the survey line. The exceptions occur from 150-225 m and from 415-560 m, where the bedrock is located at relatively deeper depths (depths between 10-18 m) in comparison with the rest of the survey line. Interestingly, these sections correspond quite well with section B and section A that are expected to have deeper bedrock locations based on the available ground truths.

Moreover, compared to the five boring log records, the bedrock locations were identified with acceptable accuracy (less than 1.4 m difference) using the Phase-Love method at three of the boring logs (BH153+00, BH155+00, and BH158+00) as shown in Figure 4.9a and presented in Table 4-1. However, the results of Love MASW testing at BH166+00 and BH174+00 are a bit different from the boring logs. According to Table 4-1, the bedrock location was overestimated at four locations (BH153+00, BH155+00, BH158+00, and BH174+00) and underestimated at one location (BH166+00) using Phase-Love method. The maximum difference between the boring log information and Phase-Love results was observed at the BH166+00 where the bedrock was predicted to be at a depth of 5.2 m based on the geophysical method and 7.3 m for the boring. The discrepancies in the results could be caused by the pseudo depth estimation formula (wavelength divided by 2), which provides an approximation of penetration depths for MASW. This issue can be resolved to some extent using the inverted shear wave method as it attempts to find the best subsurface layering by searching the entire space of possible solutions. Overall, comparing the bedrock locations identified from the Phase-Love method and boring logs indicates the effectiveness of MASW using Love type surface waves for bedrock detection.

The 2D Vs profile for the Westside of Highway 63 reveals a two-layer system: a stiff/dense to very stiff/ very dense soil layer, followed by a weathered rock layer. Similar to the Rayleigh waves results, bedrock is located near (at depths ranging from 1-3 m) the ground surface for the first half of the survey line from 0-175 m, and then it gets deeper (10-16 m) for the rest of the survey line.

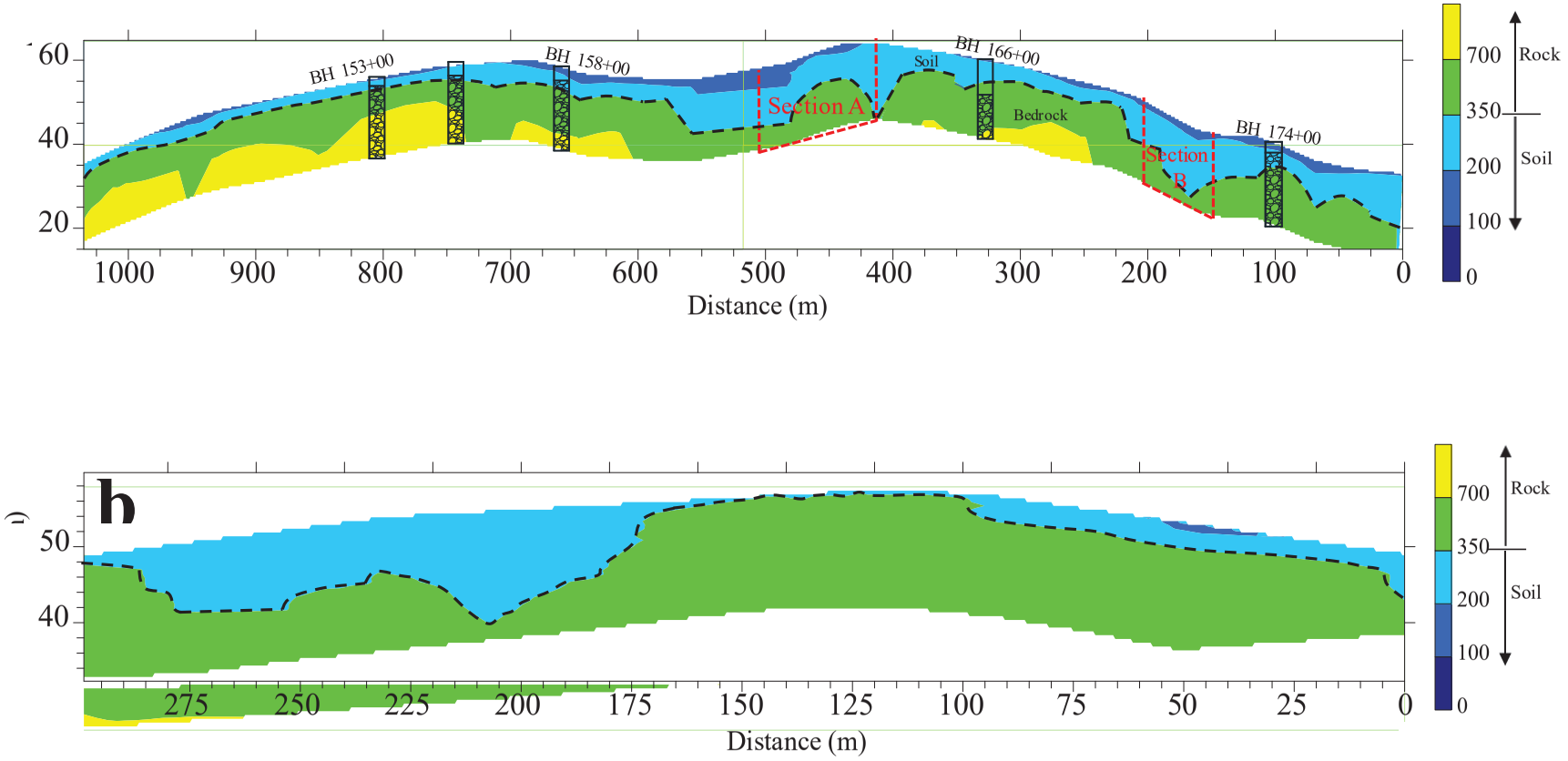

Figure 4.9- Pseudo 2D V_L cross-sections from the MASW using Love type surface waves at the Hardy site. a) the Eastside of the Highway 63 bypass, b) the Westside of the Highway 63 bypass.

4.1.2.2 Inverted shear wave velocity method

The pseudo 2D Vs cross-section using inverted shear wave velocity profiles from Love wave tests (hereafter called Shear-Love) for the Eastside and Westside of the Highway 63 bypass along with the boring logs and potential bedrock locations are presented in Figure 4.10a and b, respectively.

The pseudo 2D Shear-Love ($V_{S\text{-}L}$) cross-section for the Eastside of Highway 63 in Figure 4.10a indicates the presence of three layers, including a stiff/dense soil layer at the ground surface, a thin, very stiff/very dense soil layer, and a weathered rock layer underlain by hard rock. Examining the soil/bedrock interface defined from the MASW using Shear-Love in Figure 4.10 at the boring log locations, the results of the two methods are reasonably consistent except at the BH174+00 for which the boring log reveals 2.2 m shallower bedrock relative to the Shear-Love results. The exact depth of the bedrock determined from the Shear-Love method and boring logs information provided in Table 4-1. As reported in this table, the Shear-Love method overestimated depth to bedrock at most of the boring log locations. The differences between the boring log records and MASW using Shear-Love for bedrock mapping are less than 1 m at four of the locations (BH153+00, BH155+00, BH58+00, and BH166+00). Furthermore, unlike the Rayleigh type surface waves results in Figure 4.5a and Figure 4.7b that exhibit shallower bedrock depths at sections A and B than expected, the results of the Love type surface waves tests reveal considerably deeper bedrock depths for these sections that match the available ground truths (see Figure 4.3 and Figure 4.4). This indicates the capability of the MASW tests using Love type surface waves for bedrock detection for sites with a very shallow bedrock layer overlaid by a soil deposit. This subject is discussed in more detail later in the report.

The pseudo 2D Vs profile of the Westside of the Highway 63 bypass, presented in Figure 4.10b, contains three main layers: a stiff/dense soil layer at the ground surface, a very stiff/very dense soil layer, followed by a weathered rock layer. Although the bedrock location in Figure 4.10b is in general agreement with the results of the raw phase (Love) velocity method in Figure 4.9b, deeper bedrock is detected in this figure from 100-175 m. To explore which method is more accurate in terms of bedrock detection for this particular section, these results will be compared with the other geophysical methods later in the report.

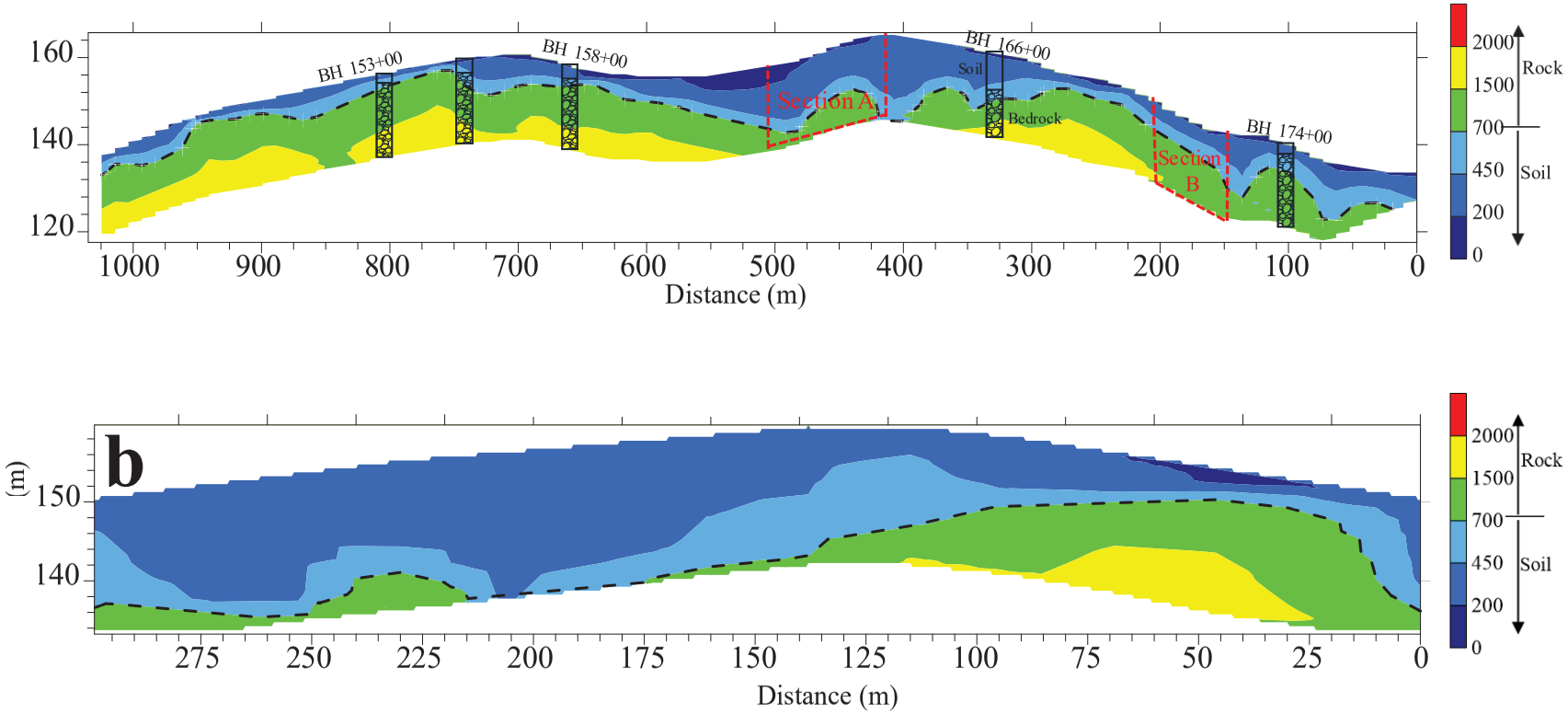

Figure 4.10- Pseudo 2D $V_{S\text{-}L}$ cross-sections from the MASW using Love type surface waves at the Hardy site. a) the Eastside of the Highway 63 bypass, b) the Westside of the Highway 63 bypass.

4.1.3 P-wave refraction

The results of the P-wave refraction surveys for the Eastside and Westside of the tested areas along with pre-existing boring logs are presented in Figure 4.11a and b, respectively. According to the rock formation available for this site and the ranges provided in Caterpillar Inc (2000), P-wave velocities higher than 1600 m/s as considered as the representative value for the bedrock materials. Using this value, the soil/bedrock interface for each profile is illustrated in Figure 4.11 with the black dashed line.

Based on the variation of the P-wave velocities in Figure 4.11a, the Eastside consists of three layers, including a stiff/dense soil, a very stiff/very dense soil, followed by the bedrock. As presented in Figure 4.11a, the bedrock locations identified by P-wave refraction correspond well with the boring logs at locations where shallow bedrock exists (BH153+00, BH158+00, BH174+00). This is verified by the values provided in Table 4-1. However, the P-wave refraction falls short of accurately predicting bedrock location at BH166+00, where the bedrock is predicted to be at a depth of 2.1 m based on the P-wave refraction results but encountered at a depth of 7.3 m in the boring log record. For section A and section B, although relatively deeper bedrock is identified based on the P-wave refraction for these sections compared to the rest of the survey line (see Figure 4.11a), these values were predicted to be much shallower than expected. This indicates one of the main limitations of the P-wave refraction method, which is the quick loss of resolution as depth increases below the ground surface. Several parameters can affect the resolution of the P-wave refraction survey, such as geophone spacing and site conditions, including seismic velocity contrast, depth to the refractors, and layering thickness. The maximum depth of exploration in P-wave refraction is a complex function of these parameters (ASTM D5777-00). Typically, P-wave refraction surveys are associated with great uncertainties for deeper refractors. Another subject leading to a reduction in the quality of the P-wave refraction survey for sites such as Hardy is the existence of multiple shallow refractors, which are quite variable along the P-wave refraction setup array. This condition makes the process of first arrival times selection more ambiguous.

The P-wave velocity 2D cross-section for the Westside of Highway 63 bypass in Figure 4.11b indicates a three layers system with a very shallow (between 1-3 m) bedrock in the first half of the survey line (from 10-175 m) and a deeper (5-10 m) bedrock from 175-255 m. Like the P-wave refraction for the Eastside, the maximum depth of exploration is shallow, approximately 10 meters.

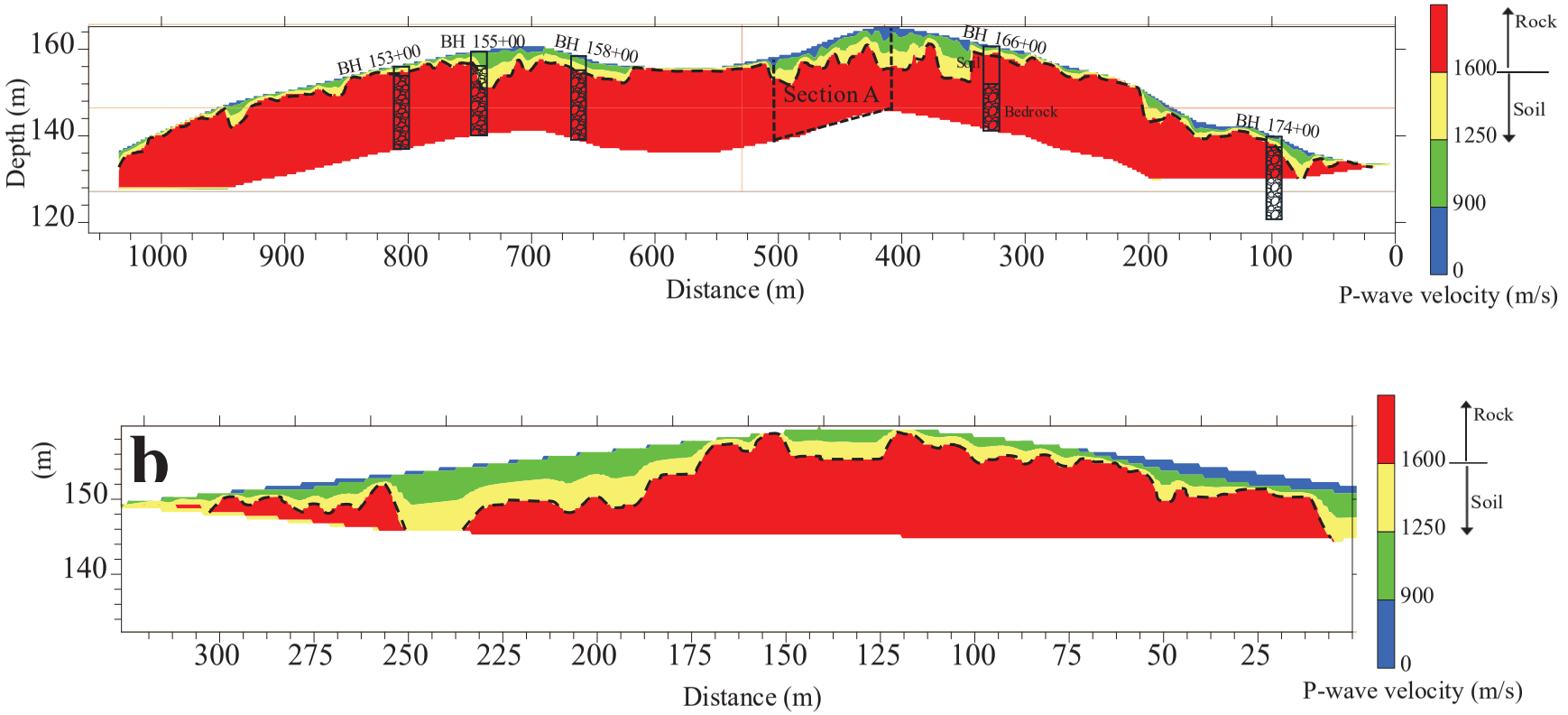

Figure 4.11- P-wave velocity 2D cross-sections from the P-wave refraction surveys at Hardy. a) the Eastside of the Highway 63 bypass, b) the Westside of the Highway 63 bypass.

4.1.4 HVSR

As mentioned in the data processing section, the final output of the HVSR method for each station is a frequency associated with the peak HVSR amplitude if the peak fulfills the requirement of a true peak (section 3.4.2). This peak can be assumed as the fundamental resonant frequency of the site, where the HVSR measurements are controlled by shear wave resonance of the soil deposits. Sediment thickness can be estimated using the frequency associated with the peak HVSR amplitude (obtained from HVSR measurements) and the quarter-wavelength equation:

$$H_{sediment} = \frac{V_{s,\,avg}}{4 \times f} \qquad 4$$

where, $V_{s,\,avg}$ is the average shear wave velocity of the sediment above the bedrock, f is the fundamental resonance frequency, and $H_{sediment}$ is the sediment thickness. According to this equation, besides the fundamental resonance frequency determined from the HVSR measurements, the average shear wave velocity of the sediment above the bedrock is also required to estimate depth to bedrock. This value can be calculated using one of the three methods presented in Rahimi et al. (2021). In the present study, the $V_{s,\,avg}$ is estimated from the co-located MASW measurements. Then, the information from the HVSR measurements and surface wave testing are used to identify bedrock location, and the results are shown in Figure 4.12a and b.

Provided in Figure 4.12a is the bedrock location identified based on the HVSR method along with the boring log information. As shown in this figure, the bedrock locations estimated from the HVSR measurements agree well with those identified from the boring logs. Comparing the bedrock depths determined from the HVSR measurements and the values recorded in the boring logs in Table 4-1, inconsistencies occur at BH153+00 and BH166+00 with the maximum difference at BH166+00, where bedrock is detected at 5.8 m with HVSR and at 7.3 m in the boring log. As presented in Table 4-1, the bedrock locations are overestimated using the HVSR technique at most of the boring log locations, including BH153+00, BH155+00, BH158+00, and BH174+00, but the differences between the two methods are in a reasonable range (maximum of 1.3 m overestimation). This indicates that the HVSR method is valuable for bedrock mapping if a reliable peak exists in the HVSR measurements. It should be mentioned that this method is only applicable when the average shear wave velocity of the sediments above bedrock is available. Deeper sediments are observed for Section A from the HVSR measurements (see Figure 4.12a) that match

the existing ground truths. However, for Section B the sediments are thinner than expected from the available ground truth (Figure 4.4).

The potential bedrock location estimated from the HVSR technique for the Westside of the Highway 63 bypass is shown in Figure 4.12b. Similar to the other methods, the HVSR results display shallow bedrock locations for the first half of the survey line, followed by relatively deep bedrock locations for the second half of the survey line. A more detailed comparison between the results of different geophysical methods is made later in the report.

Depth to the bedrock and fundamental resonant frequency are the main parameters that can be estimated using the HVSR technique. In addition, the HVSR results can be used as supplemental information for joint inversion of dispersion curves in MASW data interpretation in order to increase the reliability of the inversion process (Parolai et al. 2005; Giancarlo, 2010). A comparison of the HVSR method with the boring log information has shown the efficiency of this method for bedrock detection for both shallow and relatively deep bedrock locations.

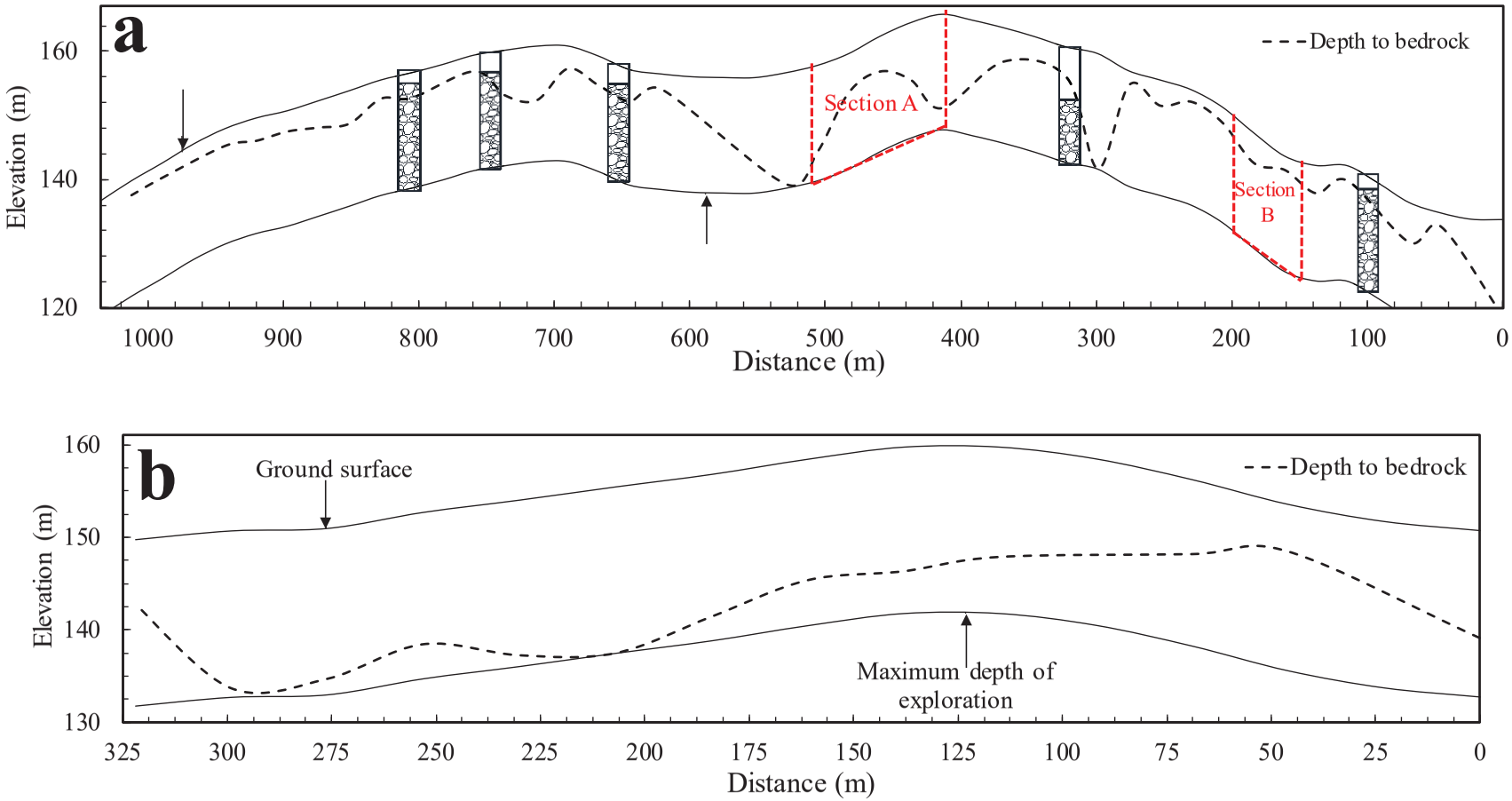

Figure 4.12- Bedrock locations identified based on the HVSR testing at Hardy. a) the Eastside of the Highway 63 bypass, b) the Westside of the Highway 63 bypass.

4.1.5 CCR

The resistivity profiles generated from the CCR tests for the Eastside and Westside of the Hardy side are shown in Figure 4.13a and b, respectively. The information from the five boring logs are also presented in these profiles. As shown in these profiles, most of the resistivity values measured in the field tests are either within the range of 30-300 ohm-m or higher than 700 ohm-m. For the Hardy site, it was found that resistivity values higher than 700 ohm-m are the best match for the rock materials since this value is related to a big jump in the resistivity values acquired in the field measurements. As shown in Figure 4.13, the maximum depth of investigation is approximately 10 m.

According to the resistivity profile in Figure 4.13a, the subsurface is comprised of two main layers, which are a thin soil layer from the surface with depths ranging from 2-5 m underlain by rock materials. In terms of bedrock detection, the results of CCR tests for the Eastside of the Hardy site, shown in Figure 4.13a, agree with the boring logs information at BH153+00, BH158+00. However, the inconsistency between the CCR and the boring logs occurs at BH155+00, BH166+00, and BH174+00 as presented in Table 4-1. The thickness of the sediments is over predicted at BH155+00 and BH174+00 by 3 m and 1.9 m, respectively, and under predicted at BH166+00 by 4.2 m. Two low resistive segments are observed in the CCR results along Section A (see Figure 4.13), indicating relatively deep sediments for these segments. However, the sediment thickness estimated by CCR along Section B is not as deep as expected. There are some other low resistive segments along the Eastside survey line (e.g. at 560, 600, and 625 m), but no supplementary information is available at these locations to validate the CCR results.

Similarly, the resistivity profile in Figure 4.13b for the Westside of the Highway 63 bypass is comprised of two main layers of soil and rock, which are quite variable along the survey line. This profile corresponds well with the results of other geophysical methods in terms of the bedrock detection exhibiting shallow bedrock locations from 0-125 m and deeper bedrock locations for the rest of the survey line. However, there are three highly resistive areas in the second half of the profile (e.g. from 205-225 m) which are inconsistent with the results of other geophysical techniques. A more detailed comparison between different geophysical methods is presented later in the report.

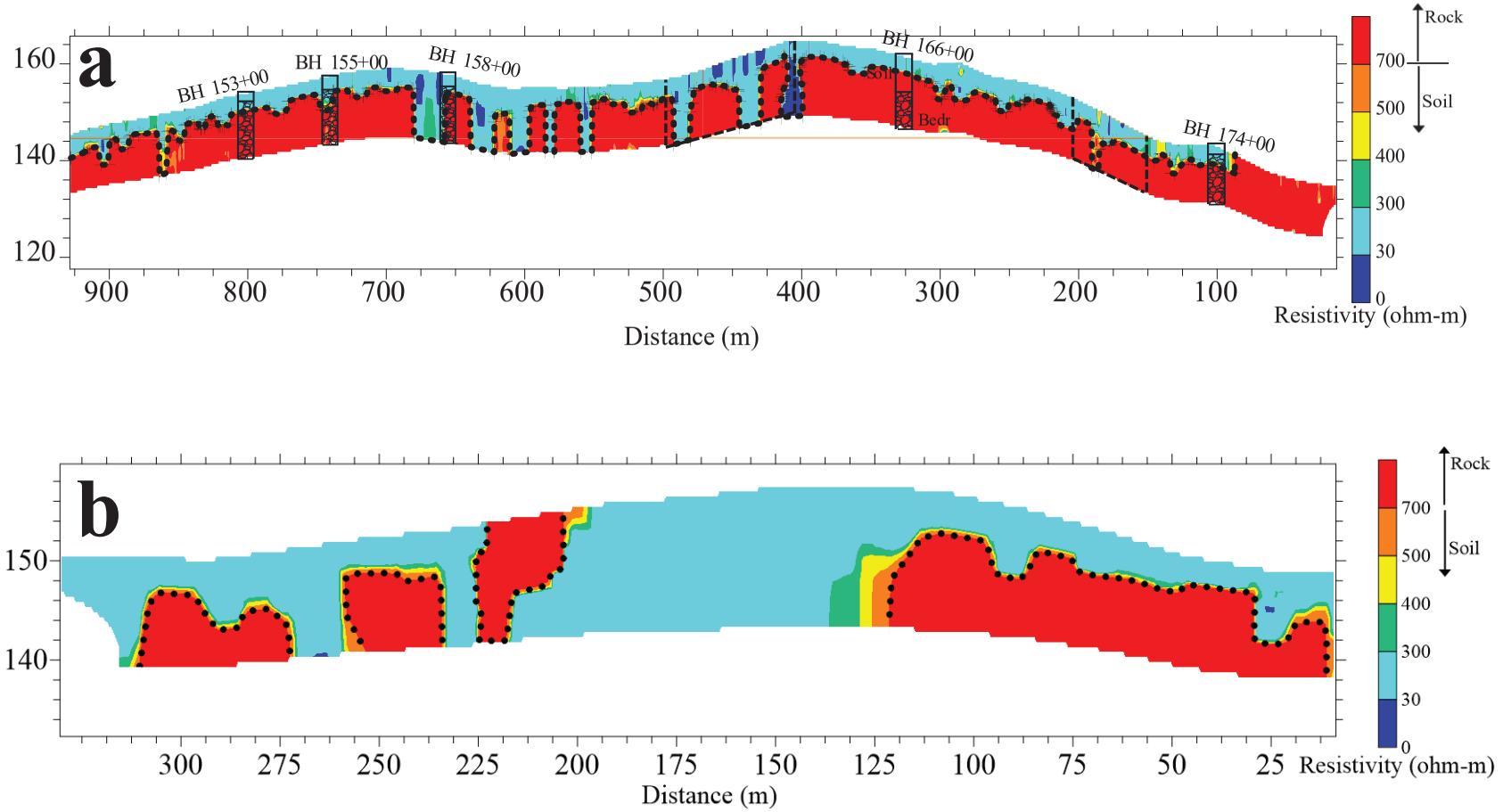

Figure 4.13- Resistivity profiles acquired from the CCR tests at Hardy. a) the Eastside of the Highway 63 bypass, b) the Westside of the Highway 63 bypass.

4.1.6 GPR

Shown in Figure 4.14a and b are the results of GPR surveys for the Eastside and Westside of the Hardy site, respectively. In addition to the travel time (ns) which is the main vertical axis, the estimated elevation (m) is also shown as the secondary vertical axis in this figure. Depth of penetration for electromagnetic waves in GPR tests can be estimated using the equation:

$$D=\frac{V_m}{2t} \quad (5)$$

where, V_m is the average velocity of electromagnetic waves for the material above the refractor, D is the penetration depth, and t is the two-way travel time of electromagnetic waves. As mentioned previously (Table 3-1 in Section 3.6.2), different ranges of velocities have been proposed for various soil types (Baker et al. 2007; ASTM D6432-11; Robinson et al. 2013). Based on the boring log information, the topsoil layer is mainly comprised of clay material; therefore the V_m value of 0.09 m/ns was used to estimate the depth of penetration for electromagnetic waves.

As shown in Figure 4.14a and b, electromagnetic energies are attenuated rapidly with depth at the Hardy site in such a way that the amplitude of GPR signals are almost negligible for depths greater than 2 m. This is likely caused by the top clay layer which exists at the Hardy site, as reported in the boring log information. Soil deposits such as clay attenuate electromagnetic energies rapidly by converting them to thermal energy. The rate of attenuation depends on the mineralogy of the clay layer. Typically, clay layers with a high concentration of heavy minerals have the highest attenuation rate among all fine-grained soils (ASTM D6432-11; Baker et al. 2007). Therefore, the maximum depth of exploration for GPR surveys would be very shallow for sites where such a clay layer exists near the surface.

For the GPR tests at the Hardy site, the amplitude of electromagnetic waves for depths greater than 2 m is almost negligible; therefore the maximum depth of exploration for a GPR survey is approximately 2 m (see red dashed line in Figure 4.14). This indicates that GPR is not useful for subsurface investigation of sites where a shallow soil layer with high attenuation exists. Even a thin shallow clay layer can kill the GPR signal trace in such a way that no refracted/reflected waves can be generated.

As marked in Figure 4.14a, large hyperbolas are observed at three locations along the GPR profile for the Eastside of the Highway 63 bypass. These hyperbolas are located at depths greater

than 2 m, which is below the maximum depth of exploration for the GPR test at the Eastside of the Hardy site, indicating that these hyperbolas should not be caused by any underground features/utilities. Examining the locations of these hyperbolas, they correspond well with the locations of the electrical transmission towers at the ground surface. The location of one of the transmission towers are presented in Figure 4.15.

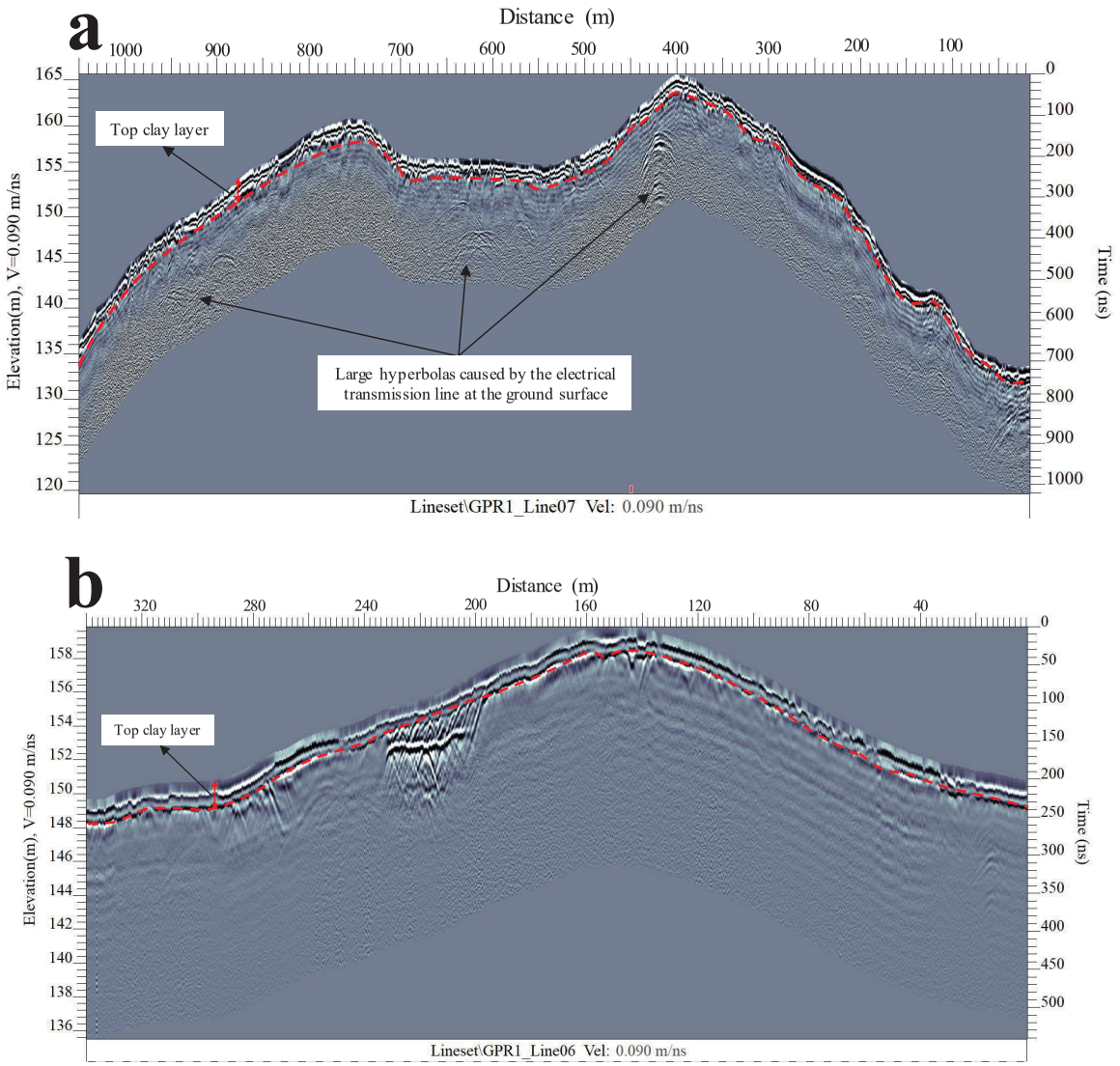

Figure 4.14- GPR profiles acquired at the Hardy site. a) the Eastside of the Highway 63 bypass, b) the Westside of the Highway 63 bypass.

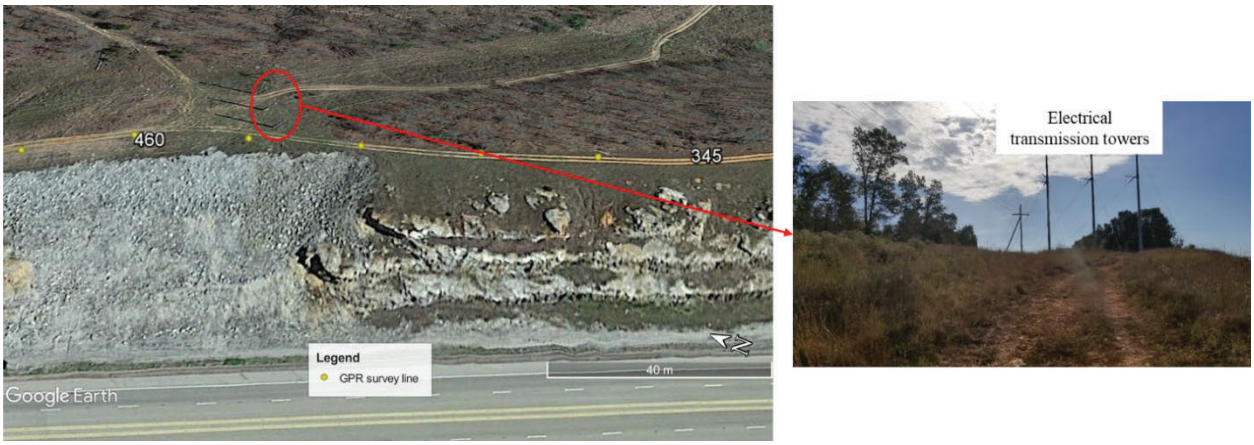

Figure 4.15- Electrical transmission towers crossing the GPR survey line at the Eastside of Highway 63 bypass.

4.1.7 EM31

As mentioned in Section 3.8.1, the main parameters recorded in EM31 surveys are the electrical conductivity of soils and in-phase value. To map subsurface conditions using EM31, the ranges of electrical conductivity related to different geomaterials should be determined. EM31 has been used mostly in agricultural studies, and as a result, the existing ranges of electrical conductivity are not accurate enough for geotechnical purposes.

The results of the EM31 survey for the Eastside and Westside of the Hardy site are shown in Figure 4.16a and b, respectively. Ranges of conductivity values proposed in previous investigations are used to separate different soil types, including sand (blue color), silt (green color), and clay (red color) (Grisso et al. 2005; Doolittle and Brevik, 2014). As shown in Figure 4.16, the conductivity values acquired for both the Eastside and Westside of Highway 63 range from 8-60 mS/m indicating the presence of fine-grained materials (silt or clay). The reason why most of the conductivity values are associated with fine-grained materials is related to the maximum penetration depth of the EM31 survey. The maximum penetration depth is expected to be between 3-5 m since a 3.66 m long boom was used in this study. According to the boring logs information, the top 2-5 m of soils mainly consist of clay material, so no information regarding the bedrock locations is determined from the EM31 survey. Examining the variations of in-phase values for the Eastside and Westside survey lines in Figure 4.16, there are several jumps in the recorded values. These jumps are likely caused by metallic objects (e.g. ATVs and electrical posts).

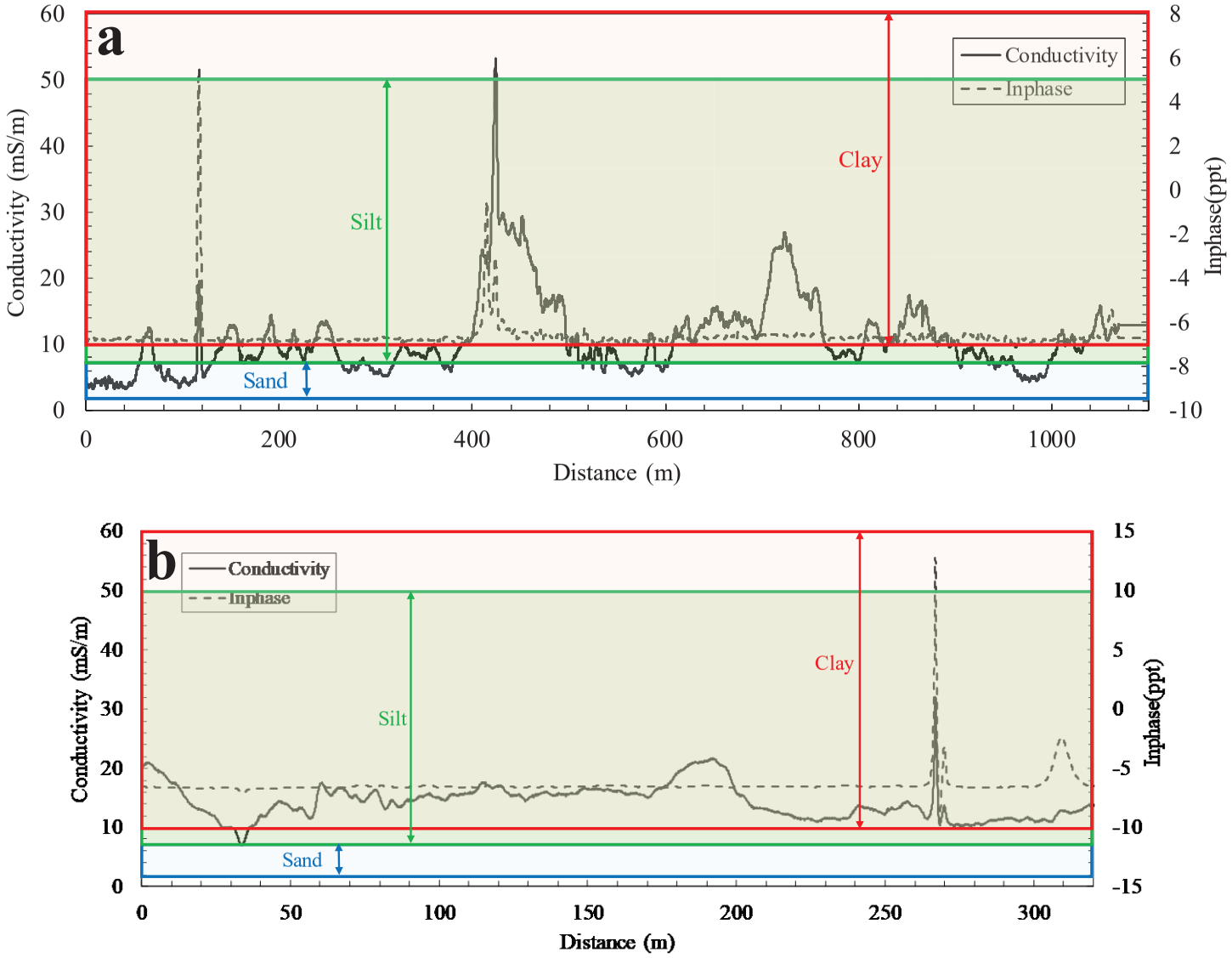

Figure 4.16- Conductivity and in-phase parameter variation from the EM31 measurements. a) Eastside of Highway 63 bypass, b) Westside of Highway 63 bypass.

4.1.8 Comparison of bedrock depths identified from different geophysical methods

In order to identify the most accurate geophysical method(s) for bedrock mapping, the results of various geophysical methods are compared below. Shown in Figure 4.17 are bedrock depths identified for the Eastside of the Highway 63 bypass from different geophysical methods (Phase-Love, Inverted-Love, Phase-Rayleigh, Inverted-Rayleigh, HVSR, CCR, and P-wave refraction) at each station along with the deviation of each method from the average values which are displayed using error bars. GPR and EM31 are not included in this plot because they were not able to predict bedrock locations. As presented in this plot, most of the error bars are in reasonable ranges (within one standard deviation), but there are several significant outliers in the results (e.g. at 500 m and 550 m). The significant outliers were observed mostly at Section A and Section B (see Figure 4.3 and Figure 4.4) in which relatively deep sediments are expected based on the existing ground truths. However, some methods fail to accurately predict the bedrock depths for these sections, including CCR and P-wave refraction. The majority of the bedrock depths estimated using the CCR and P-wave refraction techniques are considerably different from the other methods, as shown in Figure 4.17, indicating the deficiency of these methods for bedrock detection, especially for locations where deep sediments exist.

There are several parameters affecting soil resistivity, including soil gradation and mineralogy, temperature, soil cavity, and particularly soil degree of saturation. Therefore, it is difficult to characterize the subsurface based solely on CCR due to the difficulties in monitoring and recording all the parameters influencing soil resistivity during the CCR field measurements. This becomes more difficult for long survey lines because the effective parameters can change significantly along the survey line. In addition, the maximum exploration depth for the CCR technique is typically very shallow and the resistivity values related to deeper layers are associated with great uncertainties due to data averaging effects.

For the P-wave refraction survey, one of the main limitations is the quick loss of resolution with depth. The maximum depth reachable in P-wave refraction is a complex function of several parameters, including geophone spacing, site conditions including seismic velocity contrast, depth to the refractors, and layer thickness. Additionally, for sites where multiple shallow refractors (i.e. bedrock layers) are present or where refractors are quite variable along a short distance, which is the case for the Hardy site, the ambiguity in the first arrival times selection process is great. In these conditions, the results are associated with great

uncertainties, which could lead to misinterpretation in subsurface characterization, particularly bedrock mapping.

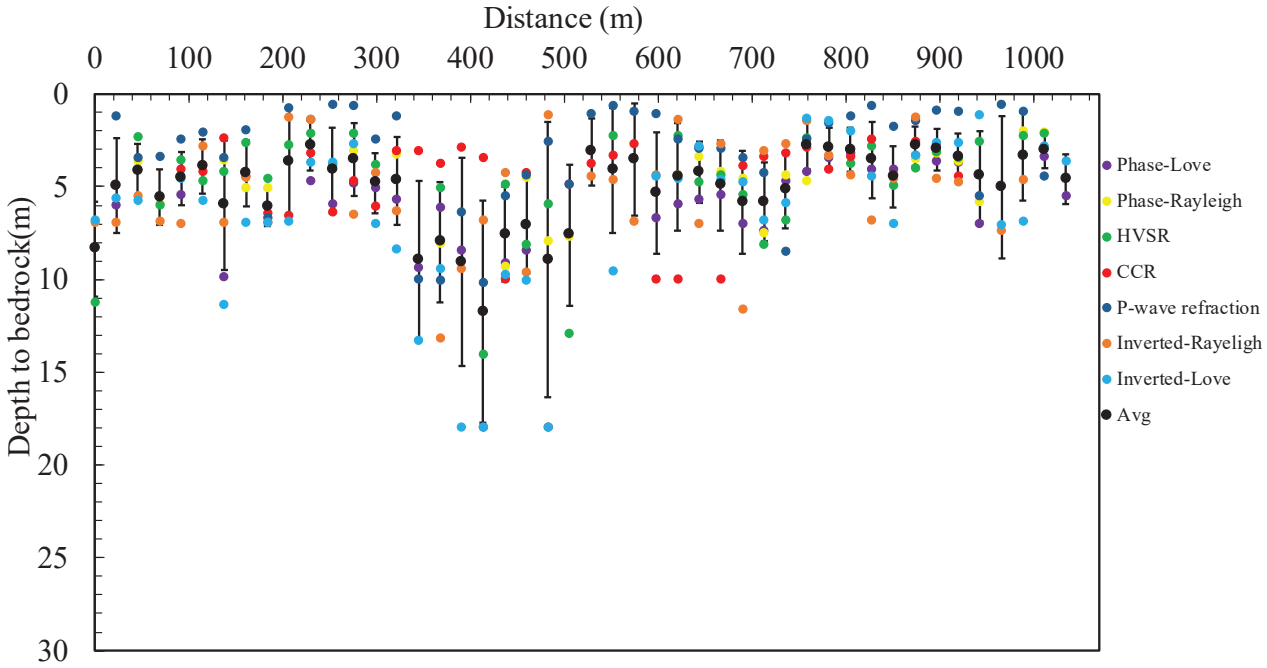

Figure 4.17- Bedrock depths identified for the Eastside of Highway 63 bypass using different geophysical methods.

Given that it is hard to visually differentiate between the results of different geophysical methods in Figure 4.17, depths to bedrock estimated from geophysical methods are compared with those actually observed at the boring logs to identify a method(s) with the highest accuracy. To accomplish this goal, an error-index value is defined to quantify the discrepancy between each method and the boring logs. The error-index (EI) value, in percent, is computed using the equation:

$$EI(\%) = \frac{\sum_1^n abs(H_{diff})}{\sum_1^n H_{bl}} \times 100 \qquad 6$$

where EI is the error-index value in percent, n is the number of samples which is equal to the number of boring logs, abs(H_{diff}) is the absolute differences between the bedrock depth estimated from the geophysical methods and boring logs, and H_{bl} is depth to bedrock based on the boring logs information. The values presented in Table 4-1 are used along with the above equation to calculate the error-index value for each geophysical method, and the results are shown in Figure 4.18. From this figure, three methods resulted in low error-index values, including Inverted-Love, Phase-Love, and HVSR, indicating these methods best match the boring logs information in terms of bedrock detection. Among all the geophysical methods, MASW using Love type surface waves, particularly the Inverted-Love method, has shown the

best performance. The reason for such observation is related to the geology of the tested area (the Eastside of the Hardy site), which is comprised of a thin stiff soil layer at the surface underlined by rock materials. Love waves mostly develop when a half-space is overlain by a soil layer with considerably lower body wave velocity relative to the half-space layer (Kramer, 1996). In this condition, one of the main parameters affecting the quality of Love wave data is the impedance ratio (see Equation 1) between the half-space and topsoil layer. For an incident wave created at the ground surface, the amount of energy transmitted or reflected at the layer interface depends on the impedance ratio of the system. If the impedance ratio is equal to 1, all of the energy will be transmitted to the second layer without any reflection. Love waves can develop in a two-layer system of a shallow soil layer underlain by a half-space with a high IR, which is the case for the Eastside of the Highway 63 bypass at Hardy.

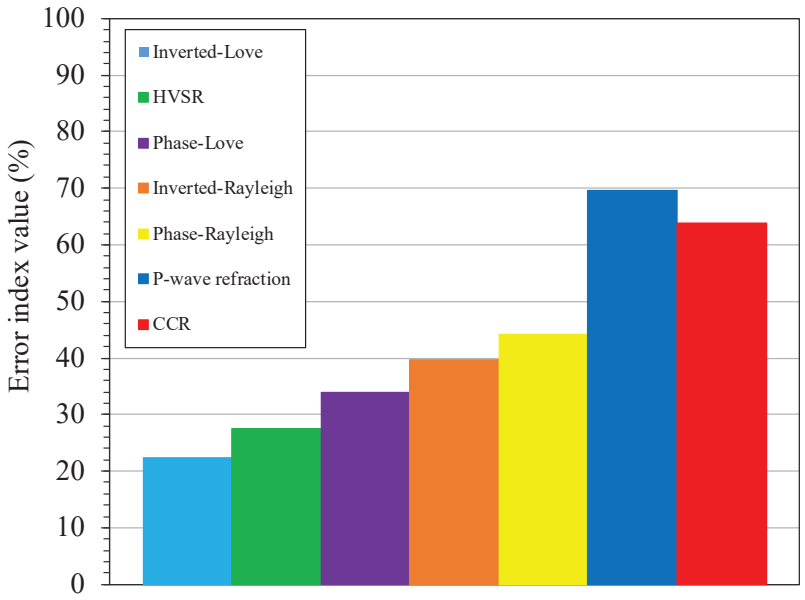

Figure 4.18- Error index values.

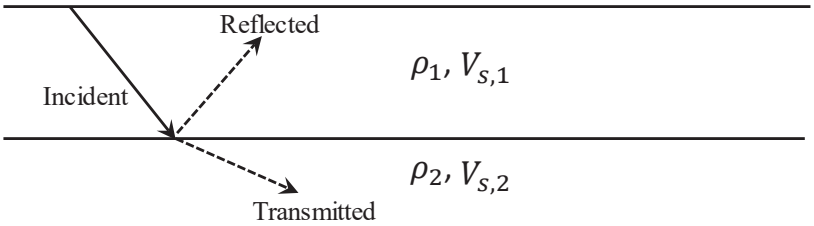

Figure 4.19- Waves propagations in a two-layer system.

Bedrock depths detected for the Westside of the Highway 63 bypass using different geophysical methods are presented in Figure 4.20. Unlike the Eastside survey line for which MASW using Love type surface waves and HVSR provided the best results, for the Westside

of the Highway the two best methods are found to be MASW using Rayleigh type surface waves and HVSR. To better illustrate this, the results of the Inverted-Rayleigh and HVSR methods along the Westside survey line are provided in Figure 4.21. As shown in this figure, apart from three locations, the error bars are small and almost negligible, indicating that bedrock depths predicted using the Inverted-Rayleigh method correspond well with those determined from HVSR measurements. For the Westside of the Highway, MASW using Love type surface waves fall short of accurately predicting bedrock locations due to the poor quality of the Love wave experimental dispersion curves. On the other hand, high-quality experimental dispersion curves were acquired from the MASW using Rayleigh type surface waves. Example experimental dispersion curves from MASW using Rayleigh and Love type surface waves are shown in Figure 4.22a and b, respectively. As shown in this figure, the Rayleigh wave experimental data points have high quality with low uncertainty regarding fundamental mode selection, whereas the Love wave dispersion data points have no useable trend causing great uncertainties in the fundamental mode selection. Almost half of the experimental dispersion data points measured from the MASW testing using Love type surface waves for the Westside of the Hardy site have very poor quality, like the one in Figure 4.22b. The poor quality of Love wave experimental dispersion curves is believed to be caused due to the existence of a gravel pavement layer on top of the stiff clay layer on the Westside of the Highway. For the Westside survey line, the subsurface consists of a thin stiff gravel layer at the ground surface, a stiff clay layer, underlain by the bedrock material. The very poor quality of the Love wave dispersion data points is caused by the low impedance ratio (IR) at the interface of the gravel/clay layer, which is probably less than 1. This means that most of the Love waves (energy) were likely reflected back to the surface without any considerable transmitted waves to deeper depths, and so, only a small portion of the experimental dispersion curve was able to be generated, as shown in Figure 4.22. This portion of the experimental dispersion curve is related to the low wavelength range (high-frequency range), which only represents the very shallow depths. It should be noted that the quality of the MASW testing could also be affected by field test configurations, but the same configurations were used for both Rayleigh and Love wave testing at the Hardy site. Therefore, the differences between the quality of Rayleigh and Love type waves are mainly controlled by geologic conditions of the Hardy site rather than the field test configuration.

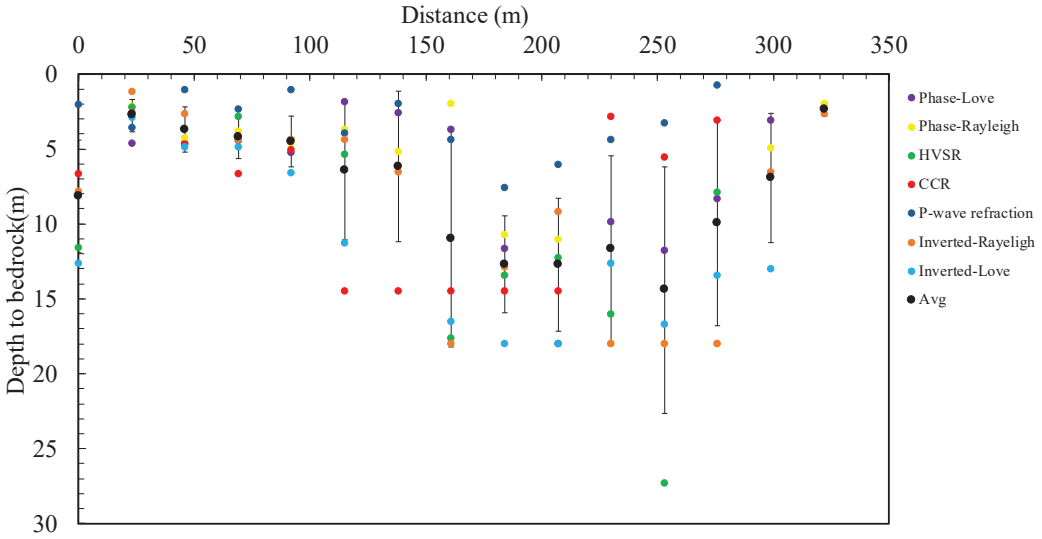

Figure 4.20- Bedrock depths identified for the Westside of Highway 63 bypass using different geophysical methods.

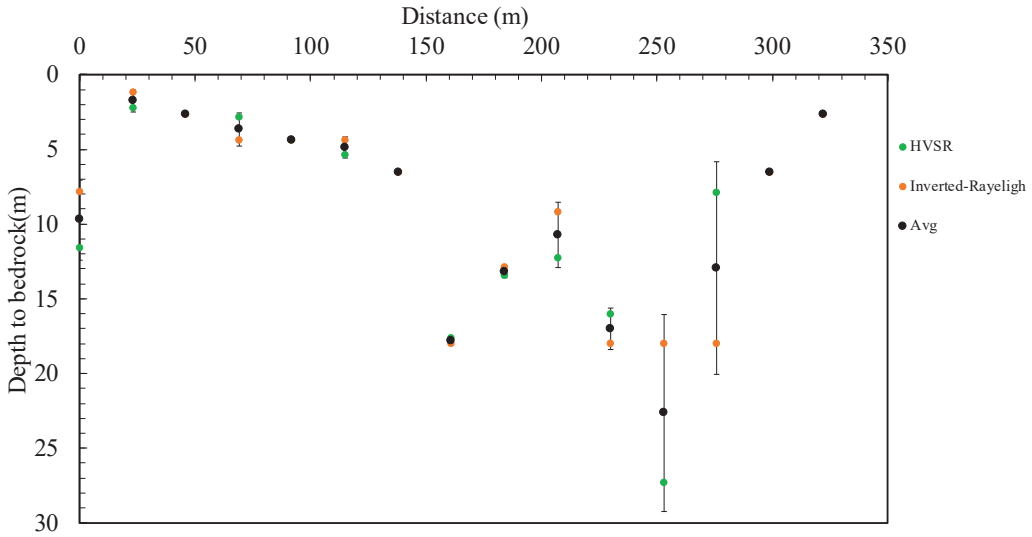

Figure 4.21- Bedrock depths identified for the Westside of Highway 63 bypass from Inverted-Rayleigh and HVSR methods.

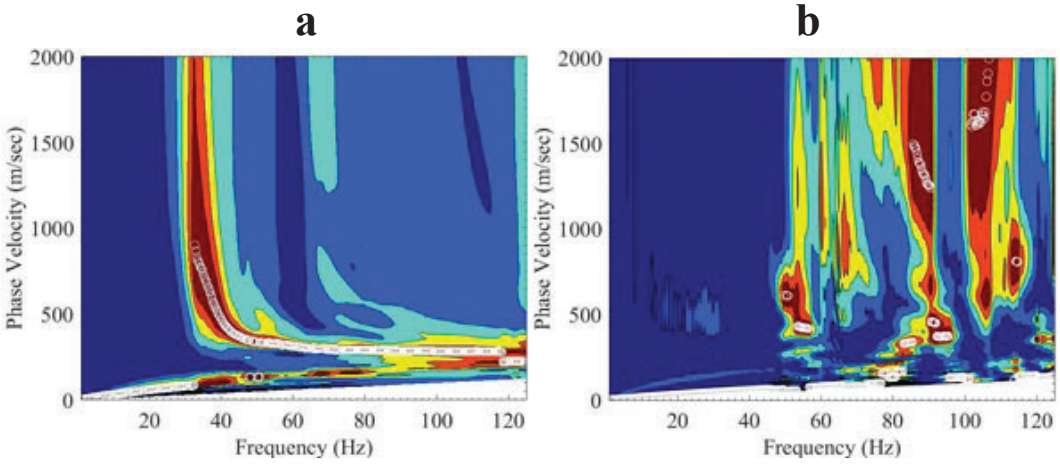

Figure 4.22- Example of the experimental dispersion data points. a) Rayleigh type surface waves, b) Love type surface waves.

The HVSR technique has been found to be valuable for bedrock mapping in cases where a reliable peak exists in the HVSR measurements and accurate information regarding average shear wave velocity of sediments above bedrock is available. Therefore, the combined use of HVSR and MASW could be the best option for bedrock detection since the average shear wave velocity of sediments above bedrock can be estimated from the MASW, and the HVSR results can be used as supplemental information for joint inversion of the dispersion curves in MASW data interpretation to increase the reliability of the inversion process.

Sand Gap site

The second site, Sand Gap, is located in the Ozark Mountains region of the northwest corner of Arkansas, along Arkansas Highway 7, as previously shown in Figure 1.3. Geophysical tests were conducted in an area that has an active slope stability issue that caused several longitudinal cracks in the pavement (See Figure 1.4). The goals of geophysical testing are mapping subsurface stratigraphy parallel and perpendicular to the highway, detecting potential bedrock locations across the area, and identifying the geometry and the lateral and vertical extent of potential slip surface(s). To do so, different geophysical tests were employed, including MASW using Rayleigh and Love waves, P-wave refraction, HVSR, CCR, GPR, and ERT. The results of each method are presented below.

4.1.9 MASW testing

Shown in Figure 4.23, are the survey paths for the MASW measurements using Rayleigh and Love type surface waves for the Sand Gap site along with the pre-existing boring log locations. The MASW measurements were conducted at the four survey paths parallel and perpendicular to Highway 7, including a 188 m long survey line parallel to Arkansas Highway 7 on the Westside (hereafter called MASW_West), a 46 m long survey line parallel to Arkansas Highway 7 on the Eastside (hereafter called MASW_East), a 48 m long survey line conducted longitudinal to the slope (hereafter called MASW_Slope), and a 70 m long survey line crossing two of the pre-existing boring logs (hereafter called MASW_Borehole). The starting (0) and ending points of each survey line are also displayed in the figure. The starting points of the MASW measurements are used as the reference points for the other geophysical testing.

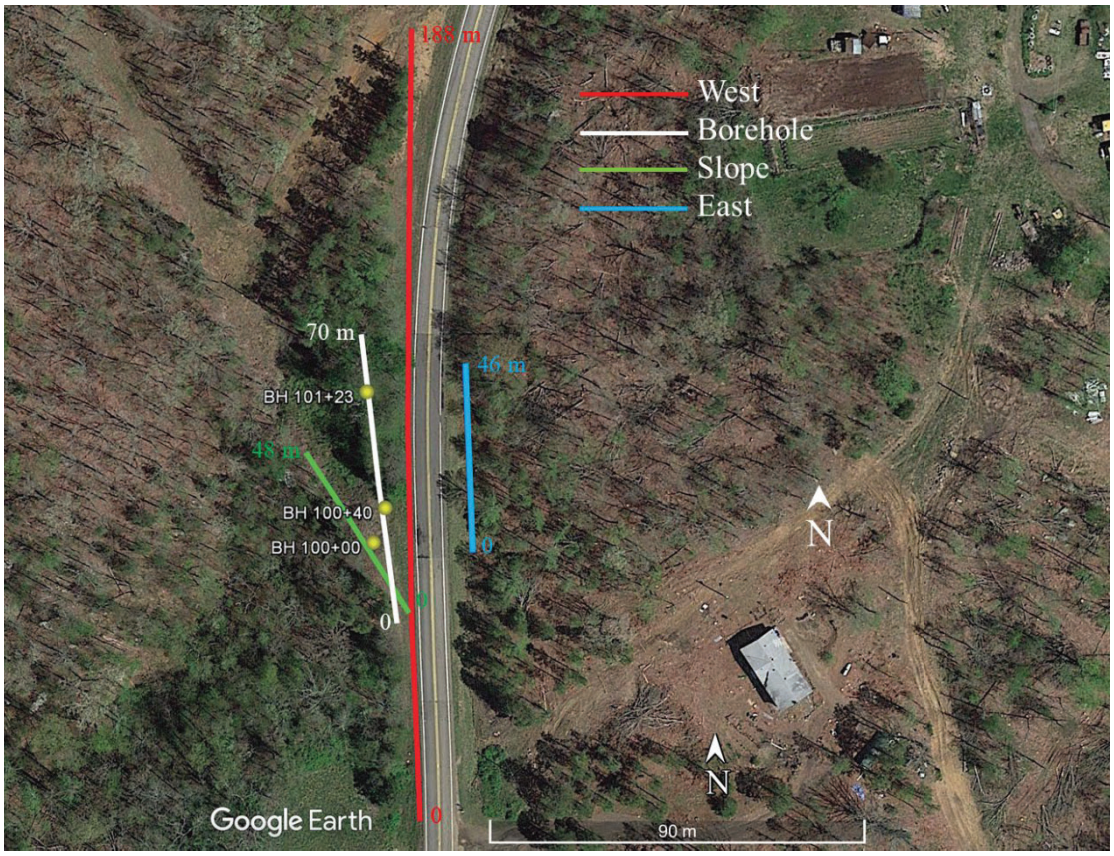

Figure 4.23- MASW survey paths for the Sand Gap site.

4.1.9.1 Inverted shear wave velocity using Love type surface waves

The pseudo 2D Shear-Love cross-section for the MASW_Borehole survey line is presented in Figure 4.24. Additionally, the information from two of the boring logs (BH101+23 and BH100+40) is provided in the pseudo Shear-Love cross-section. The potential bedrock interface is also shown with a black dashed line in Figure 4.24. The ranges of Vs associated with different materials are first determined using information from previous studies (ASTM/SEI 7-10; Anbazhagan and Sitharam, 2008; Olona et al. 2010; Sun et al. 2012; Aung and Leong, 2012; Moon et al. 2017) and obtained shear wave profiles, then adjusted to best match the boring log data.

As shown in Figure 4.24, in terms of subsurface characterization, the results of the MASW measurements using Love type surface waves correspond well with the boring logs information, indicating the effectiveness of this method for bedrock detection for the Sand Gap site. Based on the spatial variation of Vs for the MASW_Borehole survey line in Figure 4.24, the subsurface consists of four layers. A stiff/dense soil layer from the surface to a depth of 5-7 m with Vs ranging from 100-300 m/s, a completely weathered shale or a very stiff/very dense soil layer from 7-9 m with Vs between 300-360 m/s, followed by a highly weathered rock layer (sandstone based on the boring logs) with Vs ranging from 360-700 m/s, underlain by a

weathered rock material. Given that the shale material is only observed at one of the boring logs and the Vs range of 300-360 m/s can be related either to a completely weathered shale layer or a very stiff/very dense soil layer, in this report Vs values higher than 360 m/s are considered as the representative values for bedrock materials. Based on this assumption, the bedrock location is detected to be at a depth of approximately 8-10 m from the MASW tests using Love type surface waves. These locations match the bedrock detected from the boring logs at the BH101+23 and BH100+40. The completely/highly weathered rock materials probably have an RQD ranging from 0-50%, whereas the weathered rocks likely have RQD higher than 50%.

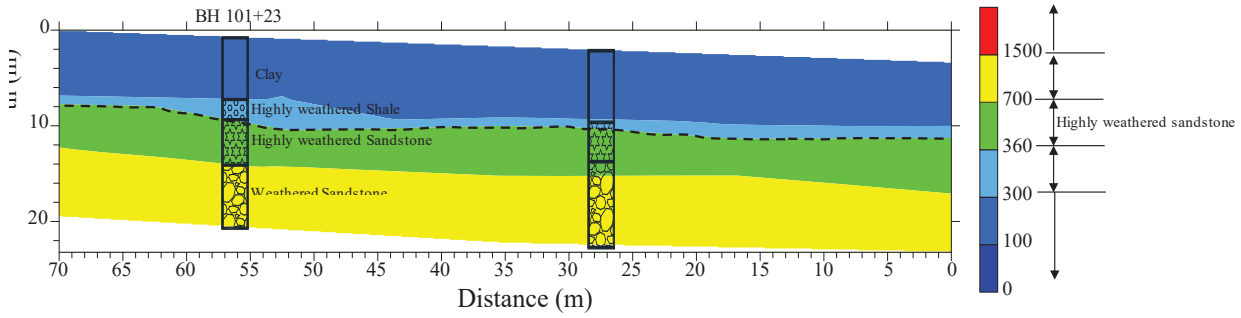

Figure 4.24- Pseudo 2D Vs cross-section from MASW using Love type surface waves for the MASW_Borehole survey line.

The 2D Shear-Love cross-section for the MASW_West survey line is shown in Figure 4.25. Similar to the MASW_Borehole survey line in Figure 4.24, the site is comprised of four layers, including a 4-6 m thick stiff/dense soil layer at the surface, a very thin completely weathered shale or a very stiff/very dense soil layer, a highly weathered rock layer (probably sandstone) extending from the base of the previous layer to depths ranging from 12-18 m, and a weathered rock material. The completely weathered shale or very stiff/very dense soil layer can be ignored since it is very thin. The bedrock location, which is quite consistent along the survey line, is identified to be at depths ranging from 6-9 m.

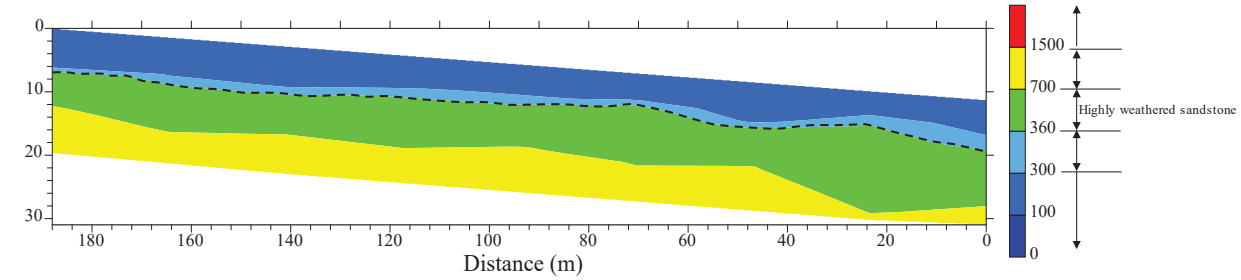

Figure 4.25- Pseudo 2D Vs cross-section from MASW using Love type surface waves for the MASW_West survey line.

Presented in Figure 4.26, is the pseudo 2D Shear-Love cross-section for the MASW_Slope survey line along with the boring log information recorded at the BH100+00. According to this cross-section, the slope is characterized by four layers of a stiff/dense soil layer at the surface, a completely weathered shale or a very stiff/very dense soil layer, followed by a highly weathered rock layer, and a weathered rock material. Unlike the other two cross-sections for the MASW_Borehole and the MASW_West that exhibit consistent bedrock locations, the location of the bedrock is variable along the MASW_Slope survey line, as shown in Figure 4.26. The depth to the bedrock varies from 4-10 m along the profile. The surface with the highest slip potential is likely the interface of the soil and rock materials since the bedrock is located at shallow depths. Due to the thinness of the topsoil layer in this profile, down-slope movements could likely occur during heavy rainfall events if water can seep into the soil. The penetrated water can be trapped at the bedrock depression location at the bottom of the slope and lead to slope failure through different mechanisms, including:

- Increasing the total weight of potential slip surface(s) by saturating the soil layers within the slip.
- Dissolving the mineral cements that hold soil particles together.
- Reducing grain-to-grain contacts leads to a reduction in soil shear strength.
- Reducing the friction between the soil and bedrock at the soil/bedrock interface.

More discussions in this regard are provided later in the report.

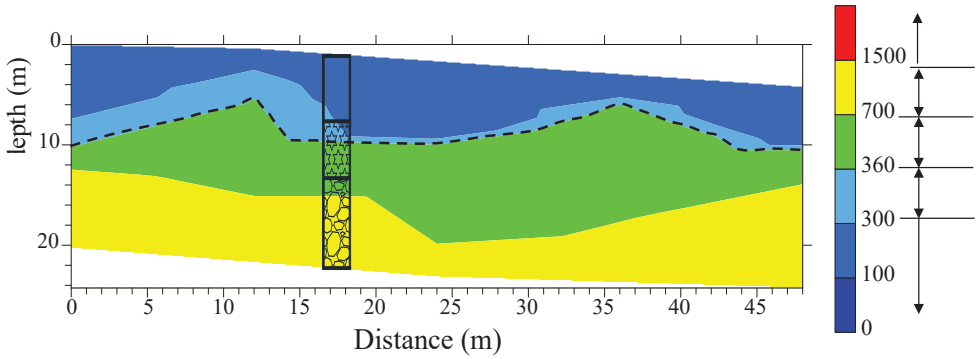

Figure 4.26- Pseudo 2D Vs cross-section from MASW using Love type surface waves for the MASW_Slope survey line.

Due to the testing configuration and shot locations used for the MASW_East survey line, only one inverted shear wave velocity profile was generated (see Figure 4.27), and therefore, it was not possible to plot a pseudo 2D cross-section for this survey line. Based on the Vs profile in Figure 4.27, the bedrock is approximately located at 9 m. This is consistent

with the results of the MASW_West survey line in Figure 4.25, indicating a consistent bedrock depth ranging between 6-9 m.

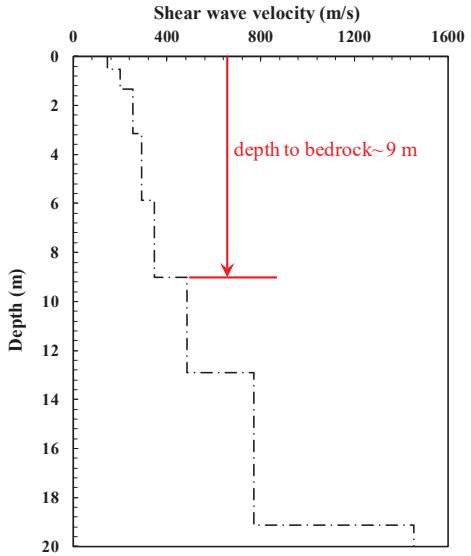

Figure 4.27- Inverted shear wave velocity profile for the MASW_East survey line using Love data.

4.1.9.2 Inverted shear wave velocity using Rayleigh type surface waves

The pseudo 2D Shear-Rayleigh cross-section is shown in Figure 4.28 with the boring log information and potential bedrock location. Although bedrock depths were estimated with a high degree of accuracy from the MASW using Rayleigh waves as presented in this profile, this method fails to accurately separate the highly weathered and weathered rock layers. The Vs results of the Rayleigh wave MASW in Figure 4.28 are generally consistent with the results of the Love wave MASW in Figure 4.24 to a depth of 12 m across the profile. However, beyond 12 m the two begin to differ particularly in differentiating the highly weathered sandstone. A major contributing factor to the difference in the results is the quality of the Rayleigh wave dispersion data collected along the MASW_Borhole survey line. An example of the experimental dispersion data points from Rayleigh wave MASW for the MASW_Borehole survey line is presented in Figure 4.29. The poor quality of the experimental dispersion data points at low frequencies (<30 Hz) leads to uncertainty in the identification of deeper stratigraphic layers (Section 3.3.2).

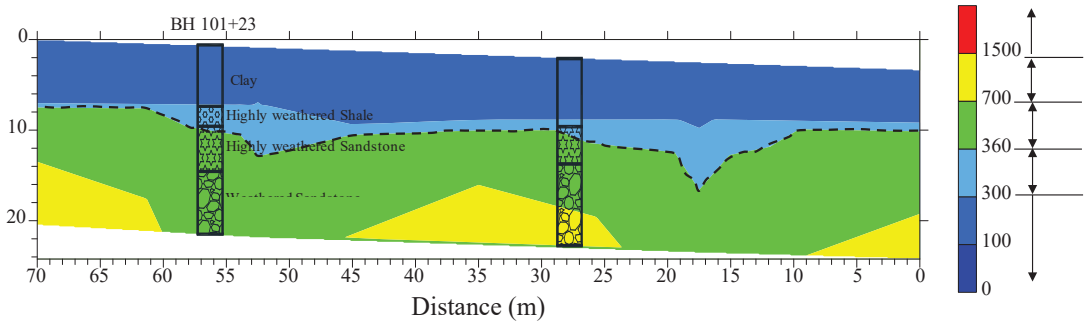

Figure 4.28- Pseudo 2D Vs cross-section from MASW using Rayleigh type surface waves for the MASW_Borehole survey line.

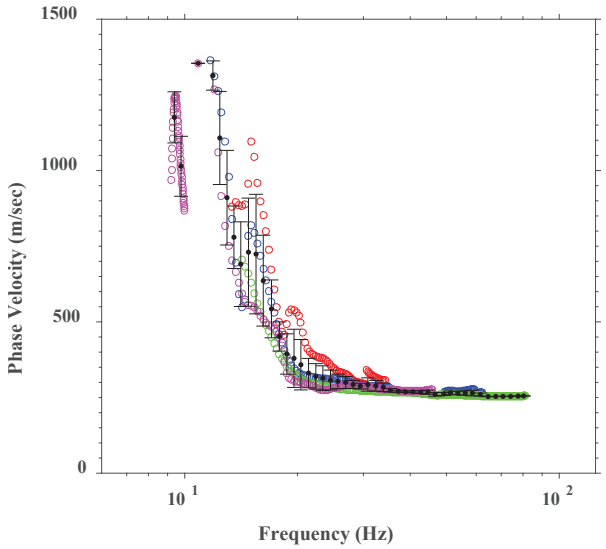

Figure 4.29- An example of experimental dispersion data points from MASW using Rayleigh type surface waves for the MASW_Borehole survey line.

Provided in Figure 4.30 is the pseudo 2D Shear-Rayleigh profile for the MASW_West survey line along with the predicted bedrock locations. The general layering of this profile agrees with that from the results of the Love wave MASW in Figure 4.25, but with slight differences regarding the exact locations of the weathered rock layer (e.g. at locations from 105-130 m).

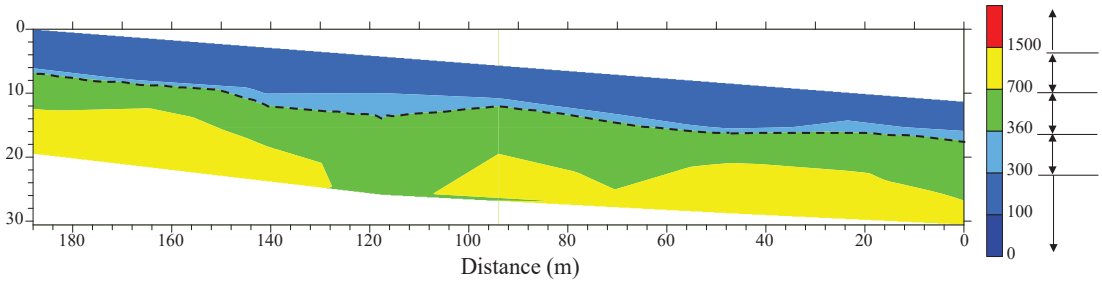

Figure 4.30- Pseudo 2D Vs cross-section from MASW using Rayleigh type surface waves for the MASW_West survey line.

For the MASW_Slope survey line, the quality of the experimental dispersion data points measured from Rayleigh waves testing is poor, with no useful trend about the location of the fundamental mode. Therefore, for the MASW_Slope survey line, no pseudo 2D cross-section was able to be generated from the field data.

The Vs profile for the MASW_East survey line is shown in Figure 4.31. Depth to the bedrock estimated from this profile corresponds with that from MASW using Love waves in Figure 4.27, but the differences between the two Vs profiles become considerable for depths greater than 10 m due to the poor quality of the experimental dispersion data points for the Rayleigh waves testing.

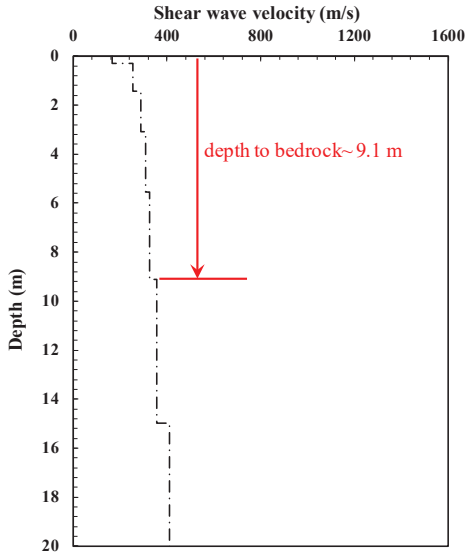

Figure 4.31- Inverted shear wave velocity profile for the MASW_East survey line using Rayleigh type surface waves.

4.1.10 P-wave refraction

P-wave refraction surveys were conducted on the same survey lines as MASW testing as presented in Figure 4.23. The 2D cross-section acquired from the P-wave refraction survey for the Borehole survey line is shown in Figure 4.32 along with the two boring log records (BH101+23 and BH100+40). The bedrock location is also displayed using a black dashed line. Based on this profile, the bedrock depth varies along the survey line with a maximum depth of 12 m. Relatively deeper bedrock locations are observed from 20-55 m in this profile. Generally, the bedrock locations identified from the P-wave refraction surveys are consistent with the boring logs; however, depth to bedrock is slightly overestimated (approximately 2 m) at the BH101+23 and BH100+40.

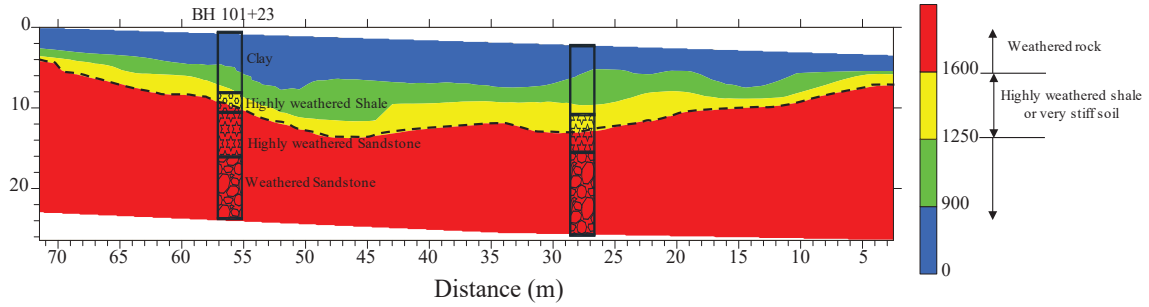

Figure 4.32- P-wave velocity 2D cross-section from the P-wave refraction survey for the Borehole survey line.

The results of the P-wave refraction survey conducted on the west side of the highway is shown in Figure 4.33. While the bedrock locations are mostly shallow (about 6 m) and consistent along the Westside survey line, there are two sections from 110-130 m and from 150-160 m in which relatively deeper (approximately 14 m) bedrock locations are measured from the P-wave refraction.

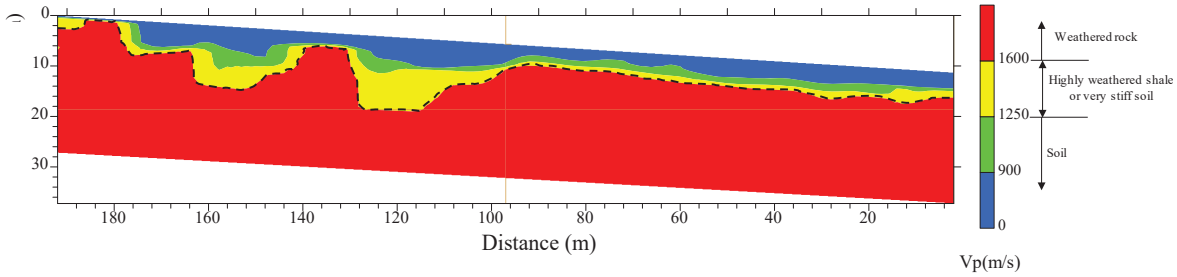

Figure 4.33- P-wave velocity 2D cross-section from the P-wave refraction survey conducted along the west side of the highway.

Shown in Figure 4.34 is the 2D cross-section from the P-wave refraction survey conducted along the slope along with the boring log data and the potential bedrock location denoted with a black dashed line. As shown in this profile, the bedrock detected from the P-wave refraction perfectly matches the boring log data at the BH100+00. The bedrock locations are very shallow along the survey line, with depths ranging from 4-8 m.

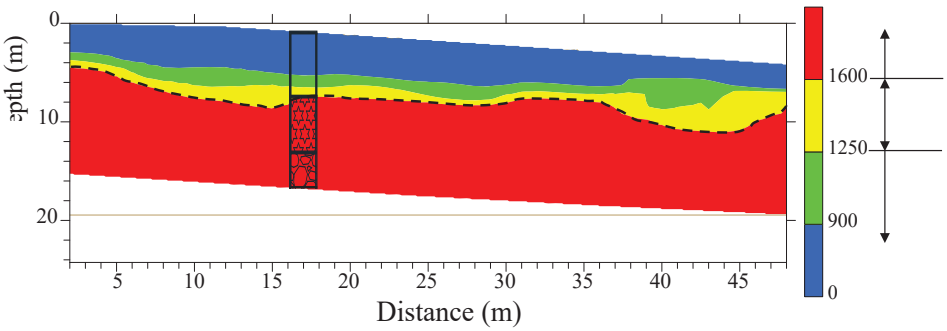

Figure 4.34- P-wave velocity 2D cross-section from the P-wave refraction survey conducted along the slope.

Unlike the results of the P-wave refraction for the Hardy site that failed to accurately predict the bedrock locations, for the Sand Gap site, the results of the P-wave refraction survey correspond well with the boring logs information and MASW profiles in terms of bedrock detection. The reason for such inconsistency in the accuracy of the P-wave refraction technique for bedrock detection was mostly caused by the differences in the subsurface layering of the two sites. For the Hardy site, the first arrival time selection was associated with high ambiguity due to the existence of multiple shallow refractors at variable depths. Therefore, this resulted in less reliable P-wave refraction results for the Hardy site.

4.1.11 HVSR

Given that it was difficult to conduct MASW measurements along the steep slopes and areas densely covered with trees and bushes at the Sand Gap site, a suite of HVSR measurements was acquired along the Eastside areas Westside of Arkansas Highway 7 to identify the bedrock locations. The locations of the HVSR measurements, which include 41 stations, are provided in Figure 4.35. Depths to the bedrock were estimated using the $H = (Vs_{,avg}/4f)$ equation. To do so, the average shear wave velocity was determined from the MASW. It should be noted that the $H=(Vs_{,avg}/4f)$ equation provides an approximation of the bedrock locations. The information from the HVSR measurements are utilized to create several cross-sections parallel and perpendicular to Arkansas Highway 7. The locations of the cross-section are shown in Figure 4.35.

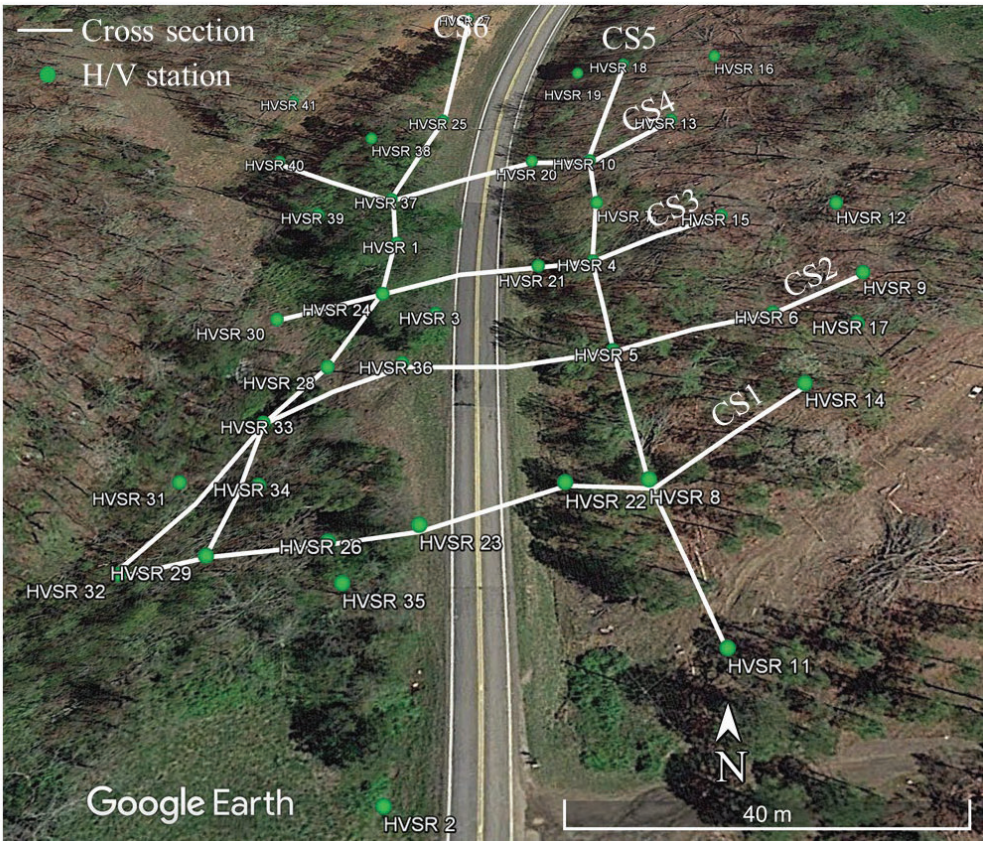

Figure 4.35- Locations of the HVSR stations and cross-sections at the Sand Gap site.

Besides information regarding the bedrock locations, the geometry of the area, which includes surface elevations, is required for accurate slope stability analyses. In this respect, the elevation data from the GPS readings were combined with the elevation data from Google Earth to create a 3D surface elevation plot, as shown in Figure 4.36. The locations of Arkansas Highway 7 and the HVSR cross-sections are also provided in the plot.

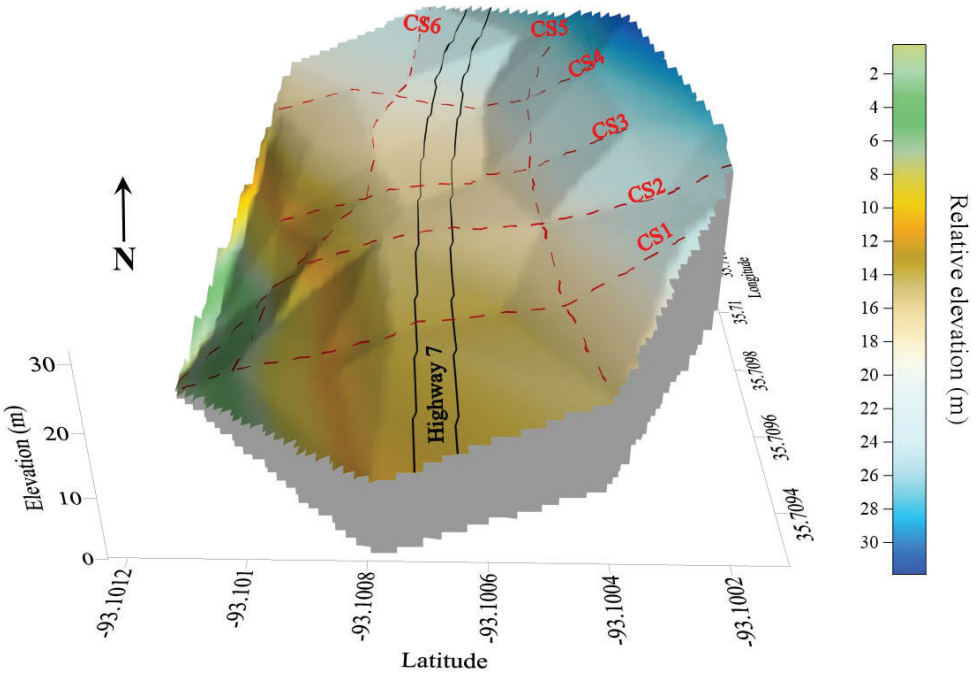

Figure 4.36- 3D plots showing the surface elevations at the Sand Gap site.

Presented in Figure 4.37a, b, c, d, e, and f are the variations of bedrock locations estimated from the HVSR measurements along the cross-sections shown in Figure 4.35. While four of the cross-sections are perpendicular to Arkansas Highway 7 (CS1, CS2, CS3, and CS4), the two other cross-sections (CS5 and CS6) are almost parallel to the highway, as illustrated in Figure 4.35. As shown in Figure 4.37a, b, c, and d, apart from CS4 in Figure 4.37d, which exhibits a very shallow sediment with a thickness of approximately 1.8 m, the sediment thickness on the Eastside of Highway 7 is almost consistent along the perpendicular cross-sections with depths varying from 3.2-5.2 m. For the Westside of Highway 7, CS1 and CS2 (Figure 4.37a and b) reveal a very thin soil layer from the surface to depths ranging from 1.8-2.4 m, whereas the two other perpendicular cross-sections, CS3 and CS4, show a relatively deeper soil layer with a thickness ranging from 5.6-8.8 m. As shown in Figure 4.37b, the HVSR measurements overestimated the bedrock depth by 2.5 m at BH100+40. This difference is acceptable since the BH100+40 is a few meters away from the CS2 cross-section. Comparing the slope of the soil/bedrock interface beneath the highway pavement for the perpendicular cross-sections in Figure 4.37, relatively steeper rock-site slopes are observed for CS2 and CS3, indicating these sections are more susceptible to slope movements compared to CS1 and CS4 that have a more gentle rock-site slope. Interestingly, these sections (CS2 and CS3) correspond quite well with the longitudinal cracks in the pavement, as presented in Figure 1.4.

The data from the HVSR measurements are also used to generate two cross-sections parallel to Arkansas Highway 7, and the results are shown in Figure 4.37e and f. As expected,

based on CS5 in Figure 4.37e, the bedrock location is consistent for the Eastside of Highway 7 except at the location where CS5 intercepts CS4. However, the estimated bedrock locations are quite variable for the Westside of Highway 7, as shown in Figure 4.37f. The bedrock detected was at depths of 4.5 m from the start of the survey line to a distance of 50 m. This is followed by a deeper bedrock location from 50-110 m with a thickness of about 8.6 m and a very shallow bedrock location from 110-150 m. A comparison of the boring log records at BH101+23 with the HVSR measurements in Figure 4.37 reveals the effectiveness of the HVSR measurements for bedrock detection. Depth to the bedrock slightly overestimated (approximately 1 m overestimation) at this location using the HVSR measurements. The soil/bedrock interface observed on the west side of the highway has a steeper slope than that of the Eastside of the highway, indicating that the west side of the highway has a higher potential for slope movements.

Provided in Figure 4.38, Figure 4.39, and Figure 4.40 are three surface contour maps presenting surface elevations from the GPS readings and Google Earth information, depths to bedrock from the HVSR measurements, and bedrock elevations from the HVSR measurements across the Sand Gap site, respectively. These contour maps can be used to estimate depth to bedrock (sediment thickness) across the tested areas for further slope stability analysis. From Figure 4.40, an increase in the bedrock elevation near the bottom of the slope survey line is observed. This is confirmed by the results of the MASW_slope survey line in Figure 4.26 in which depth to bedrock decreases from a distance of 15 m to 35 m along the profile. In addition, based on the ERT profile presented later in the report (see Figure 4.46), there is a high concentration of water in this section (low resistivity indicated by the blue colors). This hump in the bedrock elevation at the bottom of the slope may be trapping water in that area of the slope. During geophysical testing at the Sand Gap site, a small spring and wet area was observed at the hump location, which verifies the results of ERT testing. The trapped water in this section can cause slope movements due to the increase in total weight of potential slip surface/surfaces by saturating the soil layers inside the slip surfaces, reduction in soil grain-to-grain contacts which lead to a reduction in soil shear strength, and reduction in the friction between the soil and bedrock at the soil/bedrock interface. Therefore, this section is considered one of the potential slip surfaces of the area that may have a relatively low safety factor against a possible failure.

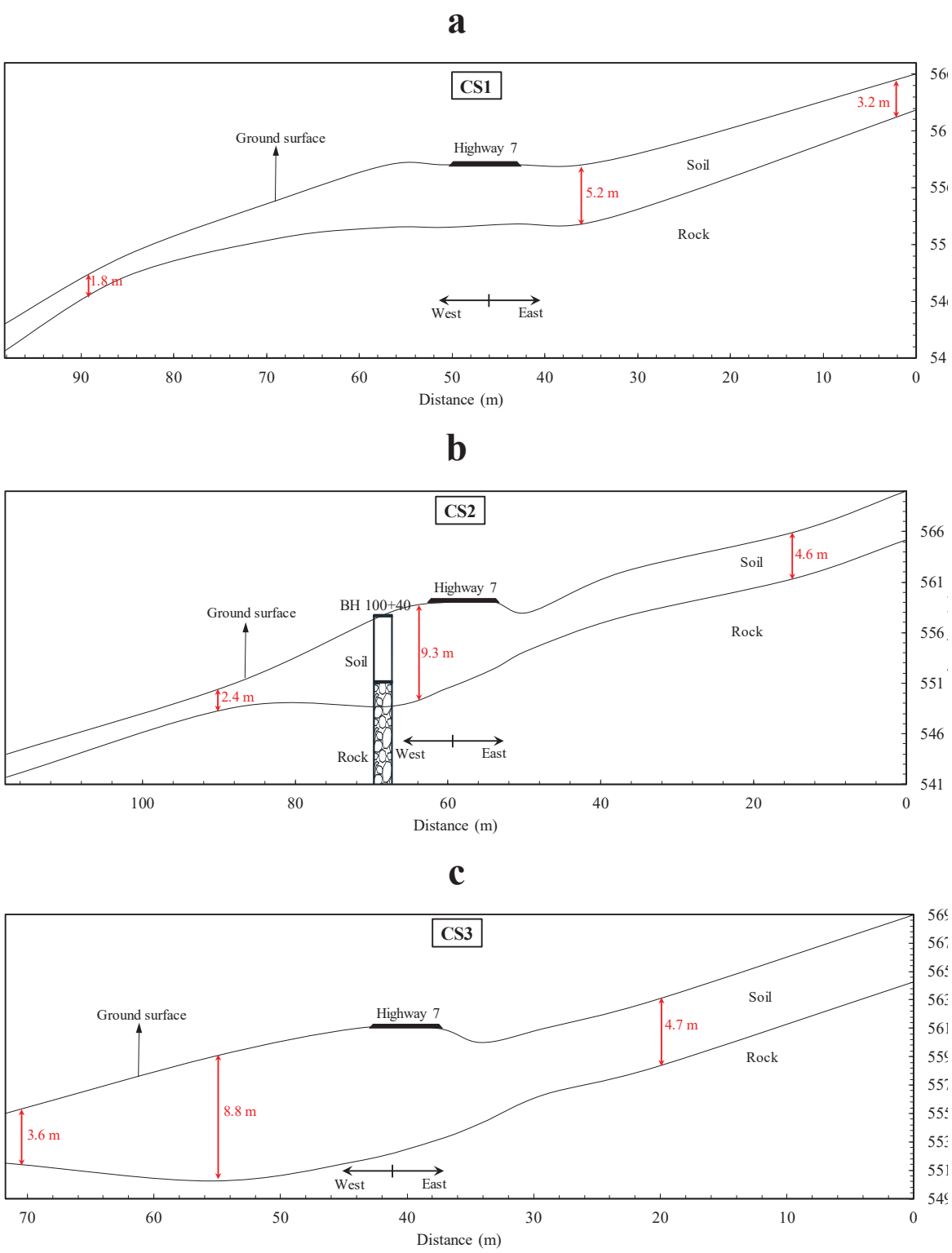

Figure 4.37- Several cross-sections showing variations of sediments' thickness (bedrock locations) across the Sand Gap site based on the information from the HVSR measurements. (a, b, c, d perpendicular to Arkansas Highway 7 and e, f parallel to Arkansas Highway 7).

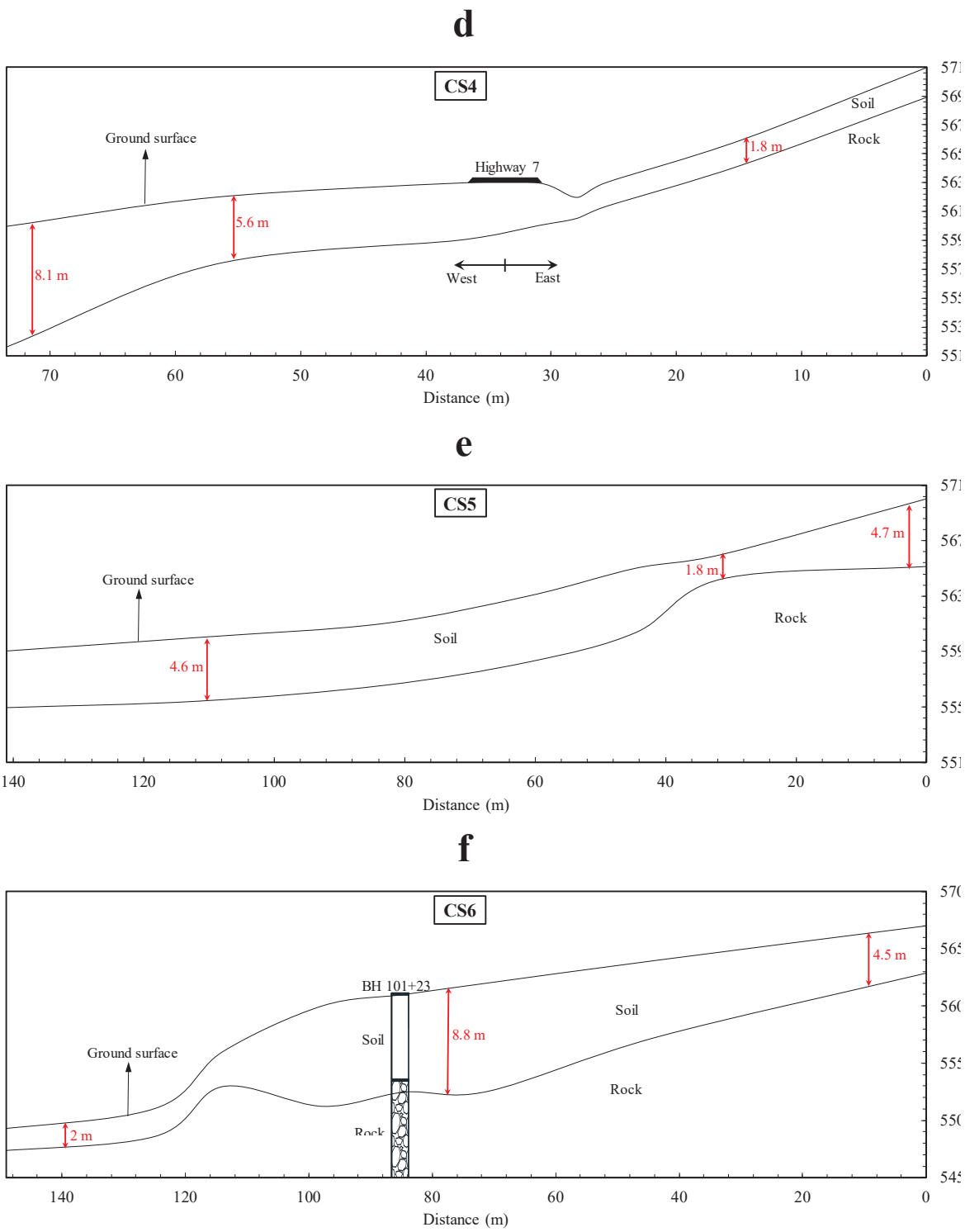

Figure 79- Continued.

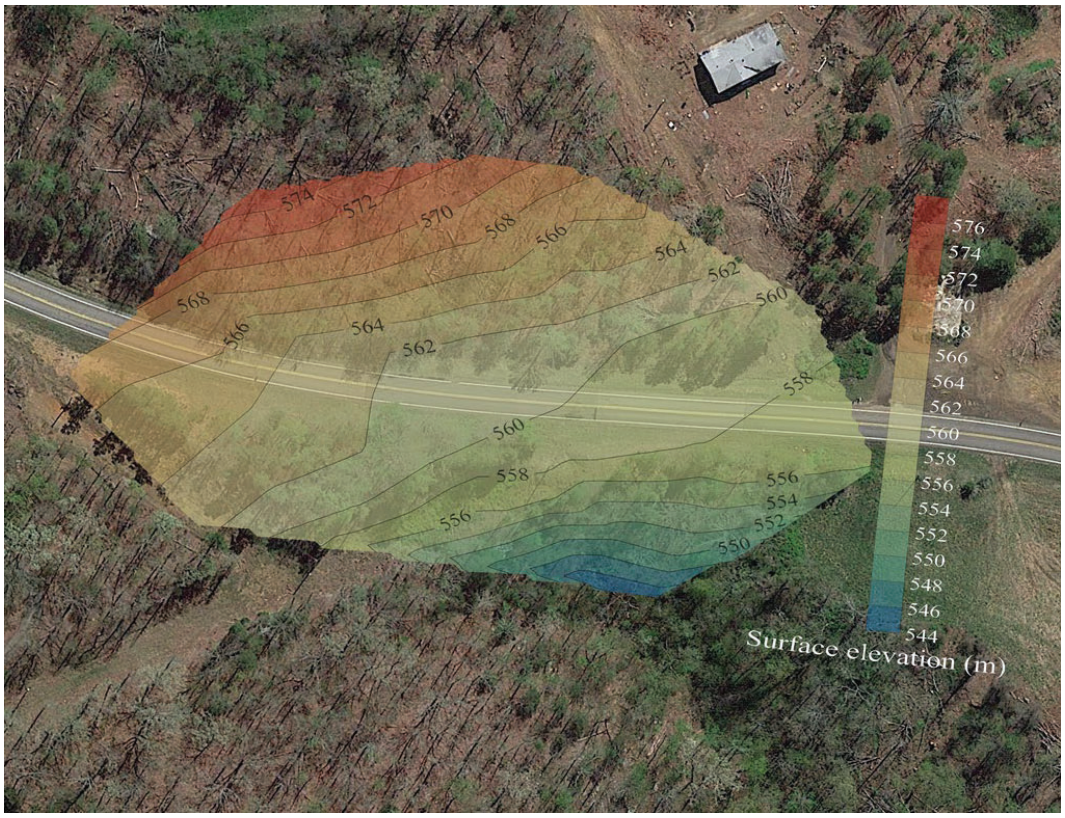

Figure 4.38- Surface elevation contour map across the Sand Gap site.

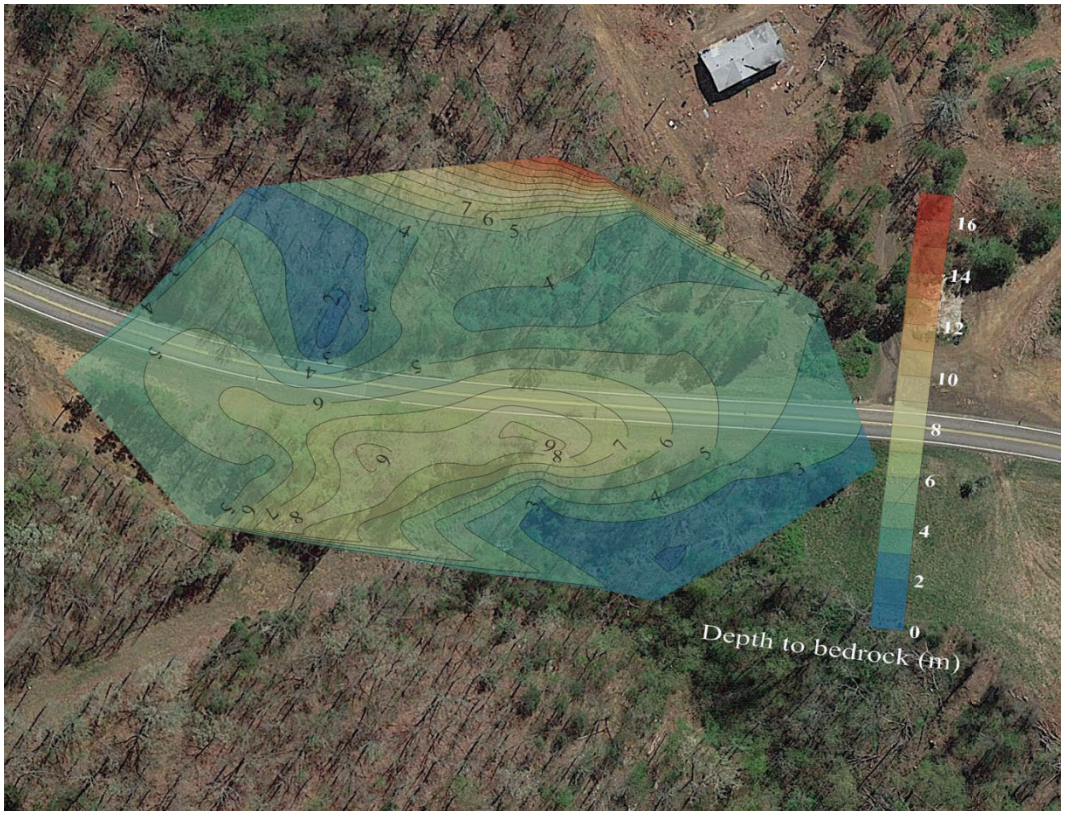

Figure 4.39- Depths to the bedrock across the Sand Gap site.

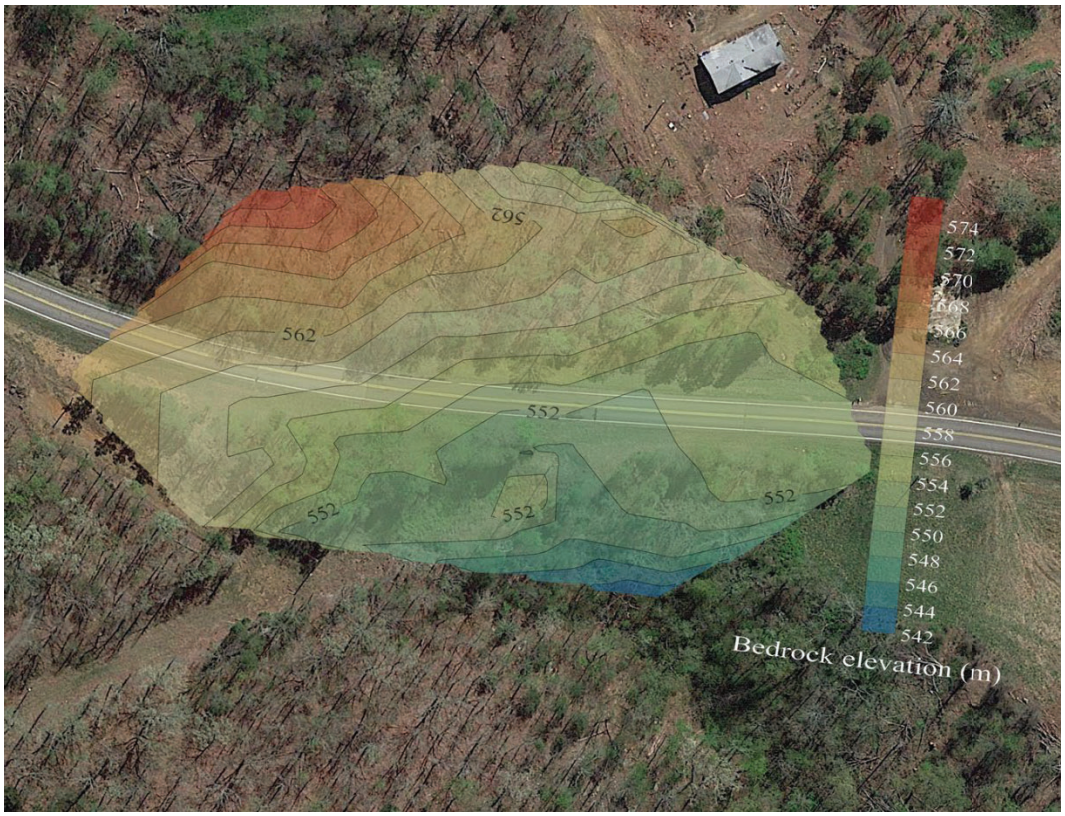

Figure 4.40- Bedrock elevations across the Sand Gap site.

4.1.12 CCR

The resistivity profiles generated for the Sand Gap site survey lines along the slope, West of the highway, and East of the highway are presented in Figure 4.41, Figure 4.42, and Figure 4.43, respectively. The maximum depth of exploration for the Slope survey line is almost half of the other two survey lines because a shorter rope length was used for the Slope survey line (rope length of 5 meters) compared to the West and East survey lines (rope length of 10 meters). Comparing the CCR results for the Slope survey line in Figure 4.41 with the boring log records at the BH100+00, CCR falls short of predicting the bedrock location. Low resistive materials are observed for a majority of sections in the three CCR profiles in Figure 4.41, Figure 4.42, and Figure 4.43, with resistivity values ranging from 0-80 (ohm-m). The low resistive materials are likely related to soils with a very high degree of saturation which is plausible since CCR testing was conducted in December 2017. The very low resistive layers can shadow the presence of other materials due to the data averaging process used in the MagMap software. However, more accurate information about the variations of soil degree of saturation is required to verify the reason behind such low resistivity materials.

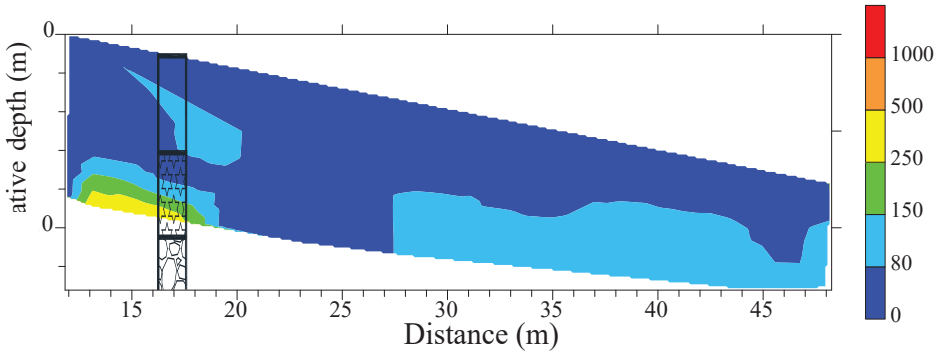

Figure 4.41- CCR profile for the Slope survey line.

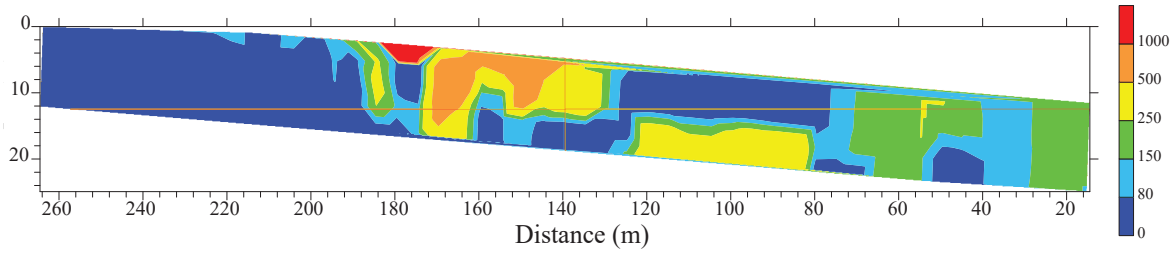

Figure 4.42- CCR profile for the west of the highway survey line.

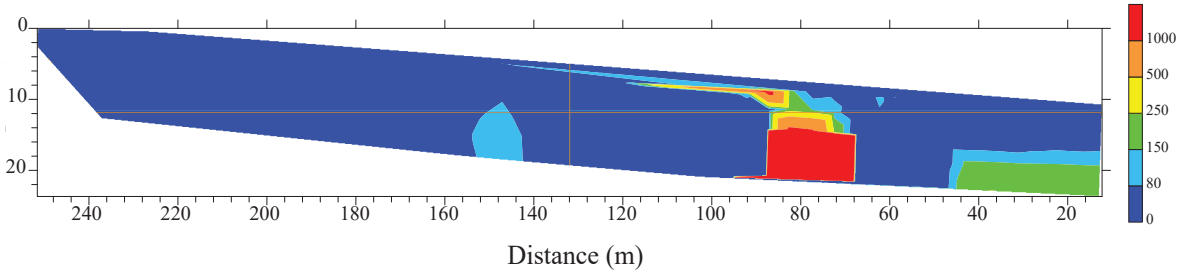

Figure 4.43- CCR profile for the East of the Highway survey line.

Overall, the CCR results are inconsistent with the other geophysical method in terms of the subsurface layering of the Sand Gap site. The CCR measurements could not provide any useful information about bedrock locations and potential slip surfaces for the Sand Gap site.

4.1.13 ERT

Shown in Figure 4.44, Figure 4.45, and Figure 4.46 are the ERT profiles for the borehole, west of the highway, and slope survey lines, respectively. As shown in Figure 4.44, for the borehole survey line, the ERT profile fails to correctly characterize the subsurface layers at the BH 100+00. This is likely caused by the soil degree of saturation that can significantly change soil resistivity. A highly resistive soil layer is observed near the surface that corresponds to the top clay layer, and this is followed by very low resistive materials from 10-40 m. The very low resistive materials in this profile are probably related to soils with a very high degree of saturation. For the west of the highway survey line in Figure 4.45, a highly resistive layer

appears from the surface to a depth ranging from 1-10 m. The thickness of this layer increases from a distance of about 80 m to the end of the profile. A highly resistive zone is also observed from the start of the survey line to a distance of 60 m at depths greater than 10 m. The ERT profile generated for the slope survey line in Figure 4.46 is in general agreement with the boring log information at the BH 100+00. The reason why the top clay layer has high resistivity near the surface and very low resistivity at depths ranging from 2-6 m is believed to be caused by a significant change in the degree of saturation. The moderate resistive layer, which is shown with a green color, matches the highly weathered sandstone and the highly resistive layer (>200 Ohm-m), which appears at the bottom of the profile corresponds to the weathered sandstone layer. The interesting part of this profile is the presence of a very low resistive zone (shown by the blue color) between the two highly resistive layers and the hump in the bedrock elevation. This hump in bedrock elevation was also observed in the MASW profile in Figure 4.26. As explained previously, this hump in the bedrock elevation may be trapping water in that section of the slope and inducing instability of the slope during or shortly after heavy rainfall.

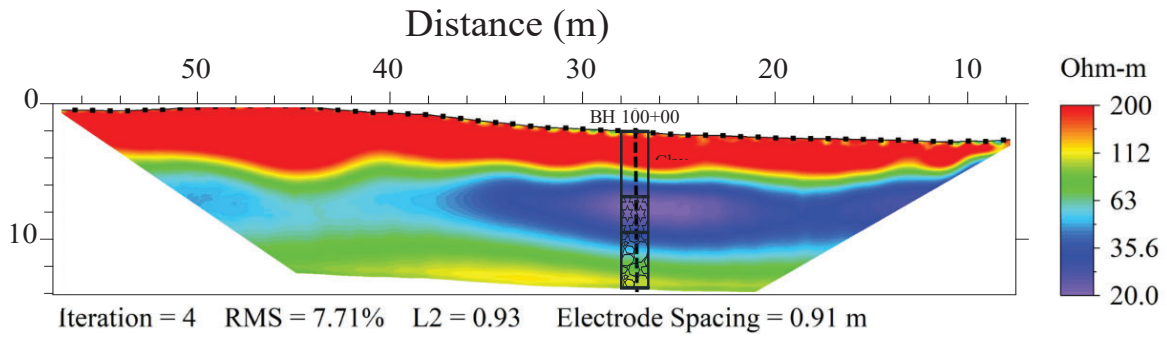

Figure 4.44- ERT profile for the Borehole survey line (modified from [1]).

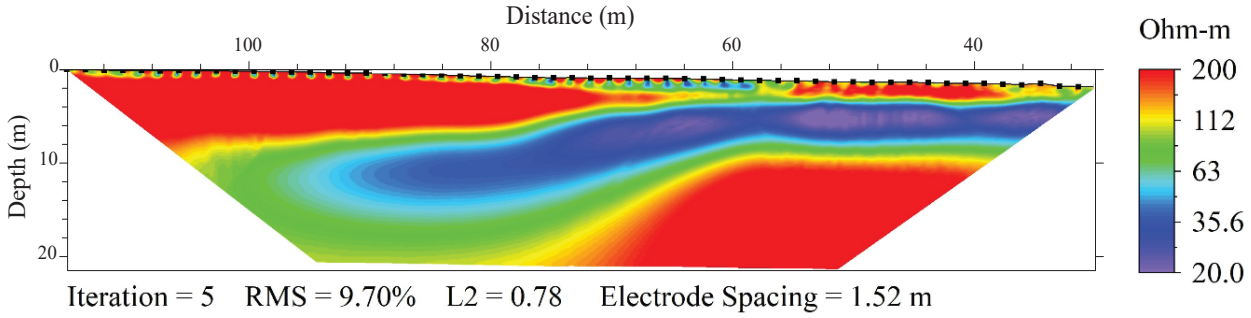

Figure 4.45- ERT profile for the west of highway survey line (modified from [1]).

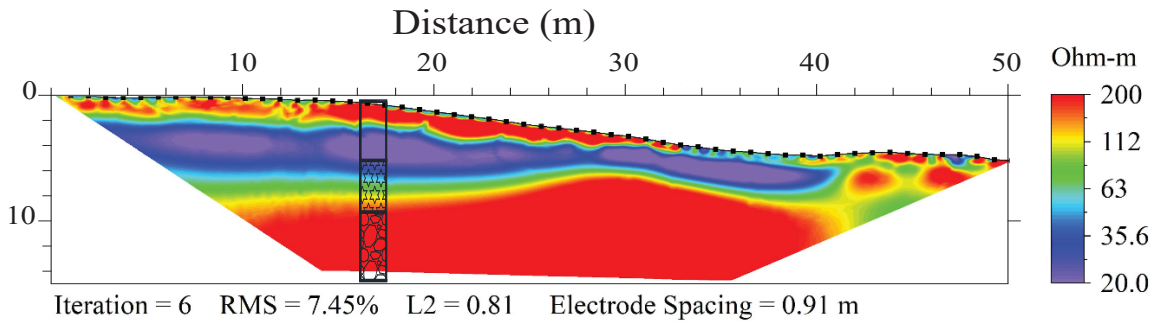

Figure 4.46- ERT profile for the Slope survey line (modified from [1]).

4.1.14 GPR

The GPR tests were conducted at the Sand Gap site using both 100 and 50 MHz antennas along the same survey lines as the MASW testing (See Figure 4.23). The results of the GPR tests for the GPR_West and GPR_Slope are shown in Figure 4.47a and b, respectively. According to the boring log records, the topsoil layer at the Sand Gap site is comprised of stiff clay or stiff clay with gravel; thus an average electromagnetic wave of 0.09 m/ns (Table 3-1 in Section 3.6.2) was used to convert travel time to penetration depth.

Based on the resolution variations for the GPR profiles in Figure 4.47, it can be concluded that the maximum penetration depth of GPR signals is approximately 4 m. For depths greater than 4 m, the amplitude of the GPR signal traces is almost negligible. Similar to the Hardy site, the presence of the top clay layer at the Sand Gap site caused quick attenuation of the GPR signals with depth. Therefore, no useful information about bedrock locations and potential slip surfaces across the Sand Gap site can be drawn from the GPR profiles. Since the GPR data acquired for the GPR_Borehole and the GPR_East survey lines have shown the same results, they are not presented in this report.

Overall, for sites such as Sand Gap with a topsoil layer that can attenuate the GPR signals quickly, which could be the case for most of the ARDOT projects, this method will not provide any useful information regarding the bedrock locations and subsurface conditions.

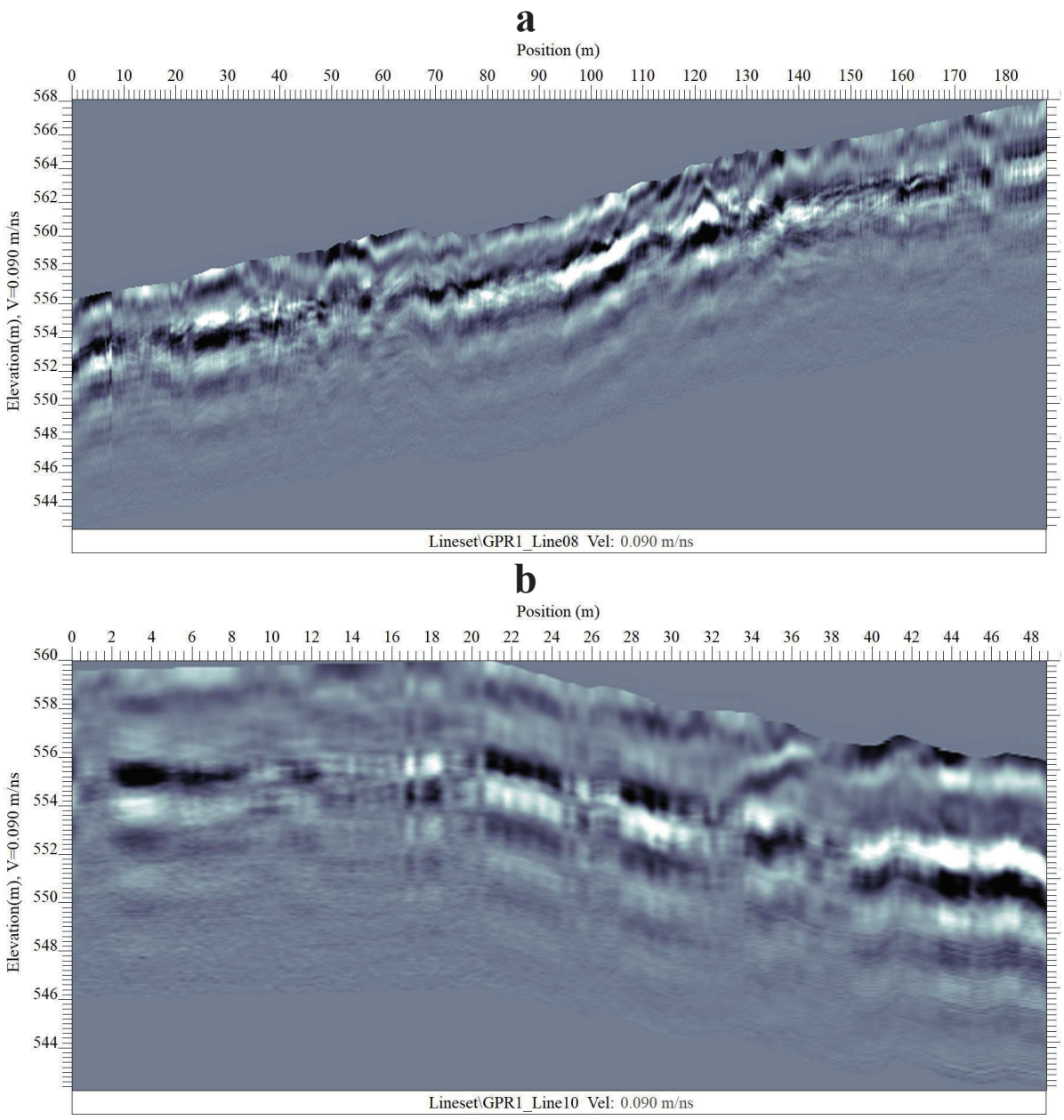

Figure 4.47- GPR profiles measured at the Sand Gap site using 50 MHz antenna. a) GPR_West, b) GPR_Slope.

4.1.15 Potential slip surface

Based on the results of the geophysical testing, the Sand Gap site is comprised of a four-layer system. A stiff/dense soil layer at the surface (clay based on the boring logs), a very thin completely weathered shale or a very stiff/very dense soil layer, and a highly weathered rock layer, underlain by a weathered rock material. The thickness of sediment varies across the site with a range from 1.8-10 m. Sandstone units mainly make up the bedrock materials of the Sand Gap site, but a very thin shale layer is also observed at some locations. The highly

weathered rock materials have RQDs ranging from 0-50%, whereas the weathered rocks likely have RQD higher than 50%.

According to the geologic stratification of the Sand Gap site interpreted from the geophysical tests, the soil/bedrock interfaces are considered the highest potential locations for the slip surface. For locations where a steep soil/bedrock interface is located near the ground surface, a slip surface that starts from the ground surface and reaches the soil/bedrock interface can occur during a heavy rainfall event. However, the most probable slip surfaces are expected to be those which start from a point in the pavement due to the surcharge loads of vehicles driving on the highway. An example of a potential slip surface is shown in Figure 4.48 based on the results of the P-wave refraction survey conducted on the slope survey line. This is corroborated by the inclinometer displacement data recorded on April 4th, 2017 by ARDOT personnel. The inclinometer is located on the Westside of Highway 7 on top of the Borehole survey line. To better clarify this, the downslope displacement measured from the inclinometer is overlaid on top of the pseudo 2D Vs cross-section acquired from the MASW testing using Love type surface waves and the results are shown in Figure 4.49. As shown in this figure, all downslope displacements recorded by the inclinometer are related to depths ranging from 0-8 m with a maximum value of about 0.9 cm at the ground surface. No displacements were observed for depths greater than 8 m. This perfectly matches the MASW profile at the inclinometer location showing that the soil/bedrock interface is located at 8.3 m below the ground surface.

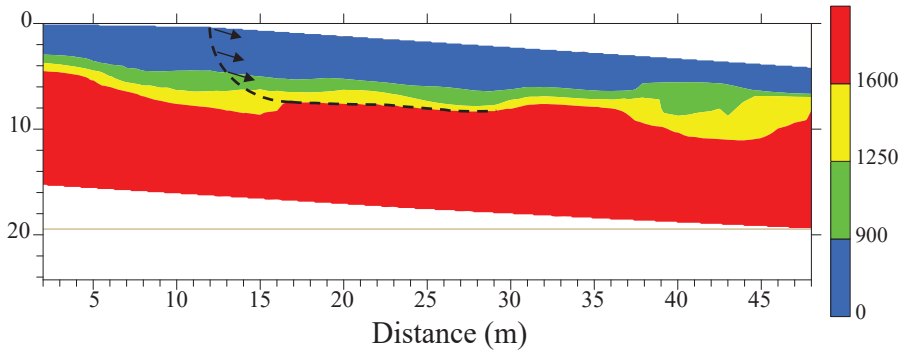

Figure 4.48- An example of potential slip surface based on the P-wave refraction survey conducted along the slope.

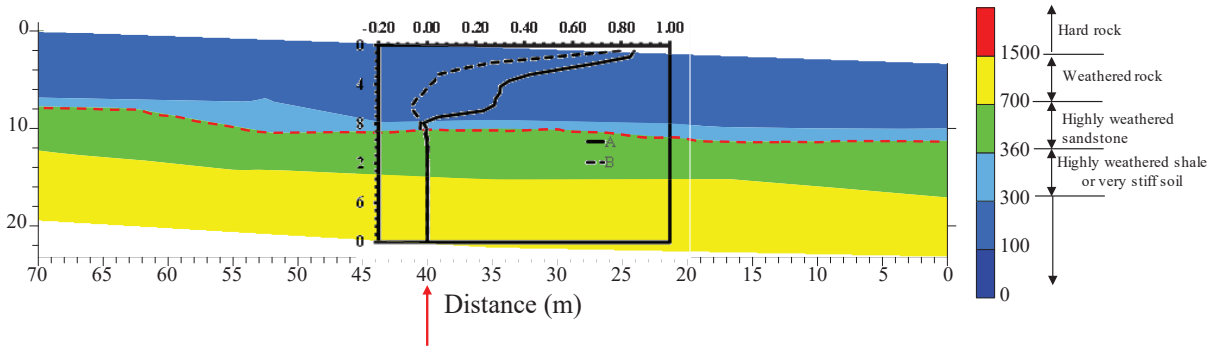

Figure 4.49- Pseudo 2D Vs cross-section from MASW using Love type surface waves for the Borehole survey line along with the displacements recorded by inclinometer.

A summary of the interesting geophysical results that provide useful information regarding the slope movements in the Sand Gap site is provided in Figure 4.50. These include the HVSR peak frequency variation shown in graduated color within the slope areas (Figure 4.50a), the contour map of the bedrock depth determined from the HVSR within the slope areas along with the cracks observed in the pavement (Figure 4.50b), the pseudo 2D Vs profile from the MASW_slope survey line (Figure 4.50c), and the ERT profile for the slope survey line (Figure 4.50d).

Overall, based on the variations of the bedrock depth in Figure 4.50, surface elevations (see Figure 4.38), and locations of the relatively steep soil/bedrock interfaces across the site (see Figure 4.37), the potential slip surfaces of the Sand Gap site are located on the Southwest of the site, where steeply bedrock and bedrock depression are found near the ground surface below the highway pavement. The slip surfaces are likely moving from Northeast to Southwest and from East to West with a start point on the pavement. These movements are confirmed by the inclinometer data (see Figure 4.49) and to some extent by several longitudinal cracks observed in the pavement. The bedrock depression at the bottom of the slope (see Figure 4.50c and d) is likely trapping the water at this location. This is confirmed by the ERT profile as it shows a very low resistive zone with resistivity close to the resistivity of water located exactly above the bedrock depression. The trapping water can trigger the slope movement through different mechanisms such as an increase in slip surface total weight due to the increase in soils degree of saturation, dissolution of mineral cements that holds the soil particles together, decrease in soil shear strength due to the reduction in grain-to-grain contacts, and friction reduction between soil particles and bedrock at soil/bedrock interfaces. Any of these mechanisms could cause slope failure during or shortly after a heavy rainfall event, particularly when this is combined with the surcharge of the heavy vehicles passing through the highway.

The exact geometries of the slip surfaces with the lowest factor of safety across the Sand Gap areas are further investigated using 2D numerical models, as presented in the following section.

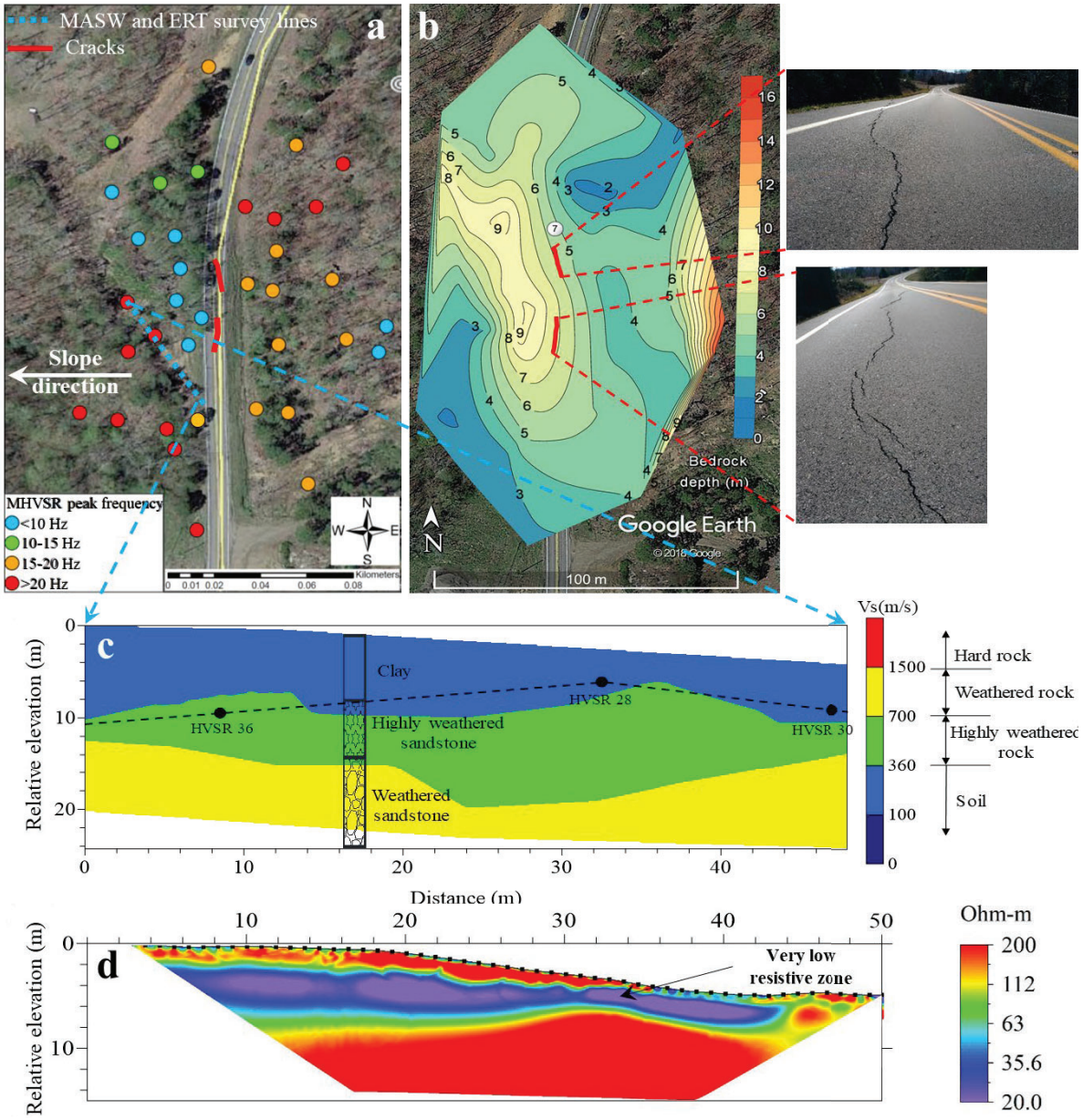

Figure 4.50- A summary of the interesting geophysical results for slope stability investigation for the Sand Gap site. a) HVSR peak frequency variation, b) Contour map of bedrock depth from the HVSR with cracks observed in the pavement, c) pseudo 2D Vs profile from the MASW_slope survey line, and d) ERT profile for the slope survey line (from Rahimi et al. 2021).

4.1.16 Numerical slope stability

4.1.16.1 Evaluation of slope stability software

Slope stability software is typically used to find the minimum factor of safety against a possible failure. Numerous methods have been developed for calculating the factor of safety in slope stability problems, with the most common of these being: limit equilibrium, numerical

analysis, artificial neural networks, and limit analysis (Pourkhosravani and Kalantari, 2011). To begin this portion of the project, several types of slope stability modeling software were evaluated. In addition to being reliable and accurate, it was also important that the software be user-friendly and cost-effective. Table 4-2 displays several of the available slope stability software packages and some of their corresponding features, as well as a summary of the licensing structure and the user capabilities. It is noted that all of the software programs included in Table 4-2 follow the limit equilibrium analysis method, which is the most common method used and it is typically the most straightforward.

Table 4-2- Comparison of Slope Stability Software.

Program	2D or 3D	Methods	Features	User Friendly Elements	Graphical Interface	Multiple person capability	Licensing Structure
Slide by Roc Science	2D	Limit Equilibrium (Fellenius, Bishop Simplified, Janbu Simplified, Janbu Collected, Spencer, Corps of Engineers #1 and #2, Lowe-Karafiath, and Morgenstern-Price)	Groundwater seepage analysis, probabilistic analysis, multi-scenario modeling, and support design.	CADD based, Click with mouse, Enter coordinates, Includes very detailed online tutorials, can import DXF files, or import photos and trace them to define model	Yes	Yes (Flexible Perpetual)	One time payment of $3995.00 and option of $600 yearly maintenance fee
SVSLOPE by Soilvision	Both	Limit Equilibrium (14 different analysis methods including classic method of slices such as Bishop, Janbu, Spencer, Morgenstern-price, GLE, and others)	Advanced stochastic analysis such as Monte Carlo, Latin Hypercube, and the Alternative Point Estimation Method (APEM). Allows the user to determine normal distributions of the factor of safety as well as the probability of failure.	Extensive tutorial manual to help lead the user through a number of different options to help educate the modeler on the steps to follow. The most important thing is that the modeler brings engineering judgement via the data input and choices for constitutive models, soils properties and appropriate calculation methods to name a few.	Yes	Yes	One time payment of $13,490.50 (for 3D) or $7192.50 (for 2D)
GEO5 Slope Stability by Fine	2D	Limit Equilibrium (Bishop, Fellenius/Peterson, Spencer, Morgenstern-Price, Sara, Janbu, Shahunyanc, ITFM)	Built-in database of soils and rocks, fast and reliable optimization of circular and polygonal slip surfaces, presence of water modeled through ground water table using pore pressure isoline, handles foliage on soils.	Commands are provided in a logical sequence, easy data entry, quick data entry, reports are easy and customizable, data exchange is easy, standards are programmed in, metric and US units are programmed in.	Yes	Yes	One time payment of $1,070.00

The only software that utilized limit equilibrium methods, more specifically the classic slice methods, were considered for this research project because it considers many different failure surfaces and has been proven to be reliable (Leshchinsky, 2015). For this method, the factor of safety is found using applied stress and mobilized strength. Slide by Roc Science software was used for the analysis presented in this report due to its availability at the university and the features and license scheme.

The slope stability analysis was broken into two models in order to assess the usefulness of the added geophysical data. Model I consisted of creating the simplest model (and most common in geotechnical practice) in which only the information available from the boring logs is used. Therefore, the material properties and soil profile (i.e. layering) were found using the boring logs, and elevations were gathered from Google Earth or DEM model. Additionally, the water table was extracted from the boring log information and assumed to be horizontal. In Model II, information from the geophysical results was added into the previous slope stability model from Phase I and then the results are compared to see how the addition of the geophysical results can change the slope stability analysis.

4.1.16.2 Model I: Using limited boring log information

For the Sand Gap site, the boring logs provided standard penetration test (SPT) blow counts, which were used to find the undrained shear strength and the unit weight for each soil layer. Slope stability models were analyzed considering two cross-sections, as shown in Figure 4.51. This includes a perpendicular cross-section (hereafter called Perpendicular) through the main longitudinal crack in the pavement that includes BH 5 and a second cross-section along the site steepest slope (hereafter called High Low) that passes between BH 3 and BH 4, as shown in Figure 4.51. For each of the slope stability models, the subsurface layers were based solely on the available boring logs and engineering judgment for areas between the boring logs. The water table was extracted from a single boring log and assumed to be horizontal in the model (Lebow, 2019). The required soil strength parameters were estimated using the SPT blow counts and the SPT soil strength parameter correlations proposed in Race and Coffman (2013). Other SPT soil strength parameter correlations were also used for the comparison, but the values obtained were deemed unrealistically high. Therefore, only the correlations proposed in Race and Coffman (2013) were used to estimate soil strength parameters.

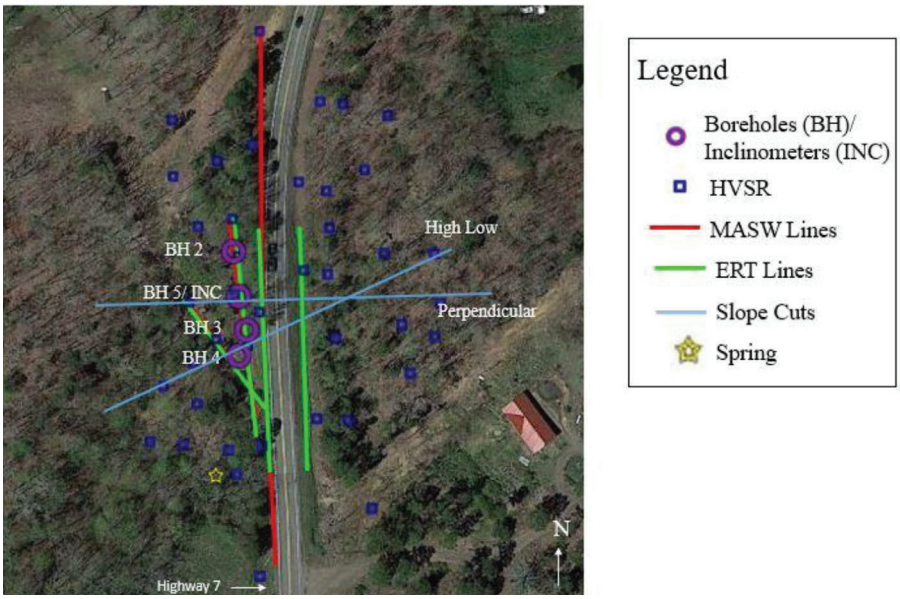

Figure 4.51- Cross-sections used for the slope models (from Lebow, 2019).

Presented in Figure 4.52a and b are the lowest factor of safety and corresponding slip surface for the slope using Janbu simplified method for the Perpendicular and the High Low cross-sections, respectively. Both non-circular and circular slip surfaces were used for the slope stability analysis. From Figure 4.52, the lowest factor of safety for both cross-sections are greater than 1.0 (2.64 for the Perpendicular and 1.15 for the High Low cross-section). Additionally, for the High Low cross-section, the lower portion of the slip surface is located on the Eastside of Highway 7 (upslope of the roadway section). However, based on the evidence at the site, the slope has shown to be unstable, and cracking through the roadway points to the slip surface extending into or beyond the roadway section. It is likely that the horizontal layers, which are assumed due to the lack of information regarding the subsurface layering, are resulting in these unrealistic conditions in the model.

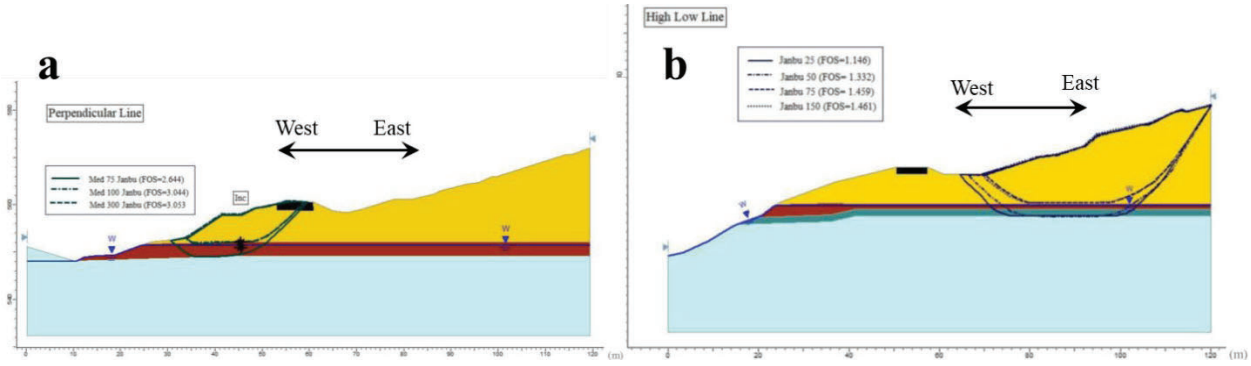

Figure 4.52- Slope stability model I using limited boring log information. a) perpendicular cross-section and b) High Low cross-section (modified from Lebow, 2019).

4.1.16.3 Model II: with addition of geophysical results

In Model II, the information from both boring logs and geophysical measurements were used to generate a more detailed image of the subsurface layering for the slope model. Additionally, a distributed load of 108 kPa was included in the slope model to consider the effects of traffic loads. This load was determined considering the worst-case scenario of the two loaded semi-trucks driving through at the same time.

Shown in Figure 4.53a and b are the lowest factor of safety and corresponding slip surface for the slope using Janbu simplified method for the Perpendicular and High Low cross-sections, respectively. Comparing the results before (Figure 4.52) and after (Figure 4.53) the addition of the geophysical results into the slope model, the lowest factor of safety decreases drastically for Model II with the addition of the geophysical results. For Model II, the lowest factor of safety for both Perpendicular and High Low cross-sections is lower than 1, indicating the need for slope remediation for this site. Additionally, for the High Low cross-section, while in Model I the slides were occurring Eastside of the road, in Model II the slides were occurring beneath and just to the Westside of the road. Therefore, the accuracy of the slope stability analysis has significantly improved with the addition of the geophysical results into the slope analysis in Model II, as the results match quite well with the inclinometer observations and the pavement cracking observed in the field. More discussions regarding the numerical slope stability analysis for the Sand Gap site are provided in Lebow, 2019.

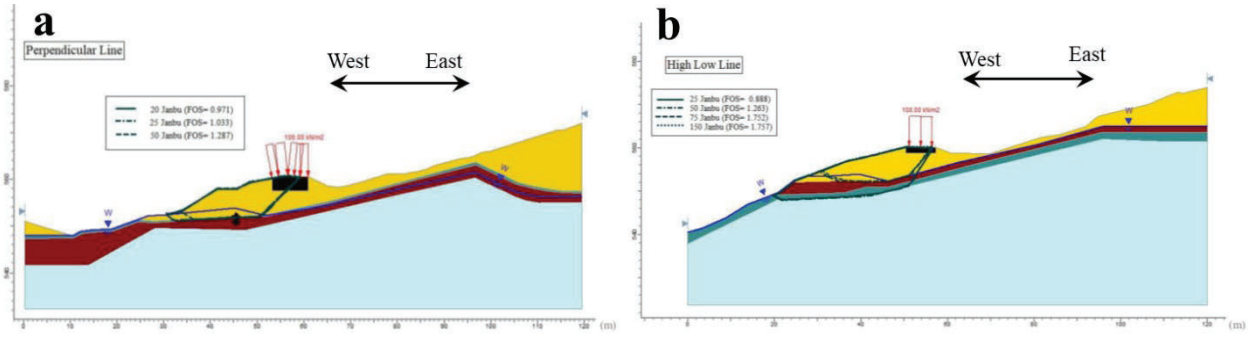

Figure 4.53- Slope stability model II with addition of geophysical results. a) perpendicular cross-section and b) High Low cross-section (modified from Lebow, 2019).

Conclusion from Phase I

Different geophysical methods, including MASW using both Rayleigh and Love type surface waves, P-wave refraction, HVSR, CCR, ERT, GPR, and EM31 were conducted at two different sites, aimed at identifying the best geophysical method(s) for detecting bedrock location and potential slip surface(s). Based on the results of the geophysical testing at the

Hardy and Sand Gap sites, the geophysical methods employed in this report are ranked from 1 to 8, with lower values indicating better performance and the results are summarized in Table 4-3. Different aspects are considered in this table, including accuracy, field testing and data processing rapidness, ambiguity in data processing and data interpretation, maximum depth of exploration, and correlations with other geotechnical parameters.

Table 4-3- Summary of geophysical testing effectiveness from various aspects

Factor / Method	Accuracy	Field test rapidness	Data processing rapidness	Data processing ambiguity	Data interpretation ambiguity	correlated with other geotechnical parameters	Maximum penetration depth
MASW_Love	1	6	6	5	2	1	3
MASW_Rayleigh	3	5	6	5	2	1	2
Refraction	4	5	5	7	3	2	5
HVSR	2	4	2	2	1	3	1
CCR	6	3	4	4	5	4	6
ERT	5	8	4	3	4	4	4
GPR	7	2	3	6	7	-	7
EM31	8	1	1	1	6	-	8

In order to get an idea of how fast the field measurements and data processing are for each geophysical method, a rough estimation of the time required for field measurements and data processing of a 1000 m long survey line are provided in Figure 4.54 and Figure 4.55. The following assumptions were made to estimate the required time of the field measurements and data processing:

- MASW testing using 24 geophones with 2 m intervals. The minimum and maximum time for the MASW field testing in Figure 4.54 is related to the MASW testing with and without using a landstreamer, respectively. The maximum time of the MASW testing using Love type surface waves is slightly more than that of Rayleigh because, for the Love type testing, geophones should be oriented cross line to the setup array orientation.
- P-wave refraction testing using 24 geophones with 2 m intervals.
- HVSR measurements at 25 m intervals using 8 sensors simultaneously.
- The required time is determined assuming that users are familiar with field testing and data processing.

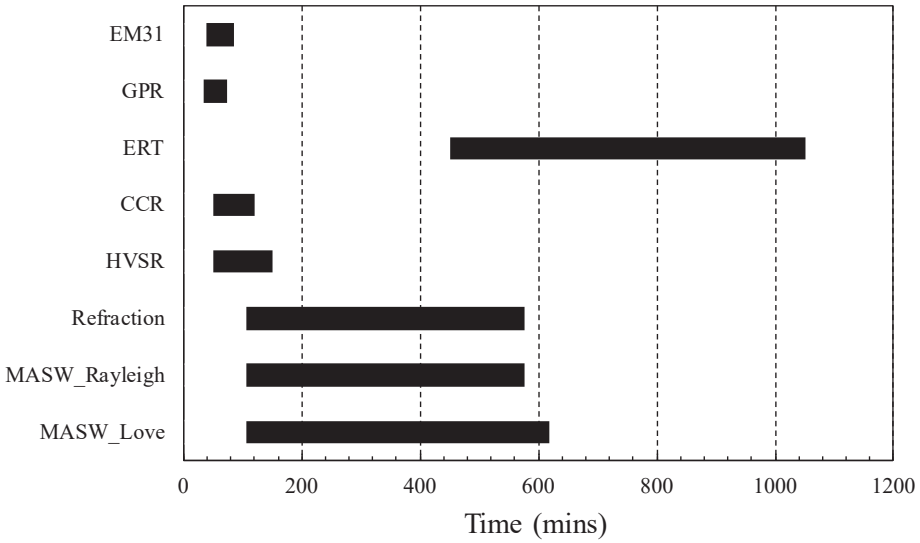

Figure 4.54- Comparison of geophysical field testing rapidness.

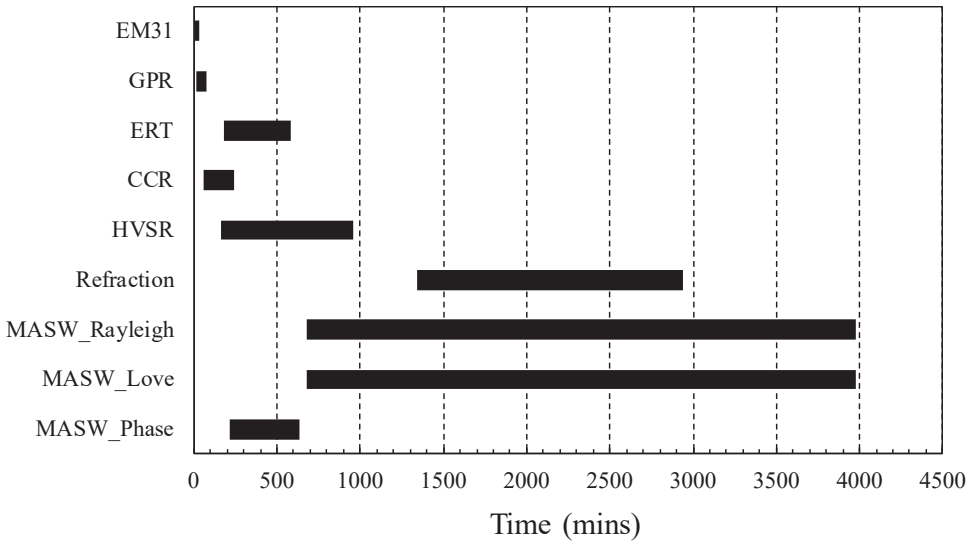

Figure 4.55- Comparison of geophysical data processing rapidness.

Based on the results from Table 4-3 and experience performing geophysical testing at the Hardy and Sand Gap sites, the EM31, GPR, and CCR could not provide accurate information regarding bedrock locations and potential slip surfaces. The reasons for the poor performance of each of these methods are discussed below.

For the EM31, the very shallow depth of penetration (< 5 m) is the main limitation of this method which makes it unsuitable for subsurface mapping and bedrock detection. Also, it should be mentioned that no appropriate representative ranges of the electrical conductivity from the EM31 which are associated with different geomaterials are available in the literature. This means that the uncertainty regarding site characterization using EM31 is great.

GPR suffers from quick loss of resolution with depth. Based on the results of the GPR testing for the Hardy and Sand Gap sites, GPR is not valuable for subsurface investigation and bedrock mapping of sites where a soil layer with high attenuation (such as clay) exists near to the surface. Even a thin shallow clay layer can kill the GPR signal trace in such a way that no refracted/reflected waves can be generated. Additionally, GPR is one of the most ambiguous geophysical methods, especially for new users, in terms of data interpretation.

CCR surveys were not effective for bedrock mapping and slip surface detection, particularly for sites where bedrock was located at depths greater than 10 m. The ineffectiveness of the CCR is mainly related to the parameters affecting soil resistivity such as soil gradation and mineralogy, temperature, soil cavity, and particularly soil degree of saturation. While these parameters are important for CCR data interpretation, it is difficult to monitor them during CCR field tests, especially for a long survey line. In addition, the maximum exploration depth for the CCR technique is typically shallow (<10 m) and the resistivity values related to deeper layers are associated with great uncertainties due to data averaging effects.

The ERT method was found to be useful for detecting the water table and predicting water content of the soil, but it could not provide an accurate estimation of the bedrock locations. The method tended to smear the interface between the bedrock and soil, causing uncertainty in the estimated depth to the bedrock. The method also does not provide any estimate of rippability of the bedrock material. Moreover, this method is too slow in terms of field testing to be considered as a viable geophysical technique for bedrock mapping for larger areas. Overall, ERT method is found to be valuable for rain-induced slope stability investigations in order to determine the highly saturated zones within the slope areas.

P-wave refraction, although capable of providing accurate information regarding bedrock and ground water table locations, suffers from the quick loss of resolution with depth. Additionally, for sites where multiple shallow refraction sources are present or where refractor layers are quite variable, such as the Hardy site, the great ambiguities in selecting the first arrival times could lead to some misinterpretations regarding bedrock locations. However, the method can provide accurate bedrock depths and rippability information and is considered a good method for bedrock mapping surveys. Similar to the ERT method, the P-wave refraction is also useful for locating the highly saturated zones of the slopes for rain-inducted slope movements.

The most viable methods for both bedrock mapping and slope stability investigations in these studies were found to be HVSR and MASW (Rayleigh/Love surface wave methods). According to the results of geophysical testing at the Hardy and Sand Gap sites, HVSR was found to be viable for bedrock detection. HVSR can be considered as the simplest geophysical method for bedrock detection if a clear and reliable peak is available from the HVSR measurements. While most of the geophysical methods investigated in this project suffer from a quick loss of resolution with depth, the HVSR technique can be used for both shallow and deep bedrock units. The information from the HVSR measurements can also be used to estimate the fundamental frequency of a site. The HVSR results can also be used as supplemental information for joint inversion of the MASW testing to increase the reliability of the inversion process. The main limitations of the HVSR technique are: 1) additional information regarding average shear wave velocity of sediments above bedrock is required along with HVSR to determine the true depth to bedrock, 2) no information about the stiffness of subsurface materials (rippability or condition of the rock) can be obtained from the HVSR, 3) in cases where no clear peak exists in the HVSR measurement, no information regarding the bedrock location can be interpreted.

MASW was also determined to be a viable method for bedrock detection or locating potential slip surfaces for sites with shallow (approximately less than 30 m) and quite variable bedrock locations. Although MASW is not as rapid as other geophysical methods in terms of data processing, it yielded much higher accuracy (Figure 4.18 in Section 4.2.8) compared to the other geophysical methods. MASW using Love type surface waves has shown the best performance for sites with a shallow soil layer underlain by a half-space with a high impedance ratio between the layers. This could be the case for most of ARDOT sites which consist of a shallow soil layer followed by rock materials. The main limitation of Love waves testing is that it can typically provide high-resolution experimental dispersion data points only for some particular stratigraphy conditions.

MASW using Rayleigh type surface waves can fill in the gaps for sites where subsurface conditions are not ideal for Love wave testing. Given that field testing configurations, data processing, and data interpretation for MASW using Love and Rayleigh waves are almost the same, switching from Love to Rayleigh or vice versa can be done with minimum effort. Therefore, the combined use of MASW using Love and Rayleigh waves can cover a variety of subsurface conditions and so can be used for any subsurface layering. In addition to the accuracy of the MASW for site characterization and bedrock detection, shear

wave velocity has been correlated with many other geotechnical properties of soils (Dikmen, 2009; Maheswari et al. 2010; Fabbrocino et al. 2015; Rahimi et al. 2019). For example, the shear wave velocities determined from MASW can be utilized for further processing to estimate the small-strain shear modulus of soil layers using the $G=\rho Vs^2$ equation. Furthermore, if any information is available regarding Poisson's ratio, it can be used to predict Young's modulus of soil layers using the following equation:

$$E=G/2(1+\nu) \quad (7)$$

Where ν is soil Poisson's ratio, G is soil shear modulus at small-strain, and E is the soil Young's modulus. The main limitations of MASW testing are 1) non-uniqueness of the solution in the inversion process, 2) longer data processing time comparing to other geophysical methods, 3) the maximum depth of exploration, and 4) the complexity of data processing. Overall, the viable geophysical techniques that can be used for bedrock mapping and slope stability studies are MASW, HVSR, P-wave refraction, and ERT. HVSR is a simple and fast geophysical method that can be used both for shallow and deep bedrock detection. This method is applicable for any site conditions such as steep slopes or sites densely covered with trees and bushes. If bedrock mapping is of primary interest, the HVSR method would be the most effective method. MASW can provide a continuous image of subsurface conditions. This image can be used to obtain information regarding soil type, soil stiffness, bedrock location, and rippability of bedrock materials. Therefore, the combined use of HVSR and MASW can be considered as a valuable tool for mapping subsurface conditions for transportation applications. Additionally, if information regarding the degree of saturation of soils or water table is important (e.g. for rain-induced slope stability sites), ERT and P-wave refraction are recommended to be used. In addition, P-wave refraction is often utilized for bedrock mapping and is a viable method for such applications.

5 Results and conclusions from Phase II

Introduction

This section provides a summary of the results of the selected geophysical methods from Phase I (MASW, HVSR, ERT, and P-wave refraction) for three ongoing ARDOT transportation projects. These projects include the slope stability slide along I40 near Ozark, a proposed highway alignment for ARDOT Job #R60140 near Hot Springs, and ARDOT Job #061331 Southridge Extension in Little Rock. The objective of Phase II of the project is to further investigate the accuracy and advantages of the selected geophysical methods for bedrock mapping and slope stability studies. It should be noted that only a summary of the results for the Ozark and Hot Springs sites are provided in this section, and the full report for each site is provided in the appendices.

Slope stability slide along I40, near Ozark

The slope stability slide for the Ozark site is located just North-West of Ozark, Arkansas, along I40 westbound, as shown in Figure 1.5. An orthomosaic image of the slope area along with the areas where long cracks were observed during the field inspection in 2019 are shown in Figure 1.5. According to the geology backgrounds and the pre-existing borings, the entire soil profile of this site consists of a shale rock formation, overlain by a stiff/very stiff clay layer with gravel. Background information regarding the Ozark slide was provided in Section 1.3.2.1. As mentioned in Section 1.3.2.1, while a slope repair was performed for this slide in 2018, big cracks (see Figure 1.5b and c) were observed during a field inspection in 2019 approximately 1 year after the repair. This indicates that the slope continues to move even after the slope repair.

MASW, HVSR, ERT, and P-wave refraction were conducted along different survey lines parallel and perpendicular to the slope area. A summary of the geophysical testing results for the Ozark site is provided below with respect to the slope stability issues. More information regarding the geophysical field measurements and results are included in Appendix A of the report.

5.1.1 Detecting potential slip surface for the Ozark site using geophysical methods

Shown in Figure 5.1 a, b, c, and d are the geophysical testing locations and the variation of the peak HVSR frequencies shown with graduated colors, a contour map of the bedrock

depth from the HVSR measurements, a pseudo 2D Vs profile from the MASW conducted along the slope, and an ERT profile performed along the slope, respectively. Additionally, in this figure, the locations of the several springs that were observed during the field measurements and a boring log where the inclinometer readings were recorded are shown in Figure 5.1b with a blue star and black circle symbols, respectively. From Figure 5.1a, similar HVSR peak frequencies are observed for the majority of the HVSR stations within the slope areas. However, remarkable HVSR peak frequency variations are observed at the very bottom of the slope, as visible in Figure 5.1a. Using the peaks from the HVSR measurements and the $V_{s,avg}$ from the MASW, a contour map of the bedrock depth was created for the slope area, as shown in Figure 5.1b. Bedrock depth is estimated to be very shallow for this site ranging between 6-14 m across the slope areas. Examining depth to the bedrock in Figure 5.1 b, several depressions in the bedrock layer are observed at the very bottom of the slope, where the bedrock layer shallows drastically. These depressions in the bedrock layer are observed very near the four spring locations at the very bottom of the slope, as shown in Figure 5.1b. This indicates that the depressions (bowl-shape features) in the bedrock layer are likely trapping the water at these locations during heavy rainfall events. Therefore, depth to the groundwater table decreases drastically at these locations, and so, the trapped water appears at the ground surface as springs (Rahimi et al. 2021).

To verify the existence of the depressions in the bedrock layer, co-located MASW and ERT measurements were performed along a survey line parallel to the slope (see Figure 5.1), and the results are presented in Figure 5.1c and d, respectively. Examining the variation of the bedrock depth from the MASW profile, a similar feature (depression) is observed in the bedrock layer at the very bottom of the slope, verifying the bedrock depressions identified from the HVSR measurements. Moreover, from the ERT profile in Figure 5.1d, several low resistive areas with resistivity values matching the resistivity of water are observed exactly above the bedrock depression at the very bottom of the slope. This confirms the fact that the bedrock depression is trapping rainfall water at this location, creating to fully saturated and soft zone at the very bottom of the slope (Rahimi et al. 2021).

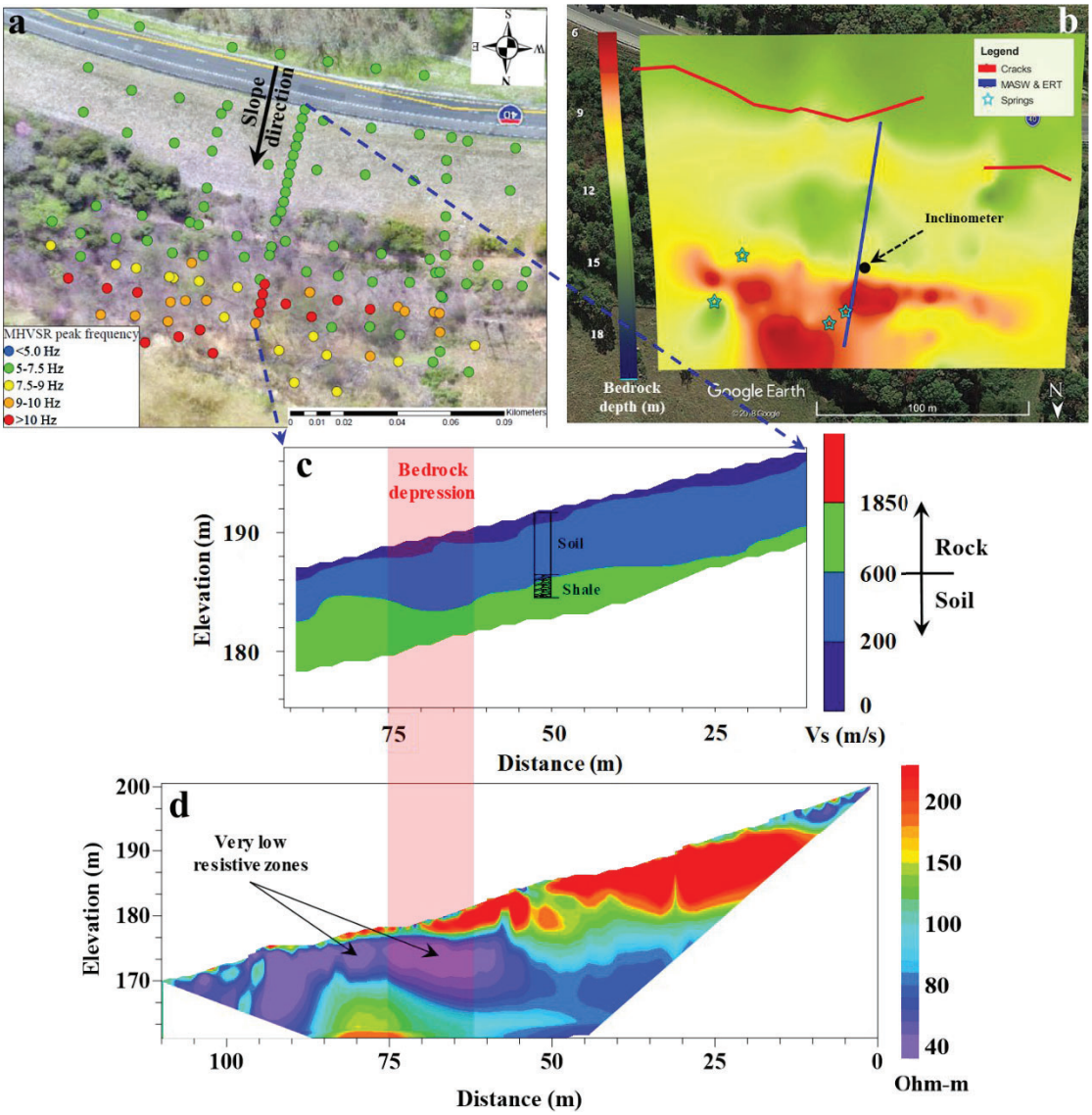

Figure 5.1- Geophysical testing results for the Ozark site. a) Locations of geophysical testing along with the cracks observed, b) Contour map of bedrock depth from MGM, c) Pseudo 2D Vs profile from MASW, d) ERT profile.

To create a full 3D map of the bedrock elevation across the slope areas, bedrock depths identified from the HVSR measurements are combined with the surface elevation determined from total station and GPS readings and LiDAR data and the results are presented in Figure 5.2. Presented in this figure are the North-South, West-East, and East-West views of the 3D map of the bedrock elevation within the slope areas. From Figure 5.2, bedrock elevation decreases sharply at the very bottom of the slope, creating several depressions in the bedrock layer. These depressions are clearly visible in the West-East, and East-West views of the 3D map of the bedrock elevation, as shown in Figure 5.2b, and c. For slopes with a very shallow bedrock topography, depression in the bedrock layer within the slope area is a key factor

contributing to the slope movements, particularly during or shortly after a heavy rainfall event, as discussed in Section 4.3.1.1 and Section 4.3.7.

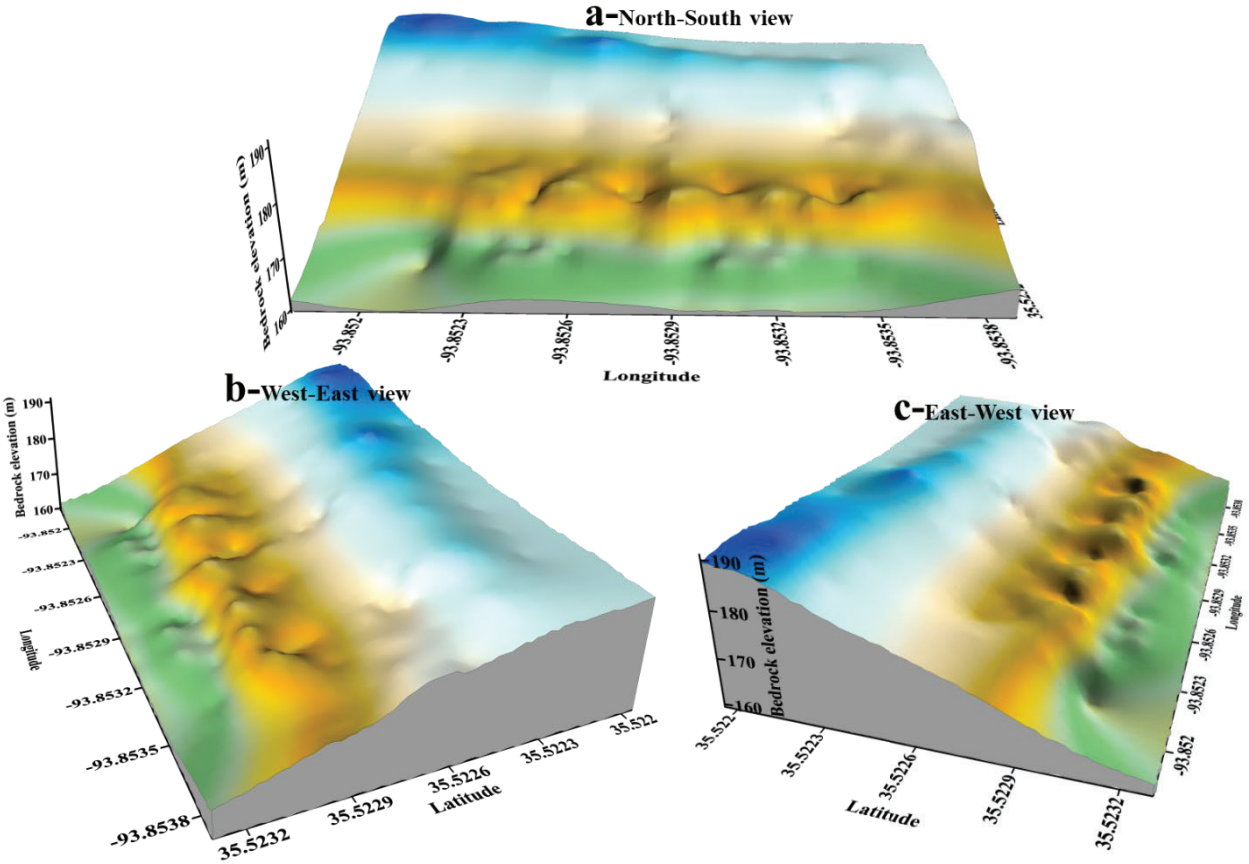

Figure 5.2- Full 3D map of bedrock elevation across the Ozark slope site.

Overall, considering the very shallow bedrock layer for the Ozark slide and the bedrock depressions observed at the very bottom of the slope, the most critical slip surfaces for this site are expected to pass along the soil/bedrock interface. This assumption is further validated by collecting data from an inclinometer located at the bottom of the slope, as shown in Figure 5.1b. Presented in Figure 5.3a and b are the co-located Vs profile from the MASW and the cumulative displacements recorded from the inclinometer in the North-South direction, respectively. As shown in Figure 5.3b, no displacement is observed for the top 10 m depth of the profile. However, a large displacement is recorded for depths ranging between 10-12 m. Also, no displacement is observed for depths greater than 12 m as displayed in Figure 5.3b. Comparing the zone of displacement from the inclinometer with the Vs profile in Figure 5.3a, this zone corresponds quite well with the depth where a big increase (sharp impedance contrast) in the Vs of the site is observed. This big jump in the Vs profile is related to the bedrock layer. This means that the zone of displacement corresponds to the soil/bedrock interface as expected. Therefore, as predicted by the HVSR method, the most critical slip surface for the Ozark site,

which caused several cracks at the top portion of the slope, passes along the soil/bedrock interface, where several depressions are observed at the very bottom of the slope. More discussions regarding the reasons behind the slope movements for the Ozark sites are provided in Section 4.3.1.1 and Section 4.3.7, and Appendix A.

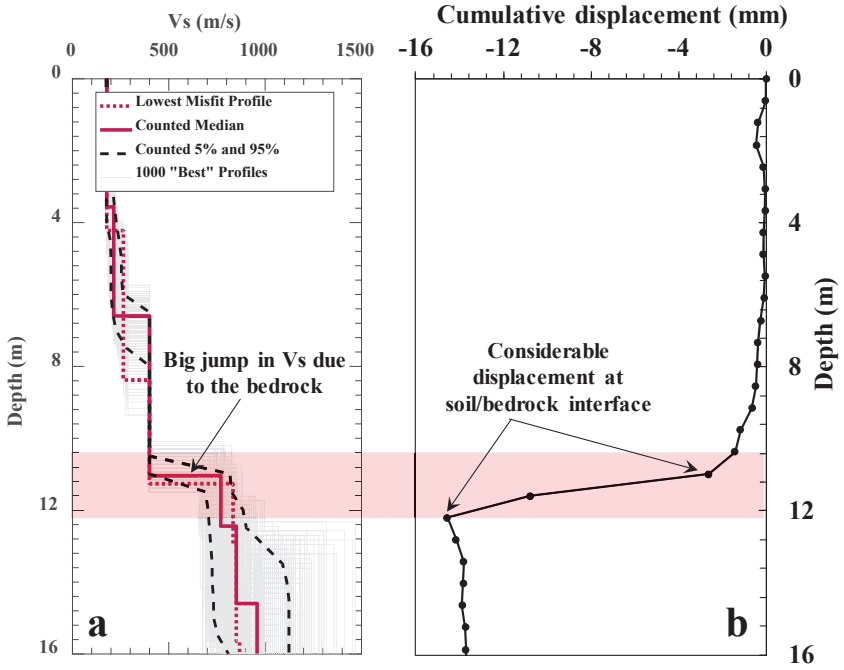

Figure 5.3- Comparison of the Vs profile from the MASW and displacements recorded using inclinometer. a) Vs profile, b) Cumulative displacement.

5.1.2 Numerical slope stability

Similar to the Sand Gap site, numerical slope stability models were analyzed for the Ozark site in two steps, including Model I using only the boring log information and Model II with the addition of the geophysical results to Model I. For Model I, the subsurface layers were based solely on the available boring logs. The required soil strength parameters were estimated using the SPT blow counts and the SPT soil strength parameter correlations proposed in Race and Coffman (2013). For Model II, the results from different geophysical methods were added to Model I. The anchors in the top section of the slope were also included in the slope stability models for both Models I and II. Here, only the results from one of the most critical slip surfaces are presented, and more discussions in this regard are provided in Lebow (2019).

Presented in Figure 5.4 a and b are the lowest factor of safety and corresponding slip surface for the slope using Janbu simplified method for Model I and Model II, respectively. Comparing the results for Model I and Model II, the lowest factor of safety has decreased a little bit for Model II (1.12 for Model I and 1.09 for Model II). Moreover, the location of the critical slip surface has slightly changed for Model II. Therefore, the addition of the

geophysical results in the slope model for this site has slightly changed the slope stability results. It should be mentioned that even if the same results are obtained for the slope stability models with and without the addition of the geophysical results, the geophysical results can significantly improve our understanding regarding the subsurface layering and can help in determining the causes of the slope movements for future remediation efforts.

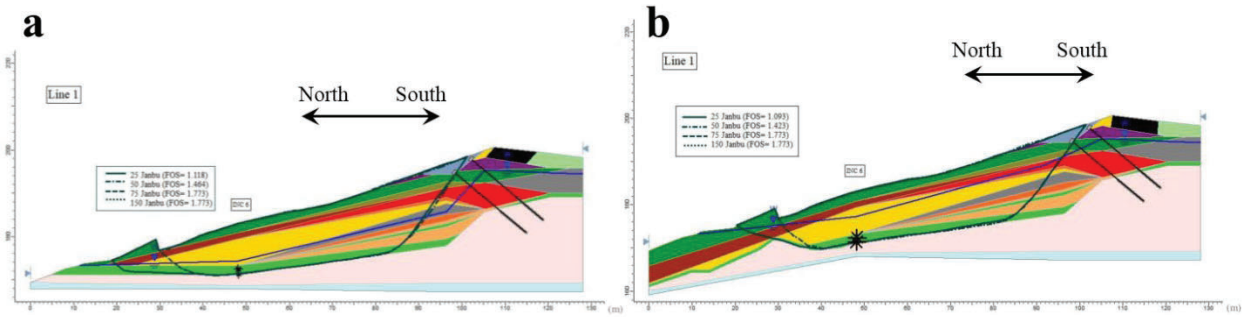

Figure 5.4- Slope stability models for the Ozark site. a) Model I using boring log information, and b) Model II with the addition of the geophysical results (Modified from Lebow, 2019).

Proposed highway alignment for ARDOT Job #R60140 near Hot Springs

The project site for ARDOT Job #R60140 is located in Garland County, just North-East of Hot Springs, Arkansas, as shown in Figure 5.5. Discussions regarding the site backgrounds and geological information were provided in Section 1.3.2.2 of the report.

Given that the proposed highway alignment of this project passes through mountainous regions with very shallow bedrock layers and so it involves a large volume of rock excavations, geophysical testing was performed with the goals of detecting bedrock depths and bedrock rippability along the proposed highway alignment. Geophysical field measurements for this project, which consist of MASW and HVSR methods, were performed along those sections of the proposed highway alignment where significant excavations are required. Co-located MASW and HVSR field measurements were conducted along different trails and roads, as presented in Figure 5.5, depending on the access in the areas of interest. Moreover, HVSR field measurements were also conducted in a tight grid pattern on steep slopes (see Figure 5.5b) and areas covered with trees and bushes, where MASW was difficult to use to map the bedrock layers. More information regarding the field measurements for the Hot Springs site are provided in Appendix B.

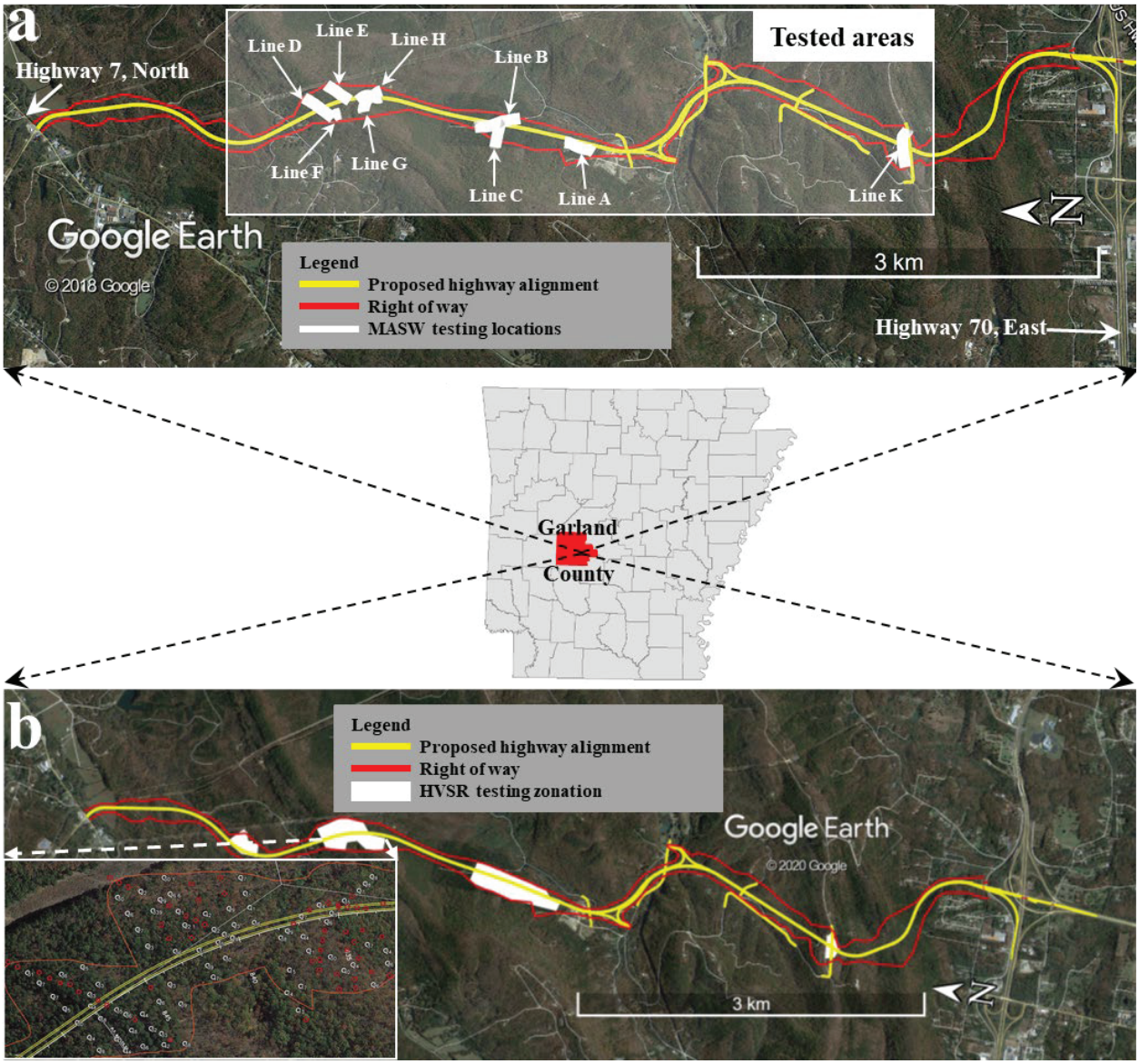

Figure 5.5- Geophysical testing locations for ARDOT Job #R6014 in Hot Springs, AR.

5.1.3 Detecting bedrock location and bedrock rippability using MASW

For each MASW array setup, a 1D Vs profile was generated, and then the 1D Vs profiles collected along a survey line were combined to create a pseudo 2D Vs profile as shown in Figure 5.6 as an example. The representative Vs ranges associated with different rippability groups (rippable, marginal rippable, and non-rippable) were developed using the representative Vp ranges recommended in the Caterpillar Handbook on Ripping (2000) and the Poisson's ratios determined from the literature (Christensen, 1996; Gercek, 2007; Yasuhara and Elsworth, 2008) and field measurements. The equation below was used in this regard:

$$V_s = V_p \times \sqrt{\frac{1-2\upsilon}{2(1-\upsilon)}} \qquad 8$$

In this study, the chart provided for the D8R Caterpillar Dozer (Caterpillar Inc, 2000) was used to develop the representative Vs ranges related to the rippable, marginal rippable, and non-rippable rock groups. From Figure 5.6, the subsurface layering for this survey line is comprised of approximately 1-3 m of soil that matches well with the soil layering from the boring logs, a rippable rock layer that extends to a depth ranging between 7.5-10 m below the surface, underlain by a 4 m thick marginal rippable rock unit, followed by a non-rippable rock unit which is observed throughout the entire survey line. Similar pseudo 2D Vs profiles were generated for the areas of interest (11 MASW survey lines) along the proposed highway alignment. These pseudo 2D Vs profiles are provided in Appendix B of this report.

Pseudo 2D Vs profiles, such as the one presented in Figure 5.6, are very beneficial for highway projects that require significant rock excavations because they can be used to prevent construction delays by providing information about rock rippability in advance, locate the most cost-effective solution for new highway alignments, estimate an accurate bid for the proposed highway alignment.

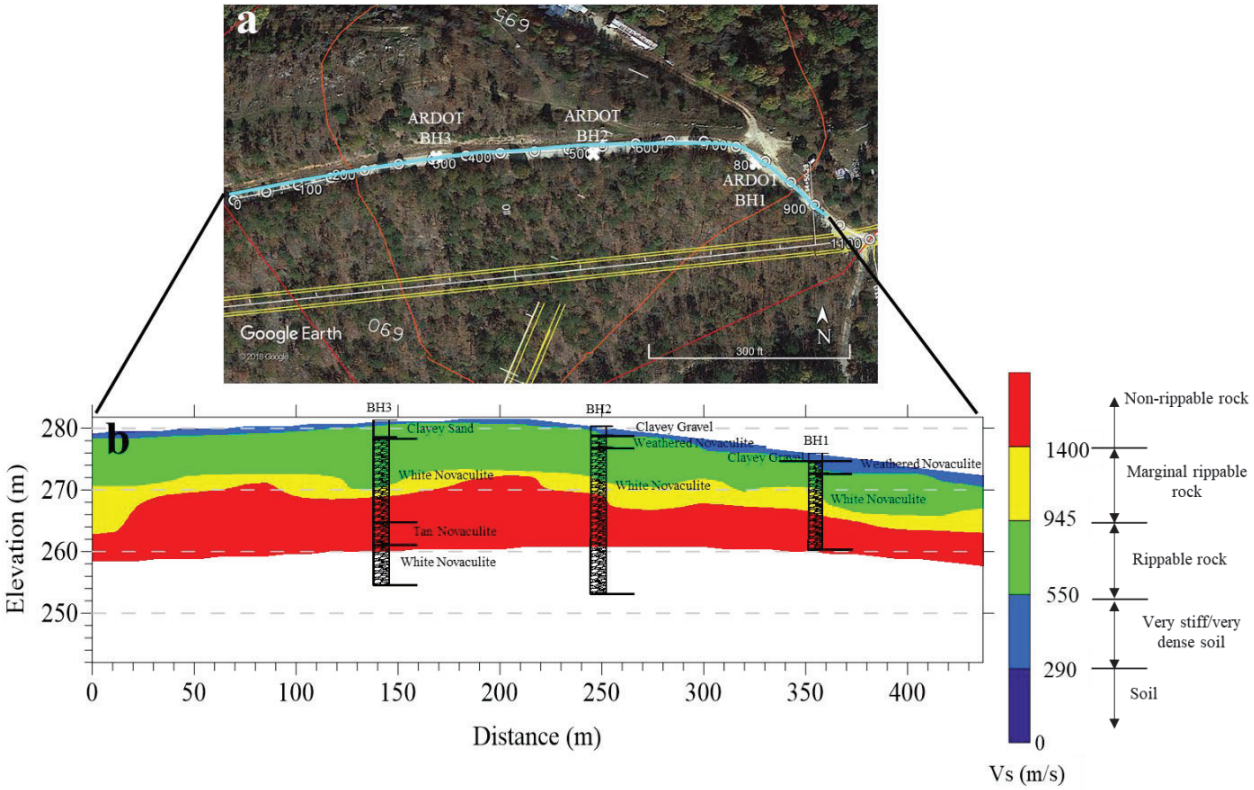

Figure 5.6- An example pseudo 2D Vs profile with information regarding bedrock depths and bedrock rippability. a) Google map view, b) pseudo 2D Vs profile from MASW.

5.1.4 Detecting bedrock location and bedrock rippability using HVSR

As mentioned previously, to cover all the sections of the proposed highway alignment that involve considerable rock excavations, HVSR measurements were collected along the areas where MASW was difficult to use (e.g. steep slopes and areas covered with trees and bush). Shown in Figure 5.7 is an example steep slope along the proposed highway alignment where a grid of the HVSR measurements was collected to map bedrock.

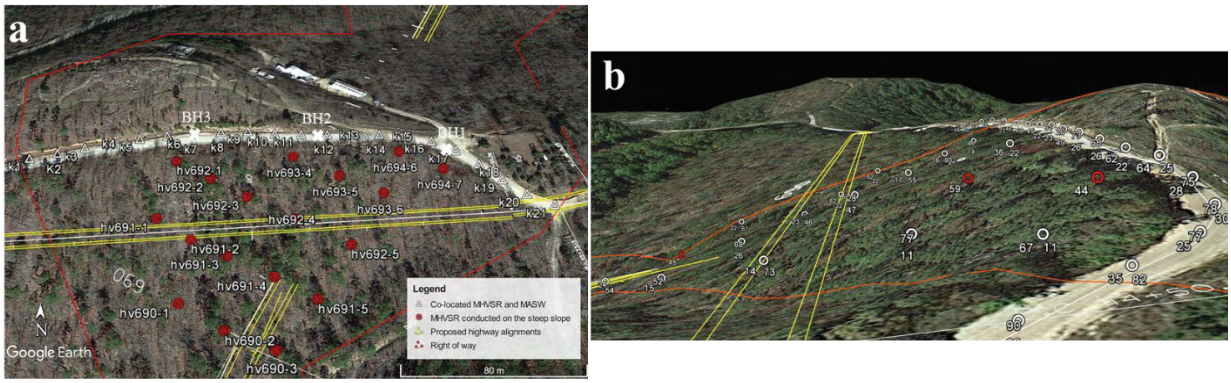

Figure 5.7- HVSR measurements within a steep slope to map bedrock along the proposed highway alignment. a) Google map plan view, b) Google map side view.

For each of the HVSR stations, the raw data was first processed individually to determine the reliable HVSR peak(s) that has a geologic origin. Additionally, the co-located MASW results were used to (1) calculate the average Vs of the sediments above the impedance contrast, (2) assess the accuracy of the HVSR results, and (3) detect the sharp impedance contrast associated with each HVSR peak.

Based on the results of the HVSR measurements for the Hot Springs site, three types of behavior were observed, including 1) HVSR with a single clear peak and MASW with a single impedance contrast in the Vs profile, (2) HVSR with two clear peaks and MASW with two impedance contrasts in the Vs profile, and (3) HVSR with three clear peaks and MASW with three impedance contrasts in the Vs profile. These behaviors are discussed in the following.

Case 1 includes HVSR measurements with one clear peak and co-located MASW measurements with one sharp impedance contrast in the Vs profile as shown in Figure 5.8a and b, respectively. In this figure, the light gray rectangles illustrate the frequency associated with the HVSR peak and the sharp impedance contrast in the Vs profile. From Figure 5.8a, the high-frequency HVSR peak (91 Hz) indicates the presence of a sharp impedance contrast (i.e. bedrock) very near the surface. This is confirmed by the Vs profile in Figure 5.8b in which only one sharp impedance contrast is observed in the Vs profile very near the surface.

Moreover, this confirms the fact that the peak from the HVSR has a stratigraphy origin (Rahimi et al. 2020).

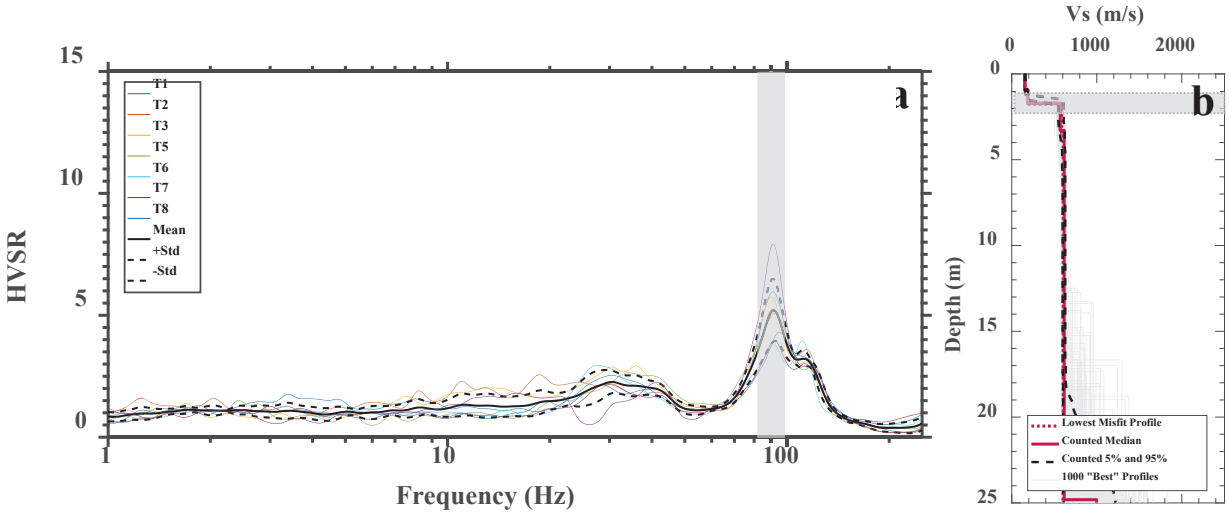

Figure 5.8- Case 1, co-locate HVSR and MASW with a single clear HVSR peak. a) HVSR result, b) 1D Vs profile from MASW (Rahimi et al. 2020).

Case 2 includes HVSR measurements with two clear peaks and co-located MASW measurements with two sharp impedance contrasts in the Vs profile, as shown in Figure 5.9a and b, respectively. Additionally, the information from a boring log that includes the Total Core Recovery (TCR) and Rock Quality Designation (RQD) are provided in Figure 5.9c to assess the reliability of the geophysical results. From Figure 5.9a, the HVSR plot exhibits a low (23 Hz) and a high (62 Hz) frequency peak, indicating the presence of two sharp impedance contrasts in the subsurface. Similarly, two sharp impedance contrasts are observed in the Vs profile in Figure 5.9b, verifying the results of the HVSR testing. Comparing the HVSR and MASW testing results with the boring log in Figure 5.9, the high-frequency peak and the first impedance contrast in the Vs profile (gray rectangles) correspond well with the medium dense sand/white Novaculite interface from the boring. Additionally, the low-frequency peak and the second impedance contrast in the Vs profile (light blue rectangles) correspond very well with the sharp increase in the RQD and TCR values from the boring. This indicates the reliability of both HVSR and MASW results for detecting bedrock locations and bedrock rippability (Rahimi et al. 2020).

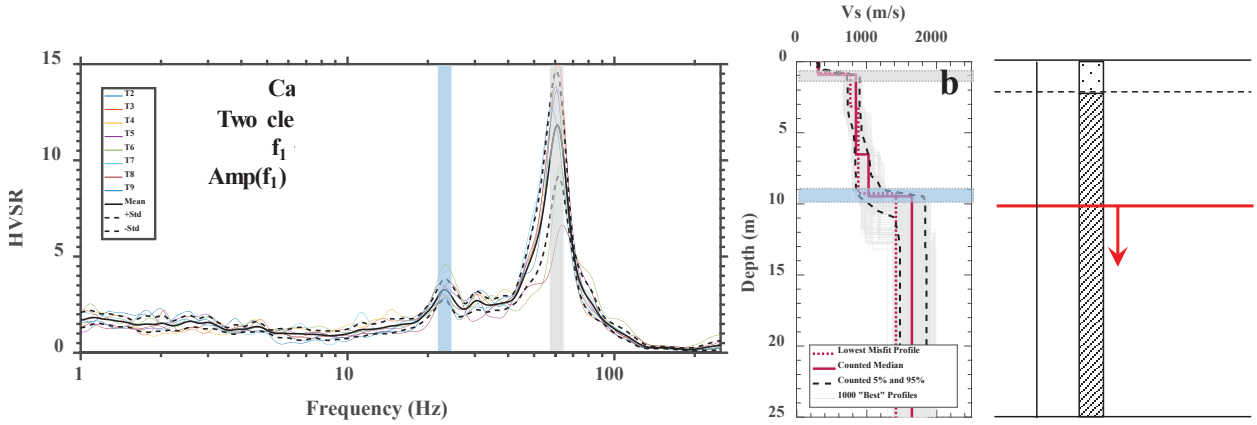

Figure 5.9- Case 2, co-locate HVSR, MASW, and boring log with two clear HVSR peaks. a) HVSR result, b) 1D Vs profile from MASW, c) boring log (Rahimi et al. 2020).

Case 3 involves HVSR measurements with three clear peaks and co-located MASW measurements with three sharp impedance contrasts in the Vs profile, as shown in Figure 5.10a and b, respectively. From Figure 5.10a, three clear and reliable HVSR peaks (f_1=21, f_2=30, and f_3=62 Hz) are observed. The peaks from the HVSR correspond well with the three sharp impedance contrasts in the Vs profile, as shown in Figure 5.10b. This indicates that all three peaks observed in the HVSR plot have a stratigraphy origin (Rahimi et al. 2020).

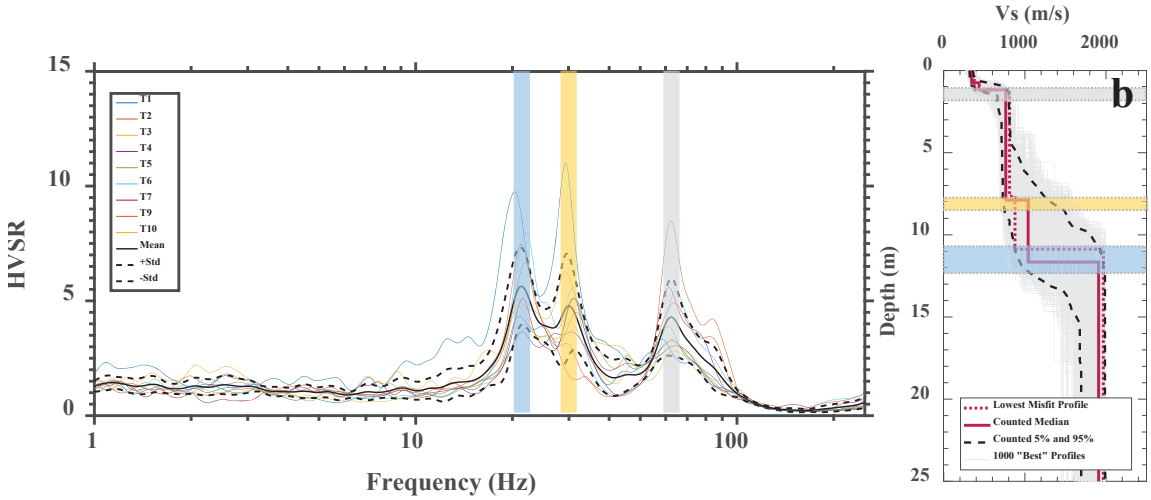

Figure 5.10- Case 3, co-locate HVSR and MASW with three clear HVSR peaks. a) HVSR result, b) 1D Vs profile from MASW (Rahimi et al. 2020).

The peaks from the HVSR measurement and the average shear wave velocity from the MASW testing are then used to estimate depth to bedrock at each HVSR station. Then, the results are combined to generate 2D and 3D maps of bedrock layers within the tested areas. Provided in Figure 5.11 and Figure 5.12 are examples of 2D and 3D maps of the subsurface layering, respectively, generated from the HVSR measurements.

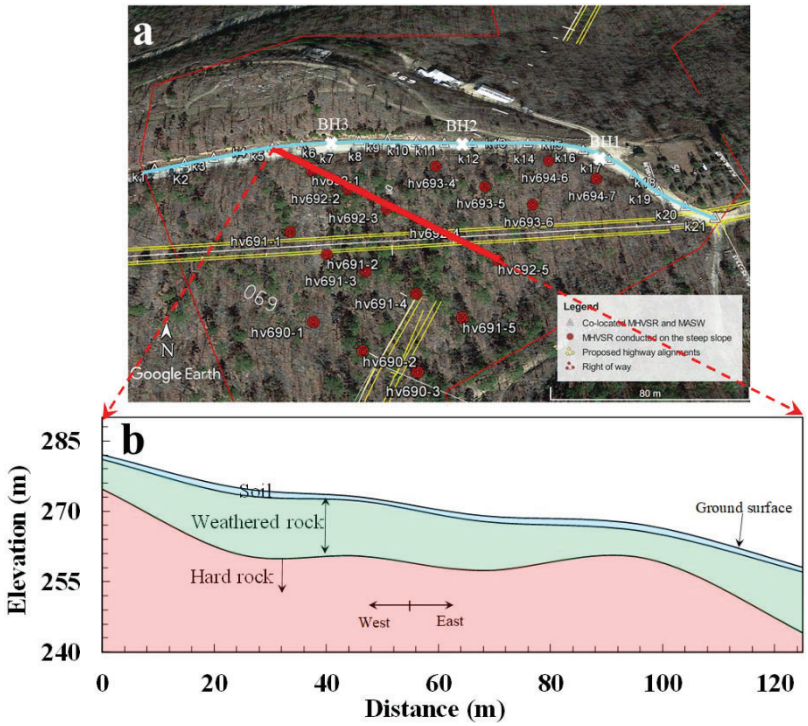

Figure 5.11- An example 2D map of subsurface layering generated from the HVSR. a) Google map view, b) 2D subsurface layering from HVSR (Rahimi et al. 2020).

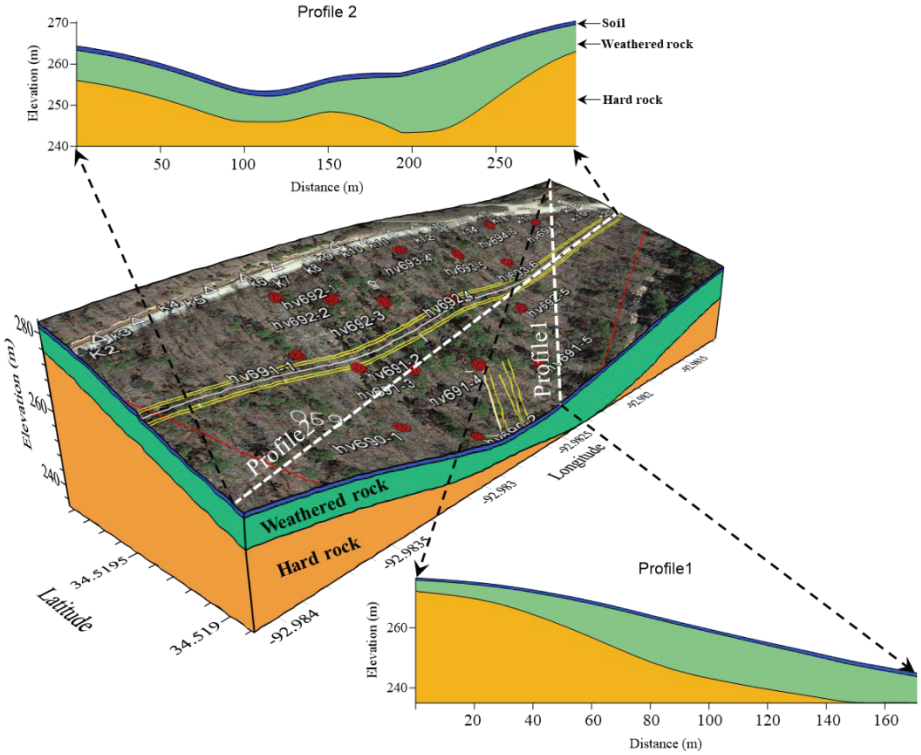

Figure 5.12- An example 3D model of the subsurface layering generated from the HVSR (Rahimi et al. 2020).

Overall, the combination of the MASW and HVSR measurements can be used as a rapid, cost-effective, and powerful tool to map subsurface conditions (particularly bedrock layer) for any kind of site conditions along a proposed highway alignment. The pseudo 2D Vs profile

from the MASW measurements and the 2D/3D model from the HVSR measurements are very beneficial for transportation projects that require significant rock excavations as they can help in: (1) locating the most suitable and cost-effective solutions for the highway alignment that requires the minimum amount of hard rock excavation, (2) estimating the excavation volume required for each of the solutions, and (3) aiding in preliminary deep foundation design for bridge construction (Rahimi et al. 2020).

5.1.5 Comparison of the rock rippability estimated from geophysical method with field observations of rock excavation

In this section, the rock rippability estimated from the geophysical measurements is compared to the field observations of rock excavations through pictures taken after the rock excavations were completed. Here, only a few example comparisons are provided. Other comparisons are provided in Appendix B.

Presented in Figure 5.13 a, b, c, and d are the Goole Earth images of testing locations for Line B and C, pseudo 2D Vs profile with rock rippability estimates for Line B, pseudo 2D Vs profile with rock rippability estimates for Line C, and the final rock cut for Station 802+50, respectively. The final rock cut shown in Figure 5.13d is located at the end of Line B and in the middle of Line C at Station 802+50. Based on the rock rippability estimates for these sections at Line B and Line C, the subsurface materials at this location include a very thin very stiff soil layer (blue), a thin rippable rock layer (green), followed by a marginal rippable rock layer (yellow) and a non-rippable rock layer (red). These layers are overlaid in the rock cut picture in Figure 5.13d. From Figure 5.13d, it is clear that the rock rippability estimates from geophysical measurements correspond well with the field observation. It is worth mentioning that based on the personal communication with the contractor (McGeorge Contracting), for Line C, for Stations 798+00 to 804+00, ripping/rock excavation was attempted but observed to be very difficult in the near-surface. Therefore, for this section of Line C between Stations 798+00 to 804+00, ripping was abandoned, and drilling and blasting were used to complete the excavation. However, based on the information from the contractor, for Stations after Station 804+00, ripping became much easier (see Figure 5.14 and Figure 5.15). This information agrees quite well with the rock rippability estimate for Line C in Figure 5.13c, where the non-rippable rock layer is observed to be near the surface from the start of the survey line (Station 801+50) to Station 803+00, and then the non-rippable rock layer is observed at deeper depths between Station 803+00 to 804+00. Additionally, for Station after Station 804+00, no non-rippable rock layer is observed within the maximum depth to investigation for this survey line.

It should be noted that the geophysical surveys were conducted away from the highway alignment in some locations as shown in Figure 5.13a. Therefore, there is some ambiguity in comparing the geophysical results to the rock cut face.

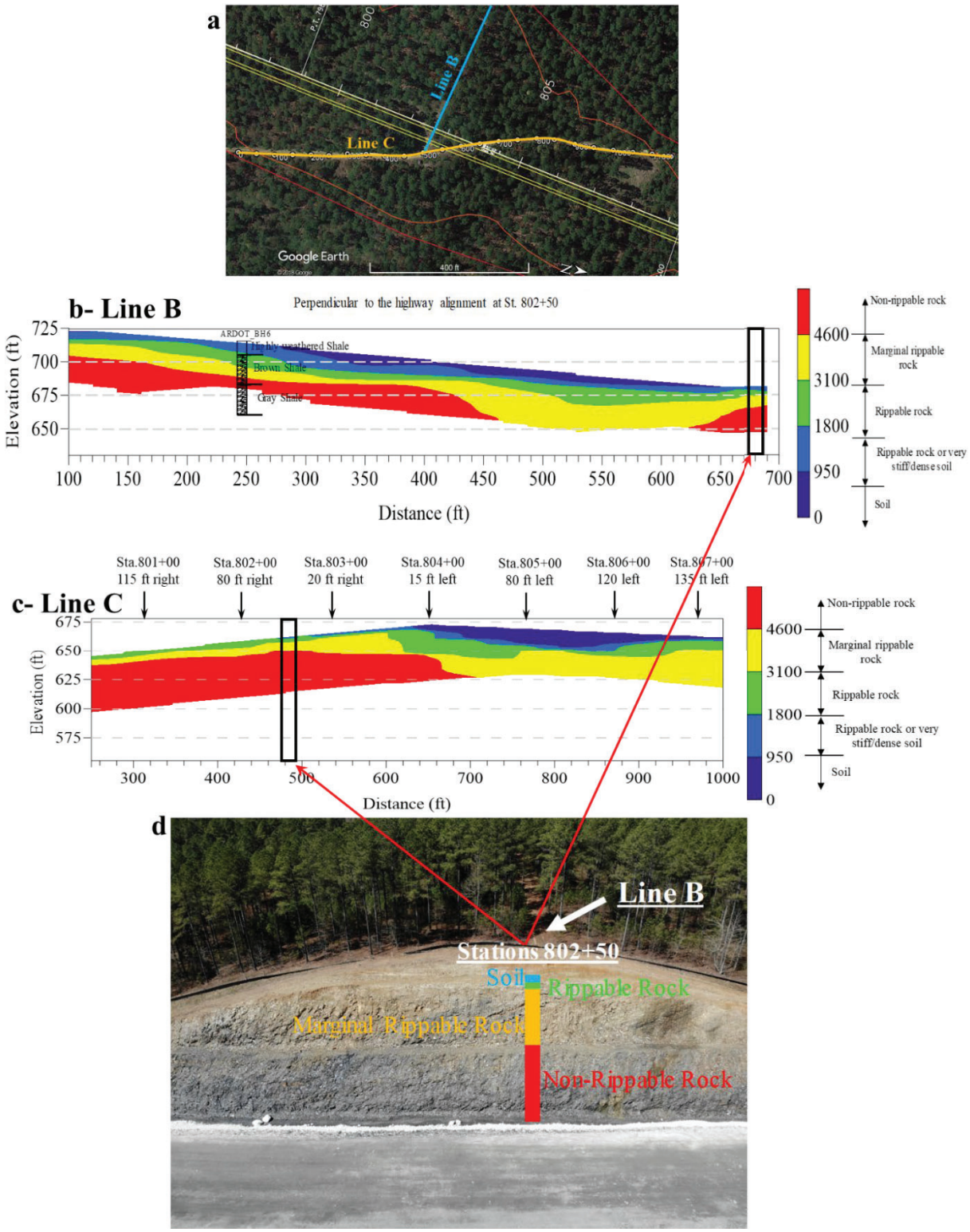

Figure 5.13- Comparison of the rock rippability estimate from geophysical measurements with the field observation for Line B and Line C. a) Google Earth image, b) pseudo 2D Vs profile of Line B, c) pseudo 2D Vs profile of Line C, d) final rock cut at Station 802+50.

Figure 5.14- Field observation for rock cut for Line C at Station 804+00.

Figure 5.15- Field observation for rock cut for Line C at Station 806+00.

Shown in Figure 5.16a and b are the pseudo 2D Vs profile for Line I with rock rippability estimate from geophysical measurements along with the rock cut observations for this line at Station 870+00, respectively. According to the pseudo 2D Vs profile, the subsurface

layering of this line is comprised of two main layers, including a stiff soil layer followed by a rippable rock layer. This matches well with the observations from field measurements, as shown in Figure 5.16b. Based on the personal communication with the contractor (McGeorge Contracting), the contactor was able to remove all the materials associated with this survey line by excavation without any blasting.

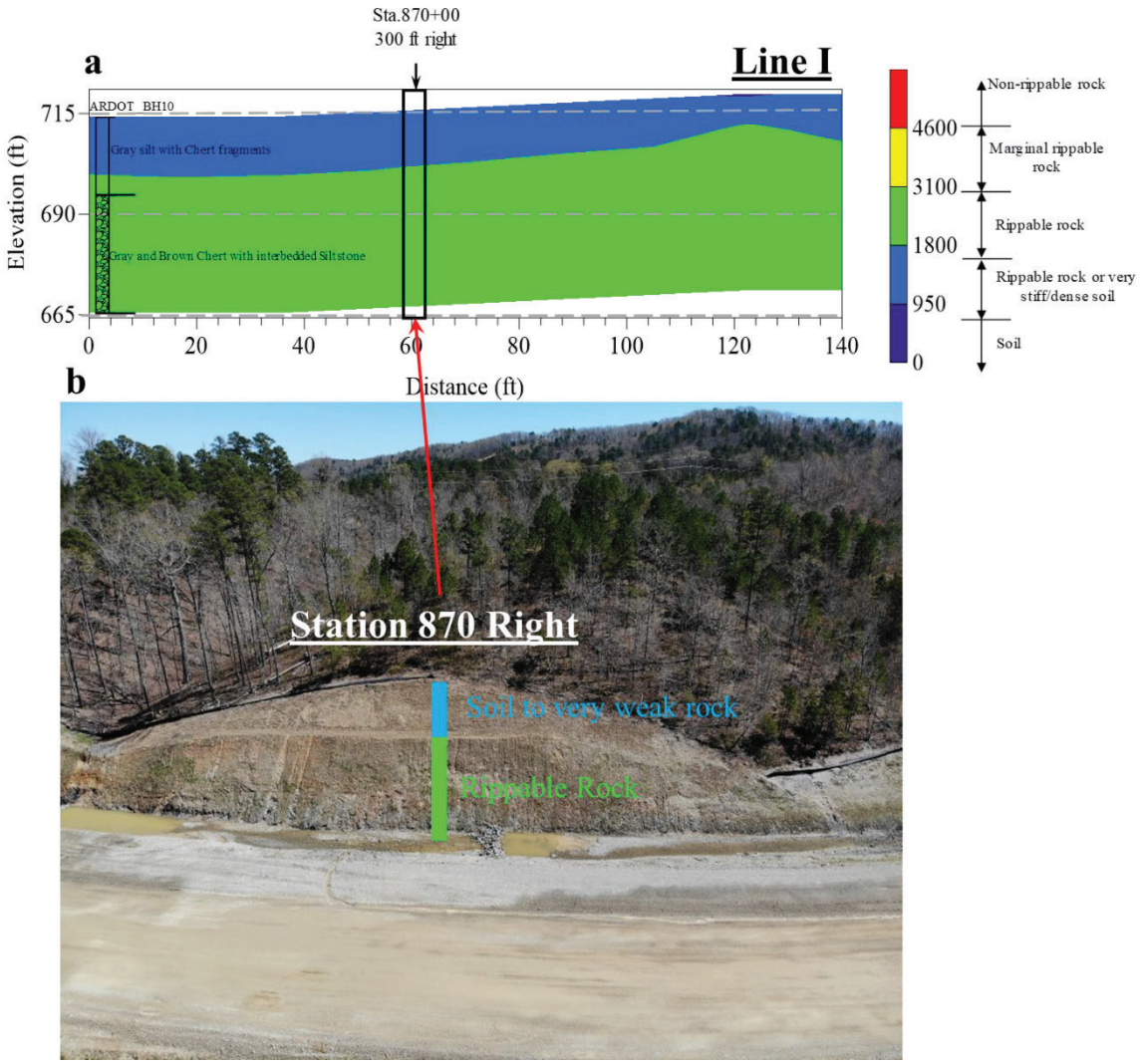

Figure 5.16- Comparison of the rock rippability estimate from geophysical measurements with the field observation for Line I. a) pseudo 2D Vs profile of Line I, b) final rock cut at Station 870+00.

Presented in Figure 5.17a and b are the pseudo 2D Vs profile for Line J with rock rippability estimate from geophysical measurements along with the rock cut observations for this line at Station 875+00, respectively. Similar to survey Line I, the subsurface layering of this line consists of two main layers, including a stiff soil layer followed by a rippable rock layer. This matches well with the observations from the field measurements, as shown in Figure

5.17b. Based on the personal communication with the contractor (McGeorge Contracting), all the materials associated with this survey line were removed by excavation without any blasting.

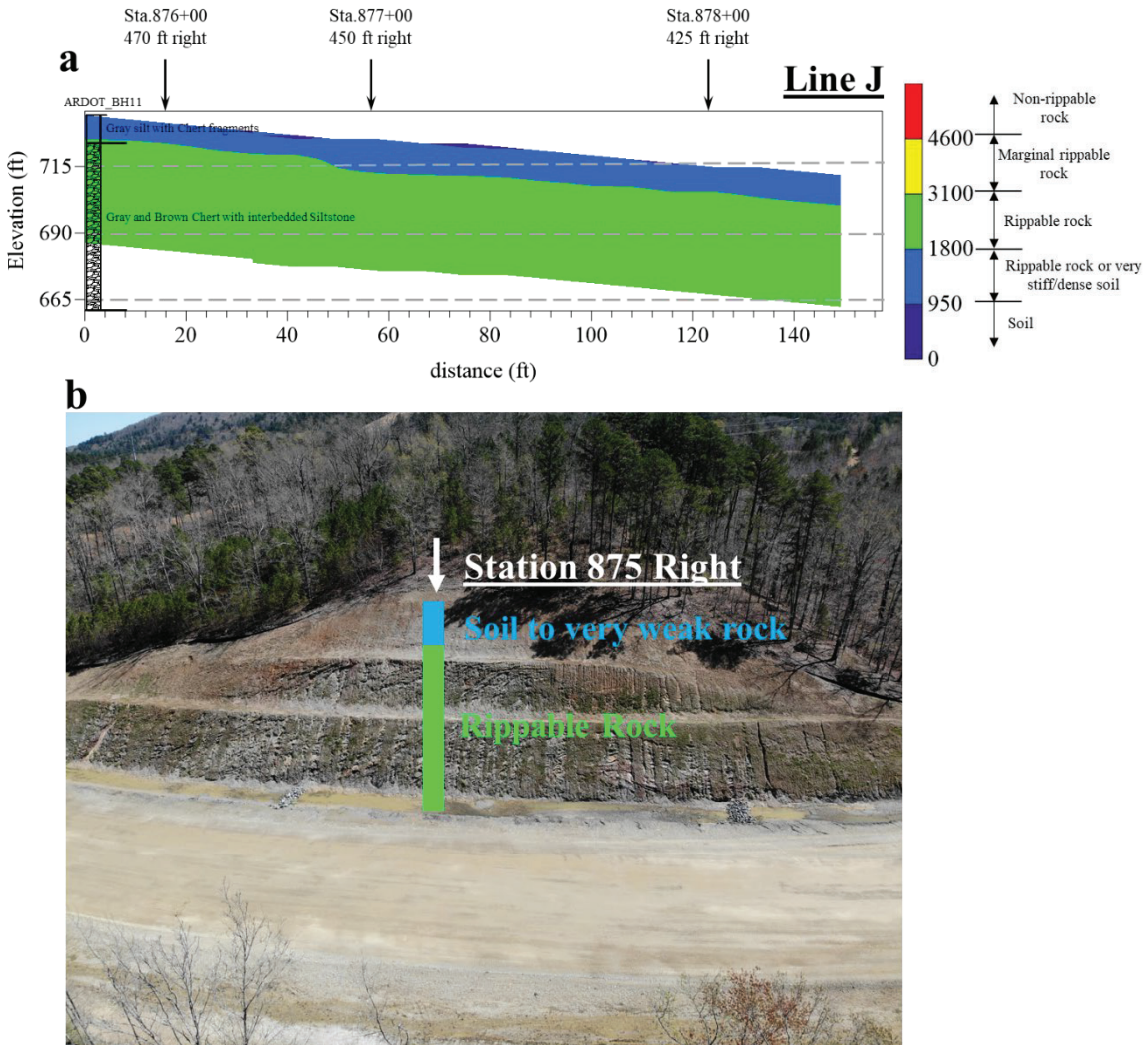

Figure 5.17- Comparison of the rock rippability estimate from geophysical measurements with the field observation for Line J. a) pseudo 2D Vs profile of Line J, b) final rock cut at Station 875+00.

6 Potential time and cost savings

This section discusses the potential benefits of implementing the geophysical methods proposed in Phase II of this report for ARDOT projects. Additionally, as an example, the potential cost and time savings for the Ozark slope stability project using the geophysical methods instead of conventional in-situ methods (e.g. drilling and sampling) are provided.

Potential benefits

Based on the performance of these methods in Phase I, four methods were selected for Phase II to further investigate and demonstrate their capabilities in bedrock mapping and slope stability assessment. These methods include MASW, HVSR, ERT, and P-wave refraction. The potential benefits of using each of the selected geophysical methods for transportation projects are briefly discussed below.

6.1.1 Potential Benefits for a Proposed Highway Alignment

For states like Arkansas, where highway alignments pass through mountainous regions, one of the main challenges of transportation projects is unexpected problematic soil and rock conditions along a proposed highway alignment. Each year ARDOT spends millions of dollars to deal with this issue. Currently, subsurface conditions are assessed using spatially limited laboratory or invasive in-situ testing along highway alignments. These methods provide an acceptable level of accuracy for projects where soil and rock layers are consistent in depth and thickness, but significant errors can occur when conditions are variable across the project area. This is because these methods only provide discrete information regarding the subsurface layering very near the boring location and material types are estimated based on engineering judgment between the boring logs. Therefore, to fully assess the subsurface conditions along a proposed highway alignment, there is a need for methods capable of providing an accurate 2D or 3D image of subsurface conditions. Geophysical methods can be utilized for this purpose to identify the subsurface conditions. The potential benefits for proposed highway alignments for each of the four geophysical methods used in Phase II of the project are discussed below.

MASW: The active MASW technique can be utilized for sites where information regarding both bedrock depth and bedrock stiffness (i.e. rippability) is required. This method is not as fast as the HVSR technique in terms of the field measurements since an array of sensors (geophones) is required. However, to increase the rate of the field testing for the MASW method, a landstreamer system can be used. The landstreamer allows all geophones in

the array to be towed as a single system across the survey line instead of coupling each geophone to the ground via a spike. Using this method, a pseudo 2D cross-section of the subsurface layering (including both soils and rocks) can be generated along a proposed highway alignment by combining the 1D shear wave profiles. An example pseudo 2D cross-section generated from the MASW testing along the proposed highway alignment for the Hot Springs project was provided in Section 5.3.1 in Figure 5.6.

HVSR: The passive HVSR technique can be used for sites where only information regarding the bedrock depth is needed (not the stiffness of the bedrock materials) or for supplementing other results over a larger spatial area. Additionally, the HVSR method can be utilized for rough terrain, where other geophysical methods are difficult to use. This method is capable of predicting both shallow and deep bedrock layers in a rapid, non-invasive, and cost-effective manner. For a proposed highway alignment, where significant rock excavation is expected to reach to the desired roadway elevation, depth to the bedrock and its variation along the highway alignment can be determined using a grid of the single station HVSR measurements. Using the results from a suite of the HVSR measurements, contour maps of depth to bedrock can be generated along the proposed highway alignment in a rapid, cost-effective manner. Examples of such contour maps generated using a grid of the HVSR measurements are shown in Figure 6.1. The contour maps provided in Figure 6.1 were generated for the proposed highway alignment for the Hot Springs project. Moreover, this information can be presented in the form of 2D (see Figure 5.11) or 3D (see Figure 5.12) maps of subsurface layering as discussed in Section 5.3.

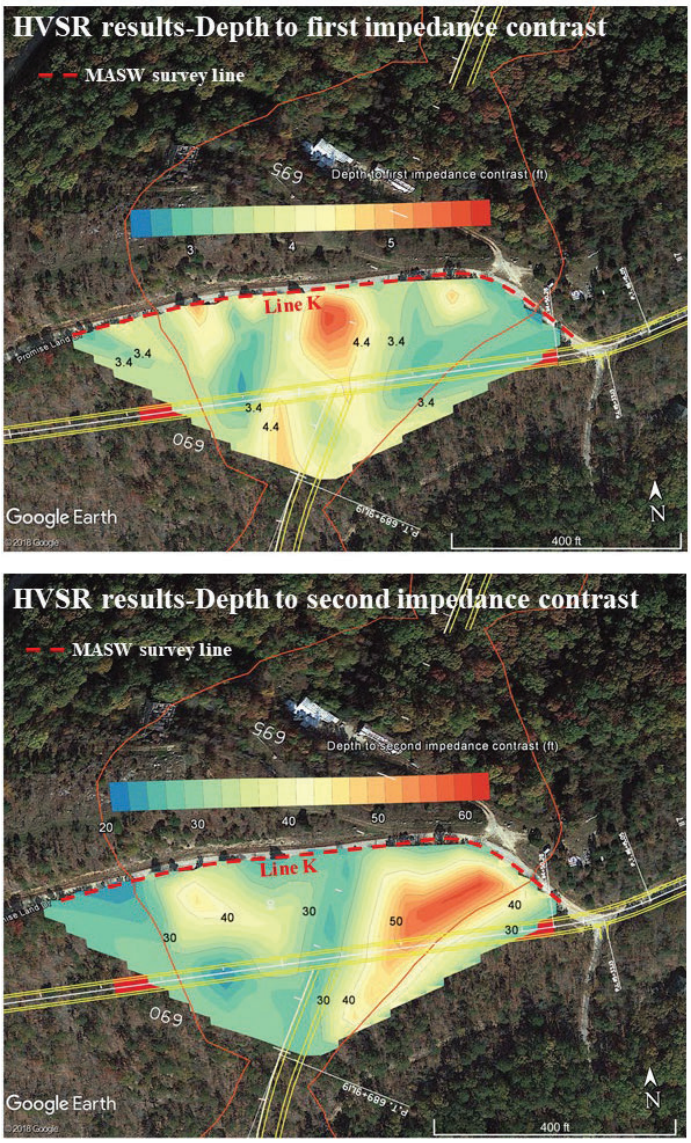

Figure 6.1- Examples of contour maps of depth to different rock layers generated using the HVSR technique along a proposed highway alignment in Hot Springs, Arkansas. Top) depth to first impedance contrast (shallow rock layer), Bottom) depth to second impedance contrast (deep rock layer).

The results of the HVSR and MASW testing can be reported on top of the roadway cross-sections of the proposed highway alignment (see Figure 6.2 as an example) to make them more useful for end users.

Using the HVSR and MASW methods, information regarding bedrock location and bedrock rippability and their variations across a proposed highway alignment can be determined. For those sections of the highway alignment that involve rough terrain or for locations where only information regarding bedrock depth is required, the HVSR method can be employed. For sections where the stiffness of the bedrock layers is also needed, the MASW method can be used. Therefore, the combination of the HVSR and the MASW provides a

powerful tool for the generation of a 2D or 3D map of subsurface conditions along a proposed highway alignment in a rapid, cost-effective, and non-invasive manner. This information is valuable for a proposed highway alignment because it can help in (1) identifying the depth of rippable and non-rippable rock at a location, (2) identifying the most cost-effective solutions for the highway alignments that requires the minimum amount of hard rock excavation, and (3) estimating the hard rock excavation volume for each of the solutions.

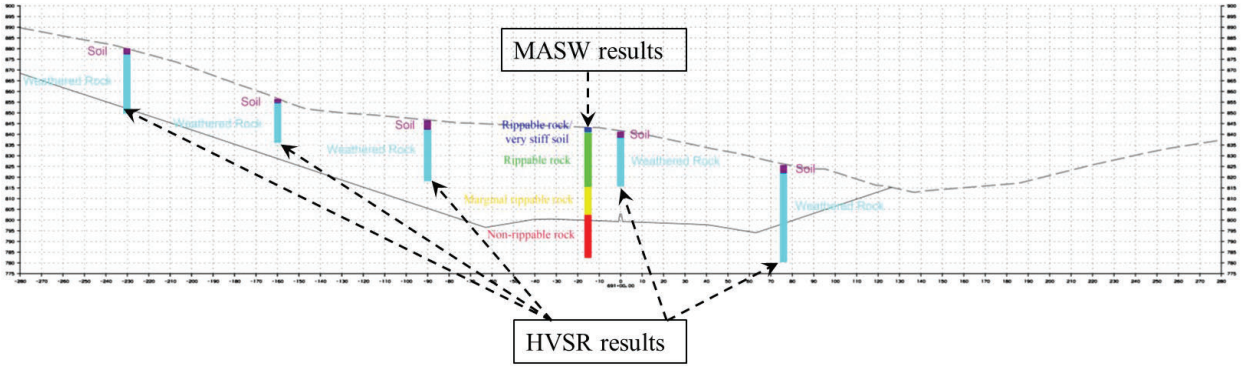

Figure 6.2- Example MASW and HVSR results shown on the cross-section for Station 691+00 for the Hot Springs project.

P-wave refraction: The P-wave refraction was not used as a primary method in this project. However, it has traditionally been used as a primary method to assess bedrock depth and rippability in many other projects. The method can provide similar results as MASW in terms of 2D profiles of bedrock depth and stiffness of the rock formations. However, in some cases, P-wave refraction data can be more difficult to collect since, generally landstreamers are not used for P-wave refraction because of the better coupling required in P-wave refraction to record high-quality time domain records for analysis. In addition, P-wave refraction often needs longer linear arrays, which can be difficult in rough terrain. While P-wave refraction has some limitations compared to MASW, it also has some advantages, including a true 2D analysis scheme rather than a pseudo 2D analysis scheme, and P-wave velocity can be directly used with the caterpillar rippability charts while S-wave velocity (from MASW) needs to be converted before use with those same charts. An example 2D profile generated using the P-wave refraction is provided in Figure 6.3 for the Sand Gap site, where the geophones were coupled into the ground using spikes. Overall, P-wave refraction is a viable method for bedrock mapping and rippability studies with a long history of use.

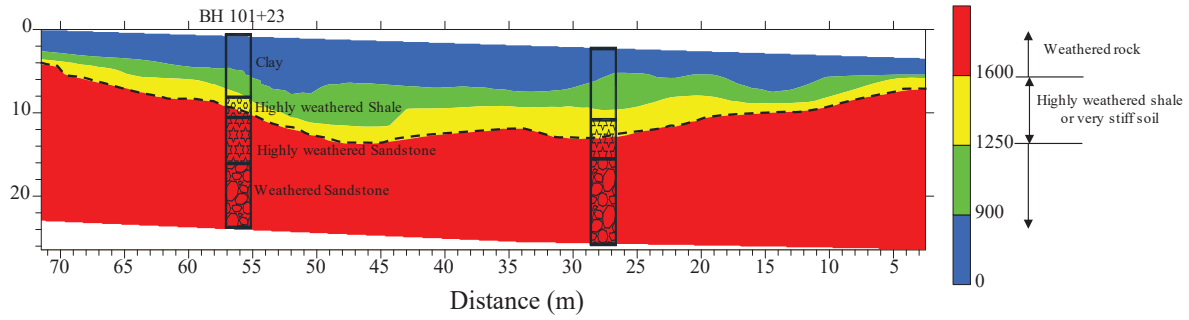

Figure 6.3- An example 2D profile from the P-wave refraction for the Sand Gap site.

ERT: The ERT method is generally not recommended to estimate bedrock depth and rippability. ERT provides no measure of the stiffness of the rock formation because electrical resistivity is not sensitive to material stiffness. In addition, ERT can have a difficult time distinguishing between some soil and rock formations (e.g. clay and shale), particularly when they are located below the water table. Therefore, the method is generally not suitable for bedrock mapping along highway alignments.

6.1.2 Potential Benefits for Improved Slope Stability Analysis

Slope stability is one of the common issues for some ARDOT projects passing through mountainous regions with shallow bedrock. For highway alignments located within a potential landslide, considering the traffic loads being applied to the slip surface, the landslide can experience serious instability issues. These instability issues become even more highlighted for landslides with a shallow bedrock layer where the body of the slip surface can easily become fully saturated during wet conditions. For such conditions, failure to accurately understand the subsurface layering of the landslides along the highway alignment can lead to a slope failure. Given that this issue is very common in the Arkansas highway system, there is a need for a rapid and cost-effective method capable of identifying potential slip surfaces and other problematic surface conditions. The main factors that can benefit slope stability investigations include a continuous image of subsurface layering, particularly bedrock location within the slope area, the water table location and its variation within the slope, and the potential slip surfaces. The potential benefits for slope stability issues for each of the four geophysical methods used in Phase II of the project are discussed below.

MASW: The MASW method can be used to determine the depth and stiffness of subsurface layers along a slope. Key features of the bedrock geometry, such as depression in

the bedrock layer, can be detected (see Figure 5.1 as an example). Additionally, the potential body of the slip surface can be estimated based on the subsurface image acquired from the MASW testing. Therefore, using the MASW method, a high-resolution image of the subsurface conditions (i.e. material type and material stiffness) can be generated. However, the MASW method provides no information regarding the water table location as surface waves and shear wave velocity is relatively insensitive to water or saturation degree of soil deposits.

HVSR: The HVSR technique can be used to generate a 3D image of the bedrock depth and its variation along the slope (see Figure 5.2 as an example). However, no information regarding the stiffness of the materials or the water table location can be identified using the HVSR technique. The HVSR technique has several advantages over other methods for slope characterization for sites with a shallow bedrock layer:

1- Unlike the other field measurement techniques (including the array-based geophysical methods), which are typically difficult to be implemented for sites with a steep slope, the HVSR technique can be easily utilized for any site conditions as it only requires a single independent sensor within the tested area.
2- Considering the time required for the field measurements and data processing of each geophysical method, the HVSR is the fastest geophysical method for the generation of a 3D image of the bedrock geometry with an acceptable level of accuracy.
3- Using this method, some key features of the bedrock geometry such as a bedrock depression can be detected. These critical features are difficult to be detected in traditional geotechnical methods such the drilling and sampling due to the distance between measurement locations.

ERT and P-wave refraction: As mentioned previously, another important factor required for slope stability investigations is the water table location or the highly saturated zones within the slope area. While no information regarding the highly saturated zones and the water table location can be identified from the HVSR and the MASW methods, the ERT and P-wave refraction are very effective for these goals (see Figure 5.1 as an example). In general, ERT is a typical method for slope stability investigations and can provide detail regarding subsurface layering and water table location. However, it should be cautioned that ERT can have difficulty resolving bedrock depth or the separation between materials for given conditions (i.e. clay with shale bedrock or unsaturated clay over saturated sand). These

conditions can lead to misinterpretations of the ERT data. P-wave refraction can be a useful secondary tool to detect saturated layers for slope investigations and can be collected at the same time as Rayleigh wave MASW data with minimal additional effort. However, it is generally not used as a primary method because bedrock depth can generally not be resolved below a saturated soil, and softer layers below stiffer layers cannot be resolved by the method.

Another benefit of performing geophysical methods for the slope stability investigation is that the information from the geophysical testing can improve the numerical slope stability models. This is particularly valuable for sites where boring information is limited because the addition of the geophysical results may significantly change the location of the most critical slip surface(s) and the factor of safety(s) associated with it (Lebow, 2019).

6.1.3 Potential Benefits for Further Use of the Results in Other Geotechnical Designs

The information acquired from HVSR, MASW, P-wave refraction, and ERT testing, which includes depth to different subsurface layers (i.e. soils and rock), their variations across the project site, their stiffness (e.g. bedrock rippability), and water table location can also be used for other geotechnical designs. Examples of such applications include the preliminary design of deep foundations for bridge construction. Additionally, the MASW and the ERT methods are capable of detecting voids and karst cavity features.

Time and cost savings

In order to provide some insights regarding the potential time and cost savings by performing geophysical methods for bedrock mapping and slope stability investigations for transportation projects, the Ozark site is provided here as an example. This example clearly illustrates how the proposed methods of this study can lead to cost savings for ARDOT projects. It should be mentioned that it is difficult to estimate the exact cost savings as a result of performing geophysical methods for a proposed highway alignment or a slope stability site since some of the cost savings are associated with the remediation process. Therefore, the values provided below are just a rough estimation of the cost savings for the Ozark project.

For the Ozark slope stability case history, using the HVSR method, depth to bedrock was estimated in a tight grid pattern across the slope area. This includes more than 160 HVSR measurements, meaning that depth to bedrock was estimated at 160 locations across the slope area. Using this information combined with the surface elevations, a 3D image of the bedrock elevation was generated (see Figure 5.2) which could be very valuable for the slope repair.

In order to determine an estimate of the cost savings for this project using the proposed method in this study, a comparison is made between the drilling and sampling and geophysical methods for the generation of a 3D image of the bedrock elevation that covers the entire slope area. The following assumptions were made to estimate the cost of each method. In the analysis, the time required to conduct each geophysical method is used in the estimate, while the time for the drilling and sampling is estimated as a much less intensive drilling program was actually conducted on the project.

- 160 boring logs are required for the bedrock depth estimation at the Ozark site to cover the entire slope area.
- Average bedrock depth is considered to be approximately 40 ft based on the previous boring log information.
- No samples are required to be collected in the drilling method.
- 5 borings can be drilled per day.
- No laboratory tests are needed since the depth to bedrock is the main information required for the generation of a 3D map of the bedrock elevation.
- 3 sensors are available for the HVSR field measurements.
- MASW and ERT testing include 5 survey lines.
- Users are familiar with the data processing of the MASW, ERT, and HVSR methods.

Using the above assumptions, the cost estimations of the drilling and sampling, HVSR, MASW, and ERT methods are tabulated in Table 6-1, Table 6-2, Table 6-3, and Table 6-4, respectively.

Table 6-1- Cost estimation for the Ozark site using the drilling and sampling method.

Item	Description	Cost	Unit	Quantity	Cost
1	Drilling and sampling	$16.5	Foot	6400	$105,600
2	Setup charge	$100.0	Boring	160	$16,000
3	Difficult site for moving equipment	$200.0	Hour	53	$10,667
4	Site preparation	$1,500.0	Day	14	$21,000
5	Drill crew-Supervisor	$147.0	Hour	320	$47,040
6	Drill crew-Technician	$49.0	Hour	320	$31,360
				Total	**$231,667**

Table 6-2- Cost estimation using the HVSR method.

Item	Description	Price	Unit	Quantity	Cost
1	Mobilization and demobilization	$1,000	Site	1	$1,000
2	Field investigation and data processing	$3,500	Day	2	$7,000
3	Report	$4,000	Site	1	$4,000
				Total	**$12,000**

Table 6-3- Cost estimation for the Ozark site using the MASW method.

Item	Description	Price	Unit	Quantity	Cost
1	Mobilization and demobilization	$1,000	Site	1	$1,000
2	Field investigation and data processing	$6,500	Day	3	$19,500
3	Report	$1,000	Line	5	$5,000
				Total	**$25,500**

Table 6-4- Cost estimation for the Ozark site using the ERT method.

Item	Description	Price	Unit	Quantity	Cost
1	Mobilization and demobilization	$1,000	Site	1	$1,000
2	Field investigation and data processing	$5,000	Day	2	$10,000
3	Report	$1,000	Line	5	$5,000
				Total	**$16,000**

Therefore, assuming 160 locations are required for the Ozark site, the total cost of the drilling and sampling is approximately $231,667. For the HVSR method, using three sensors and two personnel, the field measurements can be conducted in two days. Therefore, the total cost of the HVSR method is approximately $12,000. For the MASW testing, the field measurements can be finished in three days, and so the total cost of the MASW testing for the Ozark project is approximately $25,500. Additionally, considering 2 days required for the field measurements for the ERT testing, the total cost for the Ozark site is approximately $16,000. Shown in Figure 6.4 is a summary of the cost and time estimations for each method. As shown in this figure, the cost and time of the MASW, HVSR, or ERT testing are considerably lower than the drilling and sampling method. Even the combined cost estimation for geophysical testing is significantly lower than the drilling and sampling method, as presented in Figure 6.4.

Therefore, using the proposed methods of this study for the Ozark sites, a considerable amount of money and time can be saved. For example, a gross cost savings of approximately $219,667 is expected for the generation of a 3D map of the bedrock variation for the Ozark site using the HVSR method comparing to the drilling and sampling methods (Figure 6.4a). Additionally, the number of days required to finish this task using the HVSR method is significantly lower.

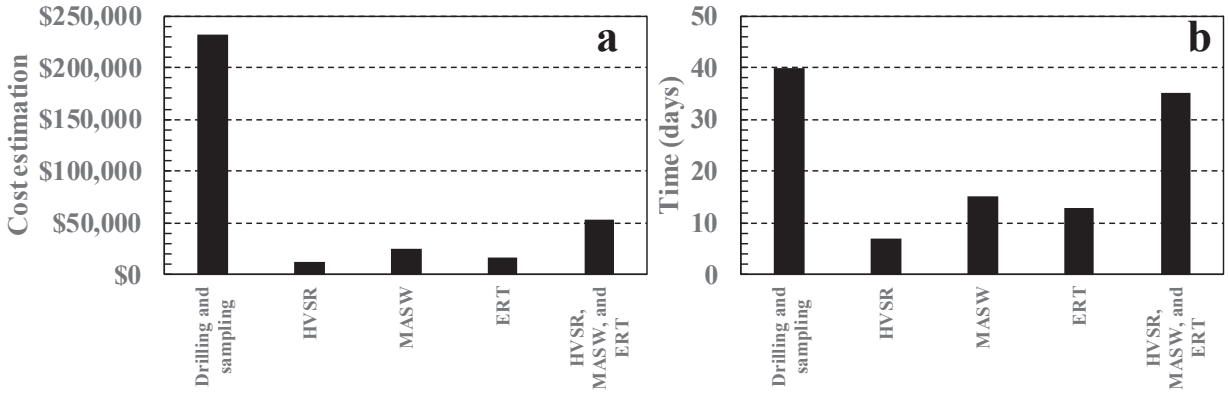

Figure 6.4- Comparison of the cost and time estimations for each method (field and office time included).

It is worth mentioning that according to the Research Informer Newsletter published by ARDOT in Fall 2019, our proposed methods have saved ARDOT $750,000 on three construction projects, including Job #061331 Southridge Extension in Little Rock, Job #R60140 Hwy. 70 East-Hwy. 7 North in Hot Springs, and slope stability slide along I40 near Ozark. This is the preliminary savings for these projects, and the savings are expected to be more than $750,000 once the results are fully implemented.

To sum up, according to the findings of this research study, for some of the ARDOT projects such as slope stability sites or proposed highway alignments that require a considerable amount of rock excavations, subsurface conditions can be evaluated in a much cheaper and faster way using geophysical methods compared to drilling and sampling. The amount of money that can be saved using the geophysical methods varies from site to site as there are numerous factors affecting the final cost of each method.

7 Conclusions

In this study, different geophysical methods, including MASW using both Rayleigh and Love type surface waves, P-wave refraction, HVSR, CCR, ERT, GPR, and EM31, were implemented for several ARDOT transportation projects. The goal of the project is to identify the potential non-invasive geophysical methods that would be valuable to address two common ARDOT transportation issues, including slope movements and unexpected subsurface conditions.

Through testing at the Hardy and Sand Gap test sites in Phase I of the project, it was determined that a number of geophysical methods provide a viable option for mapping subsurface conditions, while others did not have the accuracy to be viable for transportation applications. Based on the results from Phase I, the EM31, GPR, and CCR generally provided results that were considered below the level of the accuracy required for transportation projects and were therefore removed from consideration as the best method. The rest of the geophysical methods that include MASW, P-wave refraction, HVSR, and ERT, were implemented for three ongoing ARDOT transportation projects (two proposed highway alignments and one slope stability site) in Phase II to further investigate their capabilities for bedrock mapping and slope stability. Depending on the purpose of the project, different combinations of geophysical methods are recommended to be used.

For slope stability studies that involve shallow and complex bedrock topography, which is the case for most ARDOT slope stability projects, it was observed that a true 3D model of bedrock topography is a key factor required for the development of a detailed and accurate slope stability model. In this respect, the HVSR method is proposed as an effective tool that can be used in conjunction with other geophysical methods or drilling and sampling for slope stability investigations. The proposed method of this study includes a tight grid of HVSR measurements that covers the entire slope areas with measurement locations spaced 15-30 m apart. Using this method, a detailed high-resolution 3D image of the bedrock topography can be created within the entire slope area to reveal the potential critical zones of the slope. Obtaining such a 3D model using conventional in-situ methods (e.g. drilling and sampling) or array-based geophysical method (e.g. MASW or ERT) is extremely time and cost-prohibitive. After detecting the potential critical zones of the slope from the HVSR results, further geophysical investigations can be planned using MASW and ERT or P-wave refraction. The MASW method should be used to identify the information regarding the stiffness of the

subsurface materials along the critical zones and to evaluate the accuracy of the HVSR results. ERT or P-wave refraction are viable for rain-induced slope stability sites, which are common in Arkansas. Using any of these two methods, the groundwater table location and highly saturated zones of the critical slides can be detected. Therefore, the HVSR, MASW, and ERT or P-wave refraction combination offers a practical, rapid, and cost-effective solution for slope stability investigations. It should be mentioned that if the slope stability site is not considered as a potential rain-induced slope, the combination of MASW and HVSR should be sufficient for slope stability investigation. In this study, the capability of the proposed method for slope stability investigation was shown by implementing them for two active slopes in Arkansas (Sand Gap in Phase I and Ozark in Phase II) that have recently experienced considerable slope movements.

Another common issue for ARDOT transportation projects is unexpected subsurface conditions such as shallow bedrock. Encountering such conditions during construction can lead to significant cost overruns, change orders, and construction delays. In order to avoid these issues for a proposed highway alignment, the unexpected subsurface conditions need to be identified in advance. In this regard, a combination of MASW, HVSR, and P-wave refraction is recommended. The two primary methods which are recommended for this purpose consist of MASW and HVSR. The MASW method is recommended to use for easily accessible areas (i.e. roads and trails) to map bedrock and detect bedrock rippability. If the subsurface layering consists of a homogenous soil layer underlain by a bedrock layer, Love type surface waves are suggested to be used. Otherwise, Rayleigh type surface waves should be used. However, the best way is to first conduct the MASW method using both Rayleigh and Love type surface waves for a few array setups, and then the best option is selected based on the resolution of the experimental dispersion curves acquired from Rayleigh and Love measurements. For areas that involve rough terrain, steep slopes, and sections densely covered with trees and brush where array-based geophysical methods (MASW and P-wave refraction) are difficult to use, the HVSR method is recommended. The HVSR method can be used for bedrock detection for any kind of site conditions, and so a larger spatial extent can be covered using the HVSR method. However, the limitation of the HVSR is it requires some knowledge of the shear wave velocity of the soil, a boring log at the site, or other a-prior knowledge to estimate bedrock depth. In addition, the method only provides depth to bedrock, and no information is obtained regarding the rippability or condition of the rock. The P-wave refraction is capable of providing accurate information regarding bedrock location and bedrock rippability. However, it suffers from the

quick loss of resolution with depth, and the data processing of the P-wave wave refraction can sometimes be ambiguous for sites where multiple shallow refraction sources are present or where refractor layers are quite variable. Additionally, this method should not be used for sites with a velocity reversal layer within the target depth of the P-wave refraction measurements. However, this method is a viable method for determining bedrock location and rippability and has traditionally been used on many projects.

Overall, using the methods proposed in this research for slope stability studies and bedrock mapping for proposed highway alignments that need significant excavations, a detailed and almost continuous image of subsurface conditions can be generated in a rapid, non-invasive, and accurate manner. Additionally, this can lead to significant time and cost savings for the project, as discussed in Chapter 6 of the report.

References

Anbazhagan, P., & Sitharam, T. G. (2008). Site characterization and site response studies using shear wave velocity. Journal of Seismology and Earthquake Engineering, 10(2), 53-67.

Anderson, N. L., Croxton, N., Hoover, R., & Sirles, P. (2008). Geophysical methods commonly employed for geotechnical site characterization. Transportation Research E-Circular, (E-C130).

Arkansas Department of Transportation, (2019). Research Informer newsletter, https://www.arkansashighways.com/System_Info_and_Research/research/Fall_2019_Research_Informer.pdf

ASTM D5777-00. (2011). Standard guide for using the seismic refraction method for subsurface investigation.

ASTM D6432-11. (2011). Standard guide for using the surface ground penetrating radar method for uubsurface investigation.

ASTM/SEI 7- 10 (2013). Minimum design loads for buildings and other structures.

Aung, A. M. W., & Leong, E. C. (2012). Stiffness profiles of residual soil sites using continuous surface wave method.

Baker, G. S., Jordan, T. E., & Pardy, J. (2007). An introduction to ground penetrating radar (GPR). Special paper-geological society of America, 432, 1.

Bard, P. Y. (2004). Guidelines for the implementation of the H/V spectral ratio technique on ambient vibrations: Measurements, processing and interpretation, SESAME European Research Project, WP12—Deliverable D23, 12.

Berti, M., Bertello, L., & Squarzoni, G. (2019). Surface-wave velocity measurements of shear stiffness of moving earthflows. Landslides, 16(3), 469-484.

Bichler, A., Bobrowsky, P., Best, M., Douma, M., Hunter, J., Calvert, T., & Burns, R. (2004). Three-dimensional mapping of a landslide using a multi-geophysical approach: the Quesnel Forks landslide. Landslides, 1(1), 29-40.

Burton, B. L., & Cannia, J. C. (2011). Capacitively coupled resistivity survey of the levee surrounding the Omaha Public Power District Nebraska City Power Plant, June 2011. US Department of the Interior, US Geological Survey.

Busato, L., Boaga, J., Peruzzo, L., Himi, M., Cola, S., Bersan, S., & Cassiani, G. (2016). Combined geophysical surveys for the characterization of a reconstructed river embankment. Engineering Geology, 211, 74-84.

Cardarelli, E., Cercato, M. and De Donno, G., 2014. Characterization of an earth-filled dam through the combined use of electrical resistivity tomography, P-and SH-wave seismic tomography and surface wave data. Journal of Applied Geophysics, 106, pp.87-95.

Carrière, S. D., Chalikakis, K., Sénéchal, G., Danquigny, C., & Emblanch, C. (2013). Combining electrical resistivity tomography and ground penetrating radar to study geological structuring of karst unsaturated zone. Journal of Applied Geophysics, 94, 31-41.

Caterpillar Inc (2000). Handbook of Ripping 12th edition. http://www.dot.ca.gov/hq/esc/geotech/references/Rock_Cut_Slope_References/31_Handbook_of_Ripping_Caterpiller.pdf.

Chlaib, H. K., Mahdi, H., Al-Shukri, H., Su, M. M., Catakli, A., & Abd, N. (2014). Using ground penetrating radar in levee assessment to detect small scale animal burrows. Journal of Applied Geophysics, 103, 121-131.

Chlaib, H. K., Mahdi, H., Al-Shukri, H., Su, M. M., Catakli, A., & Abd, N. (2014). Using ground penetrating radar in levee assessment to detect small scale animal burrows. Journal of Applied Geophysics, 103, 121-131.

Christensen, N. I. (1996). Poisson's ratio and crustal seismology. Journal of Geophysical Research: Solid Earth, 101(B2), 3139-3156.
Coe, J., Brandenberg, S., Ahdi, S., & Kordjazi, A. (2018). Geophysical methods for determining the geotechnical engineering properties of earth materials. California department of transportation, Report Number CA-17-2111.
Comina, C., Foti, S., Boiero, D., & Socco, L. V. (2010). Reliability of VS, 30 evaluation from surface-wave tests. Journal of Geotechnical and Geoenvironmental engineering, 137(6), 579-586.
Cubrinovski, M., Green, R., Allen, J., Ashford, S., Bowman, E., Bradley, B. A., ... & Pender, M. (2010). Geotechnical reconnaissance of the 2010 Darfield (New Zealand) earthquake.
Dikmen, Ü. (2009). Statistical correlations of shear wave velocity and penetration resistance for soils. Journal of Geophysics and Engineering, 6(1), 61-72.
Doolittle, J. A., & Brevik, E. C. (2014). The use of electromagnetic induction techniques in soils studies. Geoderma, 223, 33-45.
Doolittle, J. A., & Brevik, E. C. (2014). The use of electromagnetic induction techniques in soils studies. Geoderma, 223, 33-45.
Eker, A. M., Koçkar, M. K., & Akgün, H. (2015). Evaluation of site effect within the tectonic basin in the northern side of Ankara. Engineering geology, 192, 76-91.
Eslick, R., Tsoflias, G., & Steeples, D. (2008). Field investigation of Love waves in near-surface seismology. Geophysics, 73(3), G1-G6.
Fabbrocino, S., Lanzano, G., Forte, G., de Magistris, F. S., & Fabbrocino, G. (2015). SPT blow count vs. shear wave velocity relationship in the structurally complex formations of the Molise Region (Italy). Engineering Geology, 187, 84-97.
Fäh, D., Kind, F., & Giardini, D. (2001). A theoretical investigation of average H/V ratios. Geophysical Journal International, 145(2), 535-549.
Foti, S., Lai, C. G., Rix, G. J., & Strobbia, C. (2014). Surface wave methods for near-surface site characterization. CRC Press.
Foti, S., Lancellotta, R., Sambuelli, L., & Socco, L. V. (2000). Notes on fk analysis of surface waves. Annals of Geophysics, 43(6).
Friedel, S., Thielen, A., & Springman, S. M. (2006). Investigation of a slope endangered by rainfall-induced landslides using 3D resistivity tomography and geotechnical testing. Journal of Applied Geophysics, 60(2), 100-114.
Gabriels, P., Snieder, R., & Nolet, G. (1987). In situ measurements of shear-wave velocity in sediments with higher-mode rayleigh waves. Geophysical Prospecting, 35(2), 187-196.
Garman, K. M., & Purcell, S. F. (2004). Applications for capacitively coupled resistivity surveys in Florida. The Leading Edge, 23(7), 697-698.
Gercek, H. (2007). Poisson's ratio values for rocks. International Journal of Rock Mechanics and Mining Sciences, 44(1), 1-13.
GF Instruments. (2016). Short guide for electromagnetic conductivity mapping and tomography.
Giancarlo, D. M. (2010). Insights on surface wave dispersion and HVSR: Joint analysis via Pareto optimality. Journal of Applied Geophysics, 72(2), 129-140.
Grelle, G., & Guadagno, F. M. (2009). Seismic refraction methodology for groundwater level determination:“Water seismic index”. Journal of Applied Geophysics, 68(3), 301-320.
Griffiths, S. C., Cox, B. R., Rathje, E. M., & Teague, D. P. (2016). Surface-wave dispersion approach for evaluating statistical models that account for shear-wave velocity uncertainty. Journal of Geotechnical and Geoenvironmental Engineering, 142(11), 04016061.

Grisso, R. D., Alley, M. M., Holshouser, D. L., & Thomason, W. E. (2005). Precision Farming Tools. Soil Electrical Conductivity.
Hack, R. (2000). Geophysics for slope stability. Surveys in geophysics, 21(4), 423-448.
Hayashi, K., & Konishi, C. (2010). Joint use of a surface-wave method and a resistivity method for safety assessment of levee systems. InGeoFlorida 2010: Advances in Analysis, Modeling & Design (pp. 1340-1349).
Hebeler, G. L., & Rix, G. J. (2007). Site characterization in Shelby County, Tennessee using advanced surface wave methods. MAE Center CD Release 06-02.
http://www.geopsy.org.
http://www.masw.com/Hardware.html
https://www.agiusa.com/agi-earthimager-2d.
https://www.geotomosoft.com/downloads.php
https://www.goldensoftware.com/products/surfer.
https://www.rocscience.com/software/slide3.
https://www.sensoft.ca/products/ekko-project/overview.
Jol, H. M. (Ed.). (2008). Ground penetrating radar theory and applications. elsevier.
Jongmans, D., Bièvre, G., Renalier, F., Schwartz, S., Beaurez, N., & Orengo, Y. (2009). Geophysical investigation of a large landslide in glaciolacustrine clays in the Trièves area (French Alps). Engineering geology, 109(1-2), 45-56.
Karim, M. Z., & Tucker-Kulesza, S. E. (2018). Predicting soil erodibility using electrical resistivity tomography. Journal of Geotechnical and Geoenvironmental Engineering, 144(4), 04018012.
Kaufman, A.A. and Hoekstra, P. (2001). Electromagnetic Soundings. Elsevier: Amsterdam.
Kaufman, A.A. and Hoekstra, P. (2001). Electromagnetic Soundings. Elsevier: Amsterdam.
Koehn, W. J., Tucker-Kulesza, S. E., LeBow, V., Rahimi, S., Bernhardt, M. L., & Wood, C. M. (2019, March). Enhanced Analysis of Landslide Failure Mechanisms in the Ozark Plateau Region with Electrical Resistivity Tomography. In Eighth International Conference on Case Histories in Geotechnical Engineering (Geo-Congress 2019) American Society of Civil Engineers.
Konno, K., & Ohmachi, T. (1998). Ground-motion characteristics estimated from spectral ratio between horizontal and vertical components of microtremor. Bulletin of the Seismological Society of America, 88(1), 228-241.
Kramer, S. L. (1996). Geotechnical earthquake engineering. In prentice–Hall international series in civil engineering and engineering mechanics. Prentice-Hall, New Jersey.
Krautblatter, M., & Draebing, D. (2014). Pseudo 3-DP wave refraction seismic monitoring of permafrost in steep unstable bedrock. Journal of Geophysical Research: Earth Surface, 119(2), 287-299.
Lacoss, R. T., Kelly, E. J., & Toksöz, M. N. (1969). Estimation of seismic noise structure using arrays. Geophysics, 34(1), 21-38.
Lai, C. G., Rix, G. J., Foti, S., & Roma, V. (2002). Simultaneous measurement and inversion of surface wave dispersion and attenuation curves. Soil Dynamics and Earthquake Engineering, 22(9-12), 923-930.
Lapenna, V., Lorenzo, P., Perrone, A., Piscitelli, S., Sdao, F., & Rizzo, E. (2003). High-resolution geoelectrical tomographies in the study of Giarrossa landslide (southern Italy). Bulletin of Engineering Geology and the Environment, 62(3), 259-268.
LeBow, V. (2019). Incorporating Geophysical Data in Slope Stability Modeling for Two Slopes in Arkansas.
Leshchinsky, Ben. (2015). Limit Equilibrium and Limit Analysis: Comparison of Benchmark Slope Stability Problems. Journal of Geotechnical and Geoenvironmental Engineering. 10.1061/(ASCE)GT.1943-5606.0001347.

Lin, Y. C., Joh, S. H., and Stokoe, K. H. (2014). Analyst J: analysis of the UTexas 1 surface wave dataset using the SASW methodology. In Geo-Congress 2014: Geo-characterization and Modeling for Sustainability (pp. 830-839).

Maheswari, R. U., Boominathan, A., & Dodagoudar, G. R. (2010). Use of surface waves in statistical correlations of shear wave velocity and penetration resistance of Chennai soils. Geotechnical and Geological Engineering, 28(2), 119-137.

Martínez-Pagán, P., Navarro, M., Pérez-Cuevas, J., García-Jerez, A., Alcalá, F. J., Sandoval-Castaño, S., & Alhama, I. (2012,). Comparative study of SPAC and MASW methods to obtain the Vs30 for seismic site effect evaluation in Lorca town, SE Spain. In Near Surface Geoscience 2012–18th European Meeting of Environmental and Engineering Geophysics (pp. cp-306). European Association of Geoscientists & Engineers.

Mayne, P. W., Christopher, B. R., & DeJong, J. (2002). Subsurface Investigations--Geotechnical Site Characterization: Reference Manual (No. FHWA-NHI-01-031). United States. Federal Highway Administration.

McMechan, G. A., & Yedlin, M. J. (1981). Analysis of dispersive waves by wave field transformation. Geophysics, 46(6), 869-874.

McMechan, G. A., & Yedlin, M. J. (1981). Analysis of dispersive waves by wave field transformation. Geophysics, 46(6), 869-874.

Merritt, A. J., Chambers, J. E., Murphy, W., Wilkinson, P. B., West, L. J., Gunn, D. A., ... & Dixon, N. (2014). 3D ground model development for an active landslide in Lias mudrocks using geophysical, remote sensing and geotechnical methods. Landslides, 11(4), 537-550.

Miller, R. D., Xia, J., Park, C. B., & Ivanov, J. M. (1999). Multichannel analysis of surface waves to map bedrock. The Leading Edge, 18(12), 1392-1396.

Moon, S. W., Hayashi, K., & Ku, T. (2017). Estimating spatial variations in bedrock depth and weathering degree in decomposed granite from surface waves. Journal of Geotechnical and Geoenvironmental Engineering, 143(7), 04017020.

Moon, S. W., Hayashi, K., & Ku, T. (2017). Estimating spatial variations in bedrock depth and weathering degree in decomposed granite from surface waves. Journal of Geotechnical and Geoenvironmental Engineering, 143(7), 04017020.

Nakamura, Y. (1989). A method for dynamic characteristics estimation of subsurface using microtremor on the ground surface. Quarterly Report of the Japanese Railway Technical Research Institute (RTRI), 30(1), 25–33

Naudet, V., Lazzari, M., Perrone, A., Loperte, A., Piscitelli, S., & Lapenna, V. (2008). Integrated geophysical and geomorphological approach to investigate the snowmelt-triggered landslide of Bosco Piccolo village (Basilicata, southern Italy). Engineering Geology, 98(3-4), 156-167.

Nogoshi, M., & Igarashi, T. (1971). On the amplitude characteristics of ambient noise (Part 2). J Seismol Soc Jpn, 24, 26-40.

Nolet, G., & Panza, G. F. (1976). Array analysis of seismic surface waves: limits and possibilities. Pure and Applied geophysics, 114(5), 775-790.

Ohio DOT (2016). Rock Slope Design Guide, Ohio Department of Transportation, https://www.dot.state.oh.us/Divisions/Engineering/Geotechnical/Geotechnical_Documents/Rock_Slope_Design_Guide.pdf.

Olafsdottir, E. A., Erlingsson, S., & Bessason, B. (2017). Tool for analysis of multichannel analysis of surface waves (MASW) field data and evaluation of shear wave velocity profiles of soils. Canadian Geotechnical Journal, 55(2), 217-233.

Olona, J., Pulgar, J. A., Fernandez-Viejo, G., Lopez-Fernandez, C., & González-Cortina, J. M. (2010). Weathering variations in a granitic massif and related geotechnical properties through seismic and electrical resistivity methods. Near Surface Geophysics, 8(6), 585-599.

Palacky, G. J. (1988). Resistivity characteristics of geologic targets. Electromagnetic methods in applied geophysics, 1, 53-129.

Park, C. B., Miller, R. D., & Xia, J. (1999). Multichannel analysis of surface waves. Geophysics, 64(3), 800-808.

Parolai, S., Picozzi, M., Richwalski, S. M., & Milkereit, C. (2005). Joint inversion of phase velocity dispersion and H/V ratio curves from seismic noise recordings using a genetic algorithm, considering higher modes. Geophysical research letters, 32(1).

Pastén, C., Sáez, M., Ruiz, S., Leyton, F., Salomón, J., & Poli, P. (2016). Deep characterization of the Santiago Basin using HVSR and cross-correlation of ambient seismic noise. Engineering geology, 201, 57-66.

Peng, J., Wang, G., Wang, Q., & Zhang, F. (2017). Shear wave velocity imaging of landslide debris deposited on an erodible bed and possible movement mechanism for a loess landslide in Jingyang, Xi'an, China. Landslides, 14(4), 1503-1512.

Pourkhosravani, A., & Kalantari, B. (2011). A review of current methods for slope stability evaluation. Electron. J. Geotech. Eng, 16, 1245-1254.

Race, M. L., & Coffman, R. A. (2013). Effect of uncertainty in site characterization on the prediction of liquefaction potential for bridge embankments in the Mississippi embayment. In Geo-Congress 2013: Stability and Performance of Slopes and Embankments III (pp. 888-897).

Rahimi, S., Moody, T., Wood, C., Kouchaki, B. M., Barry, M., Tran, K., & King, C. (2019). Mapping Subsurface Conditions and Detecting Seepage Channels for an Embankment Dam Using Geophysical Methods: A Case Study of the Kinion Lake Dam. Journal of Environmental and Engineering Geophysics, 24(3), 373-386. https://doi.org/10.2113/JEEG24.3.373

Rahimi, S., Wood, C. M., & Bernhardt-Barry, M. (2021). The MHVSR technique as a rapid, cost-effective, and noninvasive method for landslide investigation: case studies of Sand Gap and Ozark, AR, USA. Landslides, 1-16. https://doi.org/10.1007/s10346-021-01677-7

Rahimi, S., Wood, C. M., & Himel, A. K. (2020, February). Application of Microtremor Horizontal to Vertical Spectra Ratio (MHVSR) and Multichannel Analysis of Surface Wave (MASW) for Shallow Bedrock Mapping for Transportation Projects. In Geo-Congress 2020: Modeling, Geomaterials, and Site Characterization (pp. 622-632). Reston, VA: American Society of Civil Engineers. https://doi.org/10.1061/9780784482803.066.

Rahimi, S., Wood, C. M., & Wotherspoon, L. M. (2020). Influence of soil aging on SPT-Vs correlation and seismic site classification. Engineering Geology, 272, 105653. https://doi.org/10.1016/j.enggeo.2020.105653.

Rahimi, S., Wood, C. M., Bernhardt-Barry, M., & Himel, A. K. (2019). Updated Reference Shear Wave Velocity Curves for Near-Surface Site Characterization. In Geo-Congress

2019 : Engineering Geology, Site Characterization, and Geophysics. Reston, VA: American Society of Civil Engineers. https://doi.org/10.1061/9780784482131.033.

Rahimi, S., Wood, C. M., Coker, F., Moody, T., Bernhardt-Barry, M., & Kouchaki, B. M. (2018). The combined use of MASW and resistivity surveys for levee assessment: A case study of the Melvin Price Reach of the Wood River Levee. Engineering Geology, 241, 11-24. https://doi.org/10.1016/j.enggeo.2018.05.009.

Rahimi, S., Wood, C. M., Kokkali, P., & Rivers, B. (2021). Advantages of Geophysics to Improve Site Characterization and Reliability for Transportation Projects. Transportation Research Record. https://doi.org/10.1177/0361198121996362.

Rahimi, S., Wood, C. M., Rieth, R., & Himel, A. K. (2021). Application of Shear Wave Velocity to Rock Rippability Estimates Based on Poisson's Ratios Determined from Laboratory and Field Measurements. In IFCEE 2021 (pp. 339-349). https://doi.org/10.1061/9780784483428.035

Rahimi, S., Wood, C. M., Teague, D. P. (2021). Performance of Transformation Techniques for MASW Data Processing Considering Various Site Conditions, Near-Field Effects, and Modal Separation. Surveys in Geophysics.

Rahimi, S., Wood, C. M., Wotherspoon, L. M., & Green, R. A. (2020). Efficacy of Aging Correction for Liquefaction Assessment of Case Histories Recorded during the 2010 Darfield and 2011 Christchurch Earthquakes in New Zealand. Journal of Geotechnical and Geoenvironmental Engineering, 146(8), 04020059. https://doi.org/10.1061/(ASCE)GT.1943-5606.0002294.

Rahimi, S., Wood, C. M., & Himel, A. K. (2021). Practical Guidelines for Mitigating Near-field Effects for Array-based Active Surface Wave Testing. Geophysical Journal International.

Redpath, B.B. (1973). Seismic Refraction Exploration for Engineering Site Investigations, Explosive Excavation Research Laboratory, distributed by NTIS.

Rix, G. J., Hebeler, G. L., & Orozco, M. C. (2002). Near-surface Vs profiling in the New Madrid seismic zone using surface-wave methods. Seismological Research Letters, 73(3), 380-392.

Robinson, M., Bristow, C., McKinley, J., & Ruffell, A. (2013). Ground penetrating radar. Geomorphological Techniques, Part, 1, 2047-0371.

Schmutz, M., Albouy, Y., Guérin, R., Maquaire, O., Vassal, J., Schott, J. J., & Descloîtres, M. (2000). Joint electrical and time domain electromagnetism (TDEM) data inversion applied to the Super Sauze earthflow (France). Surveys in Geophysics, 21(4), 371-390.

SeisImager/2D Manual. (2009). Geometric.com.

SESAME European Research Project. (2004). Guidelines for the implementation of the H/V spectral ratio technique on ambient vibration. Measurements, processing and interpretations. Project No. EVG1-CT-2000-00026.

Sirles, P. C. (2006). Use of geophysics for transportation projects (Vol. 357). Transportation Research Board.

Słowik, M. (2012). Influence of measurement conditions on depth range and resolution of GPR images: the example of lowland valley alluvial fill (the Obra River, Poland). Journal of applied Geophysics, 85, 1-14.

Słowik, M. (2012). Influence of measurement conditions on depth range and resolution of GPR images: the example of lowland valley alluvial fill (the Obra River, Poland). Journal of Applied Geophysics, 85, 1-14.

Snapp, M., Tucker-Kulesza, S., & Koehn, W. (2017). Electrical resisitivity of mechancially stablized earth wall backfill. Journal of Applied Geophysics, 141, 98-106.

Socco, L. V., & Strobbia, C. (2004). Surface-wave method for near-surface characterization: A tutorial. Near surface geophysics, 2(4), 165-185.

Steelman, C. M., Kennedy, C. S., & Parker, B. L. (2015). Geophysical conceptualization of a fractured sedimentary bedrock riverbed using ground-penetrating radar and induced electrical conductivity. Journal of Hydrology, 521, 433-446.

Sun, C. G., Han, J. T., & Cho, W. (2012). Representative shear wave velocity of geotechnical layers by synthesizing in-situ seismic test data in Korea. The Journal of Engineering Geology, 22(3), 293-307.

Teague, D., Cox, B., Bradley, B., & Wotherspoon, L. (2018). Development of Deep Shear Wave Velocity Profiles with Estimates of Uncertainty in the Complex Interbedded Geology of Christchurch, New Zealand. Earthquake Spectra, 34(2), 639-672.

Tingey, B. E., McBride, J. H., Thompson, T. J., Stephenson, W. J., South, J. V., & Bushman, M. (2007). Study of a prehistoric landslide using seismic reflection methods integrated with geological data in the Wasatch Mountains, Utah, USA. Engineering Geology, 95(1-2), 1-29.

Tremblay, S. P., & Karray, M. (2019). Practical considerations for array-based surface-wave testing methods with respect to near-field effects and shear-wave velocity profiles. Journal of Applied Geophysics, 171, 103871.

Trevisani, S., Boaga, J., Agostini, L., & Galgaro, A. (2017). Insights into bedrock surface morphology using low-cost passive seismic surveys and integrated geostatistical analysis. Science of The Total Environment, 578, 186-202.

Vantassel, J., Cox, B., Wotherspoon, L., & Stolte, A. (2018). Mapping Depth to Bedrock, Shear Stiffness, and Fundamental Site Period at CentrePort, Wellington, Using Surface-Wave Methods: Implications for Local Seismic Site Amplification. Bulletin of the Seismological Society of America, 108(3B), 1709-1721.

Wood, C. M., Baker, E., Deschenes, M., & Himel, A. K. (2019). Deep shear wave velocity profiling in Northeastern Arkansas (No. TRC1603). University of Arkansas, Fayetteville.

Wood, C. M., Bernhardt, M., Moody, T., Kouchaki, B., & Rahimi, S. (2017). Rapid and Non-Destructive Assessment of Levees for Strength and Liquefaction Resistance.

Wood, C. M., Cox, B. R., Green, R. A., Wotherspoon, L. M., Bradley, B. A., & Cubrinovski, M. (2017). Vs-based evaluation of select liquefaction case histories from the 2010–2011 Canterbury earthquake sequence. Journal of Geotechnical and Geoenvironmental Engineering, 143(9), 04017066.

Wood, C. M., Deschenes, M., Ledezma, C., Meneses, J., Montalva, G., & Morales-Velez, A. C. (2019). Dynamic site characterization of areas affected by the 2017 Puebla-Mexico city earthquake. Soil Dynamics and Earthquake Engineering, 125, 105704.

Xia, J., Miller, R. D., Park, C. B., & Tian, G. (2003). Inversion of high frequency surface waves with fundamental and higher modes. Journal of Applied Geophysics, 52(1), 45-57.

Xu, X. Q., Su, L. J., & Zhu, H. H. (2017). Analysis on shear wave velocity structure of a gravel landslide based on dual-source surface wave method. Landslides, 14(3), 1127-1137.

Yasuhara, H., & Elsworth, D. (2008). Compaction of a rock fracture moderated by competing roles of stress corrosion and pressure solution. Pure and Applied Geophysics, 165(7), 1289-1306.

Yilmaz, O. (1987). Seismic data processing: SEG.

Zywicki, D. J. (1999). Advanced signal processing methods applied to engineering analysis of seismic surface waves (Doctoral dissertation, Georgia Institute of Technology).

Zywicki, D. J., & Rix, G. J. (2005). Mitigation of near-field effects for seismic surface wave velocity estimation with cylindrical beamformers. Journal of Geotechnical and Geoenvironmental Engineering, 131(8), 970-977.

Doc Express® Document Signing History

Contract: RSCH - TRC1803 - Mapping Subsurface Conditions Document: TRC1803 Final Report

Date	Signed By
09/23/2022	Sanghyun Chun Arkansas Department of Transportation Electronic Signature (Submitted)
09/26/2022	Sanghyun Chun Arkansas Department of Transportation Electronic Signature (Reviewed by Project Manager)
09/26/2022	Paul Tinsley Arkansas Department of Transportation Electronic Signature (Reviewed by Committee Chair)
04/25/2024	Sarah Tamayo Arkansas Department of Transportation Electronic Signature (Reviewed by Research)